Doctoral theses at NTNU, 2023:75

Alf André Orvik

Magmatic evolution of the Gállojávri ultramafic intrusion, Norway

Implicaitons for the formation of magmatic sulphide deposits in the Karasjok Greenstone Belt

Doctoral thesis

NTNU
Norwegian University of Science and Technology
Thesis for the Degree of
Philosophiae Doctor
Faculty of Engineering
Department of Geoscience and Petroleum

NTNU
Norwegian University of
Science and Technology

Alf André Orvik

Magmatic evolution of the Gállojávri ultramafic intrusion, Norway

Implicaitons for the formation of magmatic sulphide deposits in the Karasjok Greenstone Belt

Thesis for the Degree of Philosophiae Doctor

Trondheim, April 2023

Norwegian University of Science and Technology
Faculty of Engineering
Department of Geoscience and Petroleum

NTNU
Norwegian University of
Science and Technology

NTNU
Norwegian University of Science and Technology

Thesis for the Degree of Philosophiae Doctor

Faculty of Engineering
Department of Geoscience and Petroleum

ISBN 978-82-326-6934-9 (printed ver.)
ISBN 978-82-326-6130-5 (electronic ver.)
ISSN 1503-8181 (printed ver.)
ISSN 2703-8084 (online ver.)

Doctoral theses at NTNU, 2023:75

Printed by NTNU Grafisk senter

ABSTRACT

The Karasjok- and Central Lapland-Greenstone Belt of Norway and Finland define one of the largest Palaeoproterozoic greenstone belts in the Fennoscandian Shield and is characterised by sedimentary sequences, numerous bodies of (ultra)mafic intrusions and plume-derived komatiitic to picritic lavas. The intrusions, some with notable ore reserves, formed from mantle-derived melts during three magmatic episodes at 2.44, 2.22 and 2.05 Ga. These bodies are commonly characterised as highly dynamic systems that, in many cases, directly contributed to the anomalous metal concentrations. Because of Central Lapland's importance as a metal supplier and resource base, considerable geological research has been undertaken on the magmatic bodies in Finland. From this research, a metallogenic provinciality has emerged, with mineralisation styles varying over time, space and at various scales. However, there are few academic studies on the (ultra)mafic intrusions in the Karasjok area, inhibiting the correlation with the regional models.

The Gállojávri ultramafic intrusion in northern Norway is part of a small cluster of mineralised bodies in the Karasjok area, including the intrusions at Porsvann and Karenhaugen. Despite some interest from prospecting companies, the intrusion(s) has received little academic attention and the magmatic processes at work in the Gállojávri- and Karasjok-area are still largely unknown. This PhD thesis aims to address the gap and examine the petrogenesis of the Gállojávri intrusion through three objectives: 1) develop a petrogenetic model, 2) link the petrogenesis to established regional magmatic models and 3) evaluate the ore-forming and post-cumulus processes of the mineralisation. The objectives are met using a traditional petrological approach combined with trace element- and thermodynamic modelling. The approach includes petrography, major to trace element data on bulk rock and minerals, geochronology, bulk Nd-, Sr-, S- and Hf-isotopes in zircon. The results are reported in two peer-reviewed (published) papers and one manuscript.

Bulk geochemistry of cumulate rocks shows uniform enrichments in LILE, LREE, Pb and U. Analysed spinel exhibits a Fe-Ti trend characteristic of slowly cooled intrusive rocks. Mineral chemistries of major silicate phases imply a polybaric evolution, with pressure estimates forming a trend between 400 and 700 MPa. Zircon U-Pb geochronology yielded an age of 2051 ± 8 Ma. Radiogenic isotopes reveal large variations, commonly over small distances (dm to m). For example, bulk initial εNd ranges from -15 to +4 and initial zircon εHf ranges from -14 to -1. Bulk concentrations show that the Gállojávri intrusion is generally S-poor, with Cu/Pd ratios ranging from depleted to primitive mantle and $\delta^{34}S$ similar to mantle ratios. Primitive mantle-normalised Pt/Al and Pd/Al ratios show that unmineralised samples are enriched compared to mantle background values.

The spatial and temporal links between the Gállojávri intrusion and komatiite lavas suggest a cognate magma system. The uniform contamination indicated by bulk trace elements suggests that assimilation occurred in a staging magma chamber. Polybaric phase equilibria similarly indicate that fractionation took place in an earlier stage. The Fe-Ti trend exhibited by the analysed spinel is similar to compositions documented in subvolcanic intrusions of continental flood basalts and it is hypothesised that the Gállojávri intrusion represents a conduit to the coeval high-MgO plume-derived lavas in the Karasjok area.

Paper one uses thermodynamic modelling to simulate the documented variation in bulk major, minor and trace lithophile elements and major to minor element mineral compositions. The modelling shows that the parental magma could be the coeval Karasjok-type komatiites. The parent magma first intruded the Archaean lower crust where fractionation and assimilation yielded a hybrid melt. Second, the hybrid melt migrated and pooled in a mid-crustal magma chamber where it continued to fractionate and assimilate while remaining open to mantle-derived melt recharge(s).

Paper two reports and discusses radiogenic isotopes. The observed variation is largely consistent with the petrogenetic model from paper one. However, the most evolved isotopic signatures cannot be explained by interaction with the local Archaean basement, indicating the presence of unknown crustal components at depth. The spatial variation suggests incomplete mixing between isotopically distinct components. This variation is, therefore, in conflict with the initial thermodynamic models that assumes complete mixing between components. Paper two ascribes the large variations in Nd and Hf isotopic

signatures to local melting or dissolution of xenoliths and influx of variably contaminated melt into the semi-consolidated Gállojávri magma chamber.

The Galluljavri mineralisation is discussed in manuscript three, which reports bulk chalcophile elements, S isotopes and the chemistry of ore minerals. Petrography demonstrates that the mineralisation comprises primary and post-cumulus features. The remobilisation of certain chalcophile elements during alteration is indicated by variation in sulphide chemistry between primary and secondary types. Considering the contamination signatures in trace elements and radiogenic isotopes and the low S contents of the Gallujavri intrusion, the mantle-like $\delta^{34}S$ indicate that the crustal contaminants were S-poor. Modelling of bulk Cu/Pd ratios indicates minor fractionation of sulphide liquids and low silicate-to-sulphide mass ratios (i.e., R factor of 100–1000). Combined with petrography, these characteristics suggest late saturation of sulphides that is characterised by cotectic proportions. Consequently, based on the observed variation, the intrusion is neither S-rich nor sufficiently enriched in chalcophile elements to be an economic deposit.

Unmineralised samples, on the other hand, are enriched in chalcophile elements compared to the mantle background and show that the system was fertile. The system's fertility suggests that one of the primary reasons for not forming an economic deposit is the lack of early saturation of a sulphide liquid. This contrasts with the parental komatiite lavas where previous studies have indicated uniform depletion of chalcophile elements that suggests prior extraction of sulphide liquids. The volcanic plumbing system as a whole, therefore, shows concurrent chalcophile enrichment and depletion, which indicates a mineral potential in the cogenetic magmatic suite. This implies that the prospectivity for sulphide deposits in the Karasjok area needs to be revised and suggests that intrusions with characteristics like the Gállojávri intrusion should be considered potential exploration targets. Two potential prospective analogues in the region are the intrusions at Porsvann and Karenhaugen. Both intrusions have Cu/Pd ratios compatible with early S saturation and R factors large enough to promote economic metal concentrations.

ACKNOWLEDGEMENTS

In addition to the people and parties acknowledged in the original works on which this thesis is based, I would first like to thank my supervisors. I am grateful to Bjørn E. Sørensen for your open-door policy and for always being available to discuss my thoughts and ideas. Thank you, Trond Slagstad, for your wisdom and willingness to listen and discuss. Thank you again for painstakingly reviewing my writing, although having to correct the same mistakes time, and time again. I want to thank Lars Petter Nilsson, who initiated the project, for being available to share his knowledge even after retiring. Your understanding and enthusiasm for geology are truly inspiring. I am grateful to Eduardo T. Mansur for guiding me and sharing his thoughts and experience on magmatic sulphides. I consider myself fortunate to have had the chance to learn from such outstanding scientists and individuals.

I am very grateful to my partner and rock, Marianne Qvam. You went through a pregnancy and the beginnings of our small family while my mind was elsewhere. This thesis would not have been possible without your support and perseverance. To my son, Anton, thank you for being healthy, happy and patient. You may not have done it on purpose, yet you have made this thesis possible. I love you both.

TABLE OF CONTENTS

1 INTRODUCTION

The Palaeoproterozoic Karasjok Greenstone Belt (KGB) in Norway is a northward extension of the Central Lapland Greenstone Belt (CLGB) in Finland. Together, the belts can be traced all the way from the Norwegian coast in the north to the Russian border in the southeast, making it one of the largest Palaeoproterozoic greenstone belts in the Fennoscandian Shield (Hanski & Huhma, 2005, Moilanen *et al.*, 2021). The CLGB contains significant ore bodies of various types, such as iron, gold and copper-nickel and the platinum group elements (PGE), some of which are also found on the Norwegian side of the border (Eilu, 2012, Nilsson *et al.*, 2016). The strongly covered KGB has drawn the attention of gold panners and prospecting companies throughout the twentieth century, with the Gállojávri Ni-Cu-PGE mineralisation, the focus of this PhD project, being one of the most important targets (Nilsson *et al.*, 2016). Despite interest from prospecting companies, the intrusion has received little academic attention, and the processes that formed the Gállojávri intrusion are still largely unknown.

Considerable geological research has been conducted in the Finnish part of the Fennoscandian Shield, partly because of its significance as a metal supplier and resource base (Lahtinen *et al.*, 2011). This body of research has led to many papers, chapters and books that discuss the geological evolution and related metallogeny of the Fennoscandian Shield, such as Weihed *et al.* (2005), Hanski and Huhma (2005), Lahtinen *et al.* (2010), Lahtinen *et al.* (2011), Maier *et al.* (2015) and Makkonen *et al.* (2017). With a greater understanding of the distribution of ore deposits in the Fennoscandian Shield, a metallogenic provinciality has emerged, with mineralisation styles varying in time and space and at different scales (Hanski, 2015). The extensive body of isotopic studies has been critical in resolving many of the uncertainties in the timing of the formation of metal deposits and their host rocks (Hanski, 2015, Huhma *et al.*, 2018, Huhma *et al.*, 2011). Along with a better understanding of crustal evolution in the Fennoscandian Shield, the research has established a relationship between different classes of ore deposits and their tectonic settings (Hanski, 2015). In Finland, for example, the ultramafic to mafic bodies of the CLGB, some of which have significant ore reserves, formed during three magmatic episodes at approximately 2.44, 2.22, and 2.05 Ga that has been linked to mantle plumes and prolonged extension (c. 500 Ma) of the Archaean craton (Hanski & Huhma, 2005, and references therein).

This PhD project arose from a desire to better understand the petrogenesis of the Gállojávri intrusion and its associated mineralisation. Despite the local nature of this project, with a focus

on one small igneous body, it is one of the first detailed academic studies of ultramafic to mafic intrusions in the KGB. Therefore, a sub-objective of this project is to evaluate the applicability of regional petrogenetic and ore-formation models largely developed from the Finish part of the CLGB.

The thesis consists of a collection of two peer-reviewed papers and one unpublished manuscript that form the basis of the PhD project. This synthesis aims to summarise the findings, show how the pieces of the thesis are interrelated and contribute to answering the overarching research questions. To achieve the goal of this synthesis, the chapters are organised as follows:

- Chapter 2 provides context for the thesis and some theoretical considerations.
- Chapter 3 outlines the geological background required to understand the thesis.
- Chapter 4 outlines the objectives of the PhD project and how they will be realised.
- Chapter 5 summarises the papers and emphasises some of the most important findings.
- Chapter 6 provides a discussion focusing on the objectives.
- Chapter 7 presents the main conclusions.
- Chapter 8 provides some thoughts on limitations and direction of future research.

2 BACKGROUND (AND SOME THEORY)

2.1 Ultramafic-mafic intrusions

Ultramafic to mafic intrusions come in many shapes and sizes, from thin dykes and sills to massive structures, such as the Dufek intrusion (50,000 km^2) of Antarctica and the Bushveld complex (66,000 km^2) of South Africa (Frost & Frost, 2019, and references therein). Although called into question (e.g., Cashman *et al.*, 2017), the larger layered intrusions are commonly believed to be melt-dominated chambers (e.g., Kruger & Latypov, 2020) that require a substantial volume of magma in a short period of time (e.g., Annen *et al.*, 2022). The larger intrusions commonly preserve spectacular igneous textures and structures and provide important insights into the differentiation processes of mantle-derived melts. These processes are reflected in the igneous layering that commonly distinguishes these intrusions and is thought to form from a combination of processes (reviewed by Namur *et al.*, 2015), the most important being fractional crystallisation. Other processes that can (and generally do) influence the evolutionary histories of magmatic bodies include recharge, liquid immiscibility and crustal contamination (Winter, 2013).

Magmatic conduit systems represent channels in the lithosphere that funnel mantle melts to larger magma chambers (e.g., Uitkomst intrusion, South Africa; Maier *et al.*, 2018) or the crustal surface (e.g., Noril'sk and Talnakh type intrusions, Siberia; Naldrett *et al.*, 1995). The conduits tend to be smaller and more irregular, with larger surface area-to-volume ratios, where the effects of recharges and contamination have a more pronounced influence on the evolution. Magmatic conduit systems inherently have higher melt fluxes and thereby represent more dynamic environments that often involve complicated multistage and polybaric histories. Additionally, the movement of magma through the continental lithosphere offers numerous opportunities for thermal erosion and the subsequent addition of anatectic melt and country-rock residue to a magma body (Arndt & Jenner, 1986, Ding *et al.*, 2012, Fowler *et al.*, 2004, Orvik *et al.*, 2022b), in that way increasing the efficiency and proportion of crustal assimilation.

Anatectic melts formed by crustal melting typically differ significantly from mantle melts in their radiogenic and stable isotope compositions (Peate *et al.*, 2008). Therefore, adding small amounts of crustal melts can drastically alter the composition of the passing mantle-derived magma. Furthermore, the chemical and isotopic effects of crustal assimilation on magmas that move through the crustal column can reveal crucial details about the regional crustal architecture and composition (Dickin & Durant, 2002, Orvik *et al.*, 2022b, Peate *et al.*, 2008).

2.2 Mechanisms that contribute to magma diversity

2.2.1 Magmatic differentiation

Differentiation of a magmatic system requires the physical separation of two or more phases in a multiphase system. The efficacy of fractionation is determined by differences in physical properties such as viscosity, density, shape and size. As stated above, the most common differentiation process is fractional crystallisation (liquid-solid), wherein crystals either settle or float due to density contrasts. Although differentiation can also be caused by liquid-liquid and liquid-vapour separation.

The thermodynamic properties of the system determine the phase or phases that crystallise or exsolve from natural magmas, such as pressure and temperature and the major (>1 wt. %) and minor (>0.1 wt.%) element composition. Conversely, that means that the crystallisation of minerals, and subsequent formation of cumulate rocks, also record changes in the properties of the magmatic system.

Trace elements (<0.1 wt.%), in general, are too diluted to be primary stoichiometric constituents of magmatic phases and therefore do not affect phase equilibria (Hanson, 1989, Hanson & Langmuir, 1978). However, because of their low concentration and greater sensitivity to fractionation, they are critical in answering questions about magma generation and evolution. They are typically found as impurities in all phases present in a system, and the distribution is commonly described by a partition coefficient (K_D). For the relatively dilute trace elements, partitioning during crystallisation can be formulated as follows:

$$K_D^i = {C_S^i}/{C_L^i}$$

Where C is the concentration of element i in the liquid (L) and the solid (S) phase. However, in fractionating magmatic systems, multiple phases are usually saturated simultaneously. In these cases, the chemical fractionation is described by the bulk partition coefficient (D_i):

$$\mathrm{D_i} = \sum \mathrm{W_A K_D^i}$$

Where W_A is the weight fraction of phase A and K^i_D is the partition coefficient for element i and phase A.

2.2.2 Assimilation

Bowen (1928) recognised the crucial link between crustal assimilation and fractional crystallisation. He understood that under the right conditions, the cooling and crystallisation of magma could release latent heat that could raise the temperature of the wall rock above the local solidus (Fowler *et al.*, 2004). The partial melt of the wall rock (i.e., anatectic melt) is then available to be added to the magma chamber, thereby contaminating the system. Disequilibrium mineral assemblages, partially digested country-rock xenoliths, hybrid rocks and crustal geochemical signatures in mantle-derived magmas can all be used to detect crustal contamination. Isotopic signatures are likely the best way to identify assimilation, particularly the contamination of mantle-derived magmas by continental crust.

With time, the continental crust becomes progressively enriched in $^{87}Sr/^{86}Sr$ and depleted in $^{143}Nd/^{144}Nd$ and $^{176}Hf/^{177}Hf$. Therefore, primitive magmas with unusually high values of $^{87}Sr/^{86}Sr$ and low values of $^{143}Nd/^{144}Nd$ and $^{176}Hf/^{177}Hf$ are probably contaminated by ancient continental material (Winter, 2013).

For example, ^{147}Sm is a radioactive isotope that decays to ^{143}Nd with a half-life of 1.06×10^{11} years (decay constant (λ)=$6.54\times10^{-12}yr^{-1}$). The abundance of the non-radiogenic ^{144}Nd isotope is constant through time. Since ^{143}Nd increases continuously with radioactive decay, the $^{143}Nd/^{144}Nd$ ratio will increase with time as a function of the Sm/Nd ratio of the reservoir. Samarium is more compatible in solid phases than Nd due to its slightly lower ionic radius. The fractionation of Sm from Nd during melting and differentiation, therefore, modifies the Sm/Nd ratio, which changes the relative abundance of the ^{143}Nd isotope over time. The continental crust, for example, is derived by partial melting of the mantle and therefore has a lower Sm/Nd that translates to lower $^{143}Nd/^{144}Nd$ with time.

Knowing the age and measuring the present-day ratios of $^{143}Nd/^{144}Nd$ and $^{147}Sm/^{144}Nd$[1], one can compute the initial $^{143}Nd/^{144}Nd$ ratio of a closed system by the equation:

$$\left(\frac{^{143}Nd}{^{144}Nd}\right)^{t_0}_{\text{sample}} = \frac{^{143}Nd}{^{144}Nd} - \frac{^{147}Sm}{^{144}Nd}\left(e^{\lambda t_0} - 1\right)$$

where t_0 is the time of system closure.

[1] If the Sm/Nd ratio is known, it can be calculated using mass balance.

Measured isotopic signatures are often reported with the epsilon notation introduced by DePaolo and Wasserburg (1976a, b) to facilitate the visualisation and interpretation of $^{143}Nd/^{144}Nd$ ratios. The epsilon parameter εNd compares the measured $^{143}Nd/^{144}Nd$ ratio of a sample to the ratio of a hypothetical chondritic reservoir (CHUR) and is defined by the equation:

$$\varepsilon Nd_t = \left[\frac{(^{143}Nd/^{144}Nd)^t_{sample}}{(^{143}Nd/^{144}Nd)^t_{CHUR}} - 1\right] \times 10^4$$

Where time (t) is usually chosen to be t_0, the time the system separated from a source and closed (typically the crystallisation age for a magmatic rock). Depleted by melt loss, the mantle will progress towards more positive εNd with time, whereas the continental crust will progress towards increasingly negative εNd values.

2.2.3 Magma replenishment (recharge and mixing)

In addition to fractional crystallisation and assimilation, the addition of new magma batches (recharge), which are usually chemically and thermally distinct, also affects magma evolution through mixing. Furthermore, if the specific enthalpy (heat) of the recharge is higher than that of the host magma, it also provides extra energy for country-rock heating and anatexis (Fowler *et al.*, 2004). Significant changes in liquidus mineral assemblages, variations in mineral compositions or trace element ratios that differ from what fractional crystallisation predicts or changes in isotope compositions can all indicate the presence of new magma pulses (e.g., Davidson & Tepley, 1997, Ginibre *et al.*, 2007, Latypov, 2015, Luolavirta, 2018).

How well a new injection of magma is mixed with a host magma depends on the contrasts in physical properties (e.g., density and viscosity). If a new batch of magma has a lower density than the resident magma, it could produce a plume-like feature. The new pulse will turbulently mix during ascent, resulting in a density-stratified hybrid layer at the top of the chamber. In contrast, if the density of the recharge is greater than the host magma, it might produce a fountain-like feature, and mixing will be limited to a layer along the base of the chamber (Campbel *et al.*, 1983). However, the recharge of magma is not limited to melt-dominated chambers. Injection and progressive through-flow of melt in chemical disequilibrium with pre-existing crystal mushes can significantly modify the cumulates by preferentially removing or depositing new minerals (Holness *et al.*, 2007). In the Reinfjord Ultramafic Complex of Norway, for example, the central dunites formed by a reaction between semi-consolidated

pyroxene-bearing cumulates and the late injection of olivine-saturated magma that dissolved the pyroxenes to form replacive dunites (Grant *et al.*, 2016, Larsen *et al.*, 2018).

2.2.4 Combined processes

Two or more processes may operate concurrently or sequentially during the generation, migration and solidification of mantle-derived magmas. Moreover, as indicated above, two processes may operate cooperatively, like increased anatexis due to recharge. Because many of the processes have similar effects, determining the relative contribution of each with any degree of certainty may be difficult (Winter, 2013).

2.3 Magma Chamber Simulator

Several thermodynamic tools, such as the MELTS engine family (Ghiorso & Gualda, 2015, Ghiorso & Sack, 1995, Gualda *et al.*, 2012), are available to compute the compositional evolution of magmatic systems as governed by the principles of phase equilibria. However, most tools are not well suited to model open systems characterised by mixed processes. The Magma Chamber Simulator (MCS) represents a significant step forward in overcoming these issues as it is designed to model the multicomponent and multiphase behaviours of magmatic systems (Bohrson *et al.*, 2014). More information on the use and design of the modelling tool can be found in several papers introducing MCS (e.g., Bohrson *et al.*, 2014, Bohrson *et al.*, 2020, Heinonen *et al.*, 2020, Heinonen *et al.*, 2021, Heinonen *et al.*, 2019), on which this section is based.

The MCS is a mass- and energy-constrained tool for modelling the magmatic evolution of open systems experiencing concurrent fractional crystallisation, recharge(s) and assimilation. The resident magma, recharge magma and wall-rock subsystems, for which the MCS calculates the phase equilibria (MELTS engine) and geochemical evolution, are separated by boundaries capable of transferring heat and mass. For example, if enough heat is transferred to the country rock from the resident magma, it may exceed its solidus temperature and partially melt. In simulations where the wall-rock melt fraction exceeds a pre-determined percolation threshold (i.e., a critical melt-volume fraction), the surplus anatectic melt is added to the chamber and mixed with the resident magma. Multiple recharges of melt or magma can also be added to the resident magma chamber; each recharge with a specified mass, temperature and bulk chemical composition. The progress variable of the MCS is the resident magma temperature, and the wall-rock and magma chamber evolve due to mass and heat exchange, with phase equilibria

calculated at pre-determined temperature decrements. The simulation progresses until the resident magma and wall-rock reach thermal equilibrium.

Trace elements are treated separately in MCS using the MCS-*Traces* tool as they are too dilute to influence phase equilibria. However, information on the relative quantities of stable phases in magmatic systems is required to calculate D_i. As a result, it is impossible to model trace elements (and isotopes) with MCS without first recording major and minor element phase equilibria and mass fractions. The MCS-*Traces* tool reads the primary output as the stepwise progression of the magmatic system and then calculates isotopic ratios and trace element concentrations for each step. The K_D for each relevant phase and element, as well as initial trace element concentrations and isotopic compositions for the resident chamber and wall-rock subsystems, are required to complete these calculations. The exception is the recharge subsystems, which only require initial trace element concentrations and isotopic ratios.

2.4 Orthomagmatic sulphide deposits

Magmatic Ni-Cu-PGE deposits are formed by accumulating immiscible sulphide liquids that have scavenged chalcophile elements from a coexisting silicate melt (Barnes *et al.*, 2017a, Campbell & Naldrett, 1979, Naldrett, 2004). The deposits are naturally divided into two groups: those valued primarily for their Ni (and Cu), which tend to be sulphide-rich, and those valued primarily for their PGE, which tend to be sulphide-poor (Naldrett, 2011, Naldrett, 2004). The Ni-dominated deposits are often contained in small mafic to ultramafic intrusions that are commonly identified as magma conduits (Lightfoot & Evans-Lamswood, 2015) or komatiite flows and their subvolcanic counterparts (Barnes, 2006, Barnes *et al.*, 2017a). The PGE-dominated deposits are primarily stratiform accumulations within large layered mafic to ultramafic intrusions (Barnes *et al.*, 2017a, Naldrett, 2004, Naldrett *et al.*, 2008).

The formation of an economic sulphide deposit is contingent on both lithospheric-scale and deposit-scale processes (Barnes *et al.*, 2016). These processes include mechanisms of magma generation, ascent and the formation of an immiscible sulphide liquid that collects metals and becomes concentrated in an accessible part of the system (e.g., Barnes & Maier, 1999). This review briefly aims to cover the main characteristics and features of orthomagmatic sulphide deposits. An emphasis is made on Ni-dominated deposits hosted by mafic-ultramafic intrusive bodies, although these processes broadly apply to PGE-dominated ore genesis (Naldrett, 2004). While PGE-dominated deposits form a continuum of chemical compositions with Ni-dominant

deposits (Barnes *et al.*, 2016, Naldrett, 2004), they call for specific process controls outside the scope of this review.

2.4.1 Sulphide solubility

Sulphur solubility is simply the amount of sulphur required in a melt to achieve saturation. This parameter controls how much S is dissolved during partial melting of the mantle and whether an immiscible fraction develops in a given magma once it is separated from the source. The sulphur solubility in silicate melts is commonly expressed as the sulphur concentration at sulphide (S^{2-}) saturation (SCSS; Shima & Naldrett, 1975), representing the maximum amount of sulphur a melt can dissolve before a sulphide phase segregates. The SCSS in mafic to ultramafic magmas is influenced by several variables, including pressure, temperature, oxygen fugacity and a set of major element oxides in the host silicate melt (Virtanen *et al.*, 2022). For example, the SCSS in a mafic magma increases as a function of increasing temperature and FeO content but decreases with increasing pressure and SiO_2 content (Fig. 1A to C; reviewed in Naldrett, 2011).

2.4.2 Generation and ascent of magmas

The primary source of the metals in magmatic ores is the transporting magma (Barnes *et al.*, 2016). Therefore, adequate metal concentrations in the parental magma is a prerequisite for forming a magmatic deposit, which ultimately reflects the source of the melt. Because crustal rocks are depleted in elements such as PGE and Ni, magmas that give rise to magmatic Ni–PGE deposits are thought to have originated in the mantle (Maier, 2015). The major mineral in the mantle is olivine, which hosts most of the Ni in its crystal lattice. Copper and Pd do not partition into olivine, so their concentration in the mantle is controlled by sulphides (Barnes & Lightfoot, 2005)

The degree of mantle melting must be relatively high for mantle magmas to be fertile in chalcophile metals (Maier, 2015). When mantle olivine melts, Ni is released, with concentrations increasing in the magma as the degree of melting increases. Because Cu and PGE are primarily hosted by mantle sulphide, their concentration in the partial melt depends on the solubility of S (Barnes & Maier, 1999). As mafic to ultramafic melts have relatively low S solubilities at mantle pressures (Fig. 1B), experimental studies have indicated that a minimum of 20-40% partial melting would be required to absorb all of the sulphides (Barnes & Lightfoot, 2005, and references therein). Figure 1D reflects this relationship; palladium increases sharply

as the sulphide is dissolved and is diluted as the melt fraction increases, whereas Ni increases throughout mantle melting as it is mostly supplied by olivine.

As noted by Barnes and Maier (1999), the required fraction of partial melt for dissolving sulphides is very loosely constrained. Depending on assumptions about S concentrations in the mantle and S solubility at high pressures, the required fraction of partial melt could be as low as 12% or as high as 50% (Barnes, 1987). Nonetheless, most PGE and Ni deposits tend to be associated with rocks that crystallised from magmas with >8–10 wt.% MgO, broadly consistent with the theoretical considerations (Maier, 2015). Another point to consider is that if a large deposit is to form, a large amount of mantle must undergo this high degree of partial melting. The tectonomagmatic conditions that favour this type of melting are typically associated with mantle plume events that generate large amounts of magma (Barnes & Lightfoot, 2005).

The spatial and temporal distribution of magmatic sulphide deposits suggest an empirical relationship with major lithospheric boundaries, specifically craton margins (Begg *et al.*, 2010). In addition, most magmatic sulphide deposits occur within long-lived magmatic pathways for mantle-derived magmas (Barnes *et al.*, 2016). The pathways are believed to facilitate rapid magma ascent, thereby delaying differentiation and metal loss due to the segregation of olivine and sulphides (Maier, 2015). A mantle plume intersecting a continental rift is an ideal location for all of these processes (Barnes & Lightfoot, 2005). The plume provides a large volume of high-degree partial melts and the rifted lithosphere allows easy access through the crust.

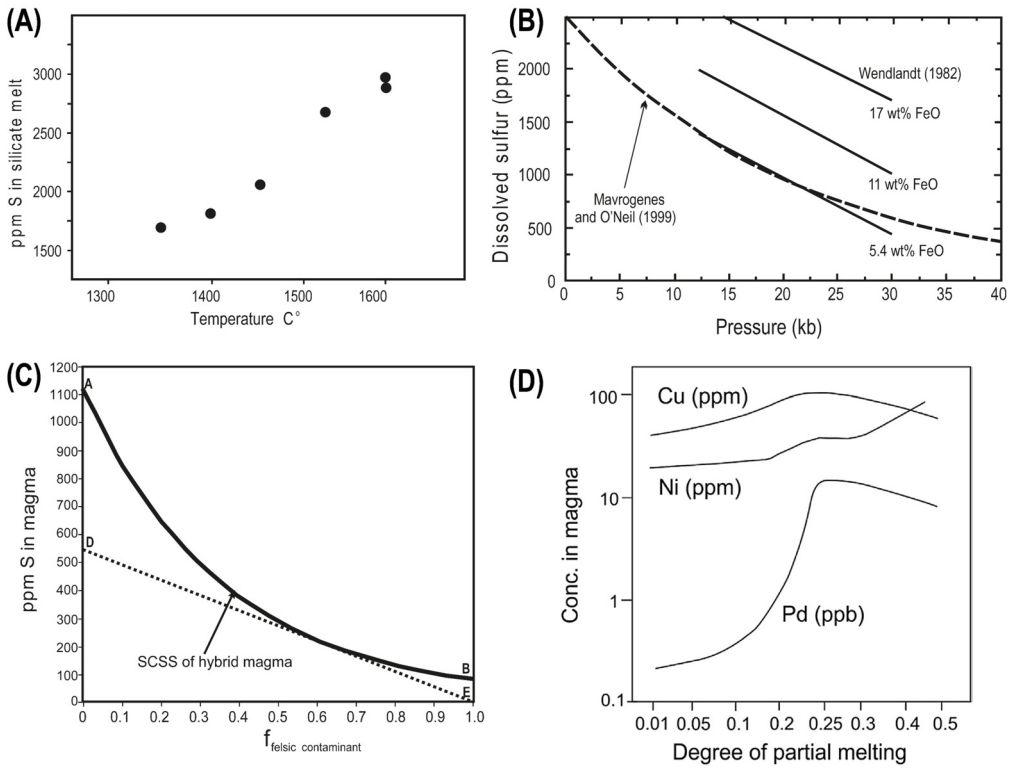

Figure 1: (A) The temperature effect on the SCSS. (B) Experimental determination of sulphur solubility in basaltic melts with varying FeO content as a function of pressure at 1,400°C. Data from Wendlandt (1982) and Mavrogenes and O'Neill (1999). (C) SCSS of a contaminated mafic magma plotted against the mass fraction (f) of a S-free, Si-rich contaminant. The sulphide saturation values for the end members are represented by points A and B. The contaminant S concentration (0 ppm) is represented by point E. Sulphide saturation can be achieved by mixing a siliceous melt with a mafic magma that has a S concentration greater than that represented by point D. (D) Palladium, Cu and Ni concentrations in partial mantle melts. Fig A to C modified from Naldrett (2011); Fig D from Maier (2015).

2.4.3 Sulphide saturation

High-degree mantle melts are typically undersaturated in S in the mantle (Bekker *et al.*, 2009), and the negative pressure feedback on SCSS limits sulphide saturation in mafic magmas as it rises (Fig. 1B; Mavrogenes & O'Neill, 1999, Wendlandt, 1982). Closed magmatic systems may reach sulphide saturation at crustal levels through cooling and crystallisation and crystallise sulphide in cotectic proportions, which are generally not large enough to be economically viable[2] (Ripley & Li, 2013, Virtanen *et al.*, 2022). Furthermore, if sulphide saturation occurs late in the crystallisation history of a magma, Ni and PGE may already have been extracted

[2] This is not necessarily the case for large intrusions containing S-poor and PGE-dominated deposits (Maier, 2015, Ripley & Li, 2013).

(Robb, 2020). Therefore, a situation in which magmas become saturated early in the crystallisation history is by many considered key for developing a Ni sulphide deposit (e.g., Barnes & Lightfoot, 2005, Li & Ripley, 2009, Ripley & Li, 2013). A process that can facilitate sulphide saturation has already been indicated in Fig. 1C: the mixing of components, either by recharge or contamination by country rocks.

Adding sulphur is probably the simplest method of promoting saturation (e.g., Li & Ripley, 2009, Ripley & Li, 2013). However, recent research has also indicated that some magmatic sulphide deposits may have only contained mantle-derived S (e.g., Seat *et al.*, 2009). The importance of assimilation of S-bearing crustal rocks during ascent and emplacement of mafic-ultramafic intrusions is commonly assessed using S isotopes (e.g., Barnes & Ripley, 2016, Ripley & Chusi, 2007, Ripley & Li, 2003).

Because ^{34}S and ^{32}S are the two most abundant S isotopes, these are the ones that are frequently measured (Sharp, 2017). The isotopic ratio is commonly reported as $\delta^{34}S‰$, relative to the international scale Vienna-Canyon Diablo Troilite (V-CDT), expressed as:

$$\delta^{34}S_{sample} = \left(\frac{(R)_{sample}}{(R)_{V-CDT}}\right) \times 1000$$

where $R = {}^{34}S/{}^{32}S$.

The mantle $\delta^{34}S$ values are typically thought to range from 0±2‰ (Ripley & Li, 2003), but some studies suggest a wider range around 0‰ (Seal, 2006). Significant deviations from the mantle range indicate the addition of external sulphur. However, there are two things to consider (Lesher, 2017): 1) The observation that the $\delta^{34}S‰$ value is similar to the mantle does not prove that the S came from the mantle. It simply means that the S isotopes in the source or contaminant have not fractionated from the mantle. 2) Sulphur isotopes are sensitive to resetting in dynamic magmatic systems, where $\delta^{34}S$ values can be shifted toward mantle values as coexisting sulphide and silicate liquids interact (e.g., Lesher & Burnham, 2001).

2.4.4 Sulphide-silicate K_D and the collection of metals via sulphide exsolution

The ability of an immiscible sulphide melt to concentrate metals depends on the extent to which metals partition themselves between the coexisting sulphide and silicate melts. Experimentally determined partition coefficients ($K_{Sul\text{-}Sil}$) for Ni and Cu lie in the 100 to 1000 range, whereas the PGE range from c. 10^4 to 10^5 (reviewed in Barnes & Maier, 1999). Suppose an immiscible

sulphide liquid equilibrates with an unlimited reservoir of magma. In that case, the concentration of a trace metal in that sulphide liquid is just the product of the $K_{Sul\text{-}Sil}$ and the initial concentration of the metal in the coexisting silicate melt. This is not normally the case, and the metal collected by a sulphide liquid will depend on the mass ratio of silicate-to-sulphide liquids (R factor). Campbell and Naldrett (1979) provided the first mathematical formulation that relates the R factor to the distribution of chalcophile metals between coexisting sulphide and silicate liquids:

$$C_{sul} = C_0 K_{sul-sil}(\mathrm{R}+1)/(\mathrm{R}+K_{sul-sil})$$

where C_{sul} is the concentration in the sulphide liquid; C_0 is the initial metal concentration in the silicate magma; R is the mass ratio of silicate magma to sulphide liquid. When $R>10K_{sul\text{-}sil}$, variations in R have relatively little effect on C_{sul} (Campbell & Naldrett, 1979).

Late sulphide saturation, for example, may have a low R factor simply because the volume of remaining silicate magma is small (Robb, 2020), whereas early saturation, in which a sulphide liquid sinks through a column of magma (or turbulently mixes) equates to a high R factor (Barnes & Maier, 2002, Brügmann *et al.*, 1993).

2.4.5 Concentration and fractionation of sulphides

The immiscible sulphide liquid must be concentrated in a specific (and accessible) location within the magmatic system to form a sulphide deposit. Otherwise, the rocks may contain widely disseminated sulphides of too low grade to be considered economical (Barnes & Lightfoot, 2005). Massive to semi-massive Ni-Cu-PGE mineralisations are frequently found in footwall embayments, dyke dilations, magma conduit throats and horizontal segments of dyke-chonolith and dyke-sill complexes, which act as fluid-dynamic traps for dense sulphide liquids (Lesher, 2017, Lesher, 2019).

Many sulphide ore deposits are compositionally zoned with an Fe-rich component enriched in Rh and IPGE (Os, Ir and Ru) and a Cu-rich component enriched in Pt, Pd and Au (Barnes & Maier, 1999). This zonation is thought to occur when magmatic sulphide liquid crystallises into an Fe-rich monosulphide solid solution (MSS) and a refractory Cu-rich liquid that later crystallises intermediate solid solution (ISS) and possibly platinum group minerals (PGM).

As reviewed by Mansur *et al.* (2021), upon cooling, a sulphide liquid (below 1190°C) will start to crystallise MSS and incorporate elements such as Fe, Ni, Rh and IPGE, whereas Cu, Pt, Pd

and Au are incompatible (Li *et al.*, 1996, Liu & Brenan, 2015, Mungall, 2007, Mungall *et al.*, 2005, Sinyakova *et al.*, 2016, Sinyakova *et al.*, 2019). Below 950°C, the residual Cu-rich liquid crystallises Cu-rich ISS (Cabri, 1973, Kosyakov *et al.*, 2012). The trapped sulphide liquid may become sufficiently enriched in incompatible elements (particularly Pt and Pd) to saturate composite PGM (Dare *et al.*, 2014, Liu & Brenan, 2015, Mansur *et al.*, 2020a).

At c. 650°C MSS exsolves into pyrrhotite + pentlandite ± chalcopyrite, with MSS-compatible elements (e.g., Rh and IPGE) partitioning between pyrrhotite and pentlandite (Kelly & Vaughan, 1983, Mansur *et al.*, 2020a). If the MSS is S-rich, pyrite can exsolve during cooling at the expense of pentlandite (Kullerud & Yoder, 1959). Furthermore, pentlandite and pyrite cannot coexsolve until 230°C, when the tie line in the ternary Fe-Ni-S system breaks down (Naldrett & Kullerud, 1967, Naldrett *et al.*, 1967). Upon cooling, the ISS exsolves to either (depending on the S content of the system) chalcopyrite + pyrite (high fS_2), chalcopyrite + pyrrhotite (intermediate fS_2) or cubanite + pyrrhotite (low fS_2; Lusk & Maxwell Bray, 2002, Mansur *et al.*, 2021). Additionally, the MSS and ISS may get saturated in PGE during progressive cooling and PGM may exsolve from the MSS and ISS (Duran *et al.*, 2017, Godel & Barnes, 2008, Godel *et al.*, 2007, Mansur & Barnes, 2020).

The development of magmatic sulphide deposits can be considered a series of igneous processes, however, the final result may have been influenced by factors such as interaction with late magmatic fluids, deformation and metamorphism (Mansur *et al.*, 2021). For example, pyrite is typically observed replacing magmatic sulphide assemblages (mainly pyrrhotite) as a result of postcumulus re-equilibration with late magmatic fluids (Dare *et al.*, 2011, Duran *et al.*, 2015, Holwell *et al.*, 2017, Piña *et al.*, 2013, Piña *et al.*, 2016).

3 GEOLOGICAL BACKGROUND

The Palaeoproterozoic tectonic evolution of the Karelian craton, the Archaean nucleus of the Fennoscandian Shield, includes a long period of rifting (c. 2.5-2.0 Ga), which eventually led to continental breakup (Lahtinen *et al.*, 2005). The rifting caused significant mafic volcanism and the formation of Palaeoproterozoic greenstone belts, including the CLGB (Fig. 2; Hanski & Huhma, 2005). The final closure of the rift basins occurred by continent-continent collision during the composite Svecofennian orogeny (c. 1.9–1.8 Ga; Lahtinen *et al.*, 2005).

3.1 Central Lapland Greenstone Belt

The CLGB records depositional formation during a considerable period, starting with mafic magmatism and sedimentation on top of the Archaean basement at c. 2.44 Ga and culminating in orogenic deformation at c. 1.9 Ga (Hanski & Huhma, 2005). The belt is characterised by thick sequences of sedimentary and volcanic rocks formed in various geotectonic environments during the supracrustal evolution. In addition to the supracrustal rocks, three episodes of intrusive magmatism produced ultramafic to mafic bodies at c. 2.44, 2.22 and 2.05 Ga (Hanski & Huhma, 2005, and references therein). See Hanski and Huhma (2005), Hanski and Melezhik (2013) and Hanski (2013) for detailed summaries of the Palaeoproterozoic depositional and magmatic evolution of the CLGB.

The onset of the evolution is marked by metavolcanic rocks and the formation of layered intrusions in northern Finland. Ages of both extrusive and intrusive rocks converge to a narrow range of about 2.45-2.43 Ga (Amelin *et al.*, 1995, Hanski & Huhma, 2005, Mutanen & Huhma, 2001, Puchtel *et al.*, 1997). The metavolcanic rocks belong to the Onkamo Group and have been linked to an emerging mantle plume during the early stages of rifting. In this regard, the metavolcanic rocks bear similarities to more recent continental flood basalts deposited in intracontinental basins (Amelin *et al.*, 1995, Hanski & Huhma, 2005, Hanski *et al.*, 2001c, Puchtel *et al.*, 2001). Terrigenous arkoses and polymictic conglomerates are the associated sedimentary rocks, likely reflecting a regional domal uplift related to the thermal anomaly provided by the plume (Hanski & Huhma, 2005).

Following the brief mantle plume magmatism, a lengthy period of cratonic sedimentation resulted in thick sequences of quartzites, mica schists and sporadic mafic volcanism. The sedimentary rocks grade transgressively to phyllites and graphite- and sulphide-bearing schists of the Savukoski Group, indicating a deepening of the basin (Hanski & Huhma, 2005).

Common for the quartzites are c. 2.2 Ga mafic sills (Hanski *et al.*, 2001b) that form concordant and density-differentiated sheets that may reach several hundred metres in thickness and can commonly be traced for several kilometres (Hanski & Huhma, 2005).

The metasedimentary rocks are overlain by c. 2.05 Ga primitive high-MgO volcanic rocks described as the upper komatiites, or the komatiite-picrite association of northern Finland and Norway (Fig. 2; Barnes & Often, 1990, Hanski & Huhma, 2005, Hanski *et al.*, 2001a, Krill, 1985a, Puchtel *et al.*, 2020). These rocks can be followed for more than 400 km from the Russian border in the east through the CLGB and KGB to the Norwegian coast in the north (Barnes & Often, 1990, Hanski *et al.*, 2001a, Puchtel *et al.*, 2020). Similarly aged mafic intrusions can be found in many parts of northern Finland, especially in the Savukoski Group (Hanski & Huhma, 2005, Rastas *et al.*, 2001). Such as the Savukoski Group hosted 2058±4 Ma Kevitsa intrusion (Mutanen & Huhma, 2001), the host of a significant Cu-Ni-PGE sulphide deposit (Luolavirta *et al.*, 2018c, Mutanen, 1997, Santaguida *et al.*, 2015).

The U-Pb and Sm-Nd data available on mafic rocks in the Fennoscandian Shield show several stages of Palaeoproterozoic lithospheric rifting (Huhma *et al.*, 2018), although the exact moment of breaking up is unknown (Hanski & Huhma, 2005). According to Korsman *et al.* (1999), a marginal sea developed between 2.10 and 2.06 Ga in Fennoscandia (Hanski & Huhma, 2005). However, the best evidence for the final breakup comes from ophiolite complexes, which demonstrate that by c. 2.00 Ga, continental fragmentation had progressed to sea-floor spreading (Hanski & Huhma, 2005).

3.1.1 The Karasjok Greenstone Belt

The northernmost section of the CLGB, the KGB, is a c. 160 km-long and 20–40 km-wide linear feature (Barnes & Often, 1990, Krill, 1985b, Melezhik *et al.*, 2015, Often, 1985). To the north, the KGB is overlain by autochthonous Ediacaran to Cambrian sedimentary successions of the Dividal Group and allochthonous Caledonian nappes (Barnes & Often, 1990, Siedlecka & Roberts, 1996). To the west, the volcano-sedimentary succession of the KGB unconformably overlies and is partly thrust over the tonalite-trondhjemite-granodiorite-granite (TTGG)-dominated Archaean Jergul Gneiss Complex (Bingen *et al.*, 2015, Melezhik *et al.*, 2015, Often, 1985). To the east, the belt dips under the Tanaelv Migmatite Complex, which in turn is overthrust by the Lapland Granulite Belt (Fig. 2; Krill, 1985b, Often, 1985).

In the Lakselv area, the volcano-sedimentary succession of the KGB has no significant tectonic breaks and therefore is likely to represent a coherent lithostratigraphical succession (Fig. 3; Braathen & Davidsen, 2000). Several lithostratigraphic subdivisions have been proposed for different parts of the KGB (e.g., Often, 1985, Siedlecka, 1985, Siedlecka *et al.*, 1985); Here, the subdivision proposed by Davidsen (1994) and Braathen and Davidsen (2000) for the Lakselv valley (Fig. 3B) is adopted, where we find the most complete sections through the KGB. From bottom to top, the lithostratigraphy consists of the Lavtevárri Formation, the Čorgaš Formation, the Briitágielas Formation and the Fossestrand Formation. In the following review of the geology, the prefix 'meta' is omitted, however, it should be noted that the KGB lithostratigraphy underwent greenschist- to amphibolite-facies metamorphism during the Svecofennian orogeny (Braathen & Davidsen, 2000, Melezhik *et al.*, 2015) and has since undergone variable low-temperature alteration.

The lowest unit in the KGB lithostratigraphy is the Lavtevárri Formation (50–150 m thick), which rests unconformably on the Jergul Gneiss Complex (Braathen & Davidsen, 2000, Melezhik *et al.*, 2015). The Lavtevárri Formation consists of carbonate-bearing feldspathic to mica schists (locally fuchsite-bearing), intervals of basal conglomerates, amphibolites and psammites with subordinate komatiites, high-MgO amphibolites, rhyolites, mica-schists and marbles (Braathen & Davidsen, 2000, Davidsen, 1994).

The Čorgaš Formation (250–700 m) comprises (bottom to top) quartzitic, quartzofelspathic and mica schists, conglomerates and marbles (Braathen & Davidsen, 2000). The Lavtevárri Formation is missing locally and the Čorgaš Formation lies conformably on the Jergul Gneiss Complex in parts of the belt (Often, 1985). Ultramafic to mafic intrusions are common in the Čorgaš Formation, including the Gállojávri intrusion. There are no published ages for these intrusions, however, carbonate isotope chemostratigraphy in the Čorgaš Formation suggests a depositional age of c. 2.22 and 2.14 Ga (Melezhik *et al.*, 2015), suggesting that the intrusions are part of the c. 2.05 Ga group of magmatic rocks in the CLGB.

A 300-700 m-thick marble unit marks the lower contact of the Briitágielas Formation with the Čorgaš Formation (Braathen & Davidsen, 2000). Above the marble, the formation consists of kyanite-bearing garnet-mica schists and calc-alkaline dacitic volcanites with intervals of graphite-bearing schists (Braathen & Davidsen, 2000, Davidsen, 1994). The dominant rock assemblage in this formation is tholeiitic basalts with four interlayered units, each up to 70 m

thick, of pillowed and volcaniclastic komatiite (Braathen & Davidsen, 2000). The formation contains several sulphide-rich intervals (Melezhik *et al.*, 2015).

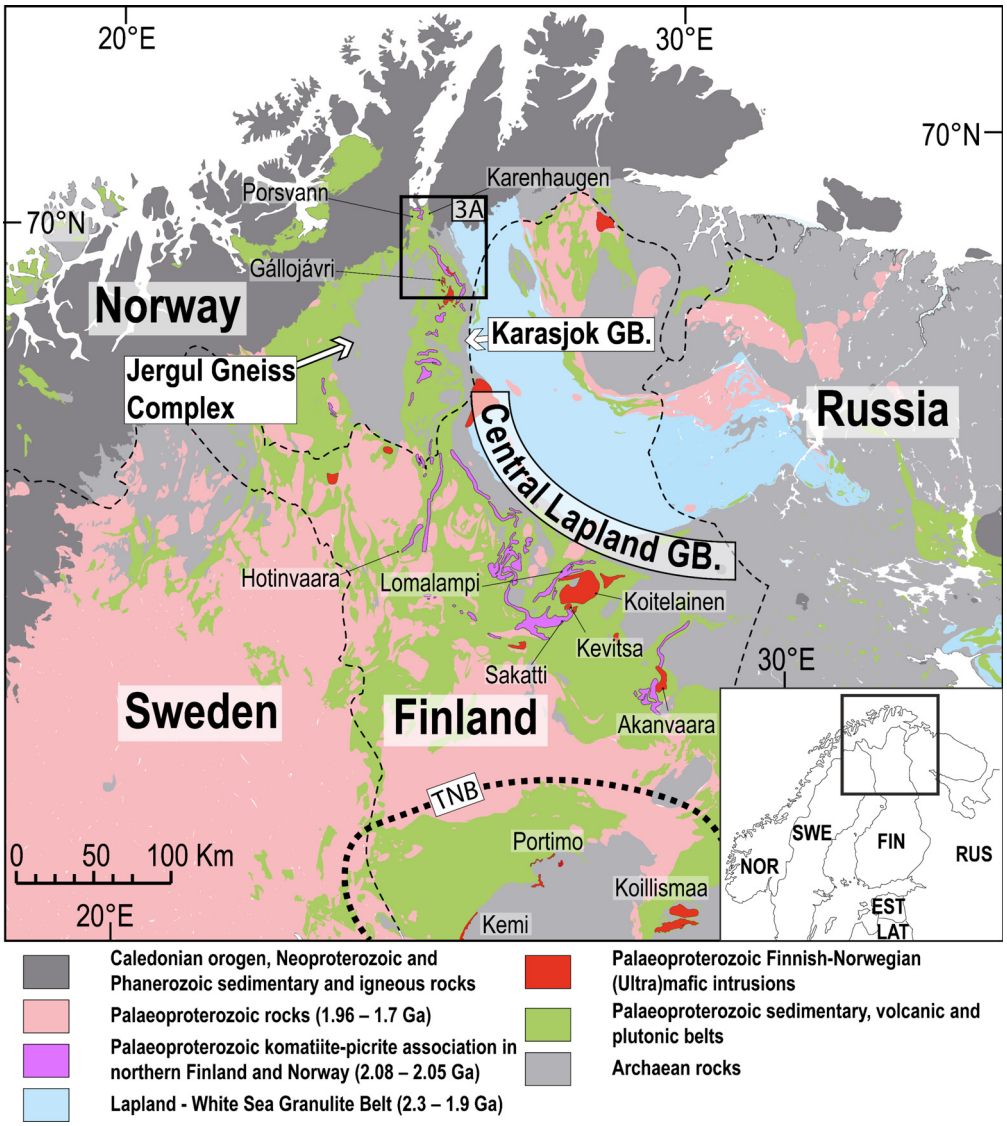

Figure 2 Simplified map of northern Fennoscandia based on Koistinen *et al.* (2001), modified from Bingen *et al.* (2015), Hanski *et al.* (2001a), Hanski and Huhma (2005) and Puchtel *et al.* (2020). Red bodies mark anorthosite and (ultra)mafic intrusions. The purple bodies represent the Palaeoproterozoic komatiite-picrite association of northern Finland and Norway. The black box indicates the location of Fig. 3A. GB, greenstone belt; TNB, Tornio-Näränkävaara belt.

The Fossestrand Formation has a minimum thickness of 250–300 m (Melezhik *et al.*, 2015). The lower contact towards the Briitágielas Formation consists of two thick pillow lava flows and coarse-grained mafic rocks. Upwards, the formation is dominated by lava flows and agglomerates (Braathen & Davidsen, 2000). The presence of pillows indicates a subaqueous environment, whereas the presence of vesicles in the same pillows and the abundance of pyroclastic material suggest a relatively shallow-water setting (Melezhik *et al.*, 2015, Often, 1985).

Braathen and Davidsen (2000) interpreted the lithostratigraphy to have been deposited in an intracratonic setting, as suggested by the pyroclastic rocks, graphite schists and depositional contacts against the Archaean basement. In addition, the extensive metasedimentary units are dominated by material from granitoid sources, suggesting cratonic source areas (Braathen & Davidsen, 2000, Davidsen, 1994).

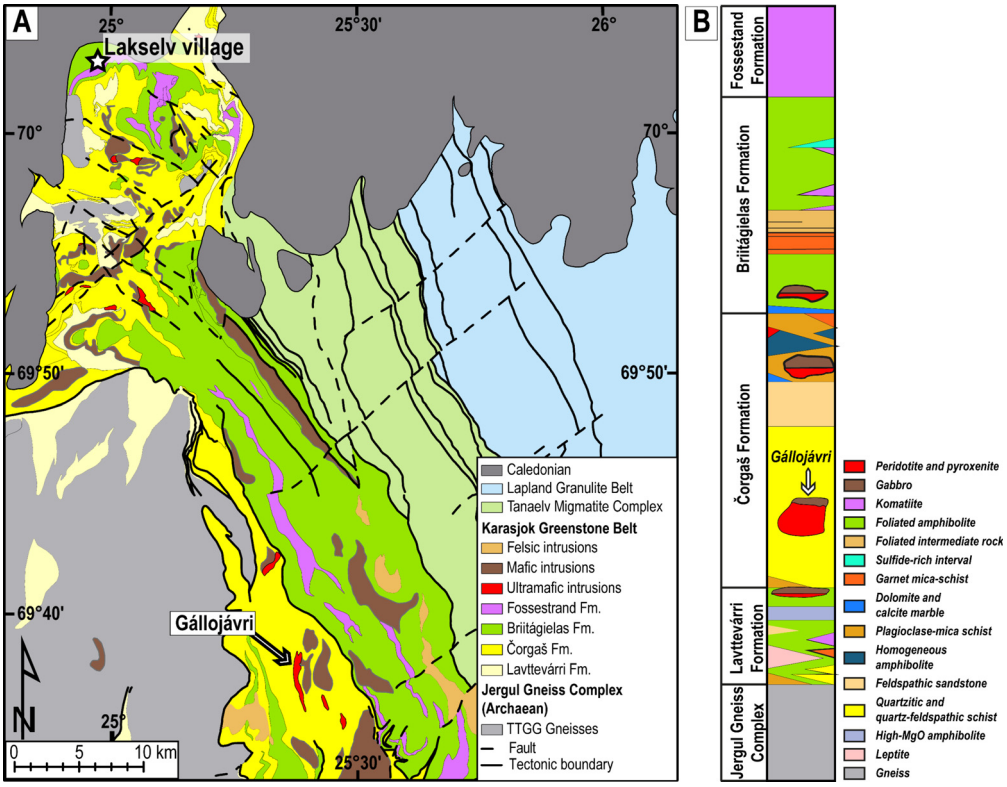

Figure 3: (A) Simplified geological map of the northern Karasjok Greenstone Belt. Modified from the NGU N250 bedrock database. (B) The lithostratigraphy of the Karasjok Greenstone belt, modified from Orvik *et al.* (2022a), Hansen *et al.* (2020) and based on Braathen and Davidsen (2000).

3.1.2 Palaeoproterozoic komatiite and picrite lavas

The Paleoproterozoic high-MgO magmatism of the CLGB occurs at two stratigraphic levels designated as the lower and upper komatiites by Hanski *et al.* (2001a). The inferred c. 2.44 Ga lower komatiites (c. 250 m thick), which belong to the Onkamo Group, are found near the bottom of the succession and locally rest directly on the Archaean TTGG basement (Hanski & Huhma, 2005, Heggie *et al.*, 2013, Puchtel *et al.*, 2020). The Onkamo Group εNd_t signatures range from -9 to -0.2 and indicate strong interaction with continental crust (Hanski & Huhma, 2005). As mentioned above, these komatiites have been linked to impingement of a c. 2.45 Ga mantle plume (Hanski & Huhma, 2005) and the start of rifting of the Archaean craton. Although not directly dated, the lower komatiites can be correlated stratigraphically to komatiitic lavas of the Vetreny Belt in the SW part of the Fennoscandian Shield, with Sm-Nd isochron ages of 2449±35 and 2410±34 Ma (Hanski & Huhma, 2005) and a Re-Os isochron age of 2407±6 Ma (Puchtel *et al.*, 2020, Puchtel *et al.*, 2016). Similarly, one can speculate that the lower komatiites are represented by the subordinate komatiites and high-MgO amphibolites of the Lavtevárri Formation in the KGB.

The upper komatiites are associated with phyllites and black schists of the Savukoski Group in northern Finland (Hanski *et al.*, 2001a) and the upper Briitágielas- and the Fossestrand Formation in the KGB (together designated as the Báhkilvárri Formation by Barnes & Often, 1990). These highly magnesian rocks are unusually enriched in TiO_2 compared to other komatiites and are largely volcanoclastic in origin (Barnes & Often, 1990, Hanski *et al.*, 2001a). These unusual characteristics later led to the term "Karasjok-type" komatiites (Arndt, 2008, Barley *et al.*, 2000) after the KGB, where Barnes and Often (1990) first described them.

The age for the Karasjok-type komatiite sequence in Finland is indicated with an average Sm-Nd magmatic pyroxene-whole rock isochron of 2056 ± 25 Ma (Hanski *et al.*, 2001a) and a Re-Os isochron age of 2049±13 Ma (Puchtel *et al.*, 2020). A similar Sm-Nd whole-rock errorchron age of 2085±85 Ma has been obtained for the sequence in Karasjok (Krill, 1985a).

While it is unknown whether the Archaean craton had already been completely disaggregated at this point, most ultramafic to mafic magmas do not have isotopic signatures indicating interaction with continental crust (Hanski, 2015, Hanski, 2013). The Sm-Nd analysis of Hanski *et al.* (2001a) showed that the Light Rare Earth Elements (LREE)-depleted komatiites and LREE-enriched picrites have similar positive εNd_t values (+4), indicating derivation from a depleted mantle. The same characteristics have been documented for the Karasjok sequence,

with $(La/Sm)_N$ of 0.2–1.4 and average εNd_t of +4.5 ± 0.5 (Krill, 1985a). To explain the REE characteristics and large spread in trace-element ratios, Hanski *et al.* (2001a) proposed a heterogeneous mantle source region formed by dynamic depletion and enrichment processes and put forth a mantle plume model for their genesis (Hanski *et al.*, 2001a), similar to the model argued by Barnes and Often (1990) for the Karasjok komatiites.

3.1.3 Orthomagmatic mineral deposits

The Fennoscandian Shield in Finland contains a diverse suite of ore deposits, with over 50 mines in operation over the last century (Hanski, 2015). Several reference works with summaries of mineral deposits and their petrogenesis have been published, including *Mineral Deposits of Finland* by Maier *et al.* (2015) on which this section is based. Here, the emphasis will be on orthomagmatic deposits linked to the Palaeoproterozoic magmatism in the CLGB.

The c. 2.45 Ga mantle plume activity and the beginning of rifting were accompanied by the formation of large, layered ultramafic to mafic intrusions of major economic significance (Hanski, 2015, Hanski, 2013). A large volume of mafic magma rose through the fracture network of the rift and ponded close to the unconformity between the Archaean basement and the earliest supracrustal rocks (Hanski & Huhma, 2005, Hanski, 2013). Interaction between mantle-derived magmatism and the continental crust appears to have been crucial in ore formation (Hanski, 2015). The intrusive bodies appear as layered gabbro-noritic intrusions in several areas of the Fennoscandian Shield, such as the Tornio- Näränkävaara belt (TNB; Fig. 2) that hosts intrusions with stratiform Cr and Fe-Ti-V deposits, PGE-enriched reefs and Ni-Cu-PGE contact and offset mineralisations (Hanski, 2015, Hanski, 2013, and references therein). This age group of intrusions in the CLGB are represented by the 2439±3 Ma Koitelainen and 2436±6 Ma Akanvaara intrusions (Fig. 2; Hanski & Huhma, 2005, Mutanen & Huhma, 2001). Although currently uneconomic, both intrusions contain magnetite-rich cumulates and PGE-enriched stratiform chromite deposits (Hanski, 2015, Mutanen, 1997).

Despite a common association with sulphide-bearing supracrustal rocks, a favourable environment for assimilating external sulphur, the upper komatiites and picrites have no known economic deposits in the CLGB (Hanski, 2015). However, the Hotinvaara and Lomalampi komatiites show that this magmatic episode has some Ni potential (Hanski, 2015, Konnunaho *et al.*, 2015, Makkonen *et al.*, 2017). The significant 2063±35 Ma Sakatti deposit, whose intrusive versus extrusive nature is still debated, may be added to this list (Brownscombe *et al.*, 2015, Moilanen *et al.*, 2021).

Unlike the extrusive upper komatiites, the similarly aged intrusive rocks have shown much more promise for orthomagmatic sulphides, with examples such as the Ni-Cu-PGE Kevitsa deposit and possibly the Sakatti deposit (Fig. 2). This list may also include the Hietakero mafic intrusion (but no isotopic age data are available), which is host to an unusual Co-enriched Cu-Ni sulphide mineralisation (Konnunaho *et al.*, 2018). Multistage petrogenetic models have been proposed for all these deposits and appear to have played an important role in ore formation (e.g., Brownscombe *et al.*, 2015, Konnunaho *et al.*, 2018, Luolavirta *et al.*, 2018a). For example, Luolavirta *et al.* (2018b) proposed a model of multiple injections based on spatially confined but strikingly different drill core lithological and compositional profiles inside and outside the Kevitsa ore domain. The Ni-PGE ores of the intrusion were proposed to be the result of the assimilation of proto-ores deposited early in the evolution by later magma recharges (Luolavirta, 2018).

3.2 Previous work on the Gállojávri intrusion

The following presents a summary of the information that was available on the Gállojávri intrusion before onset of the PhD project. This section is based on the summary report of Nilsson and Often (2006), the derived works of Boyd and Eilu (2012) and Nilsson *et al.* (2016), and the references therein.

The Gállojávri ultramafic intrusion (Fig. 4) is located about 20 km NNW of Karasjok and 3.5 km east of Lake Iddjajavri. The intrusion is at least 500 m thick, striking roughly N-S for at least 5 km, and is hosted by east-dipping Proterozoic psammitic rocks. Lake Gállojávri covers much of the northwestern part of the intrusion, with most exposures found along the lake's eastern bank. According to aeromagnetic and gravity data, the exposed part of the Gállojávri intrusion is only the northern extension of an intrusion that may be much larger and plunges at a shallow angle to the southeast (Fig. 4B, C; Skaar, 2014).

The initial investigations included minor core drilling, geochemical sampling, ground geophysics, geological mapping and mineralogical studies on sulphide-bearing samples. According to outcrop and core logs, the intrusion is dominated by olivine-pyroxene cumulates, which are at least partially recrystallised at amphibolite facies. The distribution of ultramafic components and mineralisation in the body is described by Nilsson and Often (2006), who argued that the base of the intrusion coincides with its western contact. Four different areas of mineralisation, one exposed along a strike length of 500 m, reveal the presence of up to 5 modal% disseminated sulphides. Pentlandite, pyrrhotite and chalcopyrite have been found in

ore petrographic studies, but no distinct PGM. The highest recorded noble metal grade is 2.45 ppm Pt+Pd+Au, pointing to high metal-in-sulphide tenors.

A combined geophysical (IP and magnetic) anomaly linked to a Ni-Cu-(PGE) sulphide occurrence was the target of three holes drilled by Tertiary Minerals in 2003 (DDH 03GD001–003; Fig. 4A). While the drilling campaign did not come across PGE grades comparable to earlier surface sampling, anomalous PGE intersections were made in all three holes, with broad intersections of anomalous values in composite samples (e.g., 4m at 0.26 ppm Pt+Pd+Au) and higher values in narrow sections (e.g. 0.55m at 0.69 ppm Pt+Pd+Au; Bradley, 2003, confidential until 2018). The results were deemed inconclusive by Bradley (2003) until additional assaying and mineralogical analysis could be undertaken.

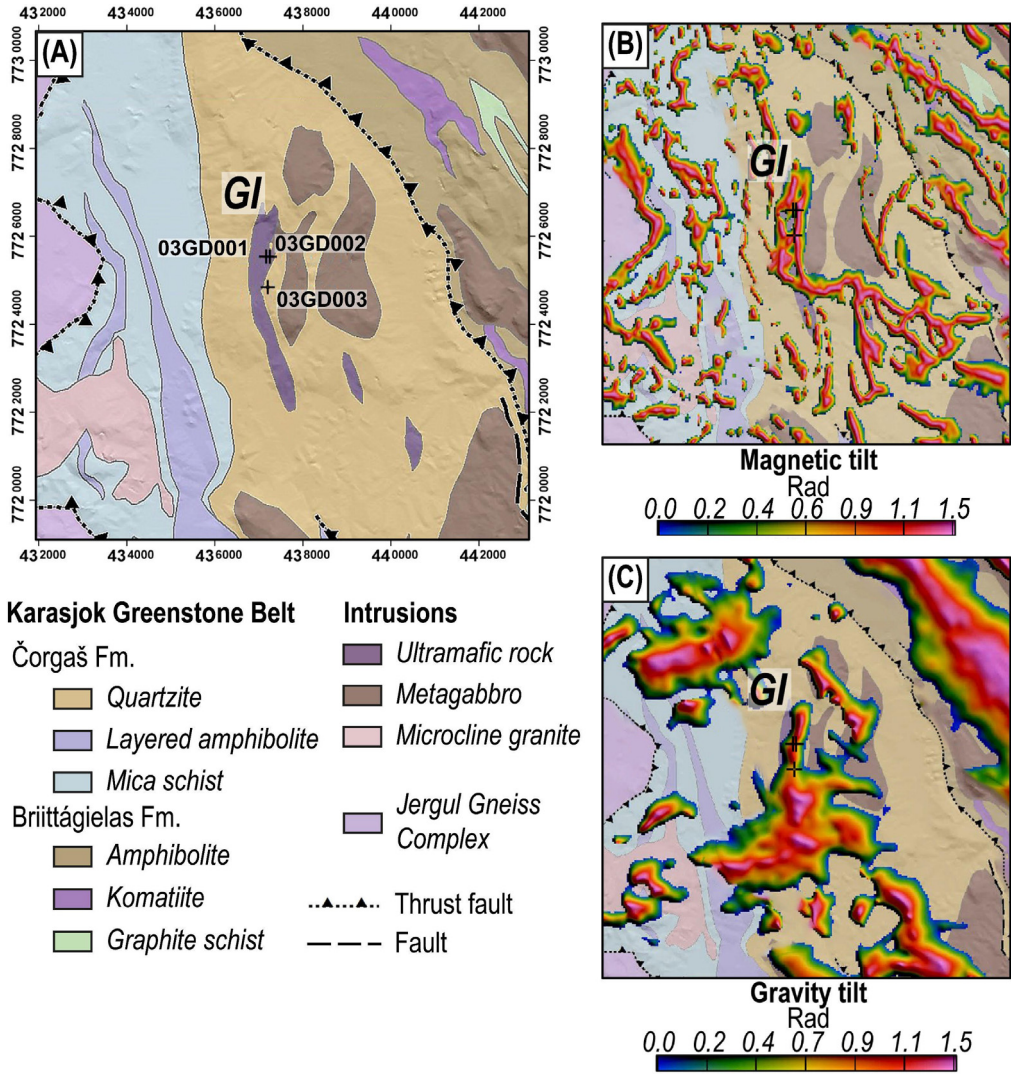

Figure 4: Geological map and geophysical anomaly maps from Skaar (2014). All three maps cover the same area. The geological map is based on Henriksen (1986). The location of drill holes 03GD001, 03GD002 and 03GD003 are marked with crosses. (A) Geological map of the Gallujavri intrusion. (B) Magnetic tilt anomalies and (C) gravity tilt anomalies superimposed on the geological map. Slightly modified from Orvik *et al.* (2022a). GI, Gállojávri intrusion.

4 PROJECT OUTLINE

The primary aim of this PhD project is to understand the petrogenesis and develop a geological model for the Gállojávri intrusion. However, because this project is the first academic study on the Gállojávri intrusion, the project has a broad scope. As such, the primary aim is subdivided into three separate objectives. The first objective is to develop a petrogenetic model; the second objective is to evaluate the link to the magmatic evolution of the CLGB; the third objective is to characterise the mineralisation and evaluate the ore-forming mechanisms. Although listed as separate objectives, these topics are naturally interconnected.

The first objective of this thesis will be addressed by defining a petrogenetic model for the Gállojávri intrusion based on a traditional petrographic approach combined with thermodynamic modelling. The traditional approach involves core logging, microscopy, electron probe microanalysis (EPMA), mineral trace element analysis and whole rock geochemistry. By simulating the magmatic evolution with the MCS, the formulated hypothesis will be tested against the observations, thus facilitating the development of a consistent petrogenetic model.

The second objective of the thesis is to provide a link to the regional evolution of the belt. Previous geochronological and isotopic data are scarce in the Karasjok area, inhibiting correlation between the Norwegian and Finnish parts of the belt. Consequently, achieving this objective involves collecting geochronological data, determining isotopic signatures and interpreting them in the evolutionary framework of the CLGB. In addition, radiogenic isotopes provide important information on the nature of the source of magma and the characteristics of potential crustal contaminants. Therefore, the findings will also contribute to the first objective.

The third objective of this thesis is to characterise the mineralisation and provide an evaluation of the ore-forming processes. Like the first objective, the third objective will be approached with traditional petrographic methods, including core logging, microscopy, EPMA and mineral trace element analysis. This approach is aided by bulk chalcophile element geochemistry and S isotopes, which provide information on the processes leading to saturation as well as the source of sulphur.

5 SUMMARY OF PAPERS

This thesis is based on two published, peer-reviewed papers and one manuscript. Here is a short summary of the work that emphasises the parts that answer the objectives outlined in the preceding chapter. As is customary for NTNU theses, the original papers and the manuscript are included at the end of this synthesis. The underlying data are available in the respective papers and online supplementary materials. The unpublished manuscript has the supporting data included in the text and the attached appendix.

Paper 1: Orvik, A.A., Slagstad, T., Hansen, H., Nilsson, L.P., Sørensen, B.E., 2022. The Palaeoproterozoic Gallujavri ultramafic intrusion, Karasjok Greenstone Belt; petrogenesis of a trans-crustal magma system. *Journal of Petrology* 63, 28.

The first paper focuses on developing a petrogenetic model for the Gállojávri intrusion based on newly acquired petrological and geochemical data. Defining a model includes distinguishing the parental melt and processes affecting the magmatic evolution of the intrusion, which in part relies on previously published data from the KGB. This paper addresses the possible genetic links between the Gállojávri intrusion and the spatially associated 2085±85 Ma Karasjok-type komatiites. A petrogenetic model is developed using the MCS tool to simulate the magmatic evolution of the Gállojávri intrusion. The model is then validated by comparing its results to the reported petrological and geochemical data.

Bulk geochemistry revealed clear evidence of contamination, such as Large-Ion Lithophile Element (LILE), LREE, Pb and U enrichment (Fig. 5A). Furthermore, the contamination is largely uniform, with no clear spatial variations. For example, the cumulate rocks have uniformly low Nb/Th ratios with an interquartile range from 0.4 to 2.4 (Fig. 5B), similar to average crustal values (c. 2.3). These characteristics suggest that assimilation occurred early, potentially in a staging chamber. In addition, the analysed spinel showed a Fe-Ti trend similar to the trends documented for subvolcanic intrusions to continental flood basalts (Fig. 5C). Polybaric crystal fractionation was indicated by geobarometric estimates that cluster at 400 MPa and tails towards 700 MPa (Fig. 5D), which again suggests some diversification in a staging magma chamber. Additionally, the stratigraphic placement of the Gállojávri intrusion suggests that it is not only spatially but also temporally associated with the Karasjok-type komatiites.

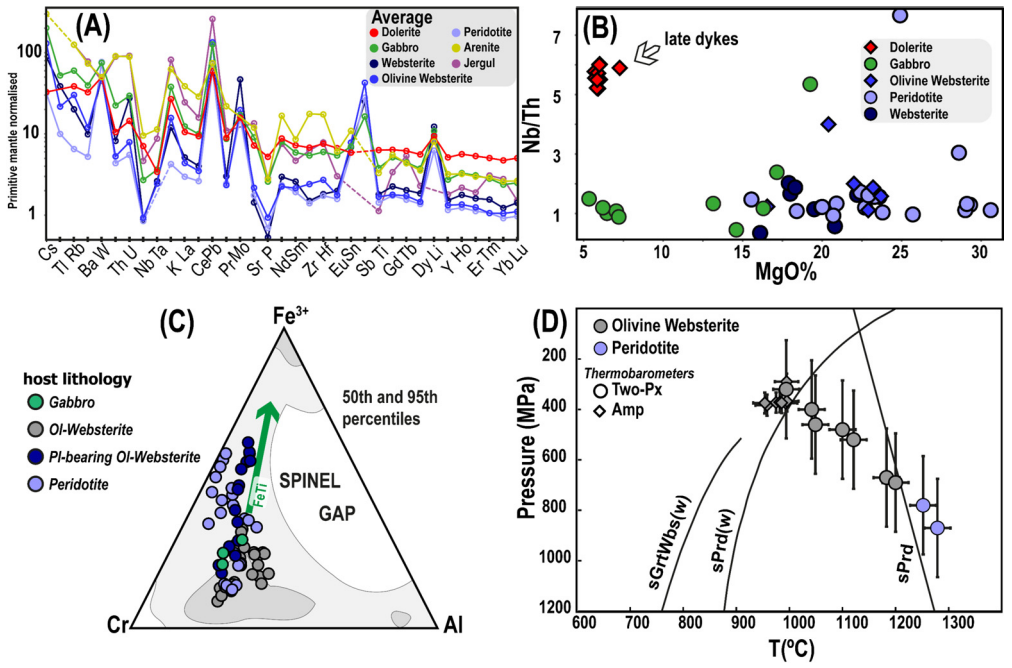

Figure 5: Slightly modified figures from Orvik *et al.* (2022a). (A) Multi-element primitive mantle-normalised (Sun & McDonough, 1989) diagram showing average compositions of the different rock types. (B) MgO wt.% versus the Nb/Th ratio for cumulate rocks and late dykes. (C) Ternary diagram relating analysed spinel compositions to the Fe–Ti trend (green arrow) and compositional fields defined by Barnes and Roeder (2001) for spinels from mafic-ultramafic igneous rocks. (D) Amphibole, orthopyroxene and clinopyroxene thermobarometry. Mineral pairs from peridotites in light blue. Mineral pairs from olivine websterites in grey. Diamonds: amphibole thermobarometer (Ridolfi *et al.*, 2009), circles: weighted averages of the two-pyroxene thermometer of Brey and Köhler (1990) and the two-pyroxene thermobarometers of Putirka (2008). Reference lines: anhydrous solidus for peridotite (sPrd; Hirschmann, 2000), hydrous peridotite solidus (sPrd(w); Boettcher et al., 1975), and hydrous garnet websterite solidus (sGrtWbs(w); Mysen & Boettcher, 1976).

The results led to the following hypothesis: 1) The Gállojávri intrusion and Karasjok-type komatiites form a cognate magma system; 2) The intrusion represents part of the volcanic plumbing system; 3) Significant crustal contamination occurred in a staging magma chamber; 4) Crystallisation ensued at depth.

The MCS tool was used to test the hypotheses, which served as the foundation for developing an overarching petrogenetic model for the Gállojávri intrusion (Fig. 6). The model revealed that magma transport via a two-stage polybaric plumbing system could explain several of the phase equilibria and bulk geochemical characteristics observed in the Gállojávri intrusion. In the model, LREE-depleted 2085 ± 85 Ma Karasjok-type komatiitic melt first intruded the lower crust with a liquidus temperature of 1698°C (stage 1; Fig. 6). The komatiitic melt heated the

surrounding TTGG country rock, leading to anatexis and contamination of the melt in the lower crustal chamber. Assimilation and fractional crystal continued until the melt had evolved into a komatiitic basalt (c. 12 wt.% MgO; like the Gállojávri chilled margin). The evolved and hybridised melt separated from the lower crustal reservoir and migrated to shallower crustal levels where it intruded with a liquidus temperature of 1273°C (stage 2; Fig. 6).

Once the hybrid melt intruded the middle crust, the assimilation and fractional crystallisation processes continued. In this stage, the country rocks were modelled with a composition like the metasedimentary rocks hosting the intrusion (Fig. 6). The modelling suggested that the middle crustal chamber remained open, requiring primitive melt recharge(s) to explain the observed phase equilibria (step 7; Fig. 6). In addition to recharge(s), the modelling suggested an anomalous thermal gradient in the middle crustal chamber, hypothesised to be due to the pre-heating of the country rock by previous magma pulses.

As with all modelling-based studies, the results depend on various assumptions and choices of conditions and parameters. Some of the ambiguities in the model are highlighted and discussed in this paper. For example, there is uncertainty about the relative proportion of crustal contamination at the different stages of the model. The host metasedimentary rocks are likely derived from the TTGG crust, giving them similar chemical compositions and therefore making them hard to distinguish. The number and composition of the recharge(s) are also uncertain. The model includes one large recharge event of primitive Karasjok-type komatiitic melt. However, one might achieve similar results with several smaller injections of varying compositions.

In addition to the petrogenetic model, this paper presents some results that have implications for the mineralisation potential of the Gállojávri intrusion, such as linear variation in whole-rock MgO versus Ni and high Ni contents in olivine (2700–3500 ppm) that are considered characteristics inconsistent with crystallisation from a previously sulphur-saturated or Ni-depleted melt. This observation suggests that the system has some Ni potential and that cogenetic intrusions of the same type as Gállojávri are appealing targets for further investigation into the petrogenesis and ore potential of the system.

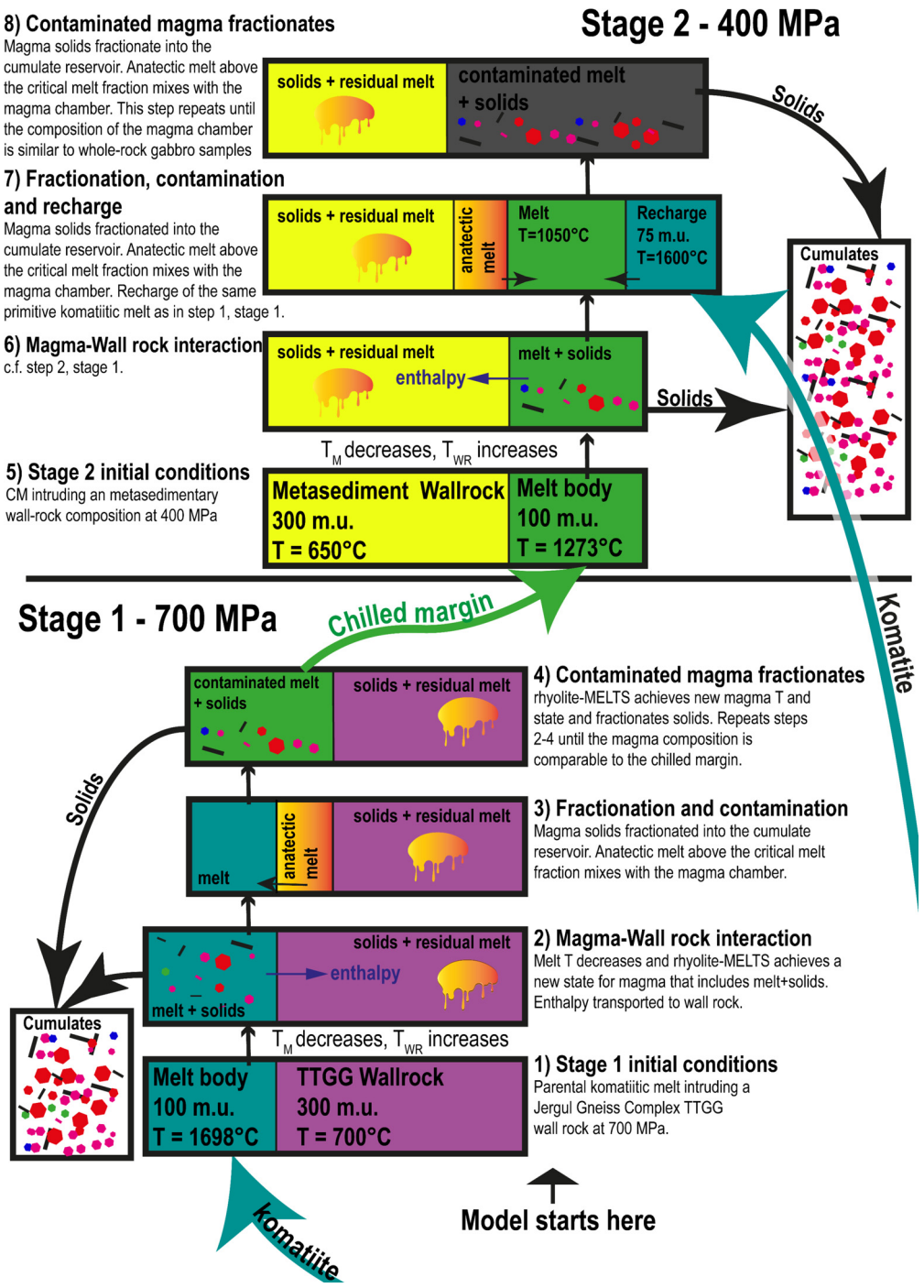

Figure 6: Schematic illustration of the petrogenetic model developed using the MCS. The figure is from Orvik *et al.* (2022a). m.u., mass unit; CM, chilled margin; TTGG, tonalite-trondhjemite-granodiorite-granite; T_M, melt temperature; T_{WR}, wall rock temperature.

Paper 2: Orvik, A.A., Slagstad, T., Sørensen, B.E., Millar, I., Hansen, H., 2022. Evolution of the Gállojávri ultramafic intrusion from U-Pb zircon ages and Rb-Sr, Sm-Nd and Lu-Hf isotope systematics. *Precambrian Research* 379, 106813.

The second paper presents radiogenic isotope signatures and zircon U-Pb geochronological data for the magmatic rocks of the Gállojávri intrusion and the country rock. The isotopic study adds to the petrogenetic discussion of the first paper, being better suited to constrain the characteristics of crustal contamination and recharge. Furthermore, being one of the first radiogenic isotope studies on magmatic rocks of the KGB, combined with the reported geochronology, forms a natural basis for discussing the magmatism in light of regional models developed for the CLGB.

The CLGB contains multiple ultramafic to mafic intrusions, some with significant ore reserves, that are thought to have formed during three episodes at c. 2.44, 2.22 and 2.05 Ga. This paper reports a magmatic zircon U-Pb age of 2051±8 Ma (Fig. 7A), interpreted to reflect the crystallisation age of the Gállojávri intrusion. Discordia lower-intercept ages indicate Caledonian lead loss. The magmatic rocks exhibit a large range of isotopic signatures, with zircon εHf_t ranging from -14 to -1 and bulk εNd_t ranging from -15 to +4 (Fig. 7B, C). In addition, bulk $(^{87}Sr/^{86}Sr)_t$ shows an apparent range from 0.504 to 0.707. A Rb-Sr errorchron yield an age of 1691±11, interpreted to reflect low-temperature alteration and Rb-Sr mobility, supported by petrographic observations and XRD analyses suggesting significant alteration. The errorchron age broadly corresponds to Svecofennian hydrothermal activity, deformation and intrusion of pegmatite elsewhere in northern Fennoscandia. The less mobile Nd and Hf systems were interpreted to represent primary magmatic signatures. In addition, this paper reports large variations in isotopic signatures over decimetres to metres in core profiles (Fig. 7C). For example, the full range in εNd_t (i.e., -15–4) is represented within a core interval of c. 4 m, all in rocks with more than 20 wt.% MgO.

The *Traces* extension of the MCS is used in this paper to test the petrogenetic model presented in the first paper with the newly reported isotopic signatures (Fig. 8). The modelling results were mostly consistent with the initial petrogenetic model but also revealed flaws and inconsistencies. Additionally, the observed spatial variation in isotopic signatures points to a more complex magmatic evolution and suggests that the MCS model is oversimplified.

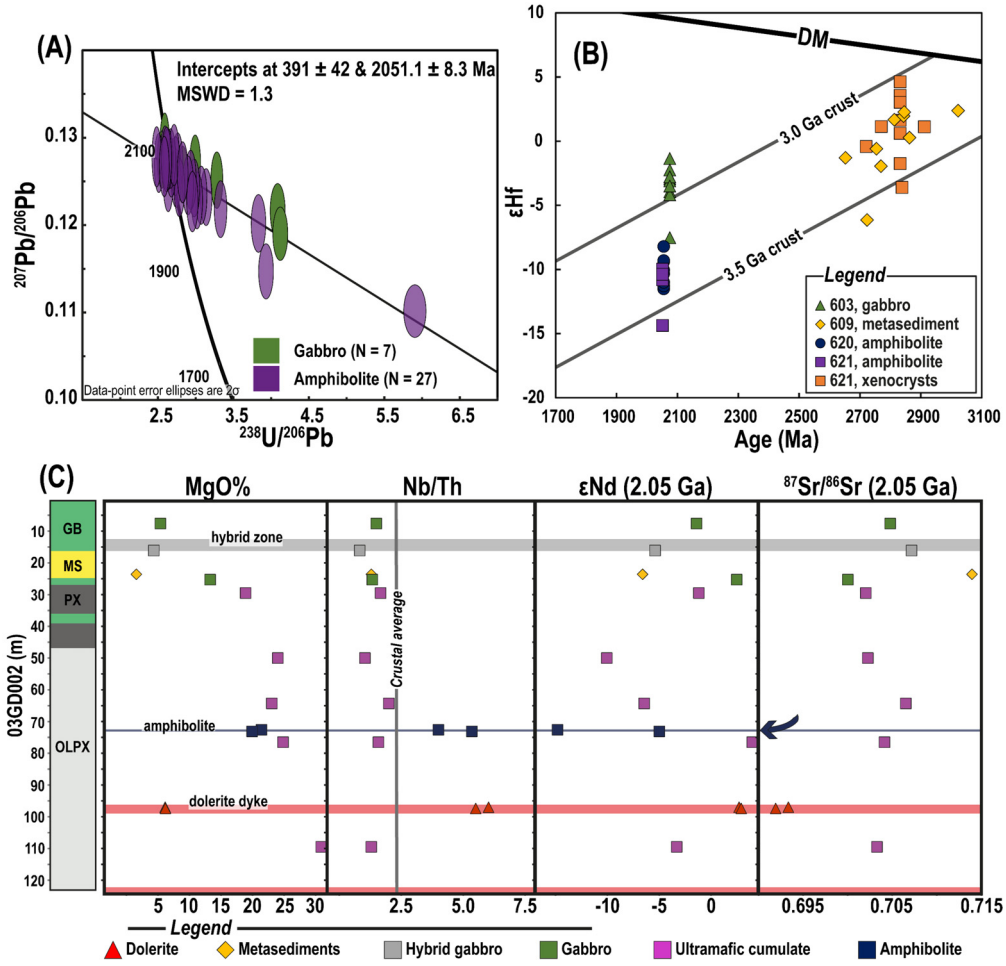

Figure 7 Slightly modified figures from Orvik *et al.* (2022b). (A) U-Pb zircon geochronology results. The figure shows a Tera-Wasserburg diagram with a discordia calculated from magmatic zircon without significant lead loss. The Tera-Wasserburg diagram was created with Isoplot 4.15.11.10.15 using decay constants λ_{238}=1.55125×10^{-10} and λ_{235}= 9.8485×10^{-10} (Steiger & Jäger, 1977). (B) Hf isotope evolution plot for the Gállojávri zircons. The isotope trajectories of continental crust (formed at c. 2.9 and 3.5 Ga with ^{176}Lu/^{177}Lu = 0.015) and depleted mantle (DM) are shown for reference. (C) Downhole variation in MgO wt.%, Nb/Th ratio, εNd (2.05 Ga) and ^{87}Sr/^{86}Sr (2.05 Ga) for drill core 03GD002. Crustal average Nb/Th from Weaver and Tarney (1984). GB, gabbro; MS, metasediments; PX, pyroxenite; OLPX, olivine-pyroxene cumulates.

The most evolved crustal (or supracrustal) rock documented had an $\varepsilon Nd_{2.05Ga}$ of c. -9. Therefore, the most unradiogenic samples from the Gállojávri intrusion had to be contaminated by a more evolved and unidentified crustal component. Furthermore, the assumed chilled margin, proposed to be the mid-crustal parental melt in the first paper, had an εNd_t of +2.5, inconsistent with significant contamination in a staging chamber (Fig. 8).

The magmatic evolution simulated with the MCS assumes complete mixing of the evolved melt in the chamber and the added anatectic- and recharged melts. This assumption is unlikely to hold based on the spatial variation in isotopic signatures reported in this paper (Fig. 7C). The heterogeneity implies incomplete mixing of isotopically distinct components of the system. The large variations in isotopic signature were, therefore, attributed to local xenolith melting and influx of variably contaminated melt into the semi-consolidated Gállojávri chamber. For example, the local juvenile domains indicate that the system was recharged with uncontaminated mantle-derived melt. It does, however, potentially imply that the recharge occurred late, resulting in isolated domains rather than mixing with the magma in the chamber.

The first two papers in the thesis point to petrogenetic similarities between the Gállojávri intrusion and the c. 2.05 Ga ultramafic to mafic bodies in Finland, such as the Kevitsa and Sakatti. The reported zircon U-Pb age further strengthens the hypothesis that the Gállojávri intrusion formed during the c. 2.05 Ga magmatic episode. A characteristic feature of this age group of intrusions is a multistage and polybaric evolution, coupled with variable contamination, which appear to have played an important role in ore formation. Identifying this type and age group of intrusions in the KGB suggests that they occur throughout the CLGB, which also carries implications for the prospectivity of the Karasjok region.

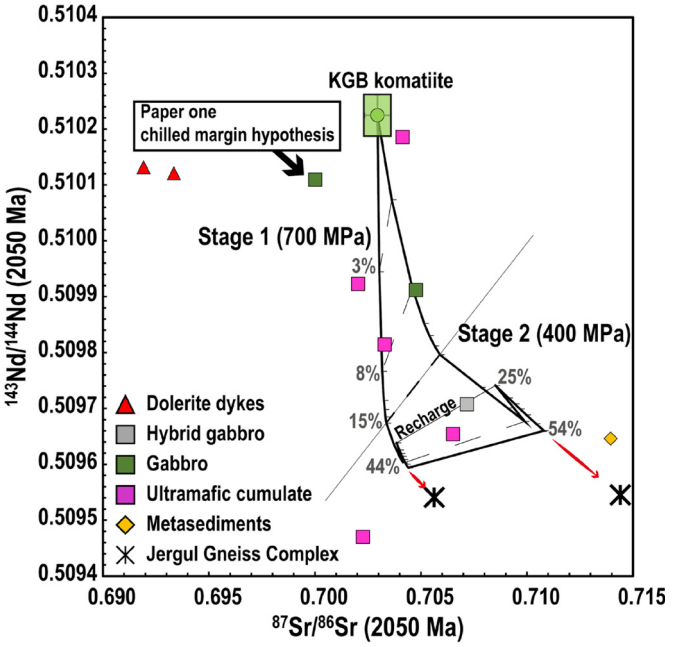

Figure 8: Whole-rock Sr and Nd isotope ratio plot with the two-stage Magma Chamber Simulator models. The primary magma Sr and Nd isotope ratios for the stage 1 model are the averages of the LREE-depleted komatiite samples presented by Krill (1985a). The percentages next to the liquid lines of descent indicate the degree of contamination. Two samples are excluded based on anomalous $^{87}Sr/^{86}Sr$ signatures. The figure has been slightly modified from that of Orvik *et al.* (2022b).

Manuscript 3: Orvik, A.A., Mansur, E., Slagstad, T., Sørensen, B.E., Drivenes, K., Nilsson, L.P., In preparation. The PGE sulphide mineralisation from the Gállojávri intrusion: implications for the formation of magmatic sulphide deposit in the Karasjok Greenstone Belt, Norway, Unpublished, 52 pp.

The third manuscript presents the first detailed petrographic description of the Gállojávri mineralisation, reported together with ore mineral chemistry, bulk chalcophile elements and S isotope ratios. The petrographic description, mineral chemistry and trace element zoning of ore mineralogy were used to characterise the mineralisation and evaluate the genesis and the effects of post-cumulus alteration. The bulk chalcophile concentrations and S isotope data were used to assess the nature of magma chamber processes and the contribution of crustal contamination to the formation of mineralisation.

This manuscript is the first to evaluate the ore genesis of a conduit-like intrusion in the KGB. Therefore, it provides important considerations for properly assessing the regional mineral potential. To this end, this manuscript compares the Gállojávri intrusion to bulk geochemical data from the Karasjok-type parental komatiite and the stratigraphically correlatable Karenhaugen- and Porsvann intrusions.

Petrography shows that the mineralisation consists of primary and post-cumulus features (Fig. 9). The primary sulphide association consists of pyrrhotite, pentlandite and chalcopyrite (Fig. 9A, B). These occur as up to 10 modal% internally differentiated disseminations and larger blebs (<1 cm). However, the Gállojávri rocks are commonly S-poor and characterised by accessory sulphide proportions that align with cotectic fractionation. Sulphur saturation seemingly occurred late in the magmatic evolution, as reflected by the internally differentiated sulphide disseminations association with trapped silicate liquid phases, such as plagioclase and phlogopite (Fig. 9D). The disseminated pyrrhotite is commonly characterised by an outer peritectic reaction zone comprising coarse pentlandite or a thin loop texture of chalcopyrite and pentlandite (Fig. 9B). Sulphur supersaturation is indicated locally. For example, one thin (5 cm) vein of massive sulphide (c. 9:1 pyrrhotite-chalcopyrite) is associated with a country rock xenolith.

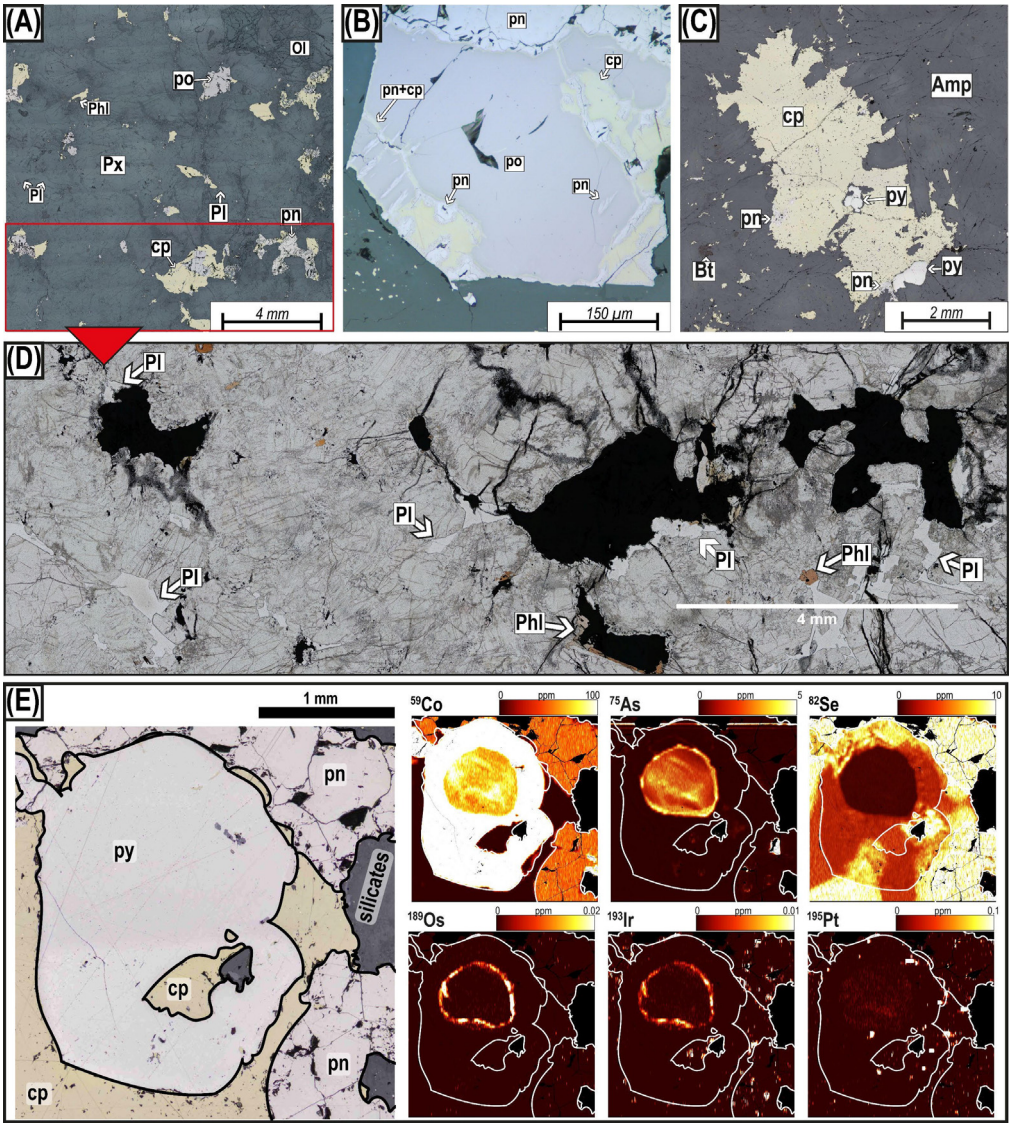

Figure 9: (A) Disseminated sulphides in olivine-pyroxene cumulate rocks. The intercumulus sulphides are composite and consist of chalcopyrite, pyrrhotite and pentlandite. (B) Pyrrhotite with loop-textured pentlandite and chalcopyrite. (C) Large recrystallised bleb of chalcopyrite in amphibolite (websterite). The chalcopyrite has some pentlandite exsolutions and encompasses a rounded pyrite. (D) Plane-polarised zoom of the area indicated in (A) showing the association with trapped interstitial phases. (E) LA-ICP-MS elemental maps showing the chalcophile element distribution in chalcopyrite, pyrite and pentlandite. The relative concentration of the elements is semi-quantitative and normalised to 1 wt.% Fe. Silicates, holes and cracks have been masked in the element maps. Amp, amphibole; Bt, biotite; cp, chalcopyrite; Ol, olivine; Phl, phlogopite; Pl, plagioclase; pn, pentlandite; po, pyrrhotite; Px, pyroxene; LA-ICP-MS, laser ablation inductively coupled plasma mass spectrometry.

The recrystallised post-cumulus sulphides consist of chalcopyrite and pyrite, commonly with serrated margins in pervasively altered rocks (Fig. 9C). However, there is a continuum between primary magmatic and recrystallised styles, with pyrite preferentially replacing pyrrhotite. The pyrite is zoned in Co, As, Se, IPGE and Pt (Fig. 9E), attributed to boundary-layer effects during the fluid-assisted replacement of primary pyrrhotite. In addition to the primary and post-cumulus styles, there are multiple examples of hydrothermal veins with fluid-precipitated sulphides.

Various noble metal minerals are associated with the primary magmatic to recrystallised sulphides, dominated by Pt-Pd-Ag-Ni bismuth tellurides. These are commonly found included in pentlandite and chalcopyrite, on the margins of chalcopyrite and in silicates near sulphides.

There is a large variation in the trace element composition of the various sulphide species and mode of occurrence (Fig. 10). For example, magmatic pentlandite has an average Pd content of c. 20 ppm, which drops to c. 3 ppm for recrystallised pentlandite. In contrast, vein-hosted pentlandite has an average Pd content of c. 0.03 ppm (Fig. 10A). Similar or inverse relationships were observed for many of the analysed elements for most of the sulphide species (Fig. 10). The observed variations are most likely due to relative elemental mobility when the sulphides interacted with late hydrothermal fluids. Additionally, the evident variation in solubility raises concerns about binary discrimination diagrams for hydrothermally modified sulphides.

The $\delta^{34}S$ values obtained in this study largely overlap with mantle values (Fig. 11A), implying that the crustal contaminant had a $\delta^{34}S$ close to the mantle range, was sulphur deficient, or both. Another consideration is that crustal $\delta^{34}S$ signatures may be modified by high R factors, masking the effect of external S addition. However, high R factors are unlikely in the case of the Gállojávri mineralisation, with the observed bulk Cu/Pd ranging from depleted to primitive mantle ratios (Fig. 11B). This is corroborated by a simple R factor model that shows that most Pd-enriched samples can be modelled by low R factors (100–1000) and sulphide concentrations close to cotectic proportions (0.1–1%). This suggests that externally derived S was not substantial, which is also supported by the generally low S contents of the Gállojávri intrusion.

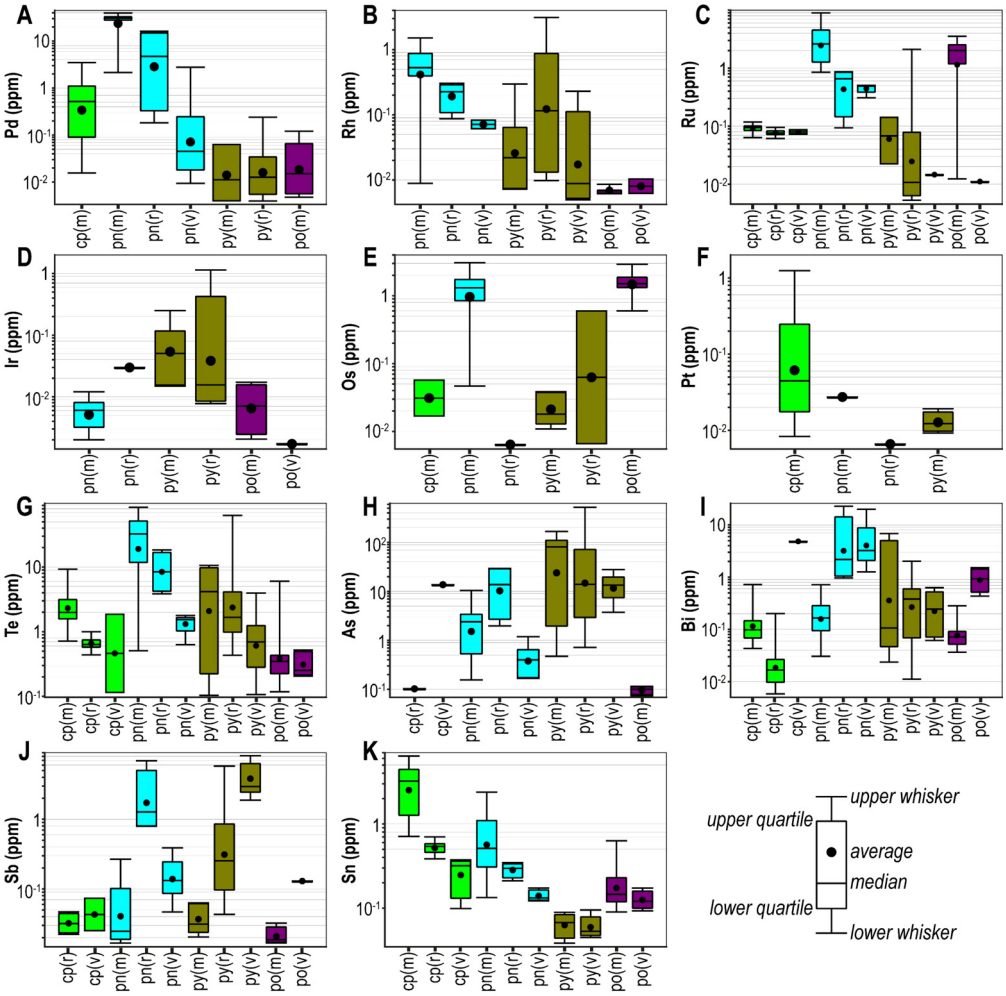

Figure 10: Box and whisker diagram of trace element concentrations in chalcopyrite (cp), pentlandite (pn), pyrite (py) and pyrrhotite (po), for magmatic (m), recrystallised (r) and vein (v) sulphides.

The S concentrations and sulphide modality increase towards country rock material, which also accounts for the thin layer of massive sulphide. However, these areas are typically characterised by depleted Cu/Pd ratios suggesting low R factors. This relationship provides evidence that local assimilation can produce more sulphides, but, in our case, without chemical interaction with large amounts of silicate magma.

The research does not support the notion that the Gállojávri intrusion represents an economic deposit. The intrusion does not exhibit high R factors and metal grades, nor is it enriched in S. However, evaluating unmineralised (without S or Ni excess) samples after correcting for

silicate fractionation (normalising to a silica-incompatible element) shows that the Gállojávri rocks are enriched in chalcophile elements relative to background mantle values (Fig. 11C). This suggests that the system has not experienced significant sulphide extraction en route. In contrast, the parental Karasjok-type komatiites are more uniformly depleted (Fig. 11C). Consequently, the system as a whole shows concurrent anomalous depletion and enrichment trends that are considered a hallmark of a prospective system and should be seen as positive for the mineral potential of the KGB.

This manuscript points to the Karenhaugen and Porsvann bodies as potential Gállojávri-type intrusions. The Pd grades and indicated endowments of both intrusions are consistent with early S saturation with sufficiently high R factors (Fig. 11B). Modelling under the assumption that they are cogenetic conduits indicates that both intrusions have apparent R factors at least one order of magnitude larger than the Gállojávri intrusion.

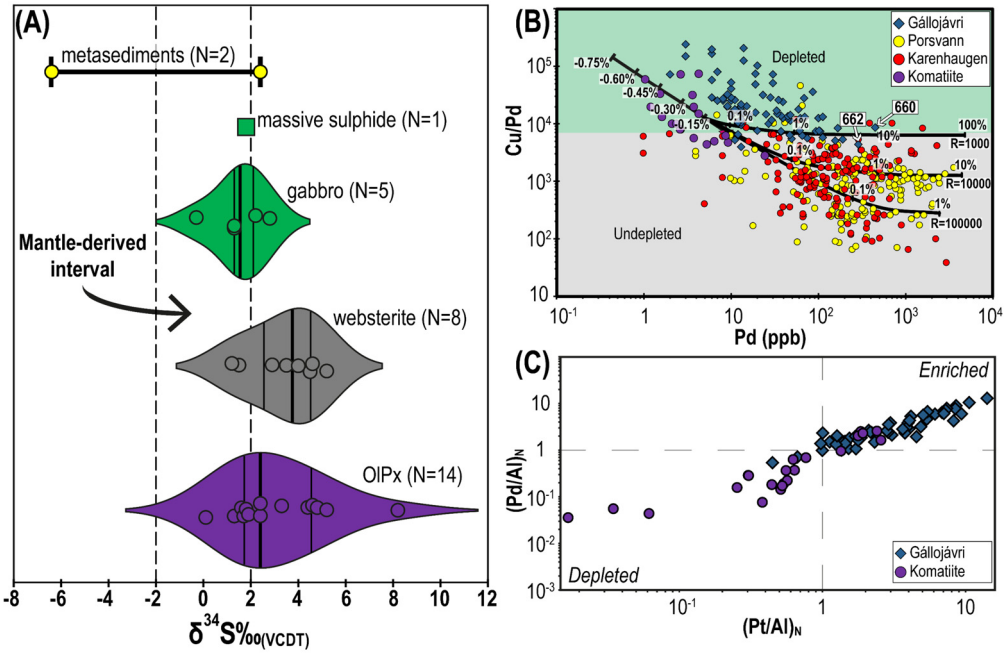

Figure 11: **(A)** The $\delta^{34}S‰$ of the Gállojávri intrusion and its host rock. The kernel density violins include vertical lines showing the median (thick) and quartiles. **(B)** Cu/Pd versus Pd plot for samples from the Karasjok komatiites and the Gállojávri, Karenhaugen, and Porsvann intrusions. The tie lines depict model sulphides crystallising from a komatiitic melt that has been slightly metal depleted at R factors ranging from 1000 to 100,000 (assuming $K_{sul\text{-}sil}^{Pd} = 100000$ and $K_{sul\text{-}sil}^{Cu} = 1000$). **(C)** Unmineralised Gállojávri samples and Karasjok komatiites plotted in a $(Pt/Al)_N$ versus $(Pd/Al)_N$ diagram to identify sulphide-related depletion and enrichment. References – Porsvann and Karenhaugen: Kingsrose (2021); Karsjok komatiites: Fiorentini *et al.* (2011); Primitive mantle normalisation factors: Becker *et al.* (2006).

6 DISCUSSION AND IMPLICATIONS

The work presented in this thesis focuses on the Gállojávri intrusion in northern Norway and how it relates to the Palaeoproterozoic magmatism of the CLGB. The primary aim of this PhD project was to develop a geological model for the intrusion, which can be subdivided into specific objectives. The first objective is to develop a petrogenetic model, the second is to evaluate the relationship to the magmatic evolution of the belt, and the third is to understand the genesis of the mineralisation.

The first paper (Orvik *et al.*, 2022a) primarily addresses the first objective and presents a detailed petrogenetic model for the Gállojávri intrusion. However, both paper two (Orvik *et al.*, 2022b) and manuscript three (Orvik *et al.*, In prep.) show that the model does not resolve all aspects of the magmatic evolution.

A growing body of evidence suggests that several mid- to upper-crustal plutons are formed by repeated injections into a crystal mush (e.g., Nebel *et al.*, 2020) or by incremental sill emplacement (e.g., Mungall *et al.*, 2016). These models contrast with the traditional view of melt-dominated intrusions characterised by gravity-driven accumulation of crystal mushes on chamber floors and margins (e.g., Kruger & Latypov, 2020). As indicated by Nilsson and Often (2006) and Orvik *et al.* (2022a), the spatial differentiation trend of the Gállojávri intrusion follows the foliation of the surrounding country rock, suggesting that it is sill-like and characterised by gravity-driven crystal settling or flotation.

There is strong evidence that the Gállojávri intrusion represents an open system with, for example, phase equilibria requiring at least one recharge. In addition, the uniform trace element signatures reported by Orvik et al. (2022a) suggest that any recharged melt was efficiently mixed (Fig. 5B), thus implying a melt-dominated chamber. The thermodynamic modelling supports this notion, which satisfactorily replicates the observations and intrinsically assumes that the system is melt-dominated (Orvik *et al.*, 2022a).

The variation in radiogenic isotopes paints a different picture, with large spatial variations in isotopic signatures (Orvik *et al.*, 2022b). The local evolved and juvenile excursions indicate inefficient mixing and homogenisation of isotopically distinct components (Fig. 7C), implying that the system was melt-poor or characterised by physical properties that inhibited mixing. Orvik *et al.* (2022b) interpreted that the large variations in isotopic signatures resulted from local dissolution or melting of xenoliths and incomplete mixing of isotopically distinct melts

injected into the hot and semi-consolidated Gállojávri chamber. It should be noted that this interpretation is based on variation in one core; to draw more definitive conclusions, a better definition of the spatial variation is required.

However, one process does not exclude the other. That is, the natural evolution of a melt-dominated chamber would be into a crystal-loaded mush. Therefore, it is not unlikely that the intrusion evolved in line with the model presented by Orvik *et al.* (2022a), followed by subsequent and smaller recharges into the semi-consolidated chamber (Orvik *et al.*, 2022b). This interpretation would be similar to the model for the Rum Layered Suite, Scotland suggested by Hepworth *et al.* (2020b), where they argued for repeated injections into pre-existing cumulates resulting in large-scale isotopic heterogeneity (Hepworth *et al.*, 2020a).

The second objective was to link the petrogenesis of the Gállojávri intrusion to the magmatic evolution of the CLGB. This is primarily treated in papers one and two. In paper one, based on stratigraphy and the spatial link with the upper komatiites, Orvik *et al.* (2022a) hypothesise that the Gállojávri is cogenetic and part of the volcanic plumbing system. This hypothesis was strengthened with the thermodynamic modelling suggesting that the Karasjok komatiites represent analogues to the parental melt, although significantly hybridised by lower-crustal assimilation (c. 15%; Orvik *et al.*, 2022a). The age of the parental Karasjok komatiites indirectly shows that Gállojávri intrusion formed as part of the c. 2.05 Ga plume magmatism.

The c. 2.05 Ga link is confirmed in the second paper that reports a zircon crystallisation age of 2051±8 Ma (Fig. 7A). In addition, the more depleted mantle-like Nd signatures of the Gállojávri (εNd_t <+4) samples are consistent with the juvenile Karasjok-type komatiites (Fig. 8; Krill, 1985a, Orvik *et al.*, 2022b). However, the most evolved Nd compositions of the Gállojávri (εNd_t as low as -15) require a more evolved continental crust than has been documented in the KGB (Orvik *et al.*, 2022b).

There is an ongoing debate surrounding the crustal architecture beneath the CLGB (Hanski, 2015) based on a clear negative correlation between age and initial εNd for the extrusive magmatic rocks in the belt. For example, the Onkamo Group lower komatiites to felsic extrusive rocks are characterised by initial $\varepsilon Nd_{2.44Ga}$ values of c. -9 to 0 (Hanski & Huhma, 2005), while the c. 2.05 Ga upper komatiites consistently have positive initial εNd similar to depleted mantle values (Hanski *et al.*, 2001a, Krill, 1985a). The decreasing level of crustal

interaction implied by the εNd values suggests that the continental lithosphere was significantly thinned or possibly completely disaggregated by c. 2.05 Ga (Hanski, 2013).

As stated above, Orvik *et al.* (2022a, b) link the Gállojávri intrusion to the Karasjok-type komatiites and show that the magmatic evolution is influenced by significant crustal contamination. In addition, identifying highly unradiogenic Nd compositions in MgO-rich rocks suggests the presence of old and evolved components in the lithospheric column at the time. Therefore, it indicates that the continental crust underlying the KGB was intact and of large enough thickness to facilitate extensive contamination of the Gállojávri rocks.

Unlike the KGB, the Finnish part of the CLGB is characterised by a transgressive deepening of the basin, as exemplified by the deep-water sedimentary rocks of the Savukoski Group (Hanski & Huhma, 2005). This deepening could indicate attenuation of the crust, which again could explain the juvenile komatiites and picrites. However, the 2058±4 Ma Kevitsa intrusion (Mutanen & Huhma, 2001), hosted by the Savukoski Group, has recently been interpreted as a conduit for coeval and juvenile picrite lavas (Luolavirta *et al.*, 2018b). Like the Gállojávri, the Kevitsa intrusion has heterogeneous isotopic signatures with initial εNd as low as -7 (Hanski *et al.*, 1997), in part lower than those of the hosting metasediments (Huhma *et al.*, 2018). Therefore, it seems interaction is identifiable throughout the CLGB, which is inconsistent with a completely rifted craton.

The third objective was to characterise the mineralisations and evaluate the ore-forming processes. This topic is primarily treated in manuscript three. However, the concentration of metals from background levels in the mantle source to economic levels in the accessible crust depends on lithospheric-scale processes (Barnes *et al.*, 2016). Therefore, both of the first two papers offer constraints and conditions for developing a mineralisation model and evaluating the implications for regional prospectivity.

The c. 2.05 Ga magmatism in the CLGB is considered highly prospective for orthomagmatic sulphides, especially when considering the Savukoski Group, which hosts the Kevitsa and Sakatti deposits. These ultramafic to mafic bodies are interpreted as open systems characterised by at least two pulses of melt that directly contributed to the concentration of metals (Brownscombe *et al.*, 2015, Luolavirta *et al.*, 2018b). In both Kevitsa and Sakatti, later magma pulses assimilated, remobilised and concentrated the sulphides crystallised in the initial stages to economic levels.

Crustal contamination is considered an important factor in the formation of orthomagmatic sulphide deposits in ultramafic and mafic systems (Barnes & Lightfoot, 2005, Li *et al.*, 2003, Ripley & Li, 2003). This is especially true for deposits linked to high-temperature magmas like komatiites (Bekker *et al.*, 2009), which have S contents well below the SCSS in their mantle sources and become more undersaturated during ascent (Barnes *et al.*, 2016, Mavrogenes & O'Neill, 1999). Magmatic conduits to mantle-derived melts are therefore regarded as favourable environments for forming economically viable sulphide deposits. A feature exemplified by that channelised sills, tubes, or blade-shape dykes with prolonged high-volume flow accounting for most known host igneous bodies to significant ore deposits worldwide (Barnes *et al.*, 2016, Lesher, 2019).

Considering the indicated metal enrichment in the Gállojávri intrusion (Nilsson *et al.*, 2016), the conduit model (Orvik *et al.*, 2022a) and the link to the prospective c. 2.05 Ga plume magmatism (Orvik *et al.*, 2022b), the intrusion seems to represent a highly prospective magmatic body in the KGB. However, as Orvik *et al.* (In prep.) conclude, the intrusion is neither S-rich nor characterised by high R factors (Fig. 11B).

The low R factors and S content is most likely due to the melts being undersaturated in S. For example, S isotope compositions are mantle-like (Fig. 11A), whereas both trace element and radiogenic signatures indicate significant contamination (Fig. 7C). This suggests that the contaminant was S-poor or had a mantle like $\delta^{34}S$ composition, or both. The former is the more realistic considering the low S contents of the Gállojávri rocks. This interpretation would also be in line with the apparent late exsolution of a sulphide liquid, commonly cotectic proportions of sulphide and apparent low R factors.

If we compare the Gállojávri intrusion to the Lomalampi and Kevitsa deposits, the biggest difference appears to be accessible external S. Both Lomalampi and Kevitsa are associated with the S-bearing supracrustal rocks of the Savukoski Group, which is also reflected in the S-isotope signatures (Fig. 12; Grinenko *et al.*, 2003, Törmänen *et al.*, 2016). In contrast, the KGB lithostratigraphy is dominated by granitoid-derived clastic rocks, with no identifiable S-rich intervals below the Briitágielas Formation (Melezhik *et al.*, 2015), stratigraphically above the Gállojávri intrusion.

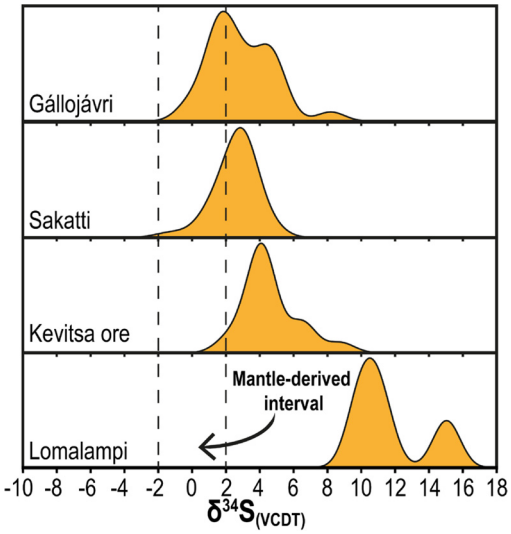

Figure 12: Relation of the δ34S data for the Gállojávri, Sakatti, Kevitsa ores and Lomalampi. references – Sakatti: Brownscombe (2015); Kevitsa: Grinenko *et al.* (2003); Lomalampi: Törmänen *et al.* (2016);

Recent research has also suggested that a few magmatic sulphide deposits formed entirely from mantle-derived S, for example, the Ni-Cu-PGE Nebo-Babel (Seat *et al.*, 2009) and Santa Rita (Lazarin, 2011) and the Luanga PGE deposit (Mansur *et al.*, 2020b). This also seems to be the case for the Sakatti deposit, which is characterised by mantle-like S signatures (Fig. 12; Brownscombe, 2015). Brownscombe *et al.* (2015) proposed that the proto-ores were formed by mantle-derived S before later being cannibalised and concentrated to economic levels in the current silicate host. This suggests that, whether or not external S is present, a conduit system should be highly dynamic and capable of assimilating, remobilising and concentrating S in order to form a deposit.

In the petrogenetic model of Orvik *et al.* (2022a), significant fractionation and assimilation occurred in a staging lower-crustal magma chamber to the Gállojávri intrusion. The hybrid melt migrated from the lower crust after it attained a composition like a komatiitic basalt (c. 12 wt.% MgO) with a significantly lower liquidus temperature. The lower temperature, narrower liquidus-solidus interval and higher viscosity suggest that the hybrid magma was less competent in forming channelised flows capable of efficient country-rock assimilation (Lesher, 2019).

Empirically, conduit mineralisations are commonly associated with the highest degree partial melts and the least fractionated magmas within any given magmatic province (Barnes *et al.*, 2016). In addition, conduit mineralisations are commonly associated with thickened adcumulate intervals characterised by high-volume flow of primitive melts (reviewed in Lesher, 2019). These features are in contrast to the observed lithological differentiation in the Gállojávri intrusion that suggests a less dynamic system, which, despite being described as open, shows no signs of thickened intervals of primitive adcumulates. In addition, late juvenile

melt injections may have been small as they formed local domains in the Gállojávri chamber (Orvik *et al.*, 2022b).

It should be noted that the interpretation that the Gállojávri intrusion does not contain a deposit is based on the variations in three short (c. 125 m) cores intersecting an intrusion that geophysical anomalies indicate is much larger. Skaar (2014), for example, interpreted that the intrusion might be 30 km long, plunging shallowly to the southeast, where it reaches a depth of c. 1 km (Nilsson *et al.*, 2016). Although rather speculative, it is not uncommon that sulphide ores form regular vertical sequences, with massive sulphides underlying net textured ores that transition upwards into disseminated sulphides (Barnes *et al.*, 2017b). Considering that the base of the Gállojávri intrusion is unconstrained, where dense sulphide liquids are likely to be concentrated, the possibility of larger sulphide accumulations in the conduit cannot be ruled out.

The results presented in this thesis indicate that the system did not reach extensive early sulphide saturation, including the earlier differentiation en route. For example, in the R factor model of Orvik *et al.* (In prep.), the parental melt is estimated to only have experienced c. 0.15% cotectic removal of sulphides prior to emplacement. Considering the high Ni in olivine (Orvik *et al.*, 2022a), this early sulphide fractionation was not enough to significantly deplete the system in chalcophile elements. Moreover, unmineralised Gállojávri samples suggest the enrichment of chalcophile elements compared to mantle background values (Fig. 11C).

Therefore, the volcanic-plumbing system, including the Gállojávri intrusion, should be considered prospective. This interpretation is strengthened by the general chalcophile element depletion of the cogenetic Karasjok-type komatiites, which strongly suggests sulphide extraction before subaerial emplacement (Heggie *et al.*, 2013). Orvik *et al.* (In prep.) propose that the stratigraphically correlatable Karenhaugen and Porsvann intrusions represent cogenetic conduits. Both intrusions have more uniformly enriched Cu/Pd ratios (Fig. 11B), which, unlike in the Gállojávri intrusion, indicates that sulphides were not removed cotectically prior to emplacement. These undifferentiated signatures imply that the parental melts to the Karenhaugen and Porsvann intrusions did not undergo significant fractionation in a staging magma chamber and thus represent more primitive, less fractionated and more prospective members of the volcanic plumbing system.

7 CONCLUSIONS

Based on the data and modelling discussed above, the following conclusions can be drawn:

- The Gállojávri intrusion represents part of a magmatic plumbing system that funnelled Karasjok-type komatiites to shallower crustal levels. The parental komatiite intruded the lower crust (c. 700 MPa), where it fractionated and assimilated Archaean TTGG country rocks. Thermobarometric estimates and phase equilibria require a second stage of assimilation, recharge and fractional crystallisation at mid-crustal levels (c. 400 MPa). The two-stage polybaric model suggests that the Gállojávri intrusion forms part of a transcrustal conduit system.
- The variation observed in the Sr-Nd-Hf isotopic data reveals the complexity of the magmatic evolution. It shows that the system remained open, with local melting of country-rock xenoliths and injections of juvenile melt resulting in large range in juvenile to evolved isotopic signatures over small distances.
- Zircon U-Pb dating demonstrates that the Gállojávri intrusion was emplaced at 2051 ± 8 Ma, suggesting it is part of a group of Karasjok-type komatiites and ultramafic to mafic intrusions of similar age in the CLGB. This magmatism has been linked to rifting and an incipient mantle plume.
- The evolved radiogenic signatures show that the Gállojávri intrusion was emplaced in an intracratonic environment and was contaminated by evolved and unidentified crustal components in the KGB basement. The contamination implies that the continental crust was intact and not completely rifted at the time.
- The Gállojávri intrusion underwent alteration and metamorphism during the Svecofennian- and Caledonian orogeny, as suggested by the Rb-Sr errorchron and zircon lead loss, respectively.
- The Gállojávri mineralisation displays both primary and secondary (post-cumulus) features. Primary features comprise intercumulus sulphides with primary magmatic assemblages of pyrrhotite, pentlandite and chalcopyrite, whereas secondary features include assemblages where pyrite has replaced pyrrhotite. The primary magmatic intercumulus sulphides are internally differentiated and commonly associated with refractory silicate phases in proportions that suggest late cotectic fractionation.
- The Gállojávri mineralisation, as observed in this study, is not economically viable. The intrusion is neither S-rich nor sufficiently enriched in PGE. Modelling shows that the

most PGE-enriched rocks of the Gállojávri intrusion can be simulated with low R factors (100–1000) and cotectic fractionation.

- Sulphur isotopes have mantle-like signatures. Combined with low S concentrations and cotectic sulphide fractions, external S addition does not appear to have played a significant role in ore formation.
- Unmineralised samples show that most rocks are enriched in chalcophile elements, indicating that the system was fertile with negligible loss of chalcophile elements during ascent from the mantle source. Overall high Ni-in-olivine concentrations corroborate this interpretation.
- Our findings suggest that dynamic conduit-like systems in the KGB, like the Gállojávri intrusion, should be considered potential exploration targets. The Karenhaugen and Porsvann intrusions, also in the KGB, are likely analoguous to the the Gállojávri intrusion but with higher prospectivities suggested by the available chemical data.

8 THOUGHTS ON FUTURE RESEARCH DIRECTIONS

Despite being a local study on one small intrusion in the north of Norway, this PhD project partly tries to answer regional questions. This range of scales reflects the strengths of some of the chosen methods (e.g., radiogenic isotopes) but also points to uncertainties because of limited data. This reasoning similarly applies to the Gállojávri intrusion, with few drill cores in a poorly constrained geometry.

As stated above, the research presented in this thesis is based on three short drill cores in an intrusion that may be much larger than the bedrock maps suggest. Therefore, the interpretations and conclusions of this thesis is likely based on only a small part of a larger intrusion. Considering the variation observed in the cores, it is not unlikely that an expanded drilling campaign would paint a different picture. Luolavirta (2018), for example, demonstrated that different evolutionary histories might be inferred from different locations within the Kevitsa intrusion. Therefore, in the case of the Gállojávri intrusion, efforts should be made to constrain its geometry by detailed geophysical modelling supplemented by a drilling campaign that penetrates the intrusion's basal contact.

The validity of the petrogenetic model presented in this study should be tested by its ability to explain additional data from a larger part of the intrusion. Furthermore, the model should be compared to the petrogenesis of other, similar conduit-type intrusions in the KGB. For example, this study hypothesises that the stratigraphically correlatable Karenhaugen and Porsvann intrusions are cogenetic. This should be tested by isotopic dating and the development of petrogenetic models similar to what has now been done for the Gállojávri intrusion. If the intrusions are of similar age and the parental melts are consistent with Karasjok-type komatiite (or derived thereof), the hypothesis may be accepted. In addition, since both Karenhaugen and Porsvann have sulphide concentrations and metal contents that suggest early saturation, a detailed study might highlight critical processes for forming a sulphide deposit in the KGB.

Based on mantle-like $\delta^{34}S$ signals, this study interpreted that external S did not contribute significantly to the Gállojávri mineralisation. However, data on possible mass-independent S fractionation is still lacking for the Gállojávri intrusion and the KGB at large, which could shed light on potential Archaean sources of contamination.

The Fennoscandian Shield is characterised by a complicated magmatic history that reflects a highly dynamic mantle source. For example, the 2.44, 2.22 and 2.05 Ga magmatic pulses have all been linked to anomalous mantle activity (Barnes & Often, 1990, Hanski & Huhma, 2005, Hanski, 2013, Stepanova *et al.*, 2021). This study leaned on the plume model presented by Barnes and Often (1990) and Hanski *et al.* (2001); however, Pt-Re-Os isotopic studies might provide valuable insights into the characteristics, evolution and metal content of the mantle through time. For example, Puchtel *et al.* (2020) documented Re-Os and Pt-Os signatures for the upper komatiites at Jeesiörova and Kevitsa. The initial γ^{187}Os and μ^{186}Os were estimated to be -0.2 and +29, respectively, which indicates suprachondritic Pt/Os in the mantle source. The 2.05 Ga Kevitsa komatiites were estimated to be derived from a mantle source with a Pt+Pd content between 115 and 125% relative to present-day Bulk Silicate Earth. Coupled with initial μ^{182}W (c. -10), they attributed the enriched mantle to either late grainy accretion (heterogeneously distributed extraterrestrial material) or the addition of chemically fractionated core material (Puchtel *et al.*, 2020).

Future research should focus on both mineralised and barren intrusions in the KGB to identify key differences. For example, in contrast to the 2.44 and 2.05 Ga group of intrusions, the c. 2.22 Ga group in the Fennoscandian Shield does not seem to have produced significant mineral deposits outside of Pechenga (Hanski, 1986, Hanski & Huhma, 2005). This group of intrusions might be represented by the barren Čoalbmejávri and Skoganvárre layered intrusions in the northern part of the KGB (Hansen, 2008, Hansen *et al.*, 2020). Detailed studies into these intrusions might reveal differences that can explain why one age group is prospective for magmatic sulphides while the other is not. Are there differences in critical processes or characteristics, such as source, magma pathways or sulphur saturation? For example, there are no known volcanic counterparts to the 2.22 Ga group intrusive rocks in the supracrustal sequences of the CLGB (Hanski, 2013). Does the lack of extrusive rocks reflect a lower production of mantle melts and lower melt fluxes in the continental crust?

One key question is whether the differences in geological processes translate to mappable features (McCuaig *et al.*, 2010). Like the rest of the CLGB, the KGB is largely covered and poorly exposed. Therefore, studies that can relate the magmatic processes of a magmatic suite to mappable targets, such as differences in geophysical response or geochemistry, would facilitate the identification of unknown examples in the poorly exposed terrain. For example, this study interprets the Gállojávri intrusion as part of a trans-crustal conduit system in an

intracontinental rift. In this model, melt fluxes greatly control the mineral potential of the system. Is it possible to link high-flux conduits to other geological features indicative of such a process? Felsic volcanic rocks coeval with komatiite rocks, for example, are widely reported in world-class komatiite nickel sulphide camps (reviewed in McCuaig *et al.*, 2010). Viscous felsic lavas, lava domes and accompanying autoclastics are a good proxy for volcanic vent sites compared to less viscous komatiite flows. The spatial distribution of felsic volcanic rocks can be established using geological mapping proxies, such as gravimetric data, and requires age information for komatiite and felsic volcanic rocks (McCuaig *et al.*, 2010).

Such studies may facilitate the development of regional prospecting tools, especially if the indirectly mapped process is critical for forming an ore deposit. For example, the spinel compositions documented in Orvik *et al.* (2022) are consistent with a sub-volcanic environment. Can spinel compositions in surficial sediments be used as an indicator in mineral exploration targeting? Similarly, can the documented Ni-rich olivine, PGM and magmatic sulphides be used as indicator minerals?

The KGB remain poorly studied compared to the rest of the CLGB, and this chapter on future research directions is by no means exhaustive. However, many of the research questions outlined above should be of equal interest to exploration geoscientists and geoscientific researchers. Collaboration between academia and industry can be advantageous to both, adding to the body of pure and applied knowledge and facilitating the development of regional exploration models.

9 BIBLIOGRAPHY

Amelin, Y. V., Heaman, L. M. & Semenov, V. S. (1995). U-Pb geochronology of layered mafic intrusions in the eastern Baltic Shield: implications for the timing and duration of Paleoproterozoic continental rifting. *Precambrian Research* **75**, 31-46.

Annen, C., Latypov, R., Chistyakova, S., Cruden, A. R. & Nielsen, T. F. D. (2022). Catastrophic growth of totally molten magma chambers in months to years. *Science Advances* **8**, eabq0394.

Arndt, N. (2008). *Komatiite*: Cambridge University Press.

Arndt, N. T. & Jenner, G. A. (1986). Crustally contaminated komatiites and basalts from Kambalda, Western Australia. *Chemical Geology* **56**, 229-255.

Barley, M. E., Kerrich, R., Reudavy, I. & Xie, Q. (2000). Late Archaean Ti–rich, Al–depleted komatiites and komatiitic volcaniclastic rocks from the Murchison Terrane in Western Australia. *Australian Journal of Earth Sciences* **47**, 873-883.

Barnes, S.-J. (1987). Unusual nickel and copper to noble-metal ratios from the Råna Layered Intrusion, northern Norway. *Norwegian Journal of Geology/Norsk geologisk tidsskrift* **67**, 215-231.

Barnes, S.-J. & Lightfoot, P. C. (2005). Formation of magmatic nickel-sulfide ore deposits and processses affecting their copper and platinum-group element contents. In: Hedenquist, J. W., Thompson, J. F. H., Goldfarb, R. J. & Richards, J. P. (eds.) *One Hundredth Anniversary Volume*. Economic Geology: Society of Economic Geologists, 179-213.

Barnes, S.-J. & Maier, W. D. (1999). The fractionation of Ni, Cu and the noble metals in silicate and sulphide liquids. *Dynamic processes in magmatic ore deposits and their application in mineral exploration*, 69-106.

Barnes, S.-J. & Maier, W. D. (2002). Platinum-group elements and microstructures of normal Merensky reef from Impala Platinum Mines, Bushveld Complex. *Journal of Petrology* **43**, 103-128.

Barnes, S.-J. & Ripley, E. M. (2016). Highly siderophile and strongly chalcophile elements in magmatic ore deposits. *Reviews in Mineralogy and Geochemistry* **81**, 725-774.

Barnes, S. J. (2006). Komatiite-Hosted Nickel Sulfide Deposits: Geology, Geochemistry, and Genesis. *Nickel Deposits of the Yilgarn Craton: Geology, Geochemistry, and Geophysics Applied to Exploration*: Society of Economic Geologists, 0.

Barnes, S. J., Cruden, A. R., Arndt, N. & Saumur, B. M. (2016). The mineral system approach applied to magmatic Ni–Cu–PGE sulphide deposits. *Ore Geology Reviews* **76**, 296-316.

Barnes, S. J., Holwell, D. A. & Le Vaillant, M. (2017a). Magmatic Sulfide Ore Deposits. *Elements* **13**, 89-95.

Barnes, S. J., Mungall, J. E., Le Vaillant, M., Godel, B., Lesher, C. M., Holwell, D., Lightfoot, P. C., Krivolutskaya, N. & Wei, B. (2017b). Sulfide-silicate textures in magmatic Ni-Cu-PGE sulfide ore deposits: Disseminated and net-textured ores. *American Mineralogist* **102**, 473-506.

Barnes, S. J. & Often, M. (1990). Ti-Rich Komatiites from Northern Norway. *Contributions to Mineralogy and Petrology* **105**, 42-54.

Barnes, S. J. & Roeder, P. L. (2001). The range of spinel compositions in terrestrial mafic and ultramafic rocks. *Journal of Petrology* **42**, 2279-2302.

Becker, H., Horan, M. F., Walker, R. J., Gao, S., Lorand, J. P. & Rudnick, R. L. (2006). Highly siderophile element composition of the Earth's primitive upper mantle: Constraints from new data on peridotite massifs and xenoliths. *Geochimica et Cosmochimica Acta* **70**, 4528-4550.

Begg, G. C., Hronsky, J. A. M., Arndt, N. T., Griffin, W. L., O'Reilly, S. Y. & Hayward, N. (2010). Lithospheric, cratonic, and geodynamic setting of Ni-Cu-PGE sulfide deposits. *Economic Geology*, 1057-1070.

Bekker, A., Barley, M. E., Fiorentini, M. L., Rouxel, O. J., Rumble, D. & Beresford, S. W. (2009). Atmospheric sulfur in Archean komatiite-hosted nickel deposits. *Science* **326**, 1086-1089.

Bingen, B., Solli, A., Viola, G., Torgersen, E., Sandstad, J. S., Whitehouse, M. J., Røhr, T. S., Ganerød, M. & Nasuti, A. (2015). Geochronology of the palaeoproterozoic kautokeino greenstone belt, finnmark, Norway: Tectonic implications in a Fennoscandia context. *Norwegian Journal of Geology* **95**, 365-396.

Boettcher, A., Mysen, B. O. & Modreski, P. (1975). Melting in the mantle: phase relationships in natural and synthetic peridotite–H2O and peridotite–H2O–CO2 systems at high pressures. *Physics and Chemistry of the Earth*: Elsevier, 855-867.

Bohrson, W. A., Spera, F. J., Ghiorso, M. S., Brown, G. A., Creamer, J. B. & Mayfield, A. (2014). Thermodynamic model for energy-constrained open-system evolution of crustal magma bodies undergoing simultaneous recharge, assimilation and crystallization: The magma chamber simulator. *Journal of Petrology* **55**, 1685-1717.

Bohrson, W. A., Spera, F. J., Heinonen, J. S., Brown, G. A., Scruggs, M. A., Adams, J. V., Takach, M. K., Zeff, G. & Suikkanen, E. (2020). Diagnosing open-system magmatic processes using the Magma Chamber Simulator (MCS): part I—major elements and phase equilibria. *Contributions to Mineralogy and Petrology* **175**, 1-29.

Bowen, N. L. (1928). *The Evolution of the Igneous Rocks*: Princeton University Press.

Boyd, R. & Eilu, P. (2012). N037 Karasjok–Lakselv Ni-Cu-PGE. In: Eilu, P. (ed.) *Mineral deposits and metallogeny of Fennoscandia*. Finland: Geological Survey of Finland Special Paper 53, 118-119.

Braathen, A. & Davidsen, B. (2000). Structure and stratigraphy of the Palaeoproterozoic Karasjok Greenstone Belt, north Norway - regional implications. *Norwegian Journal of Geology* **80**, 33-50.

Bradley, J. (2003). Finnmark Project, Diamond Drill Program - April 2003. Summary and review. Norwegian Directorate of Mining: Tertiary Gold Limited, 14.

Brey, G. P. & Köhler, T. (1990). Geothermobarometry in Four-phase Lherzolites II. New Thermobarometers, and Practical Assessment of Existing Thermobarometers. *Journal of Petrology* **31**, 1353-1378.

Brownscombe, W. (2015). The geology and geochemistry of the Sakatti Cu-Ni-PGE deposit, N. Finland. Imperial College London.

Brownscombe, W., Ihlenfeld, C., Coppard, J., Hartshorne, C., Klatt, S., Siikaluoma, J. K. & Herrington, R. J. (2015). The Sakatti Cu-Ni-PGE Sulfide Deposit in Northern Finland. In: Maier, W. D., Lahtinen, R. & O'Brien, H. (eds.) *Mineral Deposits of Finland*: Elsevier, 211-252.

Brügmann, G. E., Naldrett, A. J., Asif, M., Lightfoot, P. C., Gorbachev, N. S. & Fedorenko, V. A. (1993). Siderophile and chalcophile metals as tracers of the evolution of the Siberian Trap in the Noril'sk region, Russia. *Geochimica et Cosmochimica Acta* **57**, 2001-2018.

Cabri, L. J. (1973). New data on phase relations in the Cu-Fe-S system. *Economic Geology* **68**, 443-454.

Campbel, I. H., Naldrett, A. J. & Barnes, S. J. (1983). A Model for the Origin of the Platinum-Rich Sulfide Horizons in the Bushveld and Stillwater Complexes. *Journal of Petrology* **24**, 133-165.

Campbell, I. & Naldrett, A. (1979). The influence of silicate: sulfide ratios on the geochemistry of magmatic sulfides. *Economic Geology* **74**, 1503-1506.

Cashman, K. V., Sparks, R. S. J. & Blundy, J. D. (2017). Vertically extensive and unstable magmatic systems: A unified view of igneous processes. *Science* **355**, eaag3055.

Dare, S. A., Barnes, S.-J., Prichard, H. M. & Fisher, P. C. (2014). Mineralogy and geochemistry of Cu-rich ores from the McCreedy East Ni-Cu-PGE deposit (Sudbury, Canada): Implications for the behavior of platinum group and

chalcophile elements at the end of crystallization of a sulfide liquid. *Economic Geology* **109**, 343-366.

Dare, S. A. S., Barnes, S.-J., Prichard, H. M. & Fisher, P. C. (2011). Chalcophile and platinum-group element (PGE) concentrations in the sulfide minerals from the McCreedy East deposit, Sudbury, Canada, and the origin of PGE in pyrite. *Mineralium Deposita* **46**, 381-407.

Davidsen, B. (1994). Stratigrafi, petrologi og geokjemi med vekt på komatiittiske bergarter innen den nordligste del av Karasjok grønnsteinsbelte, Brennelv, Finnmark. Cand. scient. *Unpublished Cand. Scient. thesis. University of Tromsø*.

Davidson, J. P. & Tepley, F. J. (1997). Recharge in Volcanic Systems: Evidence from Isotope Profiles of Phenocrysts. *Science* **275**, 826-829.

DePaolo, D. J. & Wasserburg, G. (1976). Nd isotopic variations and petrogenetic models. *Geophysical Research Letters* **3**, 249-252.

Dickin, A. P. & Durant, G. P. (2002). The Blackstones Bank igneous complex: geochemistry and crustal context of a submerged Tertiary igneous centre in the Scottish Hebrides. *Geological Magazine* **139**, 199-207.

Ding, X., Ripley, E. M., Shirey, S. B. & Li, C. (2012). Os, Nd, O and S isotope constraints on country rock contamination in the conduit-related Eagle Cu–Ni–(PGE) deposit, Midcontinent Rift System, Upper Michigan. *Geochimica et Cosmochimica Acta* **89**, 10-30.

Duran, C. J., Barnes, S. J. & Corkery, J. T. (2015). Chalcophile and platinum-group element distribution in pyrites from the sulfide-rich pods of the Lac des Iles Pd deposits, Western Ontario, Canada: Implications for post-cumulus re-equilibration of the ore and the use of pyrite compositions in exploration. *Journal of Geochemical Exploration* **158**, 223-242.

Duran, C. J., Barnes, S. J., Pleše, P., Kudrna Prašek, M., Zientek, M. L. & Pagé, P. (2017). Fractional crystallization-induced variations in sulfides from the Noril'sk-Talnakh mining district (polar Siberia, Russia). *Ore Geology Reviews* **90**, 326-351.

Eilu, P. (ed.) (2012). *Mineral deposits and metallogeny of Fennoscandia*. Geological Survey of Finland

Fiorentini, M. L., Barnes, S. J., Maier, W. D., Burnham, O. M. & Heggie, G. (2011). Global Variability in the Platinum-group Element Contents of Komatiites. *Journal of Petrology* **52**, 83-112.

Fowler, S. J., Bohrson, W. A. & Spera, F. J. (2004). Magmatic evolution of the Skye igneous centre, western Scotland: Modelling of assimilation, recharge and fractional crystallization. *Journal of Petrology* **45**, 2481-2505.

Frost, B. R. & Frost, C. D. (2019). *Essentials of igneous and metamorphic petrology*: Cambridge University Press.

Ghiorso, M. S. & Gualda, G. A. R. (2015). An H2O–CO2 mixed fluid saturation model compatible with rhyolite-MELTS. *Contributions to Mineralogy and Petrology* **169**, 53.

Ghiorso, M. S. & Sack, R. O. (1995). Chemical mass transfer in magmatic processes IV. A revised and internally consistent thermodynamic model for the interpolation and extrapolation of liquid-solid equilibria in magmatic systems at elevated temperatures and pressures. *Contributions to Mineralogy and Petrology* **119**, 197-212.

Ginibre, C., Wörner, G. & Kronz, A. (2007). Crystal Zoning as an Archive for Magma Evolution. *Elements* **3**, 261-266.

Godel, B. & Barnes, S.-J. (2008). Platinum-group elements in sulfide minerals and the whole rocks of the J-M Reef (Stillwater Complex): Implication for the formation of the reef. *Chemical Geology* **248**, 272-294.

Godel, B., Barnes, S.-J. & Maier, W. D. (2007). Platinum-group elements in sulphide minerals, platinum-group minerals, and whole-rocks of the Merensky Reef (Bushveld Complex, South Africa): implications for the formation of the reef. *Journal of Petrology* **48**, 1569-1604.

Grant, T. B., Larsen, R. B., Anker-Rasch, L., Grannes, K. R., Iljina, M., McEnroe, S., Nikolaisen, E., Schanche, M. & Øen, E. (2016). Anatomy of a deep crustal volcanic conduit system; The Reinfjord Ultramafic Complex, Seiland Igneous Province, Northern Norway. *Lithos*: Elsevier B.V., 200-215.

Grinenko, L., Hanski, E. & Grinenko, V. (2003). Formation conditions of the Keivitsa Cu-Ni deposit, northern Finland: Evidence from S and C isotopes. *Geochemistry International* **41**, 154-167.

Gualda, G. A. R., Ghiorso, M. S., Lemons, R. V. & Carley, T. L. (2012). Rhyolite-MELTS: a Modified Calibration of MELTS Optimized for Silica-rich, Fluid-bearing Magmatic Systems. *Journal of Petrology* **53**, 875-890.

Hansen, H. (2008). Tectonic setting, magmatic evolution and PGE-potentiality of the layered intrusions in Karasjok Greenstone Belt, Finnmark, northern Norway. *Department of geology*. University of Tromsø: UiT.

Hansen, H., Slagstad, T. & Bergh, S. G. (2020). Geochemical volcanostratigrapy defines the tectonic evolution of the Karasjok Greenstone Belt, Finmark. *The 34th Nordic Geological Winter Meeting*. Oslo.

Hanski, E. (1986). The gabbro-wehrlite association in the eastern part of the Baltic Shield. *Geology and metallogeny of copper deposits*: Springer, 151-170.

Hanski, E. (2015). Chapter 2 - Synthesis of the Geological Evolution and Metallogeny of Finland. In: Maier, W. D., Lahtinen, R. & O'Brien, H. (eds.) *Mineral Deposits of Finland*: Elsevier, 39-71.

Hanski, E. & Huhma, H. (2005). Chapter 4 Central Lapland greenstone belt. In: Lehtinen, M., Nurmi, P. A. & Rämö, O. T. (eds.) *Precambrian Geology of Finland Key to the Evolution of the Fennoscandian Shield*: Elsevier, 139-193.

Hanski, E., Huhma, H., Rastas, P. & Kamenetsky, V. S. (2001a). The palaeoproterozoic komatiite-picrite association of Finnish lapland. *Journal of Petrology* **42**, 855-876.

Hanski, E., Huhma, H., Souminen, I. & Walker, R. (1997). Geochemical and isotopic (Os, Nd) study of the Keivitsa intrusion and its Cu-Ni deposit, northern Finland. In: Papunen, H. (ed.) *Mineral deposits: research and exploration – where do they meet? Proceedings of the fourth Biennial SGA meeting, Turku, 11–13 Aug 1997*. Rotterdam: A. A. Balkema, 435-438.

Hanski, E., Huhma, H. & Vaasjoki, M. (2001b). Geochronology of northern Finland: a summary and discussion. *Special Paper-Geological Survey of Finland*, 255-279.

Hanski, E., Walker, R., Huhma, H. & Suominen, I. (2001c). The Os and Nd isotopic systematics of c. 2.44 Ga Akanvaara and Koitelainen mafic layered intrusions in northern Finland. *Precambrian Research* **109**, 73-102.

Hanski, E. J. (2013). 3.4 Evolution of the Palaeoproterozoic (2.50–1.95 Ga) Non-orogenic Magmatism in the Eastern Part of the Fennoscandian Shield. In: Melezhik, V. A., Prave, A. R., Fallick, A. E., Kump, L. R., Strauss, H., Lepland, A. & Hanski, E. J. (eds.) *Reading the Archive of Earth's Oxygenation*: Springer Berlin Heidelberg, 179-245.

Hanski, E. J. & Melezhik, V. A. (2013). 3.2 Litho- and Chronostratigraphy of the Palaeoproterozoic Karelian Formations. In: Melezhik, V. A., Prave, A. R., Fallick, A. E., Kump, L. R., Strauss, H., Lepland, A. & Hanski, E. J. (eds.) *Reading the Archive of Earth's Oxygenation: Volume 1: The Palaeoproterozoic of Fennoscandia as Context for the Fennoscandian Arctic Russia - Drilling Early Earth Project*. Berlin, Heidelberg: Springer Berlin Heidelberg, 39-110.

Hanson, G. N. (1989). An approach to trace element modeling using a simple igneous system as an example. In: Lipin, B. R. & McKay, G. A. (eds.) *Geochemistry and Mineralogy of Rare Earth Elements*: De Gruyter, 18.

Hanson, G. N. & Langmuir, C. H. (1978). Modelling of major elements in mantle-melt systems using trace element approaches. *Geochimica et Cosmochimica Acta* **42**, 725-741.

Heggie, G., Barnes, S. & Fiorentini, M. (2013). Application of lithogeochemistry in the assessment of nickel-sulphide potential in komatiite belts from northern Finland and Norway. *Bulletin of the Geological Society of Finland* **85**.

Heinonen, J. S., Bohrson, W. A., Spera, F. J., Brown, G. A., Scruggs, M. A. & Adams, J. V. (2020). Diagnosing open-system magmatic processes using the Magma Chamber Simulator (MCS): part II—trace elements and isotopes. *Contributions to Mineralogy and Petrology* **175**, 1-21.

Heinonen, J. S., Iles, K. A., Heinonen, A., Fred, R., Virtanen, V. J., Bohrson, W. A. & Spera, F. J. (2021). From Binary Mixing to Magma Chamber Simulator: Geochemical Modeling of Assimilation in Magmatic Systems. In: Masotta, M., Beier, C. & Mollo, S. (eds.) *Crustal Magmatic System Evolution*: co-publication of the American Geophysical Union and John Wiley and Sons, Inc., 151-176.

Heinonen, J. S., Luttinen, A. V., Spera, F. J. & Bohrson, W. A. (2019). Deep open storage and shallow closed transport system for a continental flood basalt sequence revealed with Magma Chamber Simulator. *Contributions to Mineralogy and Petrology* **174**, 87-87.

Henriksen, H. (1986). Iddjajav'ri, bedrock map 2034 2. In: Often, M. & Siedlecka, A. (eds.): Geological Survey of Norway (NGU).

Hepworth, L. N., Daly, J. S., Gertisser, R., Johnson, C. G., Emeleus, C. H. & O'Driscoll, B. (2020a). Rapid crystallization of precious-metal-mineralized layers in mafic magmatic systems. *Nature Geoscience* **13**, 375-381.

Hepworth, L. N., Kaufmann, F. E. D., Hecht, L., Gertisser, R. & O'Driscoll, B. (2020b). Braided peridotite sills and metasomatism in the Rum Layered Suite, Scotland. *Contributions to Mineralogy and Petrology* **175**, 17.

Hirschmann, M. M. (2000). Mantle solidus: Experimental constraints and the effects of peridotite composition. *Geochemistry, Geophysics, Geosystems*: Blackwell Publishing Ltd.

Holness, M. B., Hallworth, M. A., Woods, A. & Sides, R. E. (2007). Infiltration Metasomatism of Cumulates by Intrusive Magma Replenishment: the Wavy Horizon, Isle of Rum, Scotland. *Journal of Petrology* **48**, 563-587.

Holwell, D. A., Adeyemi, Z., Ward, L. A., Smith, D. J., Graham, S. D., McDonald, I. & Smith, J. W. (2017). Low temperature alteration of magmatic Ni-Cu-PGE sulfides as a source for hydrothermal Ni and PGE ores: A quantitative approach using automated mineralogy. *Ore Geology Reviews* **91**, 718-740.

Huhma, H., Hanski, E., Kontinen, A., Vuollo, J., Mänttäri, I. & Lahaye, Y. (2018). Sm–Nd and U–Pb isotope geochemistry of the Palaeoproterozoic mafic magmatism in eastern and northern Finland. Geological Survey of Finland. *Bulletin* **405**, 150.

Huhma, H., O'Brien, H., Lahaye, Y. & Mänttäri, I. (2011). Isotope geology and Fennoscandian lithosphere evolution. *Geological Survey of Finland, Special Paper* **49**, 35-48.

Kelly, D. & Vaughan, D. (1983). Pyrrhotine-pentlandite ore textures: a mechanistic approach. *Mineralogical Magazine* **47**, 453-463.

Kingsrose. (2021). High Grade PGE-Copper-Nickel Mineralisation Confirmed at the Porsanger Project.

Koistinen, T., Stephens, M., Bogatchev, V., Nordgulen, Ø., Wennerström, M. & Korhonen, J. (2001). Geological map of the Fennoscandian Shield 1: 2 000 000. *Espoo: Geological Survey of Finland, Trondheim: Geological Survey of Norway, Uppsala: Geological Survey of Sweden, Moscow: Ministry of Natural Resources of Russia*.

Konnunaho, J., Halkoaho, T., Hanski, E. & Törmänen, T. (2015). Chapter 3.2 - Komatiite-Hosted Ni-Cu-PGE Deposits in Finland. In: Maier, W. D., Lahtinen, R. & O'Brien, H. (eds.) *Mineral Deposits of Finland*: Elsevier, 93-131.

Konnunaho, J. P., Hanski, E. J., Karinen, T. T., Lahaye, Y. & Makkonen, H. V. (2018). The petrology and genesis of the Paleoproterozoic mafic intrusion-hosted Co-Cu-Ni deposit at Hietakero, NW Finnish Lapland. *Bulletin of the Geological Society of Finland* **90**.

Korsman, K., Korja, T., Pajunen, M., Virransalo, P. & Ggt/Sveka Working, G. (1999). The GGT/SVEKA Transect: Structure and Evolution of the Continental Crust in the Paleoproterozoic Svecofennian Orogen in Finland. *International Geology Review* **41**, 287-333.

Kosyakov, F., Sinyakova, E. & Distler, V. (2012). Experimental simulation of phase relationships and zoning of magmatic nickel-copper sulfide ores, Russia. *Geology of Ore Deposits* **54**, 179-208.

Krill, A. G. (1985a). Rb-Sr, U-Pb and Sm-Nd isotopic dates from Precambrian rocks of Finnmark. *Geological Survey of Norway Bulletin* **403**, 37-54.

Krill, A. G. (1985b). Svecokarelian thrusting with thermal inversion in the Karasjok- Levajok area of the northern Baltic Shield. *Norges Geologiske Undersokelse Bulletin*, 89-101.

Kruger, W. & Latypov, R. (2020). Fossilized solidification fronts in the Bushveld Complex argue for liquid-dominated magmatic systems. *Nature Communications* **11**, 2909.

Kullerud, G. & Yoder, H. S. (1959). Pyrite stability relations in the Fe-S system. *Economic Geology*, 533-572.

Lahtinen, R., Hölttä, P., Kontinen, A., Niiranen, T., Nironen, M., Saalmann, K. & Sorjonen-Ward, P. (2011). Tectonic and metallogenic evolution of the Fennoscandian Shield: Key questions with emphasis on Finland. 23-33.

Lahtinen, R., Huhma, H., Kontinen, A., Kohonen, J. & Sorjonen-Ward, P. (2010). New constraints for the source characteristics, deposition and age of the 2.1–1.9Ga metasedimentary cover at the western margin of the Karelian Province. *Precambrian Research* **176**, 77-93.

Lahtinen, R., Korja, A. & Nironen, M. (2005). Chapter 11 Paleoproterozoic tectonic evolution. In: Lehtinen, M., Nurmi, P. A. & Rämö, O. T. (eds.) *Developments in Precambrian Geology*: Elsevier, 481-531.

Larsen, R. B., Grant, T., Sørensen, B. E., Tegner, C., McEnroe, S., Pastore, Z., Fichler, C., Nikolaisen, E., Grannes, K. R., Church, N., ter Maat, G. W. & Michels, A. (2018). Portrait of a giant deep-seated magmatic conduit system: The Seiland Igneous Province. *Lithos*, 600-622.

Latypov, R. (2015). Basal Reversals in Mafic Sills and Layered Intrusions. In: Charlier, B., Namur, O., Latypov, R. M. & Tegner, C. (eds.) *Layered Intrusions*: Springer Netherlands, 259-293.

Lazarin, F. d. A. (2011). Geologia, petrologia e estudos isotópicos dos depósitos de níquel-cobre sulfetados Santa Rita e Peri-Peri, Nordeste do Brasil.

Lesher, C. M. (2017). Roles of xenomelts, xenoliths, xenocrysts, xenovolatiles, residues, and skarns in the genesis, transport, and localization of magmatic Fe-Ni-Cu-PGE sulfides and chromite. *Ore Geology Reviews* **90**, 465-484.

Lesher, C. M. (2019). Up, down, or sideways: Emplacement of magmatic Fe–Ni–Cu–PGE sulfide melts in large igneous provinces. *Canadian Journal of Earth Sciences* **56**, 756-773.

Lesher, C. M. & Burnham, O. M. (2001). Multicomponent elemental and isotopic mixing in Ni–Cu–(PGE) ores at Kambalda, Western Australia. *The Canadian Mineralogist* **39**, 421-446.

Li, C., Barnes, S.-J., Makovicky, E., Rose-Hansen, J. & Makovicky, M. (1996). Partitioning of Ni, Cu, Ir, Rh, Pt and Pd between monosulfide solid solution and sulfide liquid: effects of composition and temperature. *Geochimica et Cosmochimica Acta* **60**, 1231-1238.

Li, C. & Ripley, E. M. (2009). Sulfur contents at sulfide-liquid or anhydrite saturation in silicate melts: empirical equations and example applications. *Economic Geology* **104**, 405-412.

Li, C., Ripley, E. M. & Naldrett, A. J. (2003). Compositional variations of olivine and sulfur isotopes in the Noril'sk and Talnakh intrusions, Siberia: Implications for ore-forming processes in dynamic magma conduits. *Economic Geology* **98**, 69-86.

Lightfoot, P. C. & Evans-Lamswood, D. (2015). Structural controls on the primary distribution of mafic-ultramafic intrusions containing Ni-Cu-Co-(PGE) sulfide mineralization in the roots of large igneous provinces. *Ore Geology Reviews*, 354-386.

Liu, Y. & Brenan, J. (2015). Partitioning of platinum-group elements (PGE) and chalcogens (Se, Te, As, Sb, Bi) between monosulfide-solid solution (MSS), intermediate solid solution (ISS) and sulfide liquid at controlled fO2–fS2 conditions. *Geochimica et Cosmochimica Acta* **159**, 139-161.

Luolavirta, K. (2018). Magmatic evolution of the Kevitsa igneous complex, northern Finland, and its relation to the associated Ni-Cu-(PGE) mineralization. *Res Terrae*: University of Oulu, 68.

Luolavirta, K., Hanski, E., Maier, W., Lahaye, Y., O'Brien, H. & Santaguida, F. (2018a). In situ strontium and sulfur isotope investigation of the Ni-Cu-(PGE) sulfide ore-bearing Kevitsa intrusion, northern Finland. *Mineralium Deposita* **53**, 1019-1038.

Luolavirta, K., Hanski, E., Maier, W. & Santaguida, F. (2018b). Characterization and origin of dunitic rocks in the NI-CU-(PGE) sulfide ore-bearing kevitsa intrusion, northern finland: Whole-rock and mineral chemical constraints. *Bulletin of the Geological Society of Finland* **90**, 5-32.

Luolavirta, K., Hanski, E., Maier, W. & Santaguida, F. (2018c). Whole-rock and mineral compositional constraints on the magmatic evolution of the Ni-Cu-(PGE) sulfide ore-bearing Kevitsa intrusion, northern Finland. *Lithos* **296-299**, 37-53.

Lusk, J. & Maxwell Bray, D. (2002). Phase relations and the electrochemical determination of sulfur fugacity for selected reactions in the Cu–Fe–S and Fe–S systems at 1 bar and temperatures between 185 and 460 °C. *Chemical Geology* **192**, 227-248.

Maier, W. D. (2015). Geology and Petrogenesis of Magmatic Ni-Cu-PGE-Cr-V Deposits: An Introduction and Overview. An Introduction and Overview. *Mineral Deposits of Finland*: Elsevier Inc., 73-92.

Maier, W. D., Lahtinen, R. & O'Brien, H. (2015). *Mineral deposits of Finland*: Elsevier.

Maier, W. D., Prevec, S. A., Scoates, J. S., Wall, C. J., Barnes, S. J. & Gomwe, T. (2018). The Uitkomst intrusion and Nkomati Ni-Cu-Cr-PGE deposit, South Africa: trace element geochemistry, Nd isotopes and high-precision geochronology. *Mineralium Deposita* **53**, 67-88.

Makkonen, H. V., Halkoaho, T., Konnunaho, J., Rasilainen, K., Kontinen, A. & Eilu, P. (2017). Ni-(Cu-PGE) deposits in Finland – Geology and exploration potential. *Ore Geology Reviews* **90**, 667-696.

Mansur, E. T. & Barnes, S. J. (2020). The role of Te, As, Bi, Sn and Sb during the formation of platinum-group-element reef deposits: Examples from the Bushveld and Stillwater Complexes. *Geochimica et Cosmochimica Acta* **272**, 235-258.

Mansur, E. T., Barnes, S. J. & Duran, C. J. (2021). An overview of chalcophile element contents of pyrrhotite, pentlandite, chalcopyrite, and pyrite from magmatic Ni-Cu-PGE sulfide deposits. *Mineralium Deposita* **56**, 179-204.

Mansur, E. T., Barnes, S. J., Duran, C. J. & Sluzhenikin, S. F. (2020a). Distribution of chalcophile and platinum-group elements among pyrrhotite, pentlandite, chalcopyrite and cubanite from the Noril'sk-Talnakh ores: implications for the formation of platinum-group minerals. *Mineralium Deposita* **55**, 1215-1232.

Mansur, E. T., Ferreira Filho, C. F. & Oliveira, D. P. L. (2020b). The Luanga deposit, Carajás Mineral Province, Brazil: Different styles of PGE mineralization hosted in a medium-size layered intrusion. *Ore Geology Reviews* **118**.

Mavrogenes, J. A. & O'Neill, H. S. C. (1999). The relative effects of pressure, temperature and oxygen fugacity on the solubility of sulfide in mafic magmas. *Geochimica et Cosmochimica Acta* **63**, 1173-1180.

McCuaig, T. C., Beresford, S. & Hronsky, J. (2010). Translating the mineral systems approach into an effective exploration targeting system. *Ore Geology Reviews* **38**, 128-138.

Melezhik, V. A., Solli, A., Fallick, A. E. & Davidsen, B. (2015). Chemostratigraphic constraints on the time of deposition of carbonate rocks in the Karasjok Greenstone Belt, northern Norway. *Norwegian Journal of Geology* **95**, 299-314.

Moilanen, M., Hanski, E. & Yang, S.-H. (2021). Re-Os isotope geochemistry of the Palaeoproterozoic Sakatti Cu-Ni-PGE sulphide deposit in northern Finland. *Ore Geology Reviews* **132**, 104044.

Mungall, J. E. (2007). Crystallization of magmatic sulfides: An empirical model and application to Sudbury ores. *Geochimica et Cosmochimica Acta* **71**, 2809-2819.

Mungall, J. E., Andrews, D. R., Cabri, L. J., Sylvester, P. J. & Tubrett, M. (2005). Partitioning of Cu, Ni, Au, and platinum-group elements between monosulfide solid solution and sulfide melt under controlled oxygen and sulfur fugacities. *Geochimica et Cosmochimica Acta* **69**, 4349-4360.

Mungall, J. E., Kamo, S. L. & McQuade, S. (2016). U–Pb geochronology documents out-of-sequence emplacement of ultramafic layers in the Bushveld Igneous Complex of South Africa. *Nature Communications* **7**, 13385.

Mutanen, T. (1997). *Geology and ore petrology of the Akanvaara and Koitelainen mafic layered intrusions and the Keivitsa-Satovaara layered complex, northern Finland*: Geological Survey of Finland, Bulletin 395.

Mutanen, T. & Huhma, H. (2001). U-Pb geochronology of the Koitelainen, Akanvaara and Keivitsa layered intrusions and related rocks. *Geological Survey of Finland, Special Paper* **33**, 229-246.

Mysen, B. O. & Boettcher, A. (1976). Melting of a hydrous mantle: III. Phase relations of garnet websterite+ H2O at high pressures and temperatures. *Journal of Petrology* **17**, 1-14.

Naldrett, A. (2011). Fundamentals of magmatic sulfide deposits.

Naldrett, A., Fedorenko, V., Lightfoot, P. C., Kunilov, V. I., Gorbachev, N. S., Doherty, W. & Johan, Z. (1995). Ni-Cu-PGE deposits of Noril'sk region, Siberia: their formation in conduits for flood basalt volcanism. *Transactions of the Institution of Mining and Metallurgy. Section B. Applied Earth Science* **104**.

Naldrett, A. & Kullerud, G. (1967). A study of the Strathcona mine and its bearing on the origin of the nickel-copper ores of the Sudbury district, Ontario. *Journal of Petrology* **8**, 453-531.

Naldrett, A. J. (2004). *Magmatic Sulfide Deposits*: Springer Berlin, Heidelberg.

Naldrett, A. J., Craig, J. R. & Kullerud, G. (1967). The central portion of the Fe-Ni-S system and its bearing on pentlandite exsolution in iron-nickel sulfide ores. *Economic Geology* **62**, 826-847.

Naldrett, T., Kinnaird, J., Wilson, A. & Chunnett, G. (2008). Concentration of PGE in the Earth's Crust with Special Reference to the Bushveld Complex. *Earth Science Frontiers* **15**, 264-297.

Namur, O., Abily, B., Boudreau, A. E., Blanchette, F., Bush, J. W. M., Ceuleneer, G., Charlier, B., Donaldson, C. H., Duchesne, J.-C., Higgins, M. D., Morata, D., Nielsen, T. F. D., O'Driscoll, B., Pang, K. N., Peacock, T., Spandler, C. J., Toramaru, A. & Veksler, I. V. (2015). Igneous Layering in Basaltic Magma Chambers. In: Charlier, B., Namur, O., Latypov, R. & Tegner, C. (eds.) *Layered Intrusions*: Springer Netherlands, 75-152.

Nebel, O., Sossi, P. A., Ivanic, T. J., Benard, A., Gardiner, N. J., Langford, R. L. & Arculus, R. J. (2020). Incremental Growth of Layered Mafic-Ultramafic Intrusions Through Melt Replenishment Into a Crystal Mush Zone Traced by Fe-Hf Isotope Systematics. *Frontiers in Earth Science* **8**, 1-10.

Nilsson, L. P., Ihlen, P. M., Often, M., Skaar, J. A. & Boyd, R. (2016). Gallujavri and Raitevarri – Potentially Large Deposits in the Karasjok Greenstone Belt. In: Boyd, R., Bjerkgård, T., Nordahl, B. & Schiellerup, H. (eds.) *Mineral Resources In The Arctic*: Geological Survey of Norway, 238-242.

Nilsson, L. P. & Often, M. (2006). A summary report on the Ni-Cu-PGE occurrences and their host rocks in the Precambrian of Finnmark, Northern Norway. Geological Survey of Norway, 79.

Often, M. (1985). The Early Proterozoic Karasjok Greenstone Belt, Norway. A preliminary description of lithology, stratigraphy and mineralization. *Norges Geologiske Undersokelse Bulletin* **403**, 75-88.

Orvik, A. A., Mansur, E., Slagstad, T., Sørensen, B. E., Drivenes, K. & Nilsson, L. P. (In prep.). The PGE sulphide mineralisation from the Gállojávri intrusion: implications for the formation of magmatic sulphide deposit in the Karasjok Greenstone Belt, Norway. Unpublished, 52.

Orvik, A. A., Slagstad, T., Hansen, H., Nilsson, L. P. & Sørensen, B. E. (2022a). The Palaeoproterozoic Gallujavri ultramafic intrusion, Karasjok Greenstone Belt; petrogenesis of a trans-crustal magma system. *Journal of Petrology* **63**, 28.

Orvik, A. A., Slagstad, T., Sørensen, B. E., Millar, I. & Hansen, H. (2022b). Evolution of the Gállojávri ultramafic intrusion from U-Pb zircon ages and Rb-Sr, Sm-Nd and Lu-Hf isotope systematics. *Precambrian Research* **379**, 106813.

Peate, D. W., Barker, A. K., Riishuus, M. S. & Andreasen, R. (2008). Temporal variations in crustal assimilation of magma suites in the East Greenland flood basalt province: Tracking the evolution of magmatic plumbing systems. *Lithos* **102**, 179-197.

Piña, R., Gervilla, F., Barnes, S.-J., Ortega, L. & Lunar, R. (2013). Platinum-group elements-bearing pyrite from the Aguablanca Ni-Cu sulphide deposit (SW Spain): a LA-ICP-MS study. *European Journal of Mineralogy* **25**, 241-252.

Piña, R., Gervilla, F., Barnes, S. J., Oberthür, T. & Lunar, R. (2016). Platinum-group element concentrations in pyrite from the Main Sulfide Zone of the Great Dyke of Zimbabwe. *Mineralium Deposita* **51**, 853-872.

Puchtel, I., Brügmann, G., Hofmann, A., Kulikov, V. & Kulikova, V. (2001). Os isotope systematics of komatiitic basalts from the Vetreny belt, Baltic Shield: evidence for a chondritic source of the 2.45 Ga plume. *Contributions to Mineralogy and Petrology* **140**, 588-599.

Puchtel, I. S., Haase, K. M., Hofmann, A. W., Chauvel, C., Kulikov, V. S., Garbe-Schönberg, C. D. & Nemchin, A. A. (1997). Petrology and geochemistry of crustally contaminated komatiitic basalts from the Vetreny Belt, southeastern Baltic Shield: Evidence for an early Proterozoic mantle plume beneath rifted Archean continental lithosphere. *Geochimica et Cosmochimica Acta* **61**, 1205-1222.

Puchtel, I. S., Mundl-Petermeier, A., Horan, M., Hanski, E. J., Blichert-Toft, J. & Walker, R. J. (2020). Ultra-depleted 2.05 Ga komatiites of Finnish Lapland:

Products of grainy late accretion or core-mantle interaction? *Chemical Geology* **554**, 119801.

Puchtel, I. S., Touboul, M., Blichert-Toft, J., Walker, R. J., Brandon, A. D., Nicklas, R. W., Kulikov, V. S. & Samsonov, A. V. (2016). Lithophile and siderophile element systematics of Earth's mantle at the Archean-Proterozoic boundary: Evidence from 2.4 Ga komatiites. *Geochimica et Cosmochimica Acta*: Elsevier Ltd, 227-255.

Putirka, K. D. (2008). Thermometers and Barometers for Volcanic Systems. *Minerals, Inclusions and Volcanic Processes* **69**, 61-120.

Rastas, P., Huhma, H., Hanski, E., Lehtonen, M., Harkonen, I., Kortelainen, V., Manttari, I. & Paakkola, J. (2001). U-Pb isotopic studies on the Kittila greenstone area, central Lapland, Finland. *Special Paper-Geological Survey of Finland*, 95-142.

Ridolfi, F., Renzulli, A. & Puerini, M. (2009). Stability and chemical equilibrium of amphibole in calc-alkaline magmas: An overview, new thermobarometric formulations and application to subduction-related volcanoes. *Contributions to Mineralogy and Petrology*, 45-66.

Ripley, E. M. & Chusi, L. (2007). Applications of stable and radiogenic isotopes to magmatic Cu-Ni-PGE deposits: Examples and cautions. *Earth Science Frontiers* **14**, 124-131.

Ripley, E. M. & Li, C. (2003). Sulfur isotope exchange and metal enrichment in the formation of magmatic Cu-Ni-(PGE) deposits. *Economic Geology* **98**, 635-641.

Ripley, E. M. & Li, C. (2013). Sulfide Saturation in Mafic Magmas: Is External Sulfur Required for Magmatic Ni-Cu-(PGE) Ore Genesis? *Economic Geology* **108**, 45-58.

Robb, L. (2020). *Introduction to ore-forming processes*: John Wiley & Sons.

Santaguida, F., Luolavirta, K., Lappalainen, M., Ylinen, J., Voipio, T. & Jones, S. (2015). The Kevitsa Ni-Cu-PGE Deposit in the Central Lapland Greenstone Belt in Finland. In: Maier, W. D., Lahtinen, R. & O'Brien, H. (eds.) *Mineral Deposits of Finland*. Amsterdam, Netherland: Elsevier, 195-210.

Seal, R. R. (2006). Sulfur isotope geochemistry of sulfide minerals. *Reviews in Mineralogy and Geochemistry*: GeoScienceWorld, 633-677.

Seat, Z., Beresford, S. W., Grguric, B. A., Gee, M. M. & Grassineau, N. V. (2009). Reevaluation of the role of external sulfur addition in the genesis of Ni-Cu-PGE deposits: Evidence from the Nebo-Babel Ni-Cu-PGE deposit, West Musgrave, Western Australia. *Economic Geology* **104**, 521-538.

Sharp, Z. (2017). Principles of stable isotope geochemistry.

Shima, H. & Naldrett, A. J. (1975). Solubility of sulfur in an ultramafic melt and the relevance of the system Fe-S-O. *Economic Geology* **70**, 960-967.

Siedlecka, A. (1985). Geology of Iesjav'ri-Skognavarre area, northern Finnmarksvidda, North Norway. *Norges Geologiske Undersokelse Bulletin*, 103-112.

Siedlecka, A., Krill, A. & Iversen, E. (1985). Lithostratigraphy and correlation of the Archean and Early Proterozoic rocks of Finnmarksvidda and Sørvaranger district.

Siedlecka, A. & Roberts, D. (1996). Finnmark Fylke. Berggrunnsgeologi M 1: 500 000. *Norges geologiske undersøkelse*.

Sinyakova, E., Kosyakov, V., Distler, V. & Karmanov, N. (2016). Behavior of Pt, Pd, and Au during crystallization of Cu-rich magmatic sulfide minerals. *The Canadian Mineralogist* **54**, 491-509.

Sinyakova, E., Kosyakov, V., Palyanova, G. & Karmanov, N. (2019). Experimental modeling of noble and chalcophile elements fractionation during solidification of Cu-Fe-Ni-S melt. *Minerals* **9**, 531.

Skaar, J. A. A. (2014). 3D geophysical and geological modelling of the Karasjok Greenstone Belt. *Department of Geoscience and Petroleum*. NTNU: Norwegian University of Science and Technology, 158.

Steiger, R. H. & Jäger, E. (1977). Subcommission on geochronology: convention on the use of decay constants in geo-and cosmochronology. *Earth and Planetary Science Letters* **36**, 359-362.

Stepanova, A. V., Azimov, P., Samsonov, A. V., Egorova, S. V., Babarina, I. I., Larionov, A. N., Larionova, Y. O., Kervinen, A. V. & Stepanov, V. S. (2021). Paleoproterozoic ca. 2.2 Ga high-Cl metagabbro in the Belomorian province, Eastern Fennoscandian Shield: Origin and tectonic implications. *Lithos* **400-401**, 106377.

Sun, S. S. & McDonough, W. F. (1989). Chemical and isotopic systematics of oceanic basalts: implications for mantle composition and processes. *Geological Society, London, Special Publications* **42**, 313-345.

Törmänen, T., Konnunaho, J. P., Hanski, E., Moilanen, M. & Heikura, P. (2016). The Paleoproterozoic komatiite-hosted PGE mineralization at Lomalampi, Central Lapland Greenstone Belt, northern Finland. *Mineralium Deposita* **51**, 411-430.

Virtanen, V. J., Heinonen, J. S., Barber, N. D. & Molnár, F. (2022). Complex Effects of Assimilation on Sulfide Saturation Revealed by Modeling with the Magma Chamber Simulator: A Case Study on the Duluth Complex, Minnesota, USA. *Economic Geology*.

Weaver, B. L. & Tarney, J. (1984). Empirical approach to estimating the composition of the continental crust. *Nature* **310**, 575-577.

Weihed, P., Arndt, N., Billström, K., Duchesne, J.-C., Eilu, P., Martinsson, O., Papunen, H. & Lahtinen, R. (2005). 8: Precambrian geodynamics and ore formation: The Fennoscandian Shield. *Ore Geology Reviews* **27**, 273-322.

Wendlandt, R. F. (1982). Sulfide saturation of basalt and andesite melts at high pressures and temperatures. *American Mineralogist* **67**, 877-885.

Winter, J. D. (2013). *Principles of igneous and metamorphic petrology*: Pearson education.

10 PAPERS, DECLARATION OF AUTHORSHIP AND DATA AVAILABILITY

This thesis is a compilation of two published papers and one manuscript. The manuscript is under preparation for *Ore Geology Reviews* (ISSN: 0169-1368) and the two papers have been published in international academic geological journals. The two papers and one manuscript are organised chronologically in the order they were written.

Paper 1

The Palaeoproterozoic Gállojávri Ultramafic Intrusion, Karasjok Greenstone Belt; Petrogenesis of a Trans-Crustal Magma System.

Alf Andre Orvik, Trond Slagstad, Harald Hansen, Lars Petter Nilsson, Bjørn Eske Sørensen

Journal of Petrology, Volume 63, Issue 3, March 2022, egac008.

DOI: https://doi.org/10.1093/petrology/egac008

Authorship contribution statement

Alf Andre Orvik conducted the investigation, modelling, formal interpretation and writing of the original draft. Trond Slagstad contributed with funding, data interpretation, proofreading and reviewing. Harald Hansen contributed with data and proofreading. The project was initiated by Lars Petter Nilsson, who also provided access to study materials and served as a discussion partner for the interpretation and proofreading of the manuscript. Bjørn Eske Sørensen supervised, served as a discussion partner during the data interpretation and contributed to proofreading and reviewing the draft.

Data availability statement

The data underlying this research are available in the paper and in its online supplementary material. The supplementary data to this paper can be found online at https://doi.org/10.1093/petrology/egac008.

Paper 2

Evolution of the Gállojávri ultramafic intrusion from U-Pb zircon ages and Rb-Sr, Sm-Nd and Lu-Hf isotope systematics

Alf Andre Orvik, Trond Slagstad, Bjørn Eske Sørensen, Ian Millar, Harald Hansen

Precambrian Research, Volume 379, September 2022, 106813.

DOI: https://doi.org/10.1016/j.precamres.2022.106813

Authorship contribution statement

Alf Andre Orvik conceptualised the research goals and objectives and conducted the formal investigation, modelling, interpretation, visualisation and original draft writing. Trond Slagstad contributed to the conceptualisation, data collection and curation, interpretation, supervision, writing, proofreading and editing of the draft. Bjørn Eske Sørensen contributed with data curation, supervision and proofreading. Ian Millar contributed with data collection, data curation and proofreading. Harald Hansen contributed to the data collection, provision of data and proofreading.

Data availability statement

The data underlying this research are available in the paper and its online supplementary material. The supplementary data to this paper can be found online at https://doi.org/10.1016/j.precamres.2022.106813.

Manuscript 3

The PGE sulphide mineralisation from the Gállojávri intrusion: implications for the formation of magmatic sulphide deposit in the Karasjok Greenstone Belt, Norway

Alf Andre Orvik, Eduardo Teixeira Mansur, Trond Slagstad, Bjørn Eske Sørensen, Kristian Drivenes, Lars Petter Nilsson

Unpublished

Authorship contribution statement

Alf Andre Orvik conceptualised the research goals and objectives and conducted the formal investigation, interpretation, visualisation and original draft writing. Eduardo Teixeira Mansur contributed to the conceptualisation, data collection and curation, interpretation, writing, proofreading and editing of the draft. Trond Slagstad contributed with supervision, proofreading and editing of the draft. Bjørn Eske Sørensen contributed with data curation, supervision and proofreading. Kristian Drivenes contributed with methodology, data collection, data curation and proofreading. Lars Petter Nilsson served as a discussion partner for the interpretation. He also contributed to the proofreading and reviewing of the manuscript.

Data availability statement

The data underlying this research are available in the manuscript and appendices.

Paper 1

JOURNAL OF PETROLOGY

Journal of Petrology, 2022, Vol. 63, No. 3, 1–28
https://doi.org/10.1093/petrology/egac008
Advance Access Publication Date: 14 February 2022
Original Manuscript

OXFORD

The Palaeoproterozoic Gallujavri Ultramafic Intrusion, Karasjok Greenstone Belt; Petrogenesis of a Trans-Crustal Magma System

Alf Andre Orvik[1,*], Trond Slagstad[2], Harald Hansen[3], Lars Petter Nilsson[2], and Bjørn Eske Sørensen[1]

[1]Department of Geoscience and Petroleum, Norwegian University of Science and Technology, S. P. Andersens veg 15, 7031 Trondheim, Norway [2]Geological Survey of Norway, Leiv Eirikssons vei 39, 7040 Trondheim, Norway and [3]Department of Geosciences, UiT The Arctic University of Norway, Dramsveien 201, 9037 Tromsø, Norway

*Corresponding author. Telephone: +47 93 444 158. E-mail: alf.a.orvik@ntnu.no

Received 16 August 2021; Revised 20 December 2021; Accepted 11 February 2022

Abstract

The modern concepts of magmatic plumbing systems have evolved from simple models of melt-dominated crustal magma chambers to magmatic systems that span the continental crust. The geochemistry of these systems is challenging to model numerically because of a complex polybaric and multiphase evolution, which is not well described by mathematic end-member formulas. We propose that a recent modelling tool, the Magma Chamber Simulator (MCS), can reveal part of the petrological complexities of such systems. The MCS numerically models phase equilibria, mineral chemistry and major and trace elements in multicomponent–multiphase systems by finding the extremes of the appropriate state functions. This study presents new petrographical and geochemical data from the Palaeoproterozoic Gallujavri ultramafic intrusion in the Karasjok Greenstone Belt, Arctic Norway. Our data indicate that (1) the intrusion is affected by crustal assimilation, (2) phase equilibria require polybaric crystallisation and (3) spinel compositions are similar to sub-volcanic intrusions of continental flood basalt provinces. We utilise the MCS to simulate the petrogenesis of the intrusion and test the model by comparing it against our reported petrological and geochemical data. Our modelling shows that the parental magma of the intrusion is consistent with coeval Karasjok-type komatiites observed at various places throughout the greenstone belt. First, the komatiitic primary magma intruded Archaean lower crust (c. 700 MPa), where fractionation and assimilation resulted in a hybrid melt. Second, the hybrid melt migrated and accumulated in a mid-crustal magma chamber (c. 400 MPa), where it continued to fractionate and assimilate while remaining open to recharge of mantle-derived komatiitic melts, forming the Gallujavri intrusion. We interpret the Gallujavri intrusion as part of a Palaeoproterozoic trans-crustal magma plumbing system, with many similarities to other Fennoscandian ultramafic-mafic layered intrusions.

Key words: magma plumbing systems; magma evolution; Magma Chamber Simulator; Karasjok Greenstone Belt; Gallujavri intrusion

INTRODUCTION

Interaction between Earth's crust and mantle-derived melts passing through or ponding at its base is key in controlling the chemical evolution of such melts (Ganne *et al.*, 2018). Classically, the observed petrological diversity of igneous rocks is attributed to mechanisms of melt generation, differentiation and assimilation *en route* to the surface. Of critical importance to igneous petrology is deciphering the melt storage location(s) and the routes taken towards the surface (Magee *et al.*, 2018). In the past two decades, innovations in geophysical methods have allowed imaging of zones of melt accumulation and magma migration (Magee *et al.*, 2018, and references therein). Together with accumulating evidence from geochemical, petrological, volcanological and geological observations, these data fuel an

emerging consensus that melts are stored and transported in complex and vertically extensive magmatic systems (e.g. Annen *et al.*, 2006; Blundy *et al.*, 2008; Cashman *et al.*, 2017; Hildreth & Moorbath, 1988; Sinton & Detrick, 1992; ; Tarasewicz *et al.*, 2012). In light of this knowledge, a major obstacle to geochemical modelling is that the complex and polybaric nature of the system causes chemical variations that are not easily described by classical mathematical descriptions of melt differentiation and assimilation (Cashman *et al.*, 2017). However, a recently developed tool, the Magma Chamber Simulator (MCS), quantifies concurrent recharge, assimilation and crystallisation via mass and enthalpy balance in multicomponent and polyphase systems (Bohrson *et al.*, 2014), thus representing a significant step forward in overcoming these issues.

In this contribution, we report petrographic and geochemical data from the Palaeoproterozoic Gallujavri ultramafic intrusion in Arctic Norway. The intrusion is part of the Karasjok and Central Lapland Greenstone Belt (KCLGB), extending from Norway, through Finland, into Russia, containing several types of (ultra)mafic plutonic bodies and coeval extrusive rocks (Fig. 1). The MCS tool allows us to model the petrological evolution of the Gallujavri intrusion and compare the model results against our reported petrological and geochemical data. The model reveals that magma transport via a two-stage polybaric plumbing system can be used to explain several of the phase equilibria and major and trace element characteristics of the Gallujavri intrusion. Our findings are consistent with recent models of transcrustal magma systems developed from active conduits (Farrell *et al.*, 2014; Huang *et al.*, 2015; Magee *et al.*, 2018) and show that these concepts can likely be extended to Palaeoproterozoic magmatism in Fennoscandia.

REGIONAL GEOLOGY

The Karasjok Greenstone Belt (KGB) lies in the northwestern portion of the Fennoscandian Shield (Fig. 1) and, along with the Kautokeino Greenstone Belt, constitutes the northernmost part of a nearly 100-km-wide Palaeoproterozoic tectonic belt that extends from northwestern Russia, through northern Finland, into northern Norway (Braathen & Davidsen, 2000).

The KGB has a north–south trend and is ~160 km long and between 20 and 40 km wide (Krill, 1985b; Barnes & Often, 1990) and continues into Finland, where it is named the Central Lapland Greenstone Belt, which gives a total length of ~310 km (Barnes & Often, 1990).

The KGB lithostratigraphy comprises supracrustal and intrusive rocks metamorphosed to medium grade (Fig. 2; Braathen & Davidsen, 2000). To the west, the KGB nonconformably overlies and is partly thrust over the tonalite–trondhjemite–granodiorite (TTG)-dominated Archaean Jergul Gneiss Complex (Fig. 2a; Bingen *et al.*, 2015, Hansen *et al.*, 2020). It is bounded to the east by the overthrust Tanaelv Migmatite Complex (Siedlecka, 1985; Braathen & Davidsen, 2000). To the north, the belt is overlain by sedimentary rocks and allochthonous Caledonian nappes.

The lowest unit in the KGB stratigraphy is the Lavttevàrri formation (Fig. 2b). This 50–150-m-thick formation consists mainly of fine-grained foliated amphibolites, metapelites and metakomatiites. Rocks above the basal unconformity include mica schists with carbonates and locally conglomerates consisting of granite and granitic gneisses from the basement (Braathen & Davidsen, 2000).

The Čorgaš formation (Fig. 2c) is 250–700 m thick with a lower portion comprising conglomerates, psammites and metapelites and an upper section consisting of shallow-marine sedimentary rocks and subaerial to shallow-water mafic volcanic rocks (Barnes & Often, 1990; Braathen & Davidsen, 2000; Stokmo, 2020). Carbon isotope chemostratigraphy on carbonates within the formation indicates a depositional age between 2220 and 2140 Ma (Melezhik *et al.*, 2015). The isotope chemostratigraphy provides a likely maximum age of the ultramafic and mafic intrusions that are common in this formation, including the Gallujavri intrusion, which is the topic of this contribution. Considering that the (ultra)mafic layered intrusions of the KCLGB are interpreted to have formed in discrete magmatic episodes at 2440, 2220 and 2050 Ma (Hanski & Huhma, 2005), the intrusions within the Čorgaš formation, including Gallujavri, is likely part of the last pulse. Previous studies have also highlighted many lithological similarities between the Gallujavri intrusion and the c. 2.06 Ga Kevitsa intrusion in Finland (Nilsson & Often, 2009), further corroborated by recent unpublished U–Pb geochronological data (Orvik *et al.*, in preparation).

Tholeiitic basalts represented by banded amphibolites dominate the 300 to 700 m-thick Briittágielas formation (Fig. 2d). The lower part of the formation includes calc-alkaline dacitic metavolcanic rocks and kyanite-bearing garnet-mica schists. The basal contact towards the underlying Čorgaš formation is marked by an extensive marble unit (Braathen & Davidsen, 2000). The Briittágielas formation is also distinguished by four 70-m-thick units of metakomatiite (Barnes & Often, 1990; Braathen & Davidsen, 2000).

The Fossestrand formation (Fig. 2e) appears in the core of a regional-scale isoclinal fold with an across-strike thickness of 250–300 m (Stokmo, 2020). Metakomatiitic and volcanoclastic rocks dominate the formation. The lower section consists of two thick pillowed lava flows, while the upper portion consists of lava flows and agglomerates. Coarser-grained mafic rocks have also been identified within this formation (Braathen & Davidsen, 2000).

Palaeoproterozoic komatiites and picrites occur at various stratigraphic levels in the KCLGB (Fig. 1; Barnes & Often, 1990, Hanski & Huhma, 2005, Puchtel *et al.*, 2020) and consist of both Munro-type komatiites, Karasjok-type (Ti-enriched) komatiites and ferropicritic compositions (Barnes & Often, 1990; Puchtel *et al.*, 1997; Hanski *et al.*, 2001a; Heggie *et al.*, 2013). In Finland, the Palaeoproterozoic ultramafic volcanic rocks extruded on the fine-grained metasedimentary rocks of the Savukoski group and consist of Karasjok-type komatiites and picrites (Barnes & Often, 1990; Hanski *et al.*, 2001a; Heggie *et al.*, 2013). The Savukoski group has a minimum age of deposition provided by cross-cutting intrusive bodies, such as the 2058 ± 4 Ma Kevitsa layered intrusion (Mutanen & Huhma, 2001).

Recently, Puchtel *et al.* (2020) determined a Re–Os isochron age of 2049 ± 13 Ma for komatiite whole-rock and olivine and chromite separates from the Kevitsa and Jeesiorova area. Pyroxene and whole-rock Sm–Nd pairs yielded an isochron age of 2046 ± 22 Ma. These ages are comparable to the Sm–Nd isochron age for the Jeesiorova and Kittila komatiites (2056 ± 25 Ma; Hanski *et al.*, 2001a) and komatiites of the KGB (2085 ± 85 Ma; Krill, 1985a). Puchtel *et al.* (1998) noted that the age determinations from the Karasjok komatiites use whole-rock Sm–Nd on geochemically heterogeneous samples, cautioning the significance of this age. However, the komatiites in different parts of the belt can still be correlated based on similar stratigraphic position, lithology and geochemistry (Puchtel *et al.*, 1997; Hanski *et al.*, 2001a; Heggie *et al.*, 2013), implying vast and contemporaneous outpourings of mafic–ultramafic magmas over much of the Fennoscandian Shield (Puchtel *et al.*, 1998).

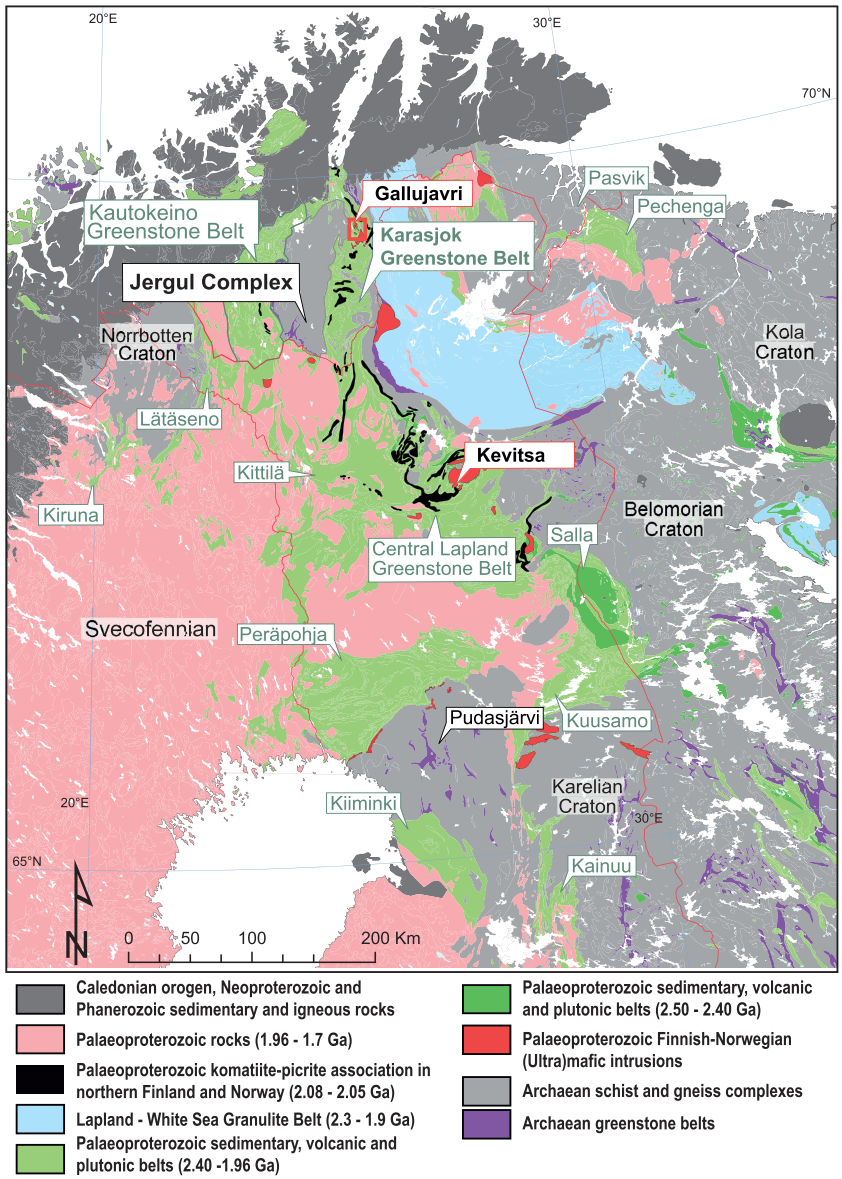

Fig. 1. Simplified map of northern Fennoscandia, modified from Bingen *et al.* (2015), Hanski *et al.* (2001a), Hanski & Huhma (2005), and Puchtel *et al.* (2020), based on Koistinen *et al.* (2001). Red bodies mark layered ultramafic-mafic intrusions and anorthosite, and black bodies mark occurrences of the Palaeoproterozoic komatiite–picrite association of Norway and northern Finland. The red box shows the location of Fig. 3 and the location of the ultramafic Gallujavri intrusion.

THE GALLUJAVRI ULTRAMAFIC INTRUSION

The Gallujavri intrusion is a small sill-like ultramafic body covering a surface area of c. 2.3 km^2 (Fig. 3). As for the rest of the KGB, exposure is limited and the intrusion shows a clear eastward continuation on geophysical maps (Fig. 3b,c; Skaar, 2014), suggesting it is larger than implied by the surface expression.

The intrusion is hosted by the 45–70° eastward-dipping quartzitic and quartz-feldspathic schists of the Corgaš Formation (Nilsson & Often, 2009, and references therein). The metasedimentary rocks are

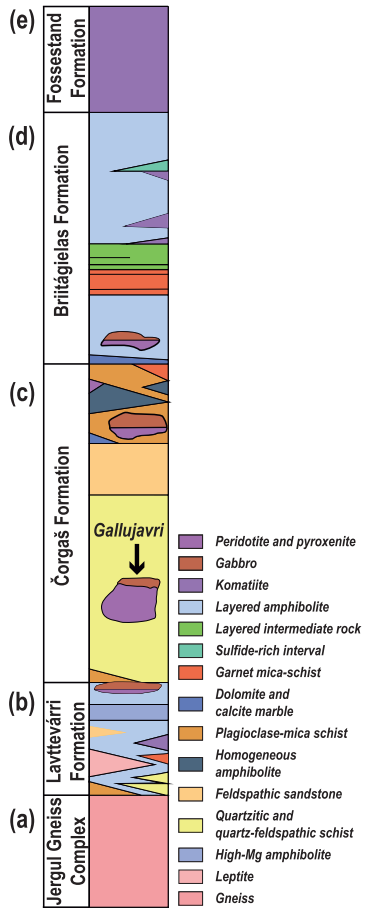

Fig. 2. The lithostratigraphy of the Karasjok Greenstone belt, modified from Hansen *et al.* (2020).

fine grained, light grey with a quartz and feldspar content of c. 80%, followed by micas, amphibole and accessory garnet (Bradley, 2003). The eastern contact of the intrusion consists of a variably altered olivine pyroxenite that grades to gabbro with c. 30% intercumulus plagioclase. Despite the alteration, primary features are locally preserved, including pristine magmatic mineralogy. The intrusion hosts mineralisations of disseminated sulphide consisting of up to 5% interstitial and intergrown chalcopyrite, pyrrhotite and pentlandite. The mineralisations are found in the ultramafic parts and gabbros but are also associated with alteration, faulting and contact zones (Bradley, 2003).

SAMPLING, ANALYTICAL AND MODELLING METHODS

Eleven holes have been drilled—eight pack-sack holes and three diamond drill holes (03GD001–003; Fig. 3) —together with geophysics, geological mapping and geochemical sampling (Boyd *et al.*, 2016). The sampling and analytical procedures reflect the exploratory nature of prior studies. Therefore, the three diamond drill cores were relogged, sampled and analysed. From the three cores, we extracted 66 samples, from which 60 samples were sent for geochemical analysis and 59 polished thin sections were made.

Major and trace element abundances

The sixty whole-rock samples from the three re-analysed drill holes were analysed at the ALS laboratories in Piteå, Sweden (Supplement 1). Major, minor and trace elements were analysed with fused bead, acid digestion using inductively coupled plasma atomic-emission spectroscopy (ICP–AES) and inductively coupled plasma mass spectrometry (ICP–MS). Base metals were analysed by ICP–AES following four-acid digestion.

Analysis of mineral compositions

Electron probe micro-analysis

Electron probe micro-analysis (EPMA) analyses were conducted on eight thin sections at the Norwegian University of Science and Technology (NTNU), Trondheim, using a JEOL JXF–8530F PLUS field-emission (FE) microprobe, set to 15 keV and 10 nA for all analyses. Counting times varied from 5 s on peak and 2 s on high and low background for Na in plagioclase to 50 s on peak and 25 s on each background for F in mica and amphibole. Most elements had counting times of 20 and 10 s on peak and backgrounds, respectively (Supplement 2). 4 wt% H_2O was added as matrix correction to the mica analyses and 2 wt% in the amphibole analyses. The mass-based model of Ridolfi *et al.* (2018) was later used to accommodate the volatile content in the amphiboles.

Laser-ablation inductively coupled plasma mass spectrometry

Minor and trace element concentrations in Fe–Ti oxides were analysed by laser-ablation inductively coupled plasma mass spectrometry (LA–ICP–MS; Supplement 3) using an ELEMENT XR at the Geological Survey of Norway, Trondheim. A total of 14 grains were analysed located in three thin sections.

The ELEMENT XR is a double-focusing sector-field inductively coupled plasma mass spectrometer linked to a New Wave UP193FX ESI excimer laser probe. The concentrations of trace elements were measured on polished thin sections (30 μm thickness). Iron concentrations determined by EPMA were used as the internal standard. The material used for external multi-standard calibration was the National Institute of Standards and Technology reference glasses NIST SRM 612 and NIST SRM 614 and the US Geological Survey references GSD–1G, GSE–1G, MASS–1 and BCR–2G.

Magma chamber simulator

The MCS is an energy and mass constrained thermodynamic tool for modelling magmatic evolution by fractional crystallisation (FC), assimilation and fractional crystallisation (AFC), recharge and fractional crystallisation (RFC) and recharge, assimilation and fractional crystallisation (RAFC) (Bohrson *et al.*, 2014). With this simulation tool, thermodynamic boundaries capable of transferring heat and mass separate the resident magma, recharge magma and wall-rock subsystems, for which the MCS calculates phase equilibria and geochemical evolution. The overall petrological and geochemical evolution is linked by the resident magma and wall-rock temperatures as the two advance towards thermal equilibrium. The resident magma

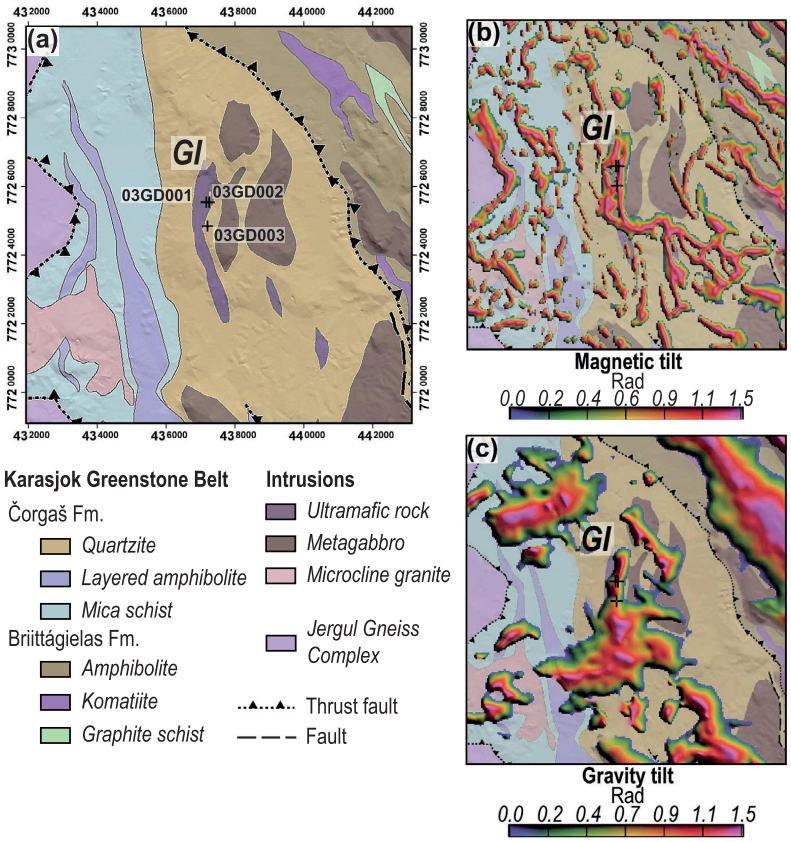

Fig. 3. Geological map and geophysical anomaly maps from Skaar (2014). All three maps cover the same area. The location of drill holes 03GD001, 03GD002 and 03GD003 are marked with crosses. (a) Geological map of the Gallujavri intrusion. (b) Magnetic tilt anomalies and (c) gravity tilt anomalies superimposed on the geological map. Gl, Gallujavri intrusion.

(with possible recharges) transfers enthalpy to the host rock so that the latter (potentially) exceeds its solidus temperature and thereby contaminates the initial melt. Assimilation of anatectic melts occurs only after exceeding a pre-determined critical melt-volume fraction defined as the percolation threshold (FmZero). The wall-rock and magma subsystems evolve due to mass and heat exchange, calculated at pre-determined temperature decrements with a selected MELTS engine (pMELTS or rhyolite-MELTS versions 1.0.x, 1.1.x, or 1.2.x; Ghiorso & Gualda, 2015, Ghiorso *et al*., 2002, Ghiorso & Sack, 1995, Gualda *et al*., 2012).

Definitions of subsystems and initial conditions

Only a brief outline of the MCS modelling parameters and boundary conditions is given here. For more information on these topics, we refer to several articles introducing MCS (e.g. Bohrson *et al*., 2014; Heinonen *et al*., 2019; Bohrson *et al*., 2020; Heinonen *et al*., 2020; Heinonen *et al*., 2021).

The progress variable of the MCS is magma temperature ($\mathbf{\Delta T}$), and each simulation is isobaric. Oxygen fugacity can be constrained to a specified redox buffer (e.g. QFM), providing a fixed f_{O2} as a function of temperature. Otherwise, the initial FeO and Fe_2O_3 concentrations can be specified for each subsystem.

The initial resident-magma subsystem (**M**) has specified bulk composition ($X^{M}_{0,i}$), where i refers to the ith chemical component and mass (M^{M}_{0}). The initial magma is completely molten at the time of intrusion, as the magma (T^{M}_{0}) temperature must be initialised at the liquidus temperature.

The next subsystem is the cumulates (**C**; solids±volatiles) that are transferred adiabatically in incremental batches from **M** to **C**. The mass transferred from **M** to **C** is determined by the mass of solids±volatiles formed (if any) in the temperature step ($\mathbf{\Delta T}$). The solids±volatiles form in thermal and chemical equilibrium with **M**, but no further chemical interaction is allowed once transferred to **C**.

The wall-rock (**WR**) subsystem thermally interacts and supplies anatectic melt (i.e. if above the percolation threshold) to **M**. The

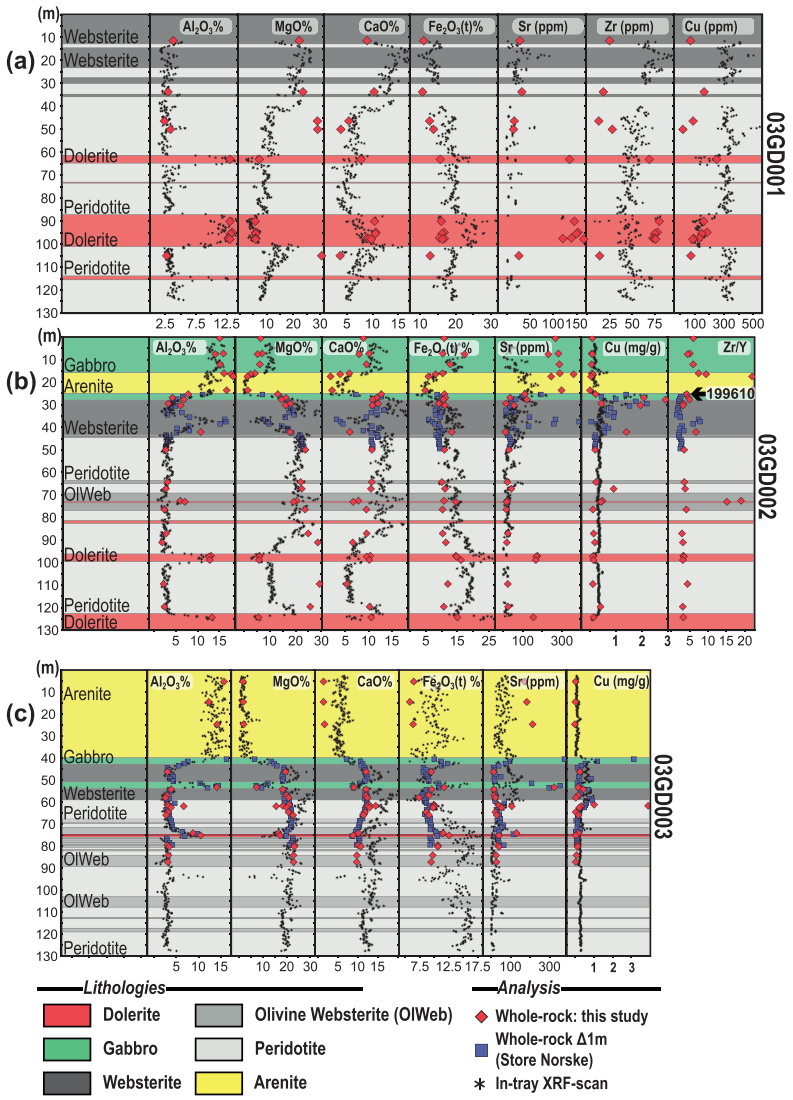

Fig. 4. Magmatic stratigraphy of drill holes logged and sampled in this study. The blue squares are whole-rock data determined by the commercial laboratory ALS for Store Norske. The red diamonds are whole-rock ICP–AES data from this study. The small black asterisks show semi-quantitative direct in-tray XRF scanning data acquired by Store Norske. We note that in some intervals, the XRF scans differ substantially from the other methods. (a) Drill hole 03GD001. (b) Drill hole 03GD002. Note the location of the CM sample 199 610. (c) Drill hole 03GD003.

wall rock (**WR**) is initialised with the specification of mass ($M^{WR}{}_0$), composition ($X^{WR}{}_{0,i}$) and initial temperature ($T^{WR}{}_0$) that is required to be below the solidus temperature. The $M^{WR}{}_0$ can be thought of as the proportion of wall rock capable of interacting with the resident magma.

Melt recharges ($\mathbf{R}_j$) can be added to **M** in j mass increments ($M^R{}_j$), each with a defined initial bulk composition ($X^R{}_{j,i}$) for i chemical components and temperature ($T^R{}_j$). Unlike **M**, the **R** magma temperature can be specified above or below the liquidus so that superheated melt or melt+crystals±volatiltes can be added to **M**. The specification of $T^R{}_j$ under the liquidus leads MCS to calculate the internal thermodynamic equilibrium (i.e. mineral modes and compositions) of the $\mathbf{R}_j$ subsystem before addition to **M**.

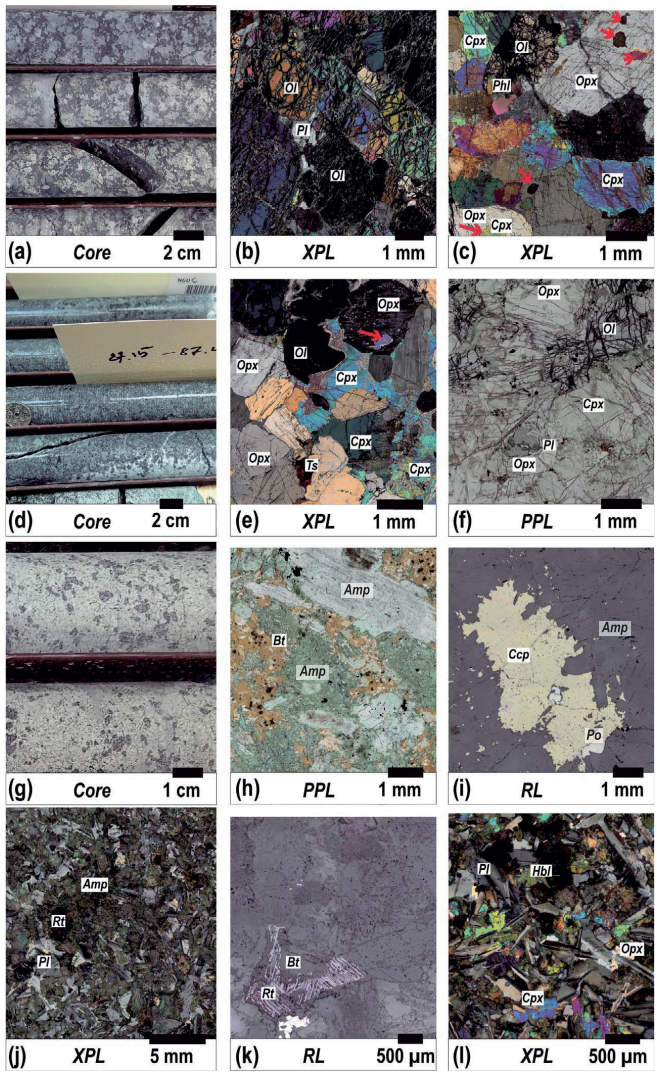

Fig. 5. Images and micrographs of common rocks of the Gallujavri ultramafic intrusion. (a) Image of a typical peridotite in drill core 03GD001. Serpentinisation and Fe-oxide alteration of primary olivine result in the black appearance in hand specimens. The white to light-green areas consist of orthopyroxene and clinopyroxene with tremolite, chlorite and serpentine alteration. (b) Micrograph showing a dunitic olivine adcumulate with interstitial plagioclase. (c) Micrograph showing a peridotite consisting of cumulate olivine and coarse-grained oikocrystic orthopyroxene. The clinopyroxene occurs as chadacrysts in orthopyroxene and as an anhedral interstitial phase. Red arrows point to examples of clinopyroxene inclusions in orthopyroxene. The intercumulus phases, together with clinopyroxene, consist of accessory phlogopite and plagioclase—the latter not visible in this image. (d) Image showing a typical olivine websteritic section in drill core 03GD003. (e) Micrograph showing an olivine, orthopyroxene and clinopyroxene mesocumulate with intercumulus clinopyroxene and hornblende. (f) Micrograph showing an olivine, clinopyroxene and oikocrystic orthopyroxene mesocumulate with intercumulus plagioclase. Clinopyroxene occurs as a cumulus phase and as chadacrysts in orthopyroxene. (g) Image of a typical websterite in drill core 03GD003. Pyroxenes and their alteration products are white to yellowish white; the dark phase is olivine. (h) Micrograph showing extensive amphibole–phlogopite alteration of a websteritic sample. Note the sizeable relict pyroxene in the upper right-hand corner replaced by amphibole. Also, note biotite with characteristic pleochroic haloes. (i) Micrograph of a large chalcopyrite grain in a groundmass of secondary amphibole. (j) Micrograph showing a coarse-grained intergranular gabbro. The spaces between the plagioclase crystals are occupied by heavily altered granules of pyroxenes and opaques. (k) Micrograph showing sagenitic-textured biotite in gabbro. (l) Micrograph showing intergranular dolerite, where the granules consist of pyroxenes and secondary Ca-amphibole. Abbreviations: cross-polarised light (XPL), plane-polarised light (PPL), reflected light (RL), plagioclase (Pl), clinopyroxene (Cpx), orthopyroxene (Opx), olivine (Ol), phlogopite (Phl), tchermakite (Ts), biotite (Bt), chalcopyrite (Ccp), pyrrhotite (Po), amphibole (Amp), rutile (Rt) and hornblende (Hbl).

RESULTS

Petrography

The three drill holes studied are oriented 45°/270° and consist of a lower section of peridotite, a middle section of pyroxenite and an upper section of gabbro (Fig. 4). The apparent internal lithological layering is perpendicular to the orientation of the drill holes, making the layering concordant or semi-concordant to the foliation of the surrounding metasedimentary rocks.

The lower part of the drilled section comprises lherzolitic to harzburgitic cumulates with variable intercumulus plagioclase (c. 0–3 modal%) and accessory hornblende and phlogopite (Fig. 5a–c). Primary olivine (50 to 80 modal%) has mesh textures consisting of serpentine and fine-grained oxides, making them black in hand specimen (Fig. 5a). In combination with accessory, primary dark-brown hornblende, there is moderate to severe amphibole alteration of clinopyroxene, whereas orthopyroxene (c. 20 modal%) generally shows more resistance to alteration. Orthopyroxene (c. 20 vol%) is generally coarse grained and unaltered and found in a ground-mass of serpentine, amphibole and chlorite.

Despite widespread alteration, many less-altered examples allow for the examination of primary igneous textures. These samples typically show considerable variation in the pyroxene-to-olivine ratio. Olivine is commonly anhedral and rounded with an average grain size of c. 2 mm. The second most abundant mineral is coarse-grained (c. 2–3 mm), commonly poikilitic orthopyroxene. Clinopyroxene (c. 0–20 modal%) occurs both as an anhedral interstitial phase and chadacrysts in olivine and orthopyroxene (Fig. 5c).

In drill holes 03GD002 and 03GD003 (Fig. 4b,c), the peridotite is interlayered with olivine websterite. These layers, however, cannot be correlated between the cores. The olivine websterite is composed primarily of cumulus orthopyroxene (5–45 modal%), clinopyroxene (6–52%) and olivine (4–20%), with interstitial plagioclase (0–5%), hornblende (0–4%) and phlogopite (0–3%) (Fig. 5d–f). Cumulus olivine and orthopyroxene both have average grain sizes of about 2 mm. Olivine is inequigranular, anhedral and rounded, while orthopyroxene generally is subhedral and equigranular. Clinopyroxene grains are less bounded by crystal faces and show greater variation in grain size than orthopyroxene. Clinopyroxene is commonly subordinate to orthopyroxene and seemingly crystallised at various melt-evolution stages, suggested by clinopyroxene appearing as cumulus grains, inclusions in orthopyroxene and as an intercumulus phase (Fig. 5e,f). Plagioclase occurs as a late interstitial phase (Fig. 5f).

The modal amounts of olivine in the peridotite and olivine websterite interlayers gradually decrease towards the top of the drill holes, becoming websteritic. The websterite is severely altered to a mineral association of green amphibole, tremolite, chlorite and mica, making most modal and textural evaluations of the primary mineralogy impossible (Fig. 5g–i). Some relicts of pyroxene indicate a coarse grain size of around 3.5 mm. Pleochroic haloes characterise secondary biotite (Fig. 5h). Examples of coarse-grained chalcopyrite (c. 6 mm) disseminations is found with minor pyrrhotite and pentlandite (Fig. 5i). In the top sections of drill holes 03GD002 and 03GD001 (Fig. 4a,b), the websterite grades into gabbro. The gabbro changes in texture and modal proportions from base to top. At the base, the gabbro is melanocratic with interstitial plagioclase (c. 20%) with an average grain size of c. 1 mm. The plagioclase is partly recrystallised, with rounded grain boundaries indicating post-magmatic reworking and grain-size reduction. The ferromagnesian minerals throughout this section are wholly recrystallised to green amphibole and chlorite. Pyrite, pentlandite, pyrrhotite and chalcopyrite are commonly present as fractionated products within millimetre-scale sulphide blebs.

Upsection, gabbros become coarser grained with almost unaltered cumulus plagioclase (Fig. 5j). The mafic minerals have suffered severe amphibole–biotite alteration—the biotite with rutile and titanite exsolution (Shau *et al.*, 1991)—giving them a beautiful and characteristic sagenitic texture (Fig. 5k). In drill hole 03GD002, a repetition of gabbro, separated by the arenitic host, represents the intrusion's chilled margin (CM; 25–28 m; cf. sample 199 610; Fig. 4b).

Throughout the magmatic stratigraphy, there are multiple examples of sheet intrusions of dolerite. These microgabbro dykes consist of plagioclase laths measuring ~500 μm along the c-axis with intergranular diopside, augite, olivine and orthopyroxene (Fig. 5l). The mafic minerals are moderate to severely altered, with green amphibole constituting 30 to 70%. At the mesoscale, these sheet intrusions have clear CMs. However, at the microscale, the fine-grained material is deformed and entirely replaced by alteration products.

Mineral chemistry

Below, we report our mineral chemical data acquired with EPMA (Table 1) and Fe–Ti oxide LA–ICP–MS (Table 2). Because of the large dataset, the ranges reported exclude outliers that are more than 1.5 times larger or smaller than the upper and lower quartiles, respectively. The complete dataset is available in Supplement 4.

Olivine from the different lithologies is homogeneous with no evidence of zoning (Fig. 6a, b). The olivine websterites have the most primitive forsterite content, with Fo_{80-82}. The plagioclase-bearing olivine websterite follows with Fo_{79-81}. The peridotites have forsterite contents spanning slightly lower values, with Fo_{78-79}, more reminiscent of olivine from a gabbroic host (Burns & Brown Jr., 1982). The forsterite content in the gabbro ranges from Fo_{76} to Fo_{77}. Depletion of CaO (<1000 ppm) is characteristic for olivine in all rock types except for the olivine websterite, which has elevated concentrations (>4500 ppm). The olivine has high Ni concentrations, with NiO in the range 2800–3500 ppm (Fig. 6b). Slightly lower values are seen in the gabbro, with NiO in the range 2700–2800 ppm.

The clinopyroxene of the intrusion is dominated by augite with a smaller amount of diopside (Fig. 6a). The peridotite hosts the most primitive clinopyroxene with xMg ($Mg/Mg+Fe^t$) in the narrow range 0.89–0.90. These samples also have the most Ca-poor clinopyroxenes with a CaO concentration of $12 \pm 0.5\%$. The xMg of the clinopyroxene hosted by the olivine websterite ranges between 0.86 and 0.89, plagioclase-bearing olivine websterite between 0.81 and 0.86 and gabbro between 0.76 and 0.86 – all of them with CaO ranging from 17 to 22%. Most of the clinopyroxene has higher xMg relative to the olivine in a sample. The feature of $xMg_{Cpx} > Fo$ is typical for high-T peridotites. It indicates an equilibrium distribution of Fe and Mg between the two phases (Fig. 6c; Barsdell, 1988, Grant *et al.*, 2016, Jagoutz *et al.*, 2007, Perkins & Vielzeuf, 1992). The disequilibrium seen in the peridotite could indicate that orthopyroxene crystallised at the expense of olivine (Jagoutz *et al.*, 2007).

The olivine pyroxenite hosts the most primitive orthopyroxene with xMg in the range of 0.84–0.86. Orthopyroxene in the peridotite ranges in xMg from 0.82 to 0.85 and the plagioclase-bearing olivine websterite from 0.78 to 0.83. The gabbro has the largest range of orthopyroxene compositions with xMg 0.74–0.83. There is an inflection point at $xMg \sim 0.8$, suggesting the beginning of plagioclase fractionation (Fig. 6d).

Table 1: EPMA mineral averages for the different lithologies. All oxides and totals are given in wt%

	Olivine							
	Gabbro		Pl OlWeb		OlWeb		Peridotite	
	N = 2	2σ	N = 7	2σ	N = 14	2σ	N = 9	2σ
SiO_2	38.47	0.32	39.01	0.77	39.26	0.58	38.96	0.81
TiO_2	bdl	n/a	0.05	n/a	bdl	n/a	bdl	n/a
Al_2O_3	bdl	n/a	bdl	n/a	0.05	0.01	bdl	n/a
FeO^t	21.64	0.65	17.83	1.16	17.36	1.37	19.15	1.71
MnO	0.31	0.04	0.27	0.05	0.26	0.05	0.31	0.07
MgO	39.01	0.85	41.75	1.21	42.44	1.44	40.60	1.70
CaO	bdl	n/a	0.06	n/a	0.19	0.37	0.05	0.04
NiO	0.27	0.01	0.33	0.05	0.31	0.05	0.29	0.04
Total	99.76	0.51	99.27	1.12	99.85	0.79	99.40	0.95
Fo	*76.02*	*0.97*	*80.40*	*1.49*	*80.95*	*1.73*	*78.77*	*2.19*
$Fo = 100*Mg/(Fe^T + Mn + Mg + Ca)$								
	Clinopyroxene							
	Gabbro		Pl OlWeb		OlWeb		Peridotite	
	N = 5	2σ	N = 66	2σ	N = 47	2σ	N = 6	2σ
SiO_2	52.66	2.42	52.89	2.22	52.83	1.59	54.91	1.07
TiO_2	0.49	0.67	0.38	0.44	0.32	0.39	0.10	0.04
Al_2O_3	2.29	1.61	2.11	1.32	2.02	1.09	2.70	1.07
FeO^t	7.22	3.02	5.98	1.73	5.19	1.85	4.49	0.34
Cr_2O_3	0.52	0.61	0.69	0.37	0.99	0.43	0.12	0.03
MnO	0.20	0.08	0.19	0.07	0.17	0.06	0.15	0.04
MgO	17.05	4.10	17.46	4.22	17.73	4.00	21.49	0.74
CaO	18.90	3.94	19.03	4.34	19.58	5.88	12.05	0.52
Na_2O	0.46	0.23	0.39	0.16	0.46	0.19	0.82	0.25
K_2O	bdl	n/a	0.06	n/a	bdl	n/a	0.07	0.03
NiO	0.07	n/a	0.08	0.02	0.08	0.01	0.09	0.03
Total	99.85	0.34	99.17	1.80	99.36	1.51	96.95	1.11
Wo	*39.19*	*8.52*	*39.72*	*10.09*	*40.59*	*12.52*	*26.51*	*1.21*
En	*49.09*	*10.50*	*50.53*	*10.55*	*51.05*	*10.39*	*65.77*	*1.65*
Fs	*11.72*	*5.22*	*9.74*	*2.93*	*8.37*	*2.79*	*7.72*	*0.66*
$Wo = 100*Ca/(Ca + Mg + Fe^T)$								
$En = 100*Mg/(Ca + Mg + Fe^T)$								
$Fs = 100*Fe^T/(Ca + Mg + Fe^T)$								
	Orthopyroxene							
	Gabbro		Pl OlWeb		OlWeb		Peridotite	
	N = 4	2σ	N = 55	2σ	N = 39	2σ	N = 6	2σ
SiO_2	54.02	2.09	54.61	1.48	55.15	1.56	55.50	1.56
TiO_2	0.33	0.33	0.23	0.18	0.17	0.17	0.24	0.36
Al_2O_3	1.93	0.75	1.76	0.96	1.38	0.76	1.42	0.55
FeO^t	13.49	4.69	12.17	3.98	9.36	1.81	10.14	2.24
Cr_2O_3	0.23	0.19	0.30	0.18	0.54	0.18	0.50	0.29
MnO	0.32	0.07	0.28	0.08	0.24	0.06	0.25	0.07
MgO	27.27	3.30	27.77	2.51	30.19	1.44	29.74	1.17
CaO	2.04	0.58	2.06	1.67	2.24	0.73	1.77	1.42

Continued

Table 1: Continued

Orthopyroxene								
	Gabbro		Pl OlWeb		OlWeb		Peridotite	
	N = 4	2σ	N = 55	2σ	N = 39	2σ	N = 6	2σ
Na_2O	0.07	0.01	0.06	0.05	0.06	0.03	0.08	0.03
K_2O	bdl	n/a	0.03	n/a	0.05	n/a	bdl	n/a
NiO	0.07	0.00	0.10	0.04	0.10	0.03	0.10	0.03
Total	99.74	0.79	99.33	1.36	99.42	1.62	99.66	1.02
Wo	*4.04*	*1.00*	*4.10*	*3.33*	*4.36*	*1.37*	*3.47*	*2.78*
En	*75.31*	*6.45*	*76.99*	*5.61*	*81.98*	*2.33*	*81.02*	*1.86*
Fs	*20.65*	*7.45*	*18.92*	*6.47*	*13.65*	*2.80*	*15.52*	*3.59*
$Wo = 100*Ca/(Ca + Mg + Fe^T)$								
$En = 100*Mg/(Ca + Mg + Fe^T)$								
$Fs = 100*Fe^T/(Ca + Mg + Fe^T)$								

Plagioclase								
	Gabbro		Pl OlWeb		OlWeb		Peridotite	
	N = 3	2σ	N = 31	2σ	N = 0	2σ	N = 0	2σ
SiO_2	56.05	1.10	55.55	1.91				
TiO_2	0.07	0.03	0.07	0.03				
Al_2O_3	27.70	0.72	27.95	1.25				
FeO^t	0.21	0.19	0.22	0.23				
MgO	0.03	0.00	0.04	0.01				
CaO	9.90	0.82	10.32	1.56				
Na_2O	5.88	0.46	5.64	0.93				
K_2O	0.14	0.27	0.11	0.15				
SrO	0.12	0.06	0.11	0.07				
Total	100.11	1.22	100.00	1.09				
An	*47.85*	*4.08*	*49.97*	*7.72*				
$An = 100*Ca/(Ca + Na + K)$								

Amphibole								
	Gabbro		Pl OlWeb		OlWeb		Peridotite	
	N = 0	2σ	N = 10	2σ	N = 2	2σ	N = 0	2σ
SiO_2			45.63	4.95	42.66	0.45		
TiO_2			1.63	3.04	5.48	1.04		
Al_2O_3			11.20	2.72	11.58	1.03		
Cr_2O_3			0.20	0.22	0.84	0.13		
FeO^t			7.78	0.84	7.59	0.96		
MnO			0.14	0.11	0.19	0.17		
NiO + ZnO			0.12	0.04	bdl	n/a		
MgO			16.41	0.93	14.90	0.80		
CaO			11.67	0.43	11.30	0.32		
Na_2O			2.20	0.69	2.66	0.07		
K_2O			0.86	0.72	1.31	0.07		
F			0.05	0.04	0.02	0.02		
Cl			0.10	0.08	0.05	0.01		
Total			97.93	0.53	98.66	0.19		

Continued

Table 1: Continued

	Spinel							
	Gabbro		Pl OlWeb		OlWeb		Peridotite	
	N = 3	2σ	N = 15	2σ	N = 25	2σ	N = 27	2σ
SiO_2	0.13	n/a	0.43	n/a	bdl	n/a	bdl	n/a
TiO_2	0.37	0.19	1.62	1.32	3.79	13.66	0.96	0.78
Al_2O_3	9.29	1.22	6.22	4.56	12.08	4.99	7.33	8.62
Cr_2O_3	39.12	7.17	28.46	15.27	34.97	14.58	33.71	11.20
FeO^t	44.78	5.97	55.54	17.90	40.55	13.42	49.46	18.42
MnO	0.52	0.02	0.56	0.15	0.45	0.17	0.55	0.12
MgO	2.11	0.15	1.37	0.79	3.95	4.19	1.83	2.52
CaO	bdl	n/a	0.06	0.07	0.03	n/a	0.06	0.04
Na_2O	1.00	n/a	0.09	0.09	0.10	0.16	0.11	0.19
NiO	0.09	0.03	0.13	0.08	0.15	0.10	0.15	0.09
Total	96.70	0.62	94.01	1.75	95.98	1.40	94.11	2.18
apfu								
Ti	0.010	0.005	0.046	0.038	0.102	0.371	0.027	0.024
Al	0.391	0.053	0.272	0.192	0.501	0.200	0.315	0.359
Cr	1.104	0.199	0.838	0.425	0.972	0.379	0.985	0.276
Fe^{2+}	0.833	0.129	0.944	0.081	0.853	0.359	0.896	0.144
Fe^{3+}	0.505	0.131	0.797	0.532	0.393	0.255	0.649	0.543
Mg	0.113	0.009	0.076	0.042	0.206	0.211	0.099	0.130
xFe^2	*0.88*	*0.01*	*0.93*	*0.04*	*0.80*	*0.22*	*0.90*	*0.13*
xFe^3	*0.25*	*0.07*	*0.42*	*0.29*	*0.20*	*0.13*	*0.33*	*0.29*
xCr	*0.74*	*0.06*	*0.76*	*0.05*	*0.66*	*0.11*	*0.78*	*0.21*

$xFe^2 = Fe^2/(Mg + Fe^2)$
$xFe^3 = Fe^3/(Cr + Al + Fe^3)$
$xCr = Cr/(Cr + Al)$

End-member mole fractions or percentages in italics. 2σ represent the population's standard deviation; if N < 2, σ is not applicable (n/a).
Pl OlWeb, Plagioclase bearing olivine websterite; OlWeb, olivine websterite; bdl, below the detection limit; An, anorthite; Fo, forsterite; Wo, wollastonite; En, enstatite; Fs, ferrosilite; apfu, atoms per formula unit.

The intercumulus plagioclase in the ultramafic rocks ranges from An_{45} to An_{53}. The plagioclase of the melanocratic gabbro primarily lies within the andesine field with An_{33-49}. The amphiboles have xMg concentrations ranging from 0.77 to 0.80 and plot in the field of magnesio-hornblende and pargasite, together with a lesser amount of sadanagaite (Hawthorne *et al.*, 2012).

The ferric iron content of the spinels in this study is calculated according to stoichiometry (Deer *et al.*, 2013). The ferrous and ferric iron contents were estimated from the total FeO using the sum of charges in the ideal XY_2O_4 formula, where X = (Fe^{2+}, Ni, Mn, Co, Zn), Y = (Cr^{3+}, Fe^{3+}, Al) and Ti allocated to an ulvöspinel component.

The spinels classify as Al-chromite, ferrian chromite and Cr-magnetite, with the majority in the ferrian chromite field. Together, they show a trend of increasing ferric iron and evolve towards magnetite (Fig. 6e), correlated with a slight increase in TiO_2. The spinels are depleted in Al, Ni, Mg and Sc and show positive Ti and Zn anomalies when normalised to MORB chromites (Fig. 6f; Page & Barnes, 2009).

Oxy-thermobarometry

The pressure and temperature were estimated based on the single-phase (amphibole) empirical thermobarometric formulation (±22°C and c. ±40 MPa) of Ridolfi *et al.* (2009), the two-pyroxene thermobarometric formulations (c. ±42°C and ± 280 MPa) of Putirka (2008) and the two-pyroxene thermometer (±50°C) of Brey & Köhler (1990). The individual estimates together with standard deviations can be found in Supplement 5.

There is a substantial variation in pressure and temperature estimates based on mineral chemistry (Fig. 7a). The densest locus in P/T space is around 400 MPa and 1000°C, with a tail of estimates along the dry peridotites solidus of Hirschmann (2000). The highest estimated pressures and temperatures are for the two-pyroxenes in the peridotites (~900 MPa, ~1250°C). However, as Fig. 6c shows, a slight Fe–Mg disequilibrium might affect this estimate.

Even disregarding the peridotites, there is still a considerable variation in pressure and temperature, which could indicate that crystallisation commenced in a staging magma chamber at depth. Geothermometers calibrated on Mg–Fe^{2+} exchange in olivine–spinel mineral pairs (Ashchepkov *et al.*, 2008) yield higher temperature estimates (Fig. 7b). Spinel commonly occurs as inclusions in olivine and likely was the first phase to crystallise and, therefore, is expected to record higher temperatures.

The spinel–olivine–orthopyroxene oxygen sensor (Ballhaus *et al.*, 1990) estimates fugacities between ~3.3 and 3.5 log f_{O2} ΔQFM (Fig. 7b; Frost, 1991). Such high oxygen fugacities are uncommon and primarily documented in xenoliths entrained in ocean island basalts (Cottrell *et al.*, 2021). We note that our estimates must be viewed as semi-quantitative as the spinel $Fe^{3+}/\sum$Fe-ratio is calculated by ideal stoichiometry without any calibration standards (Birner *et al.*, 2018).

Table 2: Spinel LA-ICP-MS averages for the different lithologies in parts per million (ppm)

	Pl OlWeb		OlWeb		Peridotite	
	N = 2	2σ	N = 4	2σ	N = 8	2σ
Li	*bdl*	n/a	7	n/a	8	2
Mg	15 028	3451	50 789	13 211	14 738	46 259
Al	61 245	9901	62 200	3091	64 525	17 463
Ca	302	n/a	381	227	*bdl*	n/a
Sc	2	1	3	1	2	7
Ti	3144	1814	5609	1007	4827	2727
V	1434.6	52.5	1368.6	360.0	1878.5	314.7
Cr	327 398	88 288	321 372	37 114	262 530	47 710
Mn	4077.3	1585.7	2567.0	604.8	3902.5	1432.4
Fe	353 676	23 319	237 080	20 195	390 599	110 954
Co	615.4	34.1	508.2	122.5	657.4	272.6
Ni	654	200	1091	402	1317	844
Cu	2	n/a	*bdl*	n/a	2	1
Zn	8072	2985	1056	186	4619	7045
Ga	51.5	10.6	48.4	6.2	92.2	45.1
As	0.3	n/a	1.0	1.5	0.3	n/a
Nb	0.18	0.06	0.20	0.05	0.15	0.06
Cd	*bdl*	n/a	*bdl*	n/a	0.3	0.1
Sn	*bdl*	n/a	0.3	0.2	0.2	0.7
Sb	*bdl*	n/a	*bdl*	n/a	0.07	0.04
Re	*bdl*	n/a	0.02	n/a	*bdl*	n/a
Ir	0.09	0.07	0.04	0.01	0.02	0.02
Pt	0.04	n/a	0.03	0.07	0.02	0.02
Tl	0.02	n/a	*bdl*	n/a	0.01	n/a
Pb	0.38	0.71	0.04	0.01	1.81	3.72
Bi	0.03	n/a	*bdl*	n/a	0.02	n/a

2σ represent the population's standard deviation; if N < 2, σ is not applicable (n/a).
Pl OlWeb, Plagioclase bearing olivine websterite; OlWeb, olivine websterite; bdl, below the detection limit.

Whole-rock major, minor and trace elements

Table 3 gives a summary of the whole-rock results acquired in this study. The ranges reported here are the groups' statistical variation with outliers excluded (cf. section on mineral chemistry). The complete dataset is presented in Supplement 6.

Selected major element oxides are presented in Fenner diagrams in Fig. 8 and downhole in Fig. 4. There is only minor variation in the major element oxide concentrations of the ultramafic rocks. The most primitive peridotites have major and minor element concentrations like the orthopyroxene average (Fig. 8b–f) and the group lies along a clinopyroxene–orthopyroxene mixing line. There is an inflection point between 20 and 25% MgO in the major and minor element data. The olivine websterites first show this change towards higher aluminium, alkalis and lower calcium with decreasing MgO (Fig. 8c–e), consistent with plagioclase accumulation. Biotite, amphibole and Fe–Ti oxide likely control the inflection in the TiO_2 vs MgO diagram (Fig. 8f), consistent with common rutile exsolutions in biotite (Fig. 5j,k). The dolerites are not distinct from the evolved gabbro major and minor element compositions (Fig. 8). However, these two rock types are distinctly different when considering the Rare Earth Elements (REE) and other trace elements (Figs 9 and 10). The dolerite and gabbro have similar LREE $(La/Sm)_N$ trends, but the dolerites consistently have lower HREE $(Gd/Yb)_N$. The dolerites have Nb/Th ratios between 5.2 and 6.0, close to the primitive mantle ratio (~8.4; Sun & McDonough, 1989), while the other lithologies have Nb/Th ratios ranging from 0.4 to 2.4 (Fig. 9c). The latter ranges are more consistent with average crustal values (~2.3; Weaver & Tarney, 1984). The difference in Nb/Th ratio between the dolerites and the other lithologies could be related to the extent of crustal assimilation (Pilet *et al.*, 2004), although isotopic data are needed to verify this assertion. Another feature to note is the near linear drop in Ni with decreasing MgO (Fig. 9d).

Figure 10 shows primitive mantle- and chondrite-normalised averages for the lithologies of the intrusion and arenitic host rock, as well as the average of two granodiorite samples from the Jergul Complex. All the lithologies of the Gallujavri intrusion show many similar features in the multi-element diagram, such as large-ion lithophile (LILE) and LREE enrichment, positive W, U and Pb and negative Nb–Ta, P, Eu and Ti anomalies normalised to primitive mantle (Fig. 10a). The dolerites break up this pattern with a more pronounced negative Ta and less pronounced positive Pb and negative P anomalies. All the ultramafic cumulates of the Gallujavri intrusion have similar REE patterns when normalised to chondrite (Fig. 10b; Sun & McDonough, 1989) with average $(La/Yb)_N$ ranging from 2.5 to 3.2. With respect to the REEs, the gabbros are most fractionated with average $(La/Yb)_N = 4.9$ and the least fractionated are the dolerites with $(La/Yb)_N = 2.1$. The igneous rocks mimic many features present in the arenite and Jergul Complex, most evident in the Th, U, Nb, Ta, K and Pb anomalies.

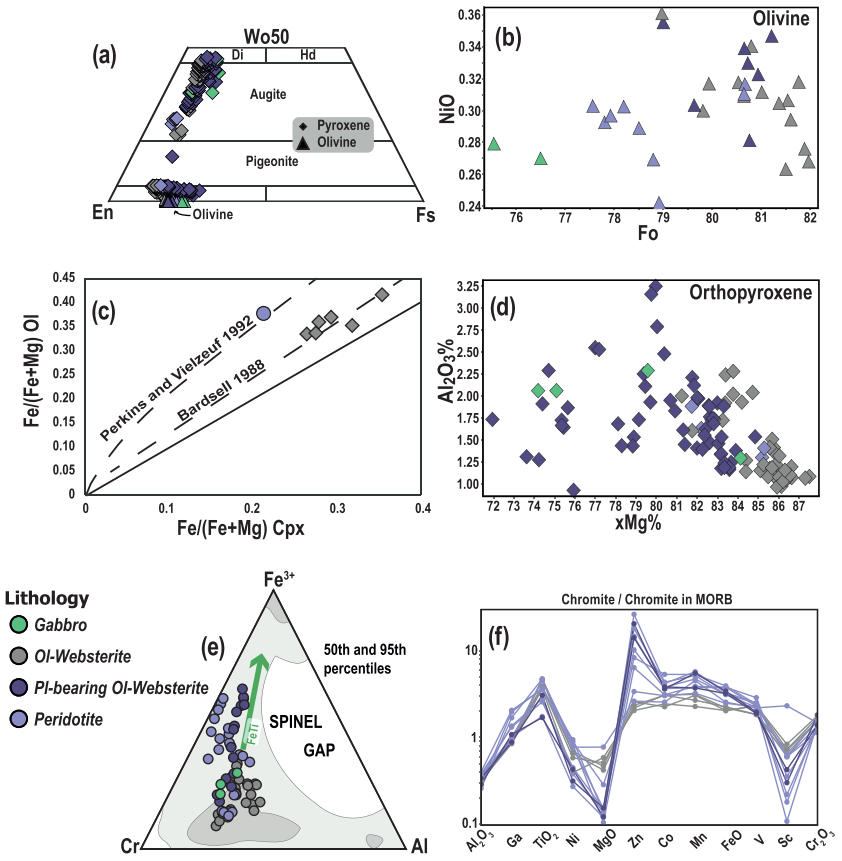

Fig. 6. Mineral chemistry and classification diagrams. (a) Pyroxene trapezoid with (end)members diopside (Di), enstatite (En), ferrosilite (Fs) and hedenbergite (Hd). Augite dominates the clinopyroxene compositions, with a small high-Ca fringe classified as diopside. Orthopyroxene clusters around En_{80} with $Wo_{0\text{–}5}$. Olivine (triangles) is included in the diagram and plot along the En–Fs join. (b) Olivine NiO vs Fo%. (c) Graph of xFe (Fe/(Fe + Mg)) in olivine (Ol) and clinopyroxene (Cpx) relative to the equilibrium curves of Barsdell (1988) and Perkins & Vielzeuf (1992). Olivine websterites in grey follow the curve of Barsdell (1988), the olivine–clinopyroxene pair from the peridotite (light blue) plots separately and slightly above the curve of Perkins & Vielzeuf (1992). (d) Al_2O_3 vs xMg% variation diagram for orthopyroxene showing a weak negative and positive correlation for xMg% > 80 and <80, respectively. (e) Ternary diagram relating our analysed spinels to the Fe–Ti trend (green arrow) and compositional fields as defined by Barnes & Roeder (2001) for spinels from mafic–ultramafic igneous rocks. (f) Analysed spinel major, minor and trace elements normalised to MORB chromites (Page & Barnes, 2009).

DISCUSSION

Modelling assumptions and parameters

Komatiitic and basaltic volcanism in the KCLGB coeval with the Gallujavri intrusions suggests that the intrusion may represent a magma conduit in an intracontinental rift (Often, 1985; Krill, 1985b; Barnes & Often, 1990). This hypothesis is consistent with previous models proposed for the Palaeoproterozoic komatiite–picrite association of the Fennoscandian Shield (Krill, 1985a; Barnes & Often, 1990; Hanski *et al.*, 2001a), and the spinel compositions yield similar trends to those documented for subvolcanic intrusions in the Siberian and Karoo flood basalt provinces (Barnes & Roeder, 2001). This spinel Fe–Ti trend likely results from the co-fractionation of spinel with olivine or pyroxene from the parental melt (Fig. 6e; Barnes & Roeder, 2001, Irvine, 1967). In combination with the parental melt evolution, the variation of xFe^{2+} in spinel likely results from the temperature-dependent partitioning of Mg and Fe^{2+} ($K_D(Mg–Fe^{2+})$) between spinel and silicates. This equilibrium favours increased xFe^{2+} in spinel with decreasing temperature, an effect that is most pronounced in rocks that cooled slowly (Irvine, 1965; Irvine, 1967; Barnes & Roeder, 2001). The major, minor and trace element trends are characteristic and comparable to spinel compositions documented for continental mafic intrusions and subvolcanic mafic intrusions from continental flood basalt terrains (Fig. 6f; Barnes & Roeder, 2001). The most commonly proposed model for forming these large igneous provinces is the partial melting of a mantle plume or the impingement of a mantle plume at the base of the crust (Lightfoot *et al.*, 1993; Duncan *et al.*, 1997;

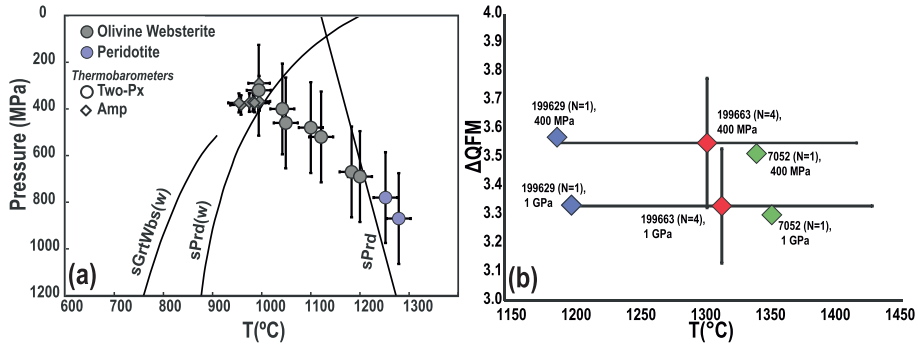

Fig. 7. Oxy-thermobarometric estimates. (a) Amphibole, orthopyroxene and clinopyroxene thermobarometry. Mineral pairs from peridotites in light blue. Mineral pairs from olivine websterites in grey. Diamonds: amphibole thermobarometer (Ridolfi *et al.*, 2009). Circles: weighted averages of the two-pyroxene thermometer of Brey & Köhler (1990) and the two-pyroxene thermobarometers of Putirka (2008). Reference lines: anhydrous solidus for peridotite (sPrd; Hirschmann, 2000), hydrous peridotite solidus (sPrd(w); Boettcher *et al.*, 1975) and hydrous garnet websterite solidus (sGrtWbs(w); Mysen & Boettcher, 1976). (b) Olivine–spinel thermometer (Ashchepkov *et al.*, 2008) and olivine–spinel–orthopyroxene oxybarometer (Ballhaus *et al.*, 1990) relative to the QFM reference buffer of Frost & McCammon (2008). The fugacity is estimated for mineral pairs from three samples: 199629 (blue diamonds; N = 1), 199 663 (red diamonds; N = 4), and 7052 (green diamonds; N = 1) assuming pressures of 400 and 1000 MPa. For sample 199 663, the error bars signify the standard deviation of the population of estimates.

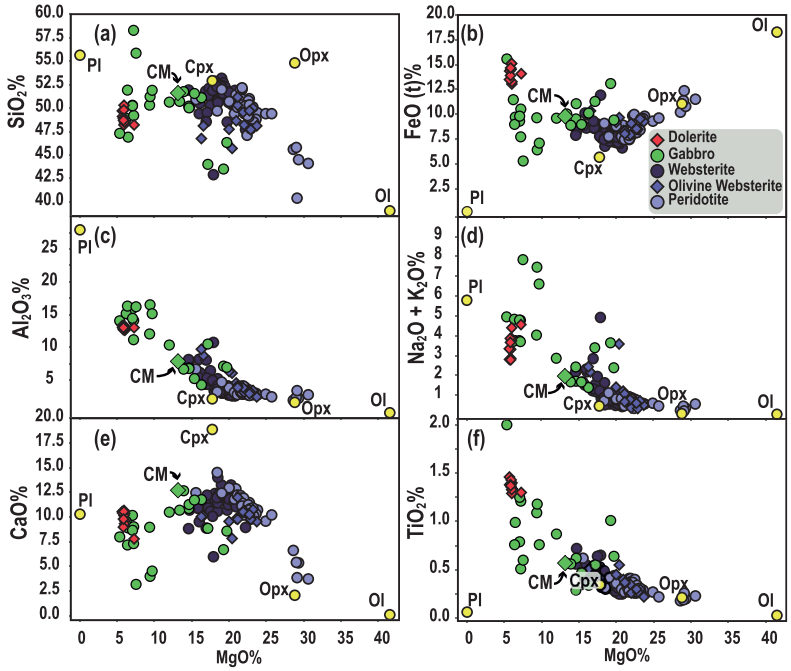

Fig. 8. Major and minor whole-rock Fenner diagrams (wt%) for rocks of the Gallujavri intrusion. Filled yellow and labelled circles mark average mineral EPMA analyses. Pl, plagioclase; Cpx, clinopyroxene; Opx, orthopyroxene; Ol, olivine.

Ernst & Jowitt, 2013, consistent with the proposed models for the Palaeoproterozoic komatiites in the KCLGB (Barnes & Often, 1990; Puchtel *et al.*, 1998; Hanski *et al.*, 2001a; Puchtel *et al.*, 2020).

The high potential temperature of komatiitic melts makes them highly susceptible to contamination by crustal material (Huppert & Sparks, 1985). As noted previously, the KCLGB komatiites are characteristic in that they are enriched in Ti and other high field strength elements relative to typical komatiites (Barnes & Often, 1990; Hanski *et al.*, 2001a). Barnes & Often (1990) dismissed crustal assimilation to explain the Ti- and LREE enrichment of the

Table 3: Whole-rock averages for different lithologies in weight percent (wt%) oxides (+LOI) and parts per million (ppm) elemental traces

	Arenite		Dolerite		Gabbro		Websterite		OlWeb		Peridotite	
	$N = 7$	2σ	$N = 11$	2σ	$N = 10$	2σ	$N = 8$	2σ	$N = 6$	2σ	$N = 18$	2σ
SiO_2	65.5	10.7	48.9	1.3	48.3	5.4	49.5	5.5	48.0	2.5	48.0	5.7
Al_2O_3	15.82	3.74	12.97	0.46	11.09	8.10	4.55	5.12	4.48	4.45	3.07	1.95
$Fe_2O_3{}^T$	6.80	3.43	15.77	1.48	12.28	4.13	9.97	3.30	10.45	1.26	10.78	2.59
CaO	2.60	3.12	9.82	1.68	9.64	3.39	10.79	4.23	9.76	1.96	9.56	6.29
MgO	2.10	1.92	6.01	0.82	11.27	10.12	19.09	3.58	21.46	4.87	23.97	8.07
Na_2O	3.27	2.39	2.75	0.69	2.23	2.12	0.67	0.64	0.62	1.07	0.47	0.48
K_2O	1.88	1.24	0.81	0.69	1.14	1.50	0.75	2.51	0.65	2.35	0.12	0.17
Cr_2O_3	0.029	0.010	0.011	0.004	0.173	0.429	0.502	0.320	0.453	0.249	0.562	0.218
TiO_2	0.72	0.58	1.37	0.10	0.91	0.98	0.36	0.23	0.33	0.22	0.28	0.19
MnO	0.06	0.07	0.25	0.06	0.16	0.05	0.16	0.02	0.17	0.07	0.18	0.03
P_2O_5	0.06	0.05	0.11	0.01	0.08	0.09	0.02	0.01	0.02	0.02	0.02	0.03
LOI	1.27	0.46	0.76	1.06	1.45	1.09	2.54	1.55	3.01	2.90	2.54	4.39
Total	100.18	1.01	99.62	1.71	98.75	3.22	98.89	1.69	99.38	1.16	99.54	1.85
Cs	2.38	1.50	0.26	0.17	1.83	5.06	1.17	3.80	1.62	6.20	0.23	0.22
Rb	80	38	24	27	43	81	28	98	30	121	4	6
Ba	514	457	228	170	275	218	137	400	98	313	36	45
Th	7.73	3.60	0.90	0.13	1.85	1.81	0.93	2.63	0.36	0.36	0.38	0.36
U	1.87	1.06	0.30	0.04	0.56	0.35	0.33	0.26	0.19	0.19	0.12	0.10
Nb	6.8	3.6	5.0	0.6	2.3	2.2	0.8	1.1	0.7	0.8	0.7	2.0
La	26.6	18.7	7.2	0.5	8.6	8.8	2.6	5.1	2.5	4.8	2.2	2.3
Ce	51.2	34.1	16.7	1.3	17.9	16.2	5.6	9.9	4.7	6.9	4.6	4.7
Pb	5	6	4	4	9	19	4	7	4	8	5	11
Pr	6.06	3.81	2.47	0.16	2.40	2.03	0.83	1.13	0.65	0.68	0.67	0.64
Sr	252	126	152	31	171	226	21	27	42	81	33	40
Nd	22.7	13.9	11.9	1.1	10.9	8.9	4.0	4.0	3.1	2.3	3.2	2.8
Sm	3.80	2.17	3.21	0.35	2.63	2.28	1.15	0.83	0.95	0.53	0.85	0.71
Zr	197	131	76	6	85	73	27	36	41	98	18	16
Hf	5.4	3.4	2.3	0.3	2.4	2.0	0.7	0.9	1.1	2.2	0.6	0.5
Eu	1.02	0.49	1.12	0.22	0.91	0.74	0.33	0.22	0.30	0.21	0.27	0.23
Gd	3.29	1.85	3.80	0.54	3.07	2.79	1.35	0.78	1.06	0.44	1.04	0.70
Tb	0.47	0.22	0.67	0.08	0.48	0.44	0.22	0.10	0.19	0.06	0.17	0.11
Dy	2.62	1.55	4.11	0.41	2.76	2.30	1.36	0.64	1.07	0.34	1.01	0.69
Li	13	9	15	13	14	10	20	28	15	10	10	n/a
Y	14.5	8.1	23.4	2.2	14.7	12.5	7.1	4.1	5.9	2.4	5.2	3.3
Ho	0.53	0.26	0.92	0.07	0.54	0.46	0.29	0.17	0.22	0.08	0.20	0.13
Er	1.43	0.72	2.56	0.30	1.48	1.28	0.77	0.51	0.60	0.19	0.54	0.34
Tm	0.21	0.09	0.37	0.05	0.21	0.18	0.12	0.07	0.08	0.03	0.08	0.06
Yb	1.28	0.44	2.33	0.21	1.17	0.75	0.60	0.56	0.52	0.23	0.45	0.29
Lu	0.20	0.08	0.37	0.06	0.19	0.13	0.11	0.08	0.08	0.04	0.07	0.05
Ga	21.01	5.98	18.30	2.15	17.16	12.31	7.73	7.34	7.27	5.72	5.35	2.72
V	143	137	377	19	250	221	106	104	94	57	62	64
Co	28	21	53	4	76	64	78	61	80	16	99	48
Cu	50	71	145	85	621	1928	606	1298	211	276	463	1743
Ni	81	42	56	12	653	1738	889	577	714	233	1155	987
Sc	14	7	43	2	26	18	33	6	27	11	28	14
Zn	54	46	94	32	81	55	60	13	55	16	53	22

2σ represent the population's standard deviation; if $N < 2$, σ is not applicable (n/a).
OlWeb, olivine websterite.

Karasjok komatiites as crustal material is too SiO_2-rich and has too high Al_2O_3/TiO_2 ratios. Later, Hanski (2001a) confirmed that the same conclusions apply to the komatiites and picrites of Jessiörova and the Peuramaan area of Finnish Lapland.

Based on the available regional geological, geochronological and geochemical data, we hypothesise the following:

(1) The spatial and temporal links between the Gallujavri ultramafic intrusion and the subaerial komatiites of the KCLGB imply that they form a cognate magma system. We hypothesise that the Gallujavri intrusion represents part of the volcanic plumbing system that fed the overlying volcanic rocks.

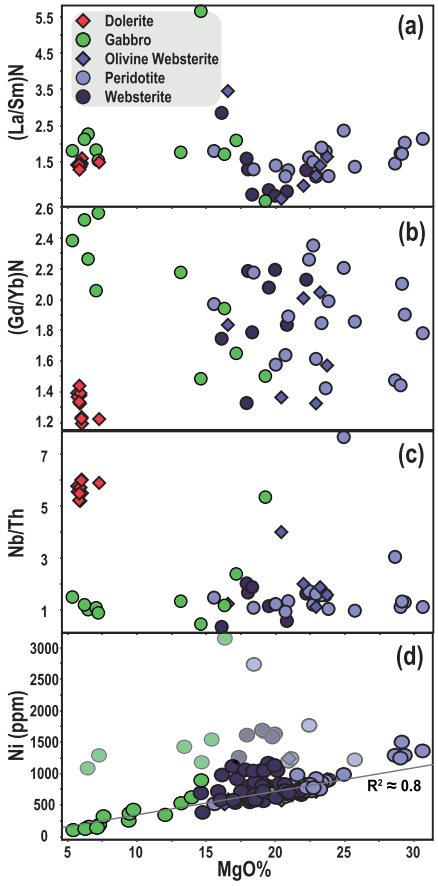

Fig. 9. REE chondrite-normalised (Boynton, 1984) ratios, Nb/Th ratio and Ni (ppm) vs MgO (wt%) for rocks of the Gallujavri intrusion. The Ni vs MgO diagram includes a least-squares linear regression line of the highlighted samples with a slope of 45.7 and intercept of 143.9 ($R^2 = 0.77$).

(2) There is clear evidence of contamination in the primitive mantle-normalised multi-element patterns, such as enrichment in LILE and LREE with positive U and Pb and negative Nb–Ta, Ti and Eu anomalies. Moreover, the stratigraphically uniform and consistently low Nb/Th-values indicate that the assimilation occurred in a staging magma chamber, where melts were partly homogenised before further ascent.
(3) A polybaric evolution is implied from our pressure estimates (Fig. 7a) that show a cluster at 400 MPa and a tail towards 700 MPa.

In the following, we present models to test these hypotheses. We subdivide our model into two stages (Fig. 11). In the first stage, we will test whether the Palaeoproterozoic komatiites of the KGB, as documented by Barnes & Often (1990), represent an analogue to the parental melt of the Gallujavri intrusion. Here, our goal is to model mineral chemistry and to examine whether AFC at 700 MPa can produce an evolved melt consistent with our CM (cf. sample 199 610; Fig. 4b).

The second stage is to model the mineral chemistry and liquid evolution of more evolved mafic whole-rock samples using the CM as the starting composition. The second-stage model assumes that the later assimilation and fractionation occurred at 400 MPa, as indicated by our pressure estimates.

Parental melt composition

The high MgO contents of the Karasjok komatiites imply high degrees of mantle melting, thus they probably approach the mantle source composition. The primitive nature and the interpretation that the Karasjok komatiites are negligibly affected by assimilation and crystal fractionation *en route* to the subsurface (Barnes & Often, 1990) make them an ideal starting composition for our models.

The primitive melt composition used in the first-stage model is taken from the geochemical data reported for three komatiitic pillow lavas in the KGB (Barnes & Often, 1990; X [M4383, DAT1/5, DAT1/8]). M4383 represents pillow lava from a 10-m-thick flow, DAT1/8 pillow interior from a 15-m-thick flow and DAT1/5 from the same pillow but at the rim. The samples are thought to represent liquid compositions as the compositions of pillow interiors and rims are similar. There is, however, evident secondary alteration with elevated $H_2O + CO_2$ concentrations ranging between c. 10% and 16%. Elements with low ionic potential, such as Rb^+, K^+, Na^+, Sr^{2+}, Eu^{2+} and Ca^{2+}, are the most susceptible to alteration in komatiites (Beswick, 1982; Ludden *et al.*, 1982; Barnes, 1985; Barnes & Often, 1990), and the three samples display irregular behaviour concerning most of these elements in mantle-normalised plots (Barnes & Often, 1990).

The parental melt (M) used as the starting composition in the first stage is the average of the three samples ($\bar{x}$; Table 4), the exceptions being H_2O, Eu (maximum value) and Sr (minimum value). Two of the samples have negative Eu anomalies that are most likely due to secondary alteration (Sun & Nesbitt, 1978; Hanski *et al.*, 2001a). There is also variation in the LILE concentrations (e.g. Sr), probably due to enrichment related to hydrothermal alteration (Frey & Green, 1974; Sun & Nesbitt, 1978).

Since the Fe oxidation state is undetermined, we calculated the Fe^{2+}/Fe^t ratio relative to the QFM buffer at the model pressure (700 MPa) and liquidus temperature ($T^{\bar{x}}_0 = 1698°C$, see below) using the MELTS_Excel interface (Gualda & Ghiorso, 2015) – no oxygen redox buffer was used in the runs themselves.

The volatile content of the parental melt is also unknown and there is much debate regarding the volatile budget of komatiites. Many maintain that komatiitic lavas were essentially dry, while others assert that komatiites contained several wt% water, in effect drastically reducing eruption temperatures (Arndt *et al.*, 1998; Sobolev *et al.*, 2016). As the Palaeoproterozoic komatiites of the KCLGB most likely have a mantle plume origin (Barnes & Often, 1990; Puchtel *et al.*, 1998; Hanski *et al.*, 2001a; Puchtel *et al.*, 2020), we used an H_2O/Ce-ratio of c. 600 ($\bar{x}$ $H_2O = 0.2\%$), which is about average between MORBs and the ranges documented for continental flood basalts (Karoo, Tarim, Snake River Plain and the Permian Emeishian LIP; Heinonen *et al.*, 2019, Liu *et al.*, 2017).

In the second stage, the CM was used as the starting melt (Table 5). Like the first stage, the Fe oxidation state is undetermined. We computed the redox state relative to the QFM buffer as we did before, but at the estimated liquidus temperature of the CM ($T^{CM}_0 = 1273°C$, see below) at 400 MPa. Although we determined

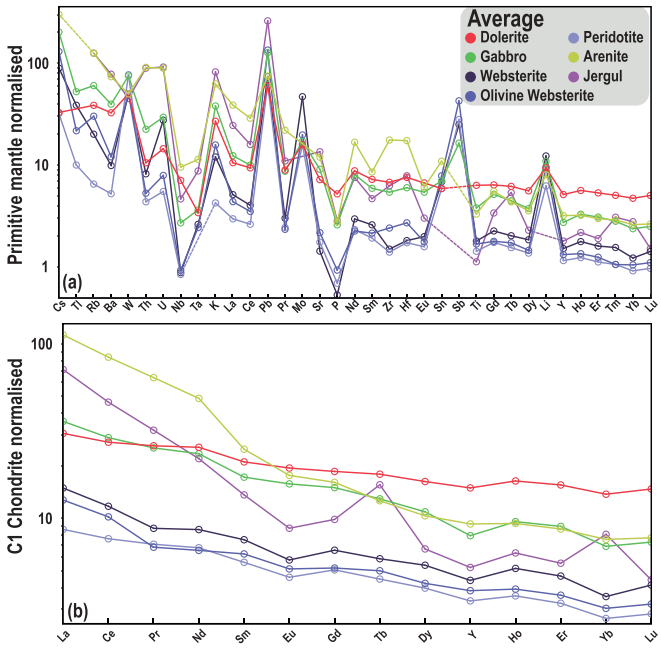

Fig. 10. (a) Multi-element primitive mantle-normalised (Sun & McDonough, 1989) diagram showing average compositions of the different rock types. (b) REE C1 Chondrite-normalised diagram for average compositions of the different rock types (Sun & McDonough, 1989).

the loss on ignition (LOI) during our whole-rock analysis (CM LOI =0.81), we normalised the oxide composition with 1 wt% water. This assumption is justified because the modelled melt compositions in stage 1 are in that range of water concentrations at similar MgO contents as the CM.

Plagioclase, orthopyroxene and clinopyroxene must be stable under this modelling stage, as indicated from petrography and the c. 400 MPa Mg–Fe equilibrium. However, orthopyroxene is not a liquidus phase of our CM at this pressure. In order to stabilise orthopyroxene in this stage, there must be an addition of a melt of different composition, therefore at 1050°C, 75 mass units (m.u.) of $\bar{x}$ (i.e. stage 1 parental melt) is recharged (Fig. 11), consistent with the presence of inferred komatiitic stage 1 parental melt erupting at the surface.

Mineral–melt partition coefficients in both stages were collected from the EarthRef database (https://earthref.org/KDD) for mafic to ultramafic melt compositions. When partition coefficient data were missing, the value was set as the MCS default or 1. The partition coefficients are listed in the MCS output files, and the individual references can be found in Supplement 7.

Wall-rock compositions

In the first stage, the source of crustal contamination is assumed to be that of the Jergul Complex, represented by sample 127 363 (Table 4). The Jergul Complex is an Archaean cratonic block of Karelian affinity, made of variably gneissic TTG plutonic rocks formed between 2975 ± 10 and 2776 ± 6 Ma (Bingen *et al.*, 2015). Sample 127 363 is a weakly peraluminous normative granodiorite. When used as the WR composition, the sample was normalised with a Fe oxidation state related to the QFM buffer close to the solidus temperature (780°C) at the model pressure of 700 MPa and a water concentration of 0.4 wt%.

In the second stage, the crustal contaminant is assumed to be the arenite host to the Gallujavri intrusion. The WR was initialised as the average of the arenitic samples documented in this study. The average was then normalised with a Fe oxidation state calculated as before (685°C, 400 MPa) and 1 wt% water.

The partition coefficients for the wall rock in both stages were collected from the EarthRef database for listed felsic compositions. The MCS output files show the partition coefficients and the individual references can be found in Supplement 7.

Pressure, temperature and mass constraints

As discussed above, we assume a polybaric evolution of the system, the first stage with a pressure of 700 MPa, representing a depth of c. 25 km assuming a crustal density of 2800 kg/m^3, and the second stage at 400 MPa (depth of c.15 km). In the first stage, the wall-rock temperature was initially at 700°C ($T_{solidus}$ ~ 780°C), giving a close-to-average crustal geothermal gradient of ~28°C/km. In the second stage, the wall rock was initially at 650°C ($T_{solidus}$ ~ 685°C), giving a geothermal gradient of ~46°C/km. We assume that previous magma pulses had already heated the wall rocks before the second stage.

In our models, the mass of the parental melt was always set to 100 m.u. (default) and the wall-rock masses in stages one and two were set to 300 m.u. Our hypothesised polybaric conduit system

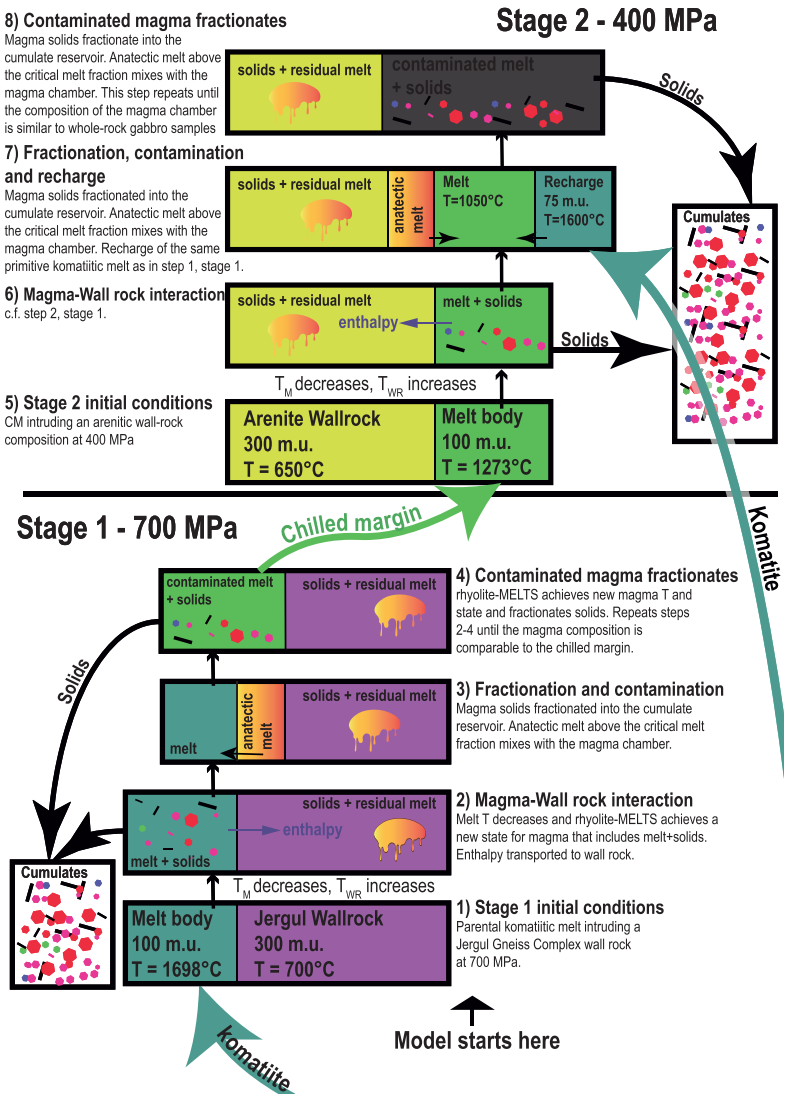

Fig. 11. Schematic illustration of the petrogenetic model, modified from Bohrson *et al.* (2014). m.u., mass unit.

suggests that the magma could have a high surface area towards heated crustal material (e.g. magma pipe). In total, along the transport direction, the surface would release a relatively high proportion of low-degree anatectic melt. The chosen masses mean that the heat available from the initial melt can thermally interact with three times as much wall-rock mass as the original intruding magma (i.e. $\Lambda = 3$). A mass ratio of three is justified because the surface-to-volume ratio increases with divergence from a sphere, increasing reactivity. Also, the enthalpy generated by the crystallisation of mafic mineral phases (spinel, olivine, clinopyroxene) is higher by a factor of two than the fusion enthalpy of the felsic phases in the wall rock (Bohrson *et al.*, 2020).

As in all modelling-based studies, the results obtained are variably contingent on a range of assumptions and choices of conditions and parameters. Therefore, such a study would not be complete without assessing the significance of these assumptions and choices on the

Table 4: Stage 1 parental melt (M) and wall-rock (WR) compositions and parameters

	M ($\bar{x}$)		WR (127363)
SiO_2	43.6		75.7
TiO_2	0.8		0.3
Al_2O_3	6.3		10.8
Fe_2O_3	2.3		0.8
Cr_2O_3	0.5		0.005
FeO	9.9		2.7
MnO	0.2		0.04
MgO	25.3		2.0
NiO	0.2		0.002
CoO	0.01		0.001
CaO	10.5		2.0
Na_2O	0.1		3.3
K_2O	0.02		1.8
P_2O_5	0.04		0.1
H_2O	0.2		0.4
Sc	27.6		8.8
V	314		50.8
Rb	2.5		58.1
Sr	75*		160
La	0.6		15.4
Ce	3.4		27.7
Nd	2.8		11.9
Sm	1.4		3
Eu	0.38**		0.7
Tb	0.3		0.6
Ho	0.3		0.6
Lu	0.1		0.2
Hf	0.8		3
Th	0.1		8.3
	FC: Melt	Wall rock	AFC: Melt
Pressure (MPa)	700	700	700
Mass (m.u.)	100	300	
Decrement, ΔT(°C)	20		20
Initial wall-rock T (°C)		700	
FmZero		0.05	

The parental melt (M) represents the average ($\bar{x}$) of three pillow komatiite samples (X = DAT 1/5, DAT 1/8, M4383) and a Jergul Gneiss Complex wall rock. The exception from the average includes *MIN(X) and **MAX(X). All oxides are reported in wt%, and all trace elements are reported in ppm.

model results. To this end, supplement 8 presents a sensitivity analysis in which we show and discuss the effects of varying the model inputs.

Modelling results

Stage 1 (700 MPa)

Supplement 9 presents the modelled cumulate stratigraphy. Modelled major element compositions are presented in Fig. 12 and trace element compositions in Fig. 13.

The parental magma initially has a liquidus temperature of $T^M{}_0 \sim 1698°C$; upon cooling, olivine and spinel crystallise at a ratio of c. 23:1. When the melt has cooled to a temperature of 1460°C, the melt fraction of the wall rock exceeds the percolation threshold of 0.05, releasing 2.93 m.u. of anatectic melt to the magma chamber.

Relative to FC-only models, the addition of anatectic melt increases the SiO_2 and H_2O of the magma chamber melt and decreases MgO and FeO. Another essential feature is that the addition of Si from the wall rock to the resident magma stabilises orthopyroxene, which starts to crystallise at 1374°C. Clinopyroxene stabilises at 1298°C. When the resident magma has a temperature of 1278°C and MgO = 11.4 wt% (cf. CM MgO = 12.0 wt%), the melt has assimilated about 15 m.u. of anatectic melt.

The modelled trace element concentrations presented in Fig. 13 represent the model interval (12–18 wt% MgO; 1298–1410 T^M(°C)) highlighted by orange ticks in Fig. 12. Figure 13a shows that there is a general agreement between the composition of the CM and the model melts of stage 1, although modelled concentrations of Rb, Th K, Hf and Ti are somewhat too high. These features are also evident in Fig. 13b but with a good overall match with the observed La/Lu trend.

The transition metals show more significant deviations (Fig. 13c), and although the primitive mantle-normalised modelled patterns are

Table 5: Stage 2 parental melt (M), wall rock (WR) and recharge (R) compositions and parameters

	M (199610)	WR (Arenite)	R ($\bar{x}$)
SiO_2	47.2	63.8	43.4
TiO_2	0.5	0.6	0.8
Al_2O_3	7.2	15.0	6.3
Fe_2O_3	2.7	2.5	2.9
Cr_2O_3	0.1	0.03	0.5
FeO	15.5	8.4	9.3
MnO	0.2	0.04	0.2
MgO	12.0	1.6	25.3
NiO	0.1	0.01	0.2
CoO	0.01	0.003	0.01
CaO	11.6	2.0	10.4
Na_2O	1.2	3.1	0.1
K_2O	0.6	1.9	0.02
P_2O_5	0.04	0.1	0.04
H_2O	1.0	1.0	0.5
Sc	43	14	28
V	258	143	314
Rb	27	80	3
Sr	109	252	75
La	5	27	1
Ce	11	51	3
Nd	8	23	3
Sm	2	4	1
Eu	1	1	0.4
Tb	0.4	0.5	0.3
Ho	0.5	1	0.3
Lu	0.2	0.2	0.1
Hf	2	5	1
Th	1	8	0.1

	FC: Melt	Wall rock	AFC: Melt	
Pressure (MPa)	400	400	400	
Mass (m.u.)	100	300		75
Decrement, ΔT(°C)	20		20	
Initial wall-rock T (°C)		650		
Initial recharge T (°C)				1600
Recharge trigger T(°C)				1050
FmZero		0.05		

The parental melt is initialised with the CM (i.e. sample 199 610), the wall rock is the average arenites and the komatiite from Sarah Jane Barnes & Often (1990) recharge magma.
All oxides are reported in wt%, and all trace elements are reported in ppm.

similar to the CM, the concentrations do not entirely overlap. We note that K, Ti, Cr, Mn, Fe, Co and Ni concentrations of the model melt are calculated based on the mineral end-member thermodynamic components specified in rhyolite–MELTS (v.1.2.x; Ghiorso & Gualda, 2015, Gualda *et al.*, 2012) and not by selecting temperature-independent partition coefficients.

Stage 2 (400 MPa)

Supplement 10 shows a model overview with the resulting cumulate stratigraphy. Figure 14 shows the major element compositions of the modelled liquid line of descent together with the modelled incremental bulk cumulates, and Fig. 15 shows the primitive mantle-normalised model result together with model members and evolved mafic samples.

Initiation of the model is with a liquidus temperature of $T^{M}_{0} \sim 1273°C$, crystallising clinopyroxene, olivine and minor spinel as it cools. When the melt has cooled to c. 1150°C, the wall-rock melt fraction passes the percolation threshold and releases 9.2 m.u. of anatectic melt to the magma chamber, increasing the saturation of spinel.

When the magma chamber has cooled to 1050°C, a recharge event is triggered, adding 75 m.u. of primitive komatiitic melt (i.e. $\bar{x}$) to the chamber. The heat supplied by the recharged liquid increases the chamber temperature to 1333°C, which provides more heat to the wall rock. When the magma again cools to a temperature of

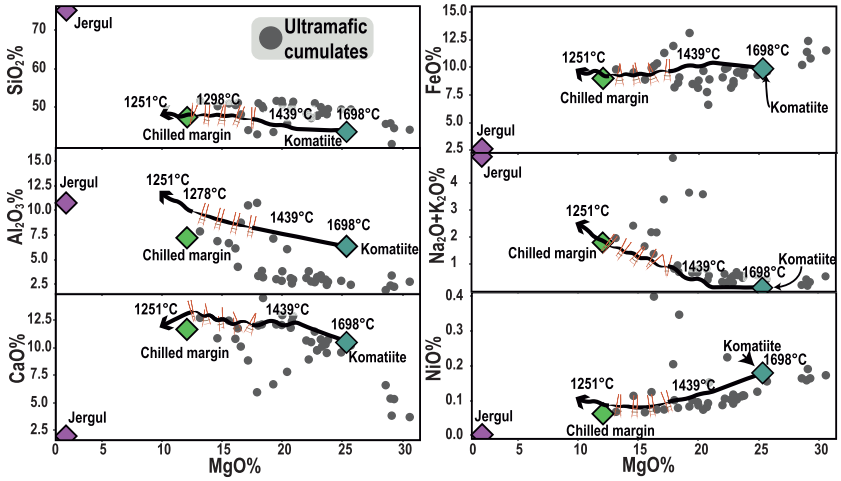

Fig. 12. Results from the MCS–PhaseEQ 700 MPa AFC simulation presented as wt% oxide Fenner diagrams. The black line represents the liquid line of descent that starts at the assumed komatiitic parental melt and evolves towards lower MgO concentrations. The orange ticked section (12–18 wt% MgO; 1298–1410 T^{M}(°C)) represents the range that has compositions comparable to the CM of the Gallujavri intrusion (cf. sample 199 610). Figure 13 presents normalised trace elements from this section.

1167°C, it has digested c. 48 m.u. of the wall rock and orthopyroxene crystallises together with spinel.

From 1143°C to when the system reaches thermal equilibrium at c. 1005°C, orthopyroxene, clinopyroxene and spinel co-precipitate. At thermal equilibrium, the magma in the chamber (i.e. M + R) has assimilated c. 79 m.u. of wall rock. The continued FC of the liquid leads to saturation of plagioclase at c. 947°C, rhombohedral (Rhm)-oxides (ilmenite) at c. 897°C and biotite at 727°C.

As demonstrated in the Fenner diagrams in Fig. 14, the liquid line of descent shows suitable matches with the mafic samples for SiO_2, CaO and the alkalis ($Na_2O + K_2O$) for comparable MgO concentrations. In the Al_2O_3 diagram, the mafic samples correlate better with the modelled liquid after the recharge event. The NiO liquid line of descent flattens out both for the initial magma and the recharged hybrid at a higher concentration than the whole-rock mafic samples and dolerites. The premature termination of crystallising olivine in the model could explain this feature or that MELTS does not include any Ni-sulphide phases. Stage 2 cumulates (pink in Fig. 14) show a good correlation in all the plots; one exception is that the simulations do not stabilise a significant potassium-bearing phase.

There is general agreement between the highlighted MCS liquid in Fig. 14 and the primitive mantle-normalised trace elements in Fig. 15. In Fig. 15a, there are similar patterns between the whole-rock evolved mafic samples and the MCS liquid. There are some differences, notably too low Sr and Ti in the MCS liquid.

The REEs in Fig. 15b have similar fractionation trends in both the MCS liquid and the whole-rock mafic samples, but with slight relative depletion of Sm and Eu in the MCS liquid. The minor positive europium anomaly exhibited by the mafic samples might be an effect of plagioclase accumulation. In Fig. 15c, the patterns are similar in the transition metal plot, but the gabbros are more depleted in Sc, Cr, Mn, Fe, Co and Ni and more enriched in Ti and V relative to the MCS liquid.

Mineral chemistry (stages 1 and 2)

Figures 16 and 17 show the modelled MCS mineral chemistries with mineral EPMA data. In Fig. 16, olivine, clinopyroxene, orthopyroxene and feldspar are presented graphically as Harker diagrams. Figure 17 presents the spinels and Rhm-oxides (i.e. ilmenite) in a TiO_2–FeO–Fe_2O_3 ternary diagram (Fig. 17a) and the spinels in Fe^{3+}–Cr–Al ternary and TiO_2 vs xFe^{3+} binary diagrams (Fig. 17b, c). In all the figures, grey symbols represent model compositions at 700 MPa (stage 1) and black symbols at 400 MPa (stage 2).

In the Harker diagrams in Fig. 16, the MCS phases replicate the observed major element compositions. The Fo content of the most primitive olivine crystallised at 700 MPa is 93% and terminates when the liquid reaches 1354°C, with Fo_{90}. The MCS pyroxenes show a good overlap with the major element data. In the TiO_2-diagram, the modelled clinopyroxene compositions are close but only touch the observed trend. In the model, only feldspar crystallised in stage 2, after thermal equilibrium with the wall rock. The modelled feldspar compositions overlap well with Al_2O_3, CaO and Na_2O of the most primitive plagioclase data but with a slight relative enrichment in K_2O (not shown in Fig. 16).

The first spinels in both the 700 and 400 MPa cases start as Al-chromite, overlapping with our EPMA data (Fig. 17a, b). Not represented in our spinel data is the subsequent evolution along the ulvöspinel–magnetite tie-line (Fig. 17a). Our measured ilmenite mineral chemistry is comparable to the modelled Rhm-oxide MELTS phase, plotting close to the ilmenite end-member in Fig. 17a. Plots with the compositional fields of Barnes & Roeder (2001) show a similar Fe–Ti trend commonly developed by chromite crystallised from parental komatiitic melts (Fig. 17b, c). However, in Fig. 17b, the modelled spinel composition diverges and crosses the empirical spinel gap for chromite in mafic and ultramafic rocks (Barnes & Roeder, 2001). This divergence is interpreted as a combination of Al loss with metamorphism (Barnes & Roeder, 2001) and a MELTS spinel thermodynamic calibration that is slightly off.

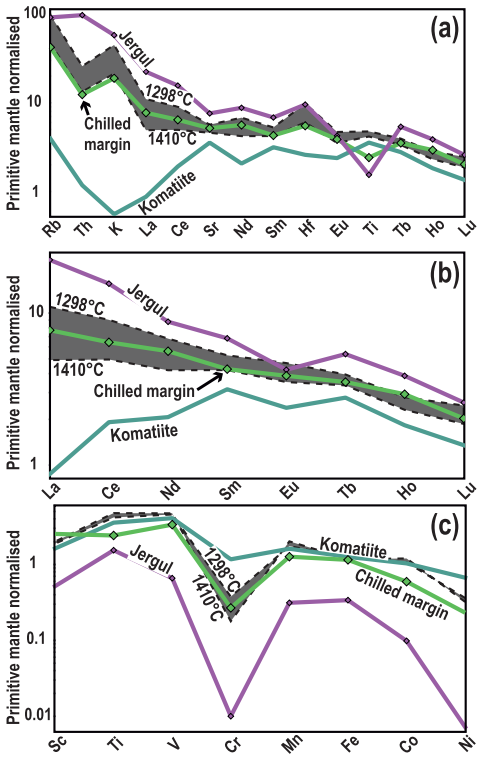

Fig. 13. The MCS–PhaseEQ 700 MPa AFC simulated liquid for the temperature range 1298–1410°C (grey field; cf. orange ticked line in Fig. 12), together with the assumed parental komatiite, Jergul Complex wall rock and Gallujavri CM. (a) Multi-element primitive mantle-normalised diagram (Sun & McDonough, 1989). (b) REE primitive mantle-normalised diagram (Sun & McDonough, 1989). (c) Transition metals primitive mantle-normalised diagram (Jagoutz *et al.*, 1979).

Implications for petrogenesis

With our defined assumptions, the overall petrological evolution of the Gallujavri intrusion replicates well with a polybaric, parental komatiite, RAFC model, which corroborates our thermobarometric data. The chemical features, such as LILE enrichment, can be explained by crustal contamination. There is, however, uncertainty as to at what crustal level the contamination occurred. The arenitic host of the Gallujavri intrusion consists of material likely derived from the Jergul Complex, giving them similar chemical features, especially regarding the LILE elements (Fig. 10a), thus identifying one or the other as the main contaminant is difficult.

The model indicates that the Gallujavri intrusion represents an open magmatic system requiring at least one recharge event to stabilise orthopyroxene at 400 MPa. There is some ambiguity as to the number and composition of the recharge(s). Based on our polybaric model, we can envision a range of possible magma-evolution scenarios. For example, the composition of the recharging melt could range from undifferentiated primitive to differentiated anywhere in the section between 400 MPa and the mantle source, or a combination. The modelling, however, shows that the recharging melt must be considerably different from the stage-2 starting composition to alter the modelled evolution trend substantially from pure FC. We chose a primitive 'undifferentiated' komatiitic melt as the recharging liquid, as at stage 2, the starting hybrid melt (i.e. CM) has diverged enough from the starting komatiite to uphold the criteria of being compositionally different.

Figure 18 summarises some of the key aspects of our petrogenetic model and is well in line with an emerging consensus of trans-crustal magma plumbing systems (Hildreth & Moorbath, 1988; Annen *et al.*, 2006; Cashman *et al.*, 2017; Ganne *et al.*, 2018; Magee *et al.*, 2018; Gualda *et al.*, 2019). Recent advances in geophysical techniques provide exciting insights into trans-crustal magma systems (Magee *et al.*, 2018). For example, in the 60-km-long Yellowstone caldera, USA, tomographic studies have imaged a large (c. 10^4 km^3) low-velocity body, 5–17 km deep and a c. 4.5 times larger lower-crustal body that acts as a link between the Yellowstone mantle plume and the shallower body (Farrell *et al.*, 2014; Huang *et al.*, 2015; Cashman *et al.*, 2017).

In our model, primitive melt first intrudes the lower crust where it perturbs the geothermal gradient creating a deep-crustal hot zone similar to models for arc environments (Annen *et al.*, 2006). When the surrounding crust exceeds the solidus, it begins to undergo partial melting, creating a hybrid melt that combines residual melts from the crystallisation of the komatiite and anatectic crustal melt. As in our model, the geothermal gradient or any localised thermal profile resulting from preceding injections would control the relative contribution of the different sources to the hybrid melt (Annen *et al.*, 2006).

In the second stage, the hybrid melt segregates from the lower-crustal reservoir and migrates to shallower crustal levels (Fig. 18). If the deeper reservoir has attained a mushy state (i.e. a system of interconnected crystals in a melt matrix), segregation requires porous media processes (Cashman *et al.*, 2017). Another possibility is that crystal segregation creates a strongly physically differentiated reservoir, resulting in a crystal poor and buoyant layer of hybrid melt (Annen *et al.*, 2006).

Once the hybrid melt intrudes the middle crust, the processes mirror those of the staging chamber (Fig. 18). The shallow chamber requires higher magma input rates to remain above the solidus as the ambient temperatures are lower (Annen *et al.*, 2006; Cashman *et al.*, 2017). To counteract this, our model proposes pre-heating the middle crust to maintain a molten Gallujavri chamber. However, the thermal requirement for maintaining middle-crustal non-eruptive crystal mushes, as opposed to a melt-rich magma chamber, are smaller (Cashman *et al.*, 2017).

The last stage in the petrogenesis of the Gallujavri intrusion is the recharge of primitive, uncontaminated komatiite. It may seem counterintuitive that melt passing through the same system should not be similarly affected by fractionation and assimilation; however, many Archaean greenstones and post-Archaean flood-basalt provinces exhibit komatiite or picrite flows cogenetic with fractionated basalts (Lister *et al.*, 1991). Furthermore, in our case, the coeval to slightly younger primitive extrusive komatiites within the KCLGB are suggestive of such a process. A possible explanation is the formation of a thermo-chemical insulator surrounding the lower- to mid-crustal plumbing system (Larsen *et al.*, 2018). For example, in the Reinfjord Ultramafic Complex, Seiland Igneous Province, Norway (Larsen *et al.*, 2018; Grant *et al.*, 2020), Grant *et al.* (2016) documented a reverse fractionation sequence whereby cumulates

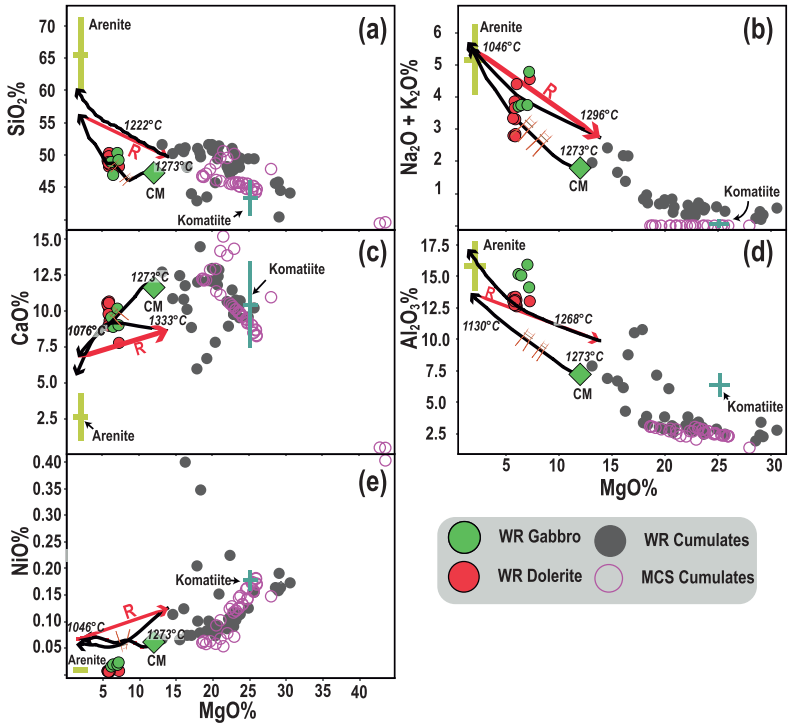

Fig. 14. Results from the MCS–PhaseEQ 400 MPa RAFC simulation presented as wt% oxide Fenner diagrams. The black line represents the liquid line of descent that starts at the composition of the CM and evolves towards lower MgO concentrations. The orange ticked section (6–9 wt% MgO; 1130–1193 T^M(°C)) represents the range that has compositions comparable to the evolved mafic samples that are assumed to approach liquid compositions. Figure 15 presents normalised trace elements from this section. The red vector labelled R indicates the **R**echarge event adding 75 m.u. of komatiitic melt to the system.

became progressively more MgO and olivine rich with time. This reverse trend was interpreted as resulting from contamination of the intrusion by the host gabbro-norite, evident in the marginal zones but limited in the central parts of the complex (Grant *et al.*, 2016; Grant *et al.*, 2020).

Our proposed multistage petrogenetic model for the Gallujavri intrusion does not serve as a unique example in the KCLGB, and similar models have been proposed for various ultramafic–mafic layered intrusions throughout its c. 400 Ma magmatic history. For example, our model resembles the petrogenetic model for the c. 2.44 Ga Akanvaara and Koitelainen mafic layered intrusions in northern Finland (Hanski *et al.*, 2001b; Hanski & Huhma, 2005). Hanski *et al.* (2001b) determined the Os isotopic compositions at different stratigraphic positions in the intrusions and found near-chondritic ratios with only slight variation and no systematic differences relative to stratigraphic position. Combined with Nd isotope systematics, Hanski *et al.* (2001b) proposed a model of deep-crustal assimilation (15%–25%), coupled with minor *in situ* assimilation of country-rock material.

Another example is the contemporary Kevitsa Complex (c. 2.06 Ga; Mutanen & Huhma, 2001). Here, Luolavirta (2018) proposed a multistage model with many parallels to the Gallujavri intrusion. The spatially confined but markedly different drill core lithological and compositional profiles inside and outside the Kevitsa ore domain led Luolavirta *et al.* (2018a) to suggest a model of multiple injections. During the first stage, the central dunite formed by accumulation in a picritic magma conduit; in the second stage, evolved basaltic liquid (fractionated at depth from the initial picritic melt) intruded through the same plumbing system (Luolavirta *et al.*, 2018a; Luolavirta *et al.*, 2018b). The third stage defines repeated injections of basaltic magma into the dynamically open, hot interior of the intrusion (Luolavirta *et al.*, 2018a; Luolavirta *et al.*, 2018b).

The polybaric and multistage model presented here is probably widely applicable to the petrogenesis of Palaeoproterozoic Fennoscandian (ultra)mafic intrusions and also a potentially effective mechanism for forming viable economic PGE Ni–Cu deposits. For example, the Ni–PGE ores of the Kevitsa intrusion, with a Ni tenor of 6%–60% (Luolavirta *et al.*, 2018b) and tens of ppm PGE (Maier & Groves, 2011), is believed to be the result of cannibalisation (assimilation) of proto-ores deposited in stage 2 by the repeated magma injections in stage 3 (Luolavirta, 2018). Thus, identifying this process using MCS modelling may be an important prospecting tool.

Although our hypothesis shows many petrogenetic similarities to many of the ore-hosting mafic–ultramafic intrusions of the

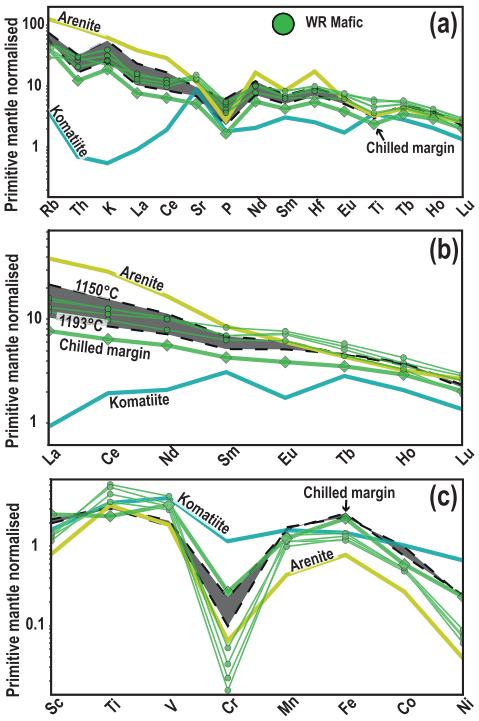

Fig. 15. The MCS–PhaseEQ 400 MPa RAFC simulated liquid for the temperature range 1130°C–1193°C (grey field; cf. orange ticked line in Fig. 14), together with evolved gabbroic samples that are assumed to approach liquid compositions (green circles), the arenite host rock, komatiite recharge and the starting liquid (i.e. CM). (a) Multi-element primitive mantle-normalised diagram (Sun & McDonough, 1989). (b) REE primitive mantle-normalised diagram (Sun & McDonough, 1989). (c) Transition metals primitive mantle-normalised diagram (Jagoutz *et al.*, 1979).

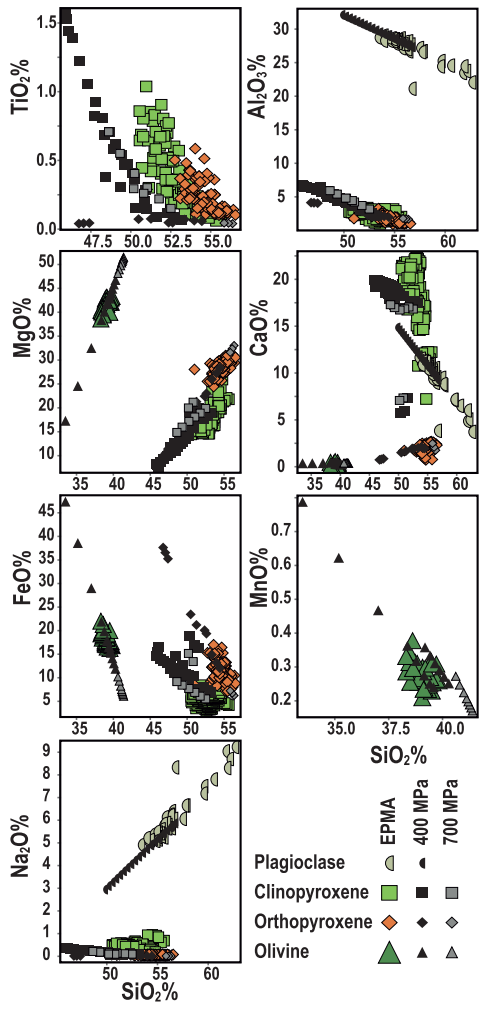

Fig. 16. Harker-type diagrams showing MCS–PhaseEQ mineral phase compositions for the 700 MPa AFC (grey) and 400 MPa RAFC (black) simulations. EPMA data are presented in colours.

Fennoscandian Shield, the size of the Gallujavri intrusion may be too small for hosting an economically viable ore (Nilsson & Often, 2009). Furthermore, there is no discernible correlation between NiO and MgO in our olivine data. These Ni contents are relatively high when considering the low Fo content and are inconsistent with crystallisation from a sulphur-saturated or Ni-depleted melt (Brenan & Caciagli, 2000). This interpretation is supported by the whole-rock NiO vs MgO (Fig. 9d), with the observed linear trends being inconsistent with a sulphur-saturated system in which immiscible sulphide melt scavenges Ni from the silicate melt. Another possibility is that if an immiscible sulphide liquid existed, restricted interaction with the silicate liquid would lower apparent sulphide–silicate liquid partition coefficients (i.e. low R-values; Campbell & Naldrett, 1979). On the other hand, both adjacent and remote intrusions of the same type as Gallujavri are poorly investigated (Nilsson & Often, 2009) and therefore represent attractive targets for further investigations into the petrogenesis and ore potential of the Palaeoproterozoic komatiitic magmatism in the KGB.

CONCLUSIONS

Uniform signs of crustal assimilation characterise the studied ultramafic Gallujavri intrusion. Combining the features of assimilation with the genetic indications of the spinel compositions, the polybaric thermobarometry and the spatial and temporal association with ultramafic volcanic rocks suggest that the Gallujavri intrusion is subvolcanic.

Based on previous geochronology and our modelling results, the parental magma of the intrusion is the Ti-rich Karasjok-type komatiite observed at various places within the Fennoscandian Shield. The komatiite intruded the Archaean lower crust (c. 700 MPa, depth of

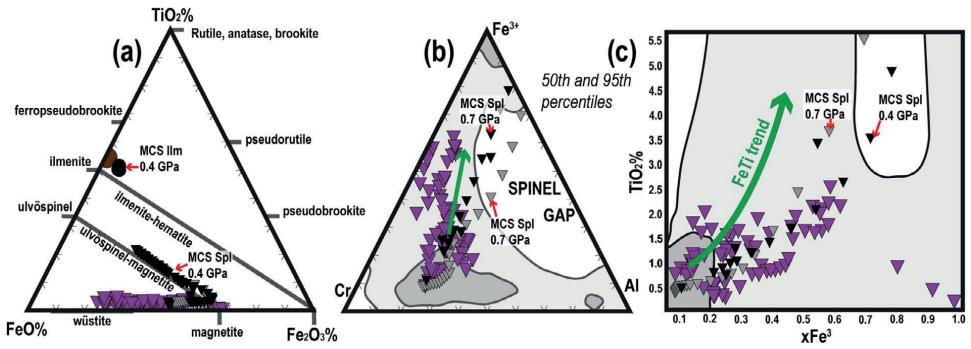

Fig. 17. Fe–Ti oxide mineral diagrams showing MCS–PhaseEQ mineral phase compositions for the 700 MPa AFC (grey) and 400 MPa RAFC (black) simulations. EPMA data are presented in colours. The contoured compositional fields and Fe–Ti trend (green arrow) in (b) & (c) from Barnes & Roeder (2001). (a) TiO_2–FeO–Fe_2O_3 ternary diagram showing the composition of the Fe–Ti oxides and the simulated phases. (b) Fe^{3+}–Cr–Al ternary diagram relating spinel compositions to the simulated phases. (c) TiO2 vs xFe^{3+} ($Fe^{3+}/(Cr + Al + Fe^{3+})$) diagram for spinel and simulated phases.

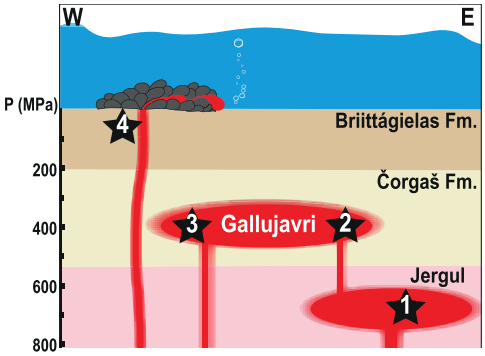

Fig. 18. Conceptual model illustrating a hypothesised trans-crustal magma plumbing system. Step 1: The dense komatiitic magma intrudes and stalls in the lower crust where the ambient temperature is high. Partial igneous differentiation occurs as the intruding melt heats the country rocks, assimilating anatectic melt of gneissic granodiorite and fractionating out solids. Step 2: The hybrid magma, expelled either by mush compaction or buoyancy, ascends to higher levels in the crust, leaving behind refractory cumulate rocks. The influx of heat pushes the host rock over the solidus, incorporating siliceous anatectic melt and fractionating out solids. Step 3: Recharge of primitive komatiite, either through the pre-established feeder or through intersecting dykes, stabilises orthopyroxene. Step 4: Trans-crustal dykes supply extrusive pillowed komatiite with little or no interaction with the crust.

c. 25 km), where fractionation and assimilation resulted in a hybrid melt consistent with the composition observed in the Gallujavri CM. Replication of our thermobarometric estimates and petrographic observations requires a second stage of recharge, assimilation and fractionation at middle crustal levels (c. 400 MPa, depth of c. 15 km).

Our modelling suggests that the Gallujavri intrusion is part of a complex and vertically extensive magmatic structure with many similarities to other Fennoscandian ultramafic–mafic layered intrusions. We interpret the Gallujavri intrusion to represent a Palaeoproterozoic example of a trans-crustal magmatic system, as defined by geophysical imaging of active magmatic plumbing structures elsewhere.

FUNDING

This study is a part of Alf Andre Orvik's PhD project on the Gallujavri intrusion in the Karasjok Greenstone Belt, funded by the Department of Geoscience and Petroleum, Faculty of Engineering, at the NTNU and the Geological Survey of Norway.

DATA AVAILABILITY STATEMENT

The data underlying this article are available in the article and in its online supplementary material.

ACKNOWLEDGEMENTS

We are thankful for the thoughtful reviews by Wolfgang Maier, Ville Järvinen and Wendy Bohrson. We acknowledge the past drilling program by Tertiary Gold Ltd., which is a prerequisite for this study. We further acknowledge Store Norske Gull AS for providing access to the company's geochemical assays and in-tray XRD scans. We are grateful to Kristian Drivenes, the operator of the microprobe at NTNU. We also want to acknowledge Øyvind Skaar at the Geological Survey of Norway for his help with the LA–ICP–MS analysis.

REFERENCES

Annen, C., Blundy, J. D. & Sparks, R. S. J. (2006). The genesis of intermediate and silicic magmas in deep crustal hot zones. *Journal of Petrology* **47**, 505–539.

Arndt, N., Ginibre, C., Chauvel, C., Albarède, F., Cheadle, M., Herzberg, C., Jenner, G., Lahaye, F. (1998). Were komatiites wet? *Geology* **26**, 739–742.

Ashchepkov, I. V., Pokhilenko, N. P., Vladykin, N. V., Rotman, A. Y., Afanasiev, V. P., Logvinova, A. M., Kostrovitsky, S. I., Pokhilenko, L. N., Karpenko, M. A., Kuligin, S. S., Malygina, E. V., Stegnitsky, Y. B., Alymova, N. A. & Khmelnikova, O. S. (2008) *Reconstruction of Mantle Sections Beneath Yakutian Kimberlite Pipes Using Monomineral Thermobarometry*. London: Geological Society of London, Special Publication, pp.335–352.

Ballhaus, C., Berry, R. F. & Green, D. H. (1990). Oxygen fugacity controls in the Earth's upper mantle. *Nature* 437–440.

Barnes, S.-J. (1985). The petrography and geochemistry of komatiite flows from the Abitibi Greenstone Belt and a model for their formation. *Lithos* **18**, 241–270.

Barnes, S. J. & Often, M. (1990). Ti-rich komatiites from Northern Norway. *Contributions to Mineralogy and Petrology* **105**, 42–54.

Barnes, S. J. & Roeder, P. L. (2001). The range of spinel compositions in terrestrial mafic and ultramafic rocks. *Journal of Petrology* **42**, 2279–2302.

Barsdell, M. (1988). Petrology and petrogenesis of clinopyroxene-rich tholeiitic lavas, Merelava volcano, Vanuatu. *Journal of Petrology* **29**, 927–964.

Beswick, A. (1982) Some geochemical aspects of alteration and genetic relations in komatiitic suites. In: (Arndt N. & Nisbet E. (eds)) *Komatiites*. London: Allen, pp.283–308.

Bingen, B., Solli, A., Viola, G., Torgersen, E., Sandstad, J. S., Whitehouse, M. J., Røhr, T. S., Ganerød, M. & Nasuti, A. (2015). Geochronology of the palaeoproterozoic kautokeino greenstone belt, Finnmark, Norway: tectonic implications in a fennoscandia context. *Norsk Geologisk Tidsskrift* **95**, 365–396.

Birner, S. K., Cottrell, E., Warren, J. M., Kelley, K. A. & Davis, F. A. (2018). Peridotites and basalts reveal broad congruence between two independent records of mantle fO2 despite local redox heterogeneity. *Earth and Planetary Science Letters* **494**, 172–189.

Blundy, J., Cashman, K. V. & Berlo, K. (2008). Evolving magma storage conditions beneath Mount St. Helens inferred from chemical variations in melt inclusions from the 1980–1986 and current (2004–2006) eruptions. US Geological Survey.

Boettcher, A., Mysen, B. O. & Modreski, P. J. (1975). Melting in the mantle: phase relationships in natural and synthetic peridotite–H2O and peridotite–H2O–CO2 systems at high pressures. In: Ahrens, L. H., Dawson, J. B., Duncan, A. R. & Erlank, A. J. (eds.) Physics and Chemistry of the Earth: Pergamon, 855–867.

Bohrson, W. A., Spera, F. J., Ghiorso, M. S., Brown, G. A., Creamer, J. B. & Mayfield, A. (2014). Thermodynamic model for energy-constrained open-system evolution of crustal magma bodies undergoing simultaneous recharge, assimilation and crystallization: the magma chamber simulator. *Journal of Petrology* **55**,1685–1717.

Bohrson, W. A., Spera, F. J., Heinonen, J. S., Brown, G. A., Scruggs, M. A., Adams, J. V., Takach, M. K., Zeff, G. & Suikkanen, E. (2020). Diagnosing open-system magmatic processes using the magma chamber simulator (MCS): part I—major elements and phase equilibria. *Contributions to Mineralogy and Petrology* **175**, 1–29.

Boyd, R., Bjerkgård, T., Nordahl, B. & Schiellerup, H. (2016) Mineral resources in the Arctic. Geological Survey of Norway.

Braathen, A. & Davidsen, B. (2000). Structure and stratigraphy of the Palaeoproterozoic Karasjok Greenstone Belt, North Norway - regional implications. *Norsk Geologisk Tidsskrift* **80**, 33–50.

Bradley, J. (2003) Finnmark Project, Diamond Drill Program - April 2003. In: *Summary and review*. Norwegian Directorate of Mining: Tertiary Gold Limited, p.14.

Brenan, J. M. & Caciagli, N. C. (2000). Fe-Ni exchange between olivine and sulphide liquid: implications for oxygen barometry in sulphide-saturated magmas. *Geochimica et Cosmochimica Acta* **64**, 307–320.

Brey, G. P. & Köhler, T. (1990). Geothermobarometry in four-phase lherzolites II. New thermobarometers, and practical assessment of existing thermobarometers. *Journal of Petrology* **31**(6), 1353–1378.

Burns, R. G. & Brown, G. E., Jr. (1982) Chapter 11. Olivines and silicate spinels. In: (Roger G. B. (ed)) *Orthosilicates*. De Gruyter, pp. 275–382.

Campbell, I. & Naldrett, A. (1979). The influence of silicate: sulfide ratios on the geochemistry of magmatic sulfides. *Economic Geology* **74**, 1503–1506.

Cashman, K. V., Sparks, R. S. J. & Blundy, J. D. (2017). Vertically extensive and unstable magmatic systems: a unified view of igneous processes. *Science* 355, eaag3055.

Cottrell, E., Birner, S., Brounce, M., Davis, F., Waters, L. & Kelley, K. (2021). Oxygen Fugacity Across Tectonic Settings. *AGU Geophysical Monograph*. In Magma Redox Geochemistry (eds R. Moretti and D.R. Neuville).

Deer, W. A.,. F. R. S., Howie, R. A. & Zussman, J. (2013) Spinel group. In: *An Introduction to the Rock-Forming Minerals*. Mineralogical Society of Great Britain and Ireland.

Duncan, R. A., Hooper, P. R., Rehacek, J., Marsh, J. S. & Duncan, A. R. (1997). The timing and duration of the Karoo igneous event, southern Gondwana. *Journal of Geophysical Research-Solid Earth* **102**, 18127–18138.

Erns, R. E. & Jowitt, S.M. (2013). Large igneous provinces (LIPs) and metallogeny. *Society of Economic Geologists Special Publication* **17**, 17–51.

Farrell, J., Smith, R. B., Husen, S. & Diehl, T. (2014). Tomography from 26 years of seismicity revealing that the spatial extent of the Yellowstone crustal magma reservoir extends well beyond the Yellowstone caldera. *Geophysical Research Letters* **41**, 3068–3073.

Frey, F. A. & Green, D. H. (1974) The mineralogy, geochemistry and origin of Iherzolite inclusions in Victorian basanites. *Geochimica et Cosmochimica Acta* **38**, 1023–1059.

Frost, B. R. (1991) Introduction to oxygen fugacity and its petrologic importance. *Reviews in Mineralogy and Geochemistry* **25**, 1–9.

Frost, D. J. & McCammon, C. A. (2008). The redox state of Earth's mantle. *Annual Review of Earth and Planetary Sciences* **36**, 389–420.

Ganne, J., Bachmann, O. & Feng, X. (2018). Deep into magma plumbing systems: interrogating the crystal cargo of volcanic deposits. *Geology* **46**, 415–418.

Ghiorso, M. S. & Gualda, G. A. R. (2015) An H2O–CO2 mixed fluid saturation model compatible with rhyolite-MELTS. In: *Contributions to Mineralogy and Petrology*. Springer, p.53.

Ghiorso, M. S., Hirschmann, M. M., Reiners, P. W. & Kress, V. C. (2002). The pMELTS: a revision of MELTS for improved calculation of phase relations and major element partitioning related to partial melting of the mantle to 3 GPa. *Geochemistry, Geophysics, Geosystems* **3**, 1–35.

Ghiorso, M. S. & Sack, R. O. (1995). Chemical mass transfer in magmatic processes IV. A revised and internally consistent thermodynamic model for the interpolation and extrapolation of liquid-solid equilibria in magmatic systems at elevated temperatures and pressures. *Contributions to Mineralogy and Petrology* **119**, 197–212.

Grant, T. B., Larsen, R. B., Anker-Rasch, L., Grannes, K. R., Iljina, M., McEnroe, S., Nikolaisen, E., Schanche, M. & Øen, E. (2016). Anatomy of a deep crustal volcanic conduit system; the Reinfjord ultramafic complex, Seiland Igneous Province, Northern Norway. *Lithos* **252–253**, 200–215.

Grant, T. B., Larsen, R. B., Brown, E. L., Müller, A. B. & McEnroe, S. (2020). Mixing of heterogeneous, high-MgO, plume-derived magmas at the base of the crust in the Central Iapetus Magmatic Province (ma 610-550): origin of parental magmas to a global LIP event. *Lithos* **364–365**, 105535.

Gualda, G. A. R. & Ghiorso, M. S. (2015). MELTS_Excel: A Microsoft Excel-based MELTS interface for research and teaching of magma properties and evolution. *Geochemistry, Geophysics, Geosystems* **16**, 315–324.

Gualda, G. A. R., Ghiorso, M. S., Lemons, R. V. & Carley, T. L. (2012). Rhyolite-MELTS: a modified calibration of MELTS optimized for silica-rich, fluid-bearing magmatic systems. *Journal of Petrology* **53**, 875–890.

Gualda, G. A. R., Gravley, D. M., Deering, C. D. & Ghiorso, M. S. (2019). Magma extraction pressures and the architecture of volcanic plumbing systems. *Earth and Planetary Science Letters* **522**, 118–124.

Hansen, H., Slagstad, T. & Bergh, S. G. (2020). Geochemical volcanostratigrapy defines the tectonic evolution of the Karasjok Greenstone Belt, Finmark. *The 34th Nordic Geological Winter Meeting, Oslo* .

Hanski, E. & Huhma, H. (2005) *Chapter 4 Central Lapland greenstone belt*. In: Lehtinen, M., Nurmi, P. A. & Rämö, O. T. (eds.) Precambrian Geology of Finland Key to the Evolution of the Fennoscandian Shield: Elsevier, pp. 139–193.

Hanski, E., Huhma, H., Rastas, P. & Kamenetsky, V. S. (2001a). The palaeoproterozoic komatiite-picrite association of Finnish Lapland. *Journal of Petrology* **42**, 855–876.

Hanski, E., Walker, R., Huhma, H. & Suominen, I. (2001b). The Os and Nd isotopic systematics of c. 2.44 Ga Akanvaara and Koitelainen mafic layered intrusions in northern Finland. *Precambrian Research* **109**, 73–102.

Hawthorne, F. C., Oberti, R., Harlow, G. E., Maresch, W. V., Martin, R. F., Schumacher, J. C. & Welch, M. D. (2012). Nomenclature of the amphibole supergroup. *American Mineralogist* **97**, 2031–2048.

Heggie, G. J., Barnes, S. J. & Fiorentini, M. L. (2013). Application of lithogeochemistry in the assessment of nickel-sulphide potential in komatiite belts from northern Finland and Norway. *Bulletin of the Geological Society of Finland* **85**, 107–126.

Heinonen, J. S., Bohrson, W. A., Spera, F. J., Brown, G. A., Scruggs, M. A. & Adams, J. V. (2020) Diagnosing open-system magmatic processes using

the magma chamber simulator (MCS): part II—trace elements and isotopes. In: *Contributions to Mineralogy and Petrology*. Berlin, Heidelberg: Springer, pp. 1–21.

Heinonen, J. S., Iles, K. A., Heinonen, A., Fred, R., Virtanen, V. J., Bohrson, A., Spera, F. J., Bohrson, W. A. & Spera, F. J. (2021) From Binary Mixing to Magma Chamber Simulator. In Crustal Magmatic System Evolution (eds M. Masotta, C. Beier and S. Mollo).

Heinonen, J. S., Luttinen, A. V., Spera, F. J. & Bohrson, W. A. (2019). Deep open storage and shallow closed transport system for a continental flood basalt sequence revealed with magma chamber simulator. *Contributions to Mineralogy and Petrology* **174**, 87–87.

Hildreth, W. & Moorbath, S. (1988). Crustal contributions to arc magmatism in the Andes of Central Chile. *Contributions to Mineralogy and Petrology* **98**, 455–489.

Hirschmann, M. M. (2000). Mantle solidus: experimental constraints and the effects of peridotite composition. *Geochemistry, Geophysics, Geosystems* .

Huang, H. H., Lin, F. C., Schmandt, B., Farrell, J., Smith, R. B. & Tsai, V. C. (2015). The Yellowstone magmatic system from the mantle plume to the upper crust. *Science* **348**, 773–776.

Huppert, H. E. & Sparks, R. S. J. (1985). Cooling and contamination of mafic and ultramafic magmas during ascent through continental-crust. *Earth and Planetary Science Letters* **74**, 371–386.

Irvine, T. N. (1965). Chromian spinel as a petrogenetic indicator: part 1. Theory. *Canadian Journal of Earth Sciences* **2**, 648–672.

Irvine, T. N. (1967). Chromian spinel as a Petrogenetic indicator: part 2. Petrologic applications. *Canadian Journal of Earth Sciences* 71–103.

Jagoutz, E., Palme, H., Baddenhausen, H., Blum, K., Cendales, M., Dreibus, G., Spettel, B., Lorenz, V. & Wänke, H. (1979). The abundances of major, minor and trace elements in the earth's mantle as derived from primitive ultramafic nodules. *Lunar and Planetary Science Conference Proceedings* 2031–2050.

Jagoutz, O., Muntener, O., Ulmer, P., Pettke, T., Burg, J. P., Dawood, H. & Hussain, S. (2007). Petrology and mineral chemistry of lower crustal intrusions: the Chilas Complex, Kohistan (NW Pakistan). *Journal of Petrology* **48**, 1895–1953.

Koistinen, T., Stephens, M., Bogatchev, V., Nordgulen, Ø., Wennerström, M. & Korhonen, J. (2001) Geological map of the Fennoscandian Shield 1: 2 000 000. Espoo: Geological Survey of Finland, Trondheim: Geological Survey of Norway, Uppsala: Geological Survey of Sweden, Moscow: Ministry of Natural Resources of Russia.

Krill, A. G. (1985a). Rb-Sr, U-Pb and Sm-Nd isotopic dates from Precambrian rocks of Finnmark. *Norges Geologiske Undersokelse Bulletin* **403**, 37–54.

Krill, A. G. (1985b). Svecokarelian thrusting with thermal inversion in the Karasjok-Levajok area of the northern Baltic shield. *Norges Geologiske Undersokelse Bulletin* **403**, 89–101.

Larsen, R. B., Grant, T., Sørensen, B. E., Tegner, C., McEnroe, S., Pastore, Z., Fichler, C., Nikolaisen, E., Grannes, K. R., Church, N., ter Maat, G. W. & Michels, A. (2018). Portrait of a giant deep-seated magmatic conduit system: the Seiland Igneous Province. *Lithos* **296–299**, 600–622.

Lightfoot, P. C., Hawkesworth, C. J., Hergt, J., Naldrett, A. J., Gorbachev, N. S., Fedorenko, V. A. & Doherty, W. (1993). Remobilisation of the continental lithosphere by a mantle plume: major-, trace-element, and Sr-, Nd-, and Pb-isotope evidence from picritic and tholeiitic lavas of the Noril'sk District, Siberian Trap, Russia. *Contributions to Mineralogy and Petrology* **114**, 171–188.

Lister, J. R., Campbell, I. H. & Kerr, R. C. (1991). The eruption of komatiites and picrites in preference to primitive basalts. *Earth and Planetary Science Letters* **105**, 343–352.

Liu, J., Xia, Q. K., Kuritani, T., Hanski, E. & Yu, H. R. (2017). Mantle hydration and the role of water in the generation of large igneous provinces. *Nature Communications* **8**, 1824.

Ludden, J., Gélinas, L. & Trudel, P. (1982). Archean metavolcanics from the Rouyn–Noranda district, Abitibi Greenstone Belt, Quebec. 2. Mobility of trace elements and petrogenetic constraints. *Canadian Journal of Earth Sciences* **19**, 2276–2287.

Luolavirta, K. (2018). Magmatic evolution of the Kevitsa igneous complex, northern Finland, and its relation to the associated Ni-Cu-(PGE) mineralization. *Res Terrae* **68**.

Luolavirta, K., Hanski, E., Maier, W. & Santaguida, F. (2018a). Characterization and origin of dunitic rocks in the NI-CU-(PGE) sulfide ore-bearing kevitsa intrusion, northern Finland: whole-rock and mineral chemical constraints. *Bulletin of the Geological Society of Finland* **90**, 5–32.

Luolavirta, K., Hanski, E., Maier, W. & Santaguida, F. (2018b). Whole-rock and mineral compositional constraints on the magmatic evolution of the Ni-cu-(PGE) sulfide ore-bearing Kevitsa intrusion, northern Finland. *Lithos* 37–53.

Magee, C., Stevenson, C. T. E., Ebmeier, S. K., Keir, D., Hammond, J. O. S., Gottsmann, J. H., Whaler, K. A., Schofield, N., Jackson, C. A. L., Petronis, M. S., O'Driscoll, B., Morgan, J., Cruden, A., Vollgger, S. A., Dering, G., Micklethwaite, S. & Jackson, M. D. (2018). Magma plumbing systems: a geophysical perspective. *Journal of Petrology* **59**, 1217–1251.

Maier, W. D. & Groves, D. I. (2011). Temporal and spatial controls on the formation of magmatic PGE and Ni–Cu deposits. *Mineralium Deposita* **46**, 841–857.

Melezhik, V. A., Solli, A., Fallick, A. E. & Davidsen, B. (2015). Chemostratigraphic constraints on the time of deposition of carbonate rocks in the Karasjok Greenstone Belt, northern Norway. *Norwegian Journal of Geology* **95**, 299–314.

Mutanen, T. & Huhma, H. (2001). U-Pb geochronology of the Koitelainen, Akanvaara and Keivitsa layered intrusions and related rocks. Special Paper of the Geological Survey of Finland, 229–246.

Mysen, B. O. & Boettcher, A. (1976). Melting of a hydrous mantle: III. Phase relations of garnet websterite+ H2O at high pressures and temperatures. *Journal of Petrology* **17**, 1–14.

Nilsson, L. P. & Often, M. (2005). A summary report on the Ni-Cu-PGE occurrences and their host rocks in the Precambrian of Finnmark, Northern Norway. *Geological Survey of Norway Report* 2005.085 79 pp.

Often, M. (1985). The Early Proterozoic Karasjok Greenstone Belt, Norway. A preliminary description of lithology, stratigraphy and mineralization. *Norges Geologiske Undersokelse Bulletin* **403**, 75–88.

Orvik, A. A., Slagstad, T., Nilsson, L. P. & Sørensen, B. E. (n.d.) U-Pb age and Rb-Sr, Sm-Nd and Lu-Hf isotopic fingerprints of the Ni-Cu-PGE mineralised Gallujavri intrusion, northern Norway, and its relationship to other intrusions of the Central Lapland Greenstone belt. Norwegian University of Science and Technology, in preparation.

Page, P. & Barnes, S.-J. (2009). Using trace elements in chromites to constrain the origin of podiform chromitites in the thetford mines ophiolite, Quebec, Canada. *Economic Geology* **104**, 997–1018.

Perkins, D. & Vielzeuf, D. (1992). Experimental investigation of Fe-Mg distribution between olivine and clinopyroxene: implications for mixing properties of Fe-Mg in clinopyroxene and garnet-clinopyroxene thermometry. *American Mineralogist* **77**, 774–783.

Pilet, S., Hernandez, J., Bussy, F. & Sylvester, P. J. (2004). Short-term metasomatic control of Nb/Th ratios in the mantle sources of intraplate basalts. *Geology* **32**, 113–116.

Puchtel, I., Arndt, N., Hofmann, A., Haase, K., Kröner, A., Kulikov, V., Kulikova, V., Garbe-Schönberg, C.-D. & Nemchin, A. (1998). Petrology of mafic lavas within the Onega plateau, Central Karelia: evidence for 2.0 Ga plume-related continental crustal growth in the Baltic Shield. *Contributions to Mineralogy and Petrology* **130**, 134–153.

Puchtel, I. S., Haase, K. M., Hofmann, A. W., Chauvel, C., Kulikov, V. S., Garbe-Schönberg, C. D. & Nemchin, A. A. (1997). Petrology and geochemistry of crustally contaminated komatiitic basalts from the Vetreny Belt, southeastern Baltic Shield: evidence for an early Proterozoic mantle plume beneath rifted Archean continental lithosphere. *Geochimica et Cosmochimica Acta* **61**, 1205–1222.

Puchtel, I. S., Mundl-Petermeier, A., Horan, M., Hanski, E. J., Blichert-Toft, J. & Walker, R. J. (2020). Ultra-depleted 2.05 Ga komatiites of Finnish Lapland: products of grainy late accretion or core-mantle interaction? *Chemical Geology* **554**, 119801.

Putirka, K. D. (2008). Thermometers and barometers for volcanic systems. *Minerals, Inclusions and Volcanic Processes* **69**, 61–120.

Ridolfi, F., Renzulli, A. & Puerini, M. (2009). Stability and chemical equilibrium of amphibole in calc-alkaline magmas: an overview, new thermobarometric formulations and application to subduction-related volcanoes. *Contributions to Mineralogy and Petrology* **160**, 45–66.

Ridolfi, F., Zanetti, A., Renzulli, A., Perugini, D., Holtz, F. & Oberti, R. (2018). AMFORM, a new mass-based model for the calculation of the unit formula of amphiboles from electron microprobe analyses. *American Mineralogist* **103**, 1112–1125.

Shau, Y.-H., Yang, H.-Y. & Peacor, D. R. (1991). On oriented titanite and rutile inclusions in sagenitic biotite. *American Mineralogist* **76**, 1205–1217.

Siedlecka, A. (1985). Geology of Iesjav'ri-Skognavarre area, northern Finnmarksvidda, North Norway. *Norges Geologiske Undersokelse Bulletin* **403**, 103–112.

Sinton, J. M. & Detrick, R. S. (1992). Mid-ocean ridge magma chambers. *Journal of Geophysical Research: Solid Earth* **97**, 197–216.

Skaar, J. A. A. (2014) 3D geophysical and geological modelling of the Karasjok Greenstone Belt. Department of Geoscience and Petroleum. NTNU: Norwegian University of Science and Technology.

Sobolev, A. V., Asafov, E. V., Gurenko, A. A., Arndt, N. T., Batanova, V. G., Portnyagin, M. V., Garbe-Schonberg, D. & Krasheninnikov, S. P. (2016). Komatiites reveal a hydrous Archaean deep-mantle reservoir. *Nature* **531**, 628–632.

Sparks, R. S. J. & Cashman, K. V. (2017). Dynamic magma systems: implications for forecasting volcanic activity. *Elements* **13**, 35–40.

Stokmo, E. B. (2020) Superimposed macro- and mesoscale folds, and their relation to ductile shear zones in the Karasjok Greenstone Belt, Finnmark, Norway. Department Of Geosciences. UiT: UiT The Arctic University of Norway.

Sun, S. S. & McDonough, W. F. (1989). Chemical and isotopic systematics of oceanic basalts: implications for mantle composition and processes. *Geological Society, London, Special Publications* **42**, 313–345.

Sun, S. S. & Nesbitt, R. W. (1978). Petrogenesis of Archaean ultrabasic and basic volcanics - evidence from rare-earth elements. *Contributions to Mineralogy and Petrology* **65**, 301–325.

Tarasewicz, J., White, R. S., Woods, A. W., Brandsdóttir, B. & Gudmundsson, M. T. (2012). Magma mobilization by downward-propagating decompression of the Eyjafjallajökull volcanic plumbing system. *Geophysical Research Letters* **39**.

Weaver, B. L. & Tarney, J. (1984). Empirical approach to estimating the composition of the continental crust. *Nature* **310**, 575–577.

Paper 2

Precambrian Research 379 (2022) 106813

Contents lists available at ScienceDirect

Precambrian Research

journal homepage: www.elsevier.com/locate/precamres

Evolution of the Gállojávri ultramafic intrusion from U-Pb zircon ages and Rb-Sr, Sm-Nd and Lu-Hf isotope systematics

Alf Andre Orvik [a,*], Trond Slagstad [b], Bjørn Eske Sørensen [a], Ian Millar [c], Harald Hansen [d]

[a] Department of Geoscience and Petroleum, Norwegian University of Science and Technology, S. P. Andersens veg 15, 7031 Trondheim, Norway
[b] Geological Survey of Norway, Leiv Eirikssons vei 39, 7040 Trondheim, Norway
[c] Geochronology and Tracers Facility, British Geological Survey, Keyworth, Nottingham NG12 5GG, UK
[d] Department of Geosciences, UiT The Arctic University of Norway, Dramsveien 201, 9037 Tromsø, Norway

ARTICLE INFO

Keywords:
Crustal contamination
Karasjok Greenstone Belt
Magma conduit
Rb-Sr isotopes
Sm-Nd isotopes
zircon Hf

ABSTRACT

The Karasjok–Central Lapland Greenstone Belt is one of the largest Palaeoproterozoic greenstone belts in the Fennoscandian Shield and includes multiple (ultra)mafic intrusions, some with notable ore reserves, formed during three episodes at 2.44, 2.22 and 2.05 Ga. This study presents new mineralogical, geochronological and isotopic data for the Gállojávri ultramafic intrusion, in the Karasjok Greenstone Belt, northern Norway. Previous petrogenetic modelling suggests that the intrusion was emplaced as a conduit system open for influx of melt with signs of polybaric fractionation and assimilation. Zircon U-Pb geochronology yields an age of 2051 ± 8 Ma, interpreted to reflect magmatic crystallisation. Large variations in isotopic signature over decimetres to metres indicate incomplete magma mixing. In bulk samples, εNd(t) ranges from −15 to 4. Zircon εHf(t) ranges from −14 to −1. Bulk $^{87}Sr/^{86}Sr(t)$ shows an apparent range from 0.5041 to 0.7072: the anomalously low values and general alteration indicates that $^{87}Sr/^{86}Sr$ is non-primary, whereas the less mobile Sm-Nd/ Lu-Hf systems are interpreted to represent primary magmatic signatures. We ascribe the large variations in the Nd and Hf isotopic signatures to local melting or dissolution of xenoliths and influx of variably contaminated melt into the semi-consolidated Gállojávri magma chamber, consistent with a conduit model involving variable replenishment and crustal interaction. The most evolved isotopic signatures cannot be accounted for by interaction with the local Archaean basement, indicating the presence of unidentified crustal components at depth. The Gállojávri intrusion shows many petrogenetic similarities to other c. 2.05 Ga (ultra)mafic intrusions in the Central Lapland Greenstone Belt.

1. Introduction

Magmatic plumbing systems represent highly dynamic environments that often involve complicated multistage and polybaric evolutionary histories. The compositional variations observed in lavas and related subvolcanic cumulates reflect the complex interplay between physical and chemical processes during magma generation, differentiation and assimilation (Fowler et al., 2004; Orvik et al., 2022). For example, the transport of magmas through the continental lithosphere offers ample opportunities for thermal erosion and the subsequent addition of anatectic melt and country-rock residue to a magma body that leads to chemical contamination of a rock suite (Arndt and Jenner, 1986; Ding et al., 2012; Fowler et al., 2004). Crustally derived anatectic melts generally have distinctly different radiogenic and stable isotope ratios from mantle melts (Peate et al., 2008). Therefore, the addition of crustal melts can significantly modify the magma composition.

The chemical and isotopic effects of assimilation on melts that pass through the crustal column can provide important information about the local crustal architecture (Dickin and Durant, 2002; Peate et al., 2008). In addition, assimilation of country rock material is critical in generating magmatic Ni-Cu-(PGE) sulphide deposits (Ding et al., 2012; Lesher, 2017, 2019), with channelised sills, tubes or blade-shape dykes characterised by prolonged high-volume flow accounting for most of the known host igneous bodies to significant ore deposits worldwide (Barnes et al., 2016).

This contribution focuses on the Palaeoproterozic Gállojávri ultramafic intrusion in Arctic Norway that forms part of the Karasjok and Central Lapland Greenstone Belt (KCLGB), extending from Norway, through Finland, into Russia, and contains several types of (ultra)mafic plutonic bodies and coeval extrusive rocks (Fig. 1; Orvik et al., 2022). In

* Corresponding author.
E-mail address: alf.a.orvik@ntnu.no (A.A. Orvik).

https://doi.org/10.1016/j.precamres.2022.106813
Received 25 April 2022; Received in revised form 27 June 2022; Accepted 27 July 2022
Available online 5 August 2022

Finland, the (ultra)mafic plutonic bodies, some with notable ore reserves, are grouped into three intrusive episodes at 2.44, 2.22 and 2.05 Ga (Hanski and Huhma, 2005, and references therein). Previous geochronological and isotopic data are very few in the Karasjok area, inhibiting the correlation with the northern Norwegian intrusions.

The Gállojávri intrusion represents a mid-crustal magma conduit that funnelled coeval komatiites towards the surface. Previous thermodynamic modelling has revealed a complex multistage magmatic history, with magma injection(s), differentiation and assimilation at different levels in the crust (Orvik et al., 2022). However, variations in mineral and whole-rock geochemical composition forming the basis of the model are not well suited to constrain the nature of the wall rock material or melt recharges. To this end, we report new mineralogical, geochronological and isotopic data for the Gállojávri intrusion to test the current petrogenetic model and to correlate the intrusion to other KCLGB examples. The data reveal large variations in isotopic signatures, typically over small distances, that provide important information on the assembly of the intrusion and shed light on the crustal architecture beneath the Karasjok area.

2. Geological setting

The Gállojávri intrusion is located in the Karasjok Greenstone Belt (KGB), the northernmost extension of the Central Lapland Greenstone Belt (CLGB). Together, the KCLGB can be followed to Russian Karelia in the southeast, making it one of the largest Palaeoproterozoic greenstone belts in the Fennoscandian Shield (Fig. 1B; Moilanen et al., 2021). The KCLGB records a prolonged extensional regime (c. 2.45–1.92 Ga) with volcano-sedimentary deposits on top of Archaean basement (Hanski and Huhma, 2005), showing a gradual deepening of the rift-basin from subaerial and shallow-water conditions to deeper-water conditions (Hanski and Huhma, 2005; Moilanen et al., 2021).

The KGB rocks have been deformed and metamorphosed under greenschist- to amphibolite-facies conditions (Braathen and Davidsen, 2000) and nonconformably overlie and are partly thrusted over the tonalite-trondhjemite-granodiorite-granite (TTGG)-dominated Archae an Jergul Gneiss Complex to the west (Fig. 1B & 2A). The variably gneissic Jergul Gneiss Complex is of Karelian affinity and formed between c. 2.98 and 2.78 Ga (Bingen et al., 2015).

The lowest unit in the KGB lithostratigraphy is the Lavtevárri formation consisting of a basal conglomerate underlying fine-grained foliated amphibolites, metapelites and metakomatiites (Fig. 2B; Braathen and Davidsen, 2000). The overlying Čorgaš formation has a lower portion of conglomerates, psammites and metapelites and an upper section of shallow-marine sedimentary rocks and subaerial to shallow-water mafic volcanic rocks (Fig. 2C; Barnes and Often, 1990; Braathen and Davidsen, 2000; Stokmo, 2020).

The basal contact of the Brittágielas formation with the underlying Čorgaš formation consists of an extensive marble unit (Fig. 2D; Braathen and Davidsen, 2000). The lower part of the Brittágielás formation

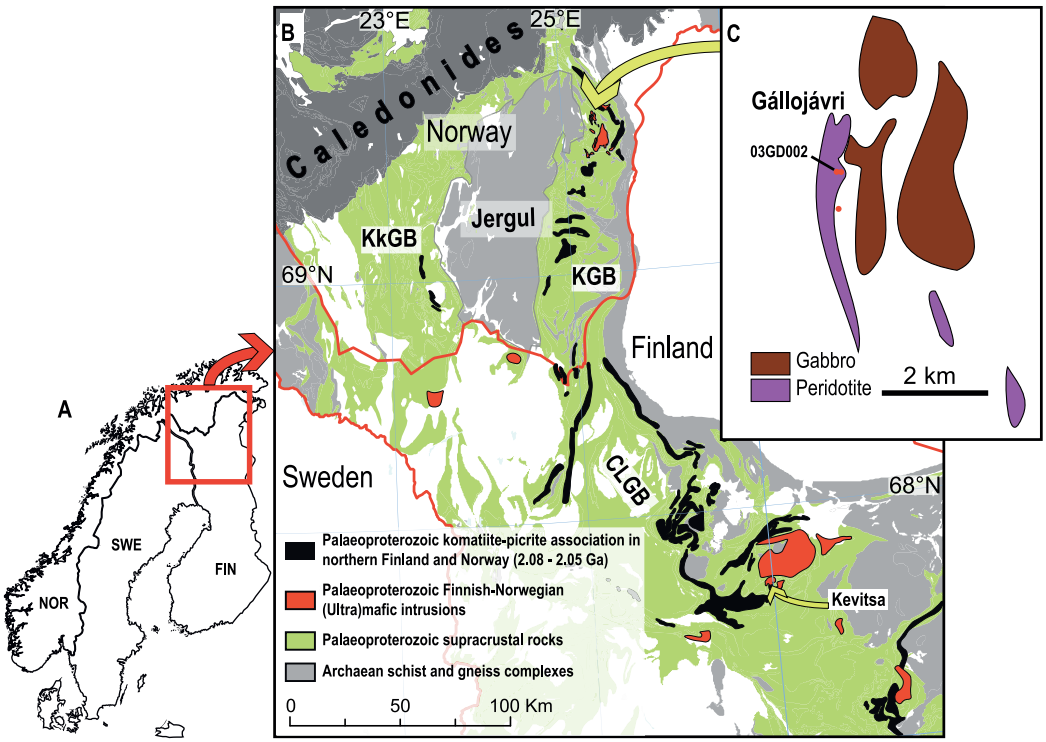

Fig. 1. (A) Sketch map of Scandinavia. The red box shows the location of the geological map in (B). (B) Simplified geological map showing the extension of the greenstone belt and distribution of Palaeoproterozoic (ultra)mafic extrusive and intrusive rocks. The map is modified from Orvik et al. (2022), Bingen et al. (2015), Hanski et al. (2001), Hanski and Huhma (2005), Puchtel et al. (2020), and based on Koistinen et al. (2001). (C) Sketch map of the Gállojávri ultramafic intrusion and adjacent intrusive rocks modified from Henriksen (1986) with the location of drill hole 03GD002 and other holes intercepting the Gállojávri intrusion (red dots). Abbreviations: Norway (NOR), Sweden (SWE), Finland (FIN), Kautokeino Greenstone Belt (KkGB), Karasjok Greenstone Belt (KGB) and the Central Lapland Greenstone Belt (CLGB). (For interpretation of the references to colour in this figure legend, the reader is referred to the web version of this article.)

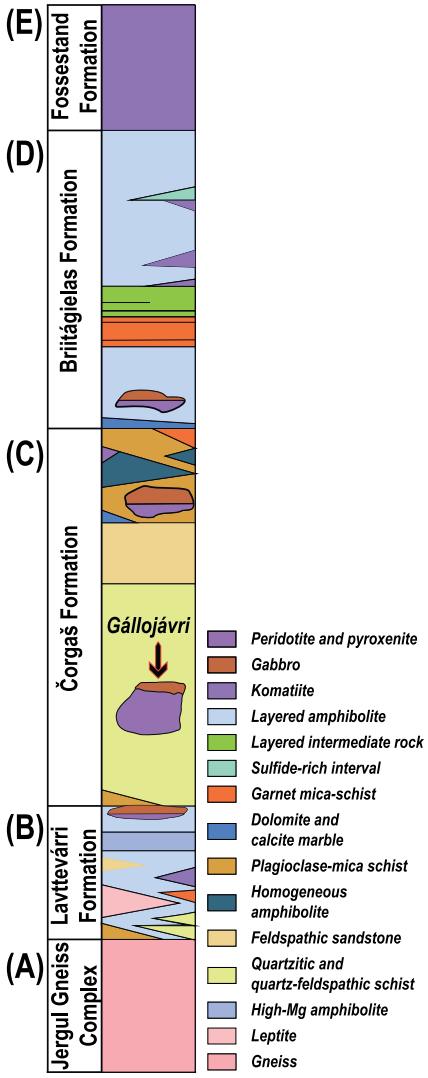

Fig. 2. The lithostratigraphy of the Karasjok Greenstone belt, modified from Orvik et al. (2022) and Hansen et al. (2020).

comprises calc-alkaline metavolcanic rocks and kyanite-bearing mica schists and an upper portion of layered amphibolites. Four 70 m-thick units of metakomatiite also distinguish the Brittágielas formation (Barnes and Often, 1990; Braathen and Davidsen, 2000). Metakomatiitic and volcanoclastic rocks dominate the upper Fossestrand formation (Fig. 2E; Stokmo, 2020). The lower portion comprises pillowed lavas that underlie lava flows and agglomerates. Mafic plutonic bodies have also been identified within the Fossestrand formation (Braathen and Davidsen, 2000).

Ultramafic to mafic intrusions are common in the Čorgaš formation. Several of these host Ni-Cu-PGE mineralisations and have drawn the interest of exploration companies, most notably the Karenhaugen-, Porsvann- and Gállojávri intrusions (Eilu, 2012). There are no published ages for these intrusions. However, carbon isotope chemostratigraphy on carbonates within the Čorgaš formation suggests a depositional age between c. 2.22 and 2.14 Ga (Melezhik et al., 2015). Bearing in mind that the (ultra)mafic intrusions of the KCLGB are interpreted to have formed in separate magmatic episodes at c. 2.44, 2.22 and 2.05 Ga (Hanski and Huhma, 2005), the maximum age provided by the isotope chemostratigraphy implies that the intrusions in the Čorgaš formation are part of the youngest group (Orvik et al., 2022).

3. The Gállojávri intrusion

The Gállojávri intrusion is a small and variably altered ultramafic body with a north-south elongation (Fig. 1C). The intrusion crops out over an area of about 2.3 km^2, but is likely larger, as observed in magnetic- and gravimetric anomaly maps (Skaar, 2014). The apparent magmatic differentiation observed in drill cores is concordant to semi-concordant with the surrounding foliation, implying a sill-like intrusion.

A petrogenetic model for the Gállojávri intrusion, based on whole-rock geochemistry, mineral chemistry and thermodynamic modelling, was presented by Orvik et al. (2022). Here, we restate some of the key aspects of the model. The reader is encouraged to consult the more extensive discussion in the original publication for further details.

The Gállojávri intrusion represents a mid-crustal magmatic body. It is part of a plumbing system that channelled komatiitic melts spatially (and temporally) associated with the Gállojávri intrusion towards the surface. Chemically, the cumulate rocks of the intrusion have high LREE/HREE and LREE/HFSE ratios and negative Nb-Ta anomalies, which suggest a significant contribution from LREE-enriched continental crust. Moreover, trace element indicators of crustal assimilation are uniform, implying that the assimilation occurred in a staging chamber. Thermobarometric estimates strengthen this interpretation with pressure estimates clustering at c. 400 MPa but extending towards c. 700 MPa.

The thermodynamic modelling demonstrated that the local Karasjok-type komatiite (Barnes and Often, 1990) is a likely parental melt analogue. The primitive komatiite first intruded the lower Archaean crust, where the melt fractionated and assimilated anatectic melt from its host rocks. In the second stage, the hybrid melt migrated to the middle crust and continued to fractionate and assimilate crustal material. The modelling revealed that the Gállojávri intrusion represents an open magmatic system requiring at least one recharge event to replicate the phase equilibria and thermobarometric estimates (Orvik et al., 2022).

4. Methods

4.1. Magma chamber simulator

The Magma Chamber Simulator (MCS; Bohrson et al., 2014) is an energy- and mass-constrained model that quantifies the phase, thermal and compositional evolution of a multiphase–multicomponent system of a fractionally crystallising resident magma body (melt + solid ± fluid), coupled with wall rock and multiple recharge reservoirs (Bohrson et al., 2020; Heinonen et al., 2020). The MCS uses the family of MELTS engines (Ghiorso and Gualda, 2015; Ghiorso et al., 2002; Ghiorso and Sack, 1995; Gualda et al., 2012) to quantify phase equilibria in the different subsystems separated by thermodynamic boundaries capable of transferring heat and mass (Bohrson et al., 2014; Heinonen et al., 2020). The phase equilibria of the magmatic subsystems at given P-T conditions are controlled by the major (±minor) element composition and the thermodynamic properties of the liquid + solid ± fluid phases present.

The MCS quantifies these parameters in an isobaric resident magma chamber. It evolves in temperature decrements while being open to the assimilation of anatectic melts and the influx of recharge melts. In the MCS, self-consistent thermodynamic modelling traces the thermal, mass and compositional evolution of the multicomponent–multiphase system

of the resident magma, wall rock and recharge reservoir by coupling the subsystems thermodynamic output with an executive Excel visual basic program (*MCS-PhaseEQ*; Bohrson et al., 2014). For more information on the use and design of the modelling tool, we refer to several articles introducing MCS (e.g., Bohrson et al., 2014; Bohrson et al., 2020; Heinonen et al., 2020; Heinonen et al., 2021; Heinonen et al., 2019) and the prior application to the Gállojávri intrusion (i.e., Orvik et al., 2022).

4.1.1. Magma chamber simulator: Trace elements and isotopes

In general, trace elements are too diluted to be primary stoichiometric constituents of magmatic phases and do not influence the phase equilibria (Hanson, 1989; Hanson and Langmuir, 1978). The distribution of trace elements is described by the partition coefficient (K_{sm}), which is the ratio of the concentration of an element in a solid phase versus the concentration in melt (Heinonen et al., 2020). In fractionating magmatic systems, multiple solid phases often crystallise simultaneously. In these cases, the bulk partition coefficient (D_{sm}) describes the chemical fractionation; that is, the sum of phase-specific K_{sm} scaled by the mass fraction of each solid phase.

Since trace elements are too dilute to influence phase equilibria, they are treated separately in MCS using the *MCS-Traces* tool (Bohrson et al., 2014). However, information on the composition and relative quantities of stable phases in magmatic systems are necessary to calculate D_{sm}. Therefore, the detailed modelling of trace elements (and isotopes) is impossible without recording major (±minor) element phase equilibria and mass fractions with the *MCS-PhaseEQ* tool. *MCS-Traces* uses the primary output of the *MCS-PhaseEQ* and reads it as the step-wise progression of the magmatic system (Bohrson et al., 2014; Heinonen et al., 2020). The *MCS-Traces* tool calculates isotopic ratios and trace element concentrations for each step defined in the primary *MCS-PhaseEQ* output. Additional input necessary to complete these calculations includes K_{sm} for each relevant phase and element and initial trace element concentrations and isotopic compositions for the melt and wall-rock reservoirs. The recharge reservoirs require only the initial trace element concentrations and isotopic ratios (Bohrson et al., 2014). For more information on the design and operational details of *MCS-Traces*, we refer to the introductory articles of Bohrson et al. (2014) and Heinonen et al. (2020).

4.2. Analytical methods

Thirteen samples selected from drill core 03GD002 (Fig. 1C; collar coordinates (DMS): N 69° 37′ 51.0672, E 25° 23′ 3.9948) were mineralogically characterised with X-ray Diffraction (XRD) and analysed for whole-rock Sr and Nd isotope compositions. Zircon from four of the 13 samples was prepared for in-situ U-Pb geochronology, trace element and Hf isotope characterisation. A detailed description of sample preparation and analytical methods is provided in Electronic supplement (ES) 1.

5. Sample petrography

Fig. 3 shows the CIPW normative mineralogy calculated from major element whole rock data (ES-2) and a simplified lithological log (Orvik et al., 2022). The labelled diamonds to the right in the figure give the locations of the samples analysed in this study. In cases where we can infer protolith lithology, we omit the prefix 'meta' for metamagmatic rocks, but note that all investigated rocks have been metamorphosed under greenschist and amphibolite facies and undergone variable low-temperature alteration.

The lower part of the drilled section consists of a coarse-grained and variably altered olivine-pyroxene cumulate unit. Sample *628*, located in the lower end (Fig. 3), is an orthocumulate with inequigranular olivine (c. 1–4 mm), orthopyroxene (c. 1–7 mm) and clinopyroxene (1–3 mm) (Fig. 4A). The olivine (c. 40–50 modal%) has a forsterite content of c. 81 % (Orvik et al., 2022) and is present as moderately serpentinised inclusions in the pyroxenes. Orthopyroxene (c. 20–30 %) is subhedral to anhedral, commonly with chaddacrysts of clinopyroxene, olivine and spinel

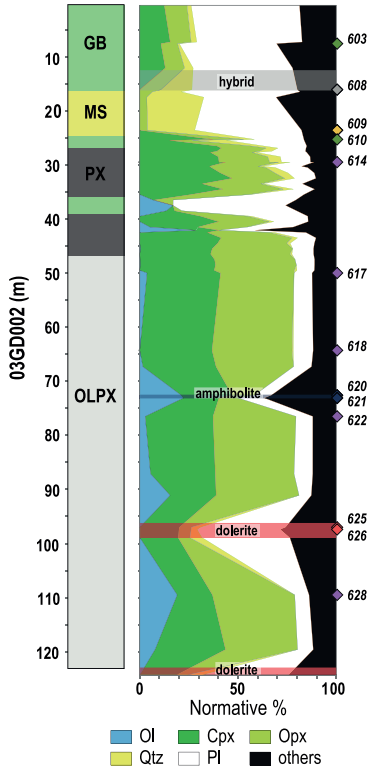

Fig. 3. Downhole CIPW normative mineralogy calculated from the major element whole-rock data of Orvik et al. (2022). Abbreviations: gabbro (GB), metasedimentary rocks (MS), pyroxenite (PX), olivine pyroxenite (OLPX), olivine (Ol), clinopyroxene (Cpx), orthopyroxene (Opx), quartz (Qtz) and plagioclase (Pl). The 'others' category includes normative hematite, orthoclase, sphene, corundum, pyrite, ilmenite, apatite, rutile, perovskite and nepheline.

(Fig. 4B). The clinopyroxene (10–20 %) is mostly interstitial and anhedral, but some examples of subhedral cumulus crystals exist (Fig. 4A). Additional interstitial minerals include primary amphibole and saussuritised plagioclase.

Sample *622* is located in the middle of the olivine-pyroxene unit (Fig. 3). The sample is strongly altered with uralised pyroxenes and serpentinised olivine, making any petrographic evaluation of modal mineralogy or primary features difficult (Fig. 4C). Relict minerals of olivine (1–3 mm) and orthopyroxene (1–2 mm) indicate a slightly finer grain size than in sample *628*. No relict clinopyroxene was observed in thin section and it is likely completely replaced by amphibole.

At the top of the olivine-pyroxene unit, sample *617* (Fig. 4D) represents a slightly altered mesocumulate of clinopyroxene (40–50 %), olivine (20–30 %) and orthopyroxene (10–20 %). Clinopyroxene has a variable grain size of 0.5–3 mm and is subhedral to anhedral. The smaller subhedral grains are present as chadacrysts in lager orthopyroxene. Olivine is inequigranular with grain sizes of 1.5–3.5 mm and is partly serpentinised, showing mesh texture. Orthopyroxene grains (1.0–3.5 mm) are subhedral to anhedral; the largest grains are typically poikilitic with clinopyroxene inclusions (Fig. 4D). Plagioclase is the main interstitial mineral together with accessory phlogopite.

Samples *620* and *621* were collected from two closely spaced zones (marked amphibolite in Fig. 3) because of elevated Zr concentrations of

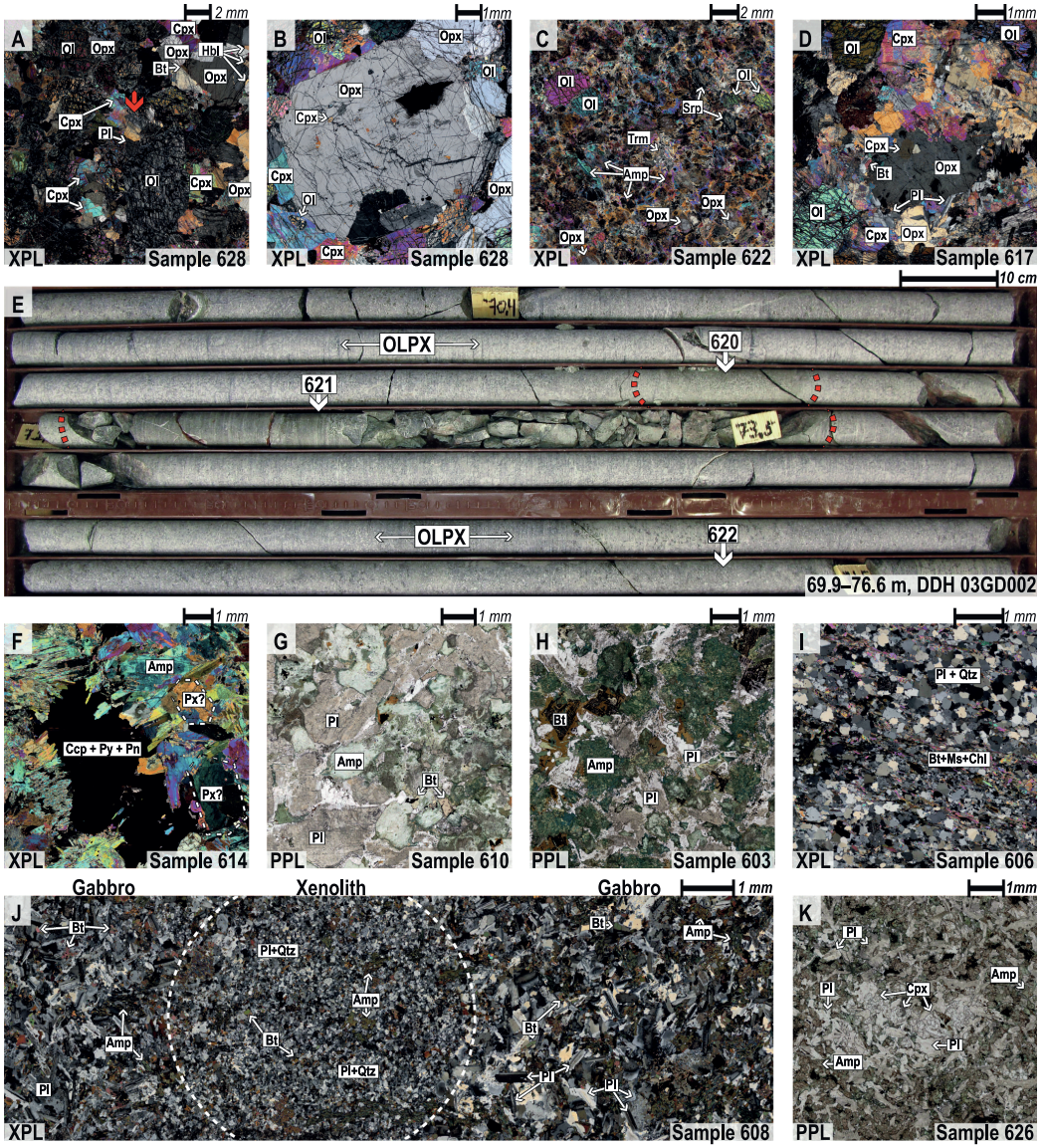

Fig. 4. Sample micrographs and images from this study. (A) Olivine-pyroxene orthocumulate. The red arrow points to subhedral cumulus clinopyroxene. (B) Large orthopyroxene with clinopyroxene chadacrysts. Note rounded olivine inclusion in interstitial clinopyroxene. (C) Extensively altered olivine-pyroxene cumulates with some relict olivine and orthopyroxene present. (D) Olivine-pyroxene mesocumulate with interstitial clinopyroxene and plagioclase. The orthopyroxene is poikilitic with chadacrysts of clinopyroxene. (E) Core section showing the location of samples 620 and 621. (F) Pyroxenite where secondary amphiboles completely replace the primary pyroxene. The stippled areas are thought to represent the relict outline of primary pyroxene. (G) Gabbro consisting of seriticized plagioclase, secondary amphibole and biotite. (H) Intergranular gabbro with partly seriticized plagioclase, secondary amphibole and sagenitic biotite. (I) Metasedimentary xenolith. (J) Hybrid intergranular gabbro with a rounded xenolith (outlined). (K) intergranular dolerite dyke. Abbreviations: cross-polarised light (XPL), plane-polarised light (PPL), olivine (Ol), orthopyroxene (Opx), clinopyroxene (Cpx), plagioclase (Pl), amphibole (Amp), tremolite (Trm), serpentine (Srp), chalcopyrite (Ccp), pyrite (Py), pentlandite (Pn), biotite (bt), quartz (Qtz), muscovite (Ms) and chlorite (Chl). (For interpretation of the references to colour in this figure legend, the reader is referred to the web version of this article.)

c. 150 ppm (ES-2; Orvik et al., 2022). These zones show gradual contact with the surrounding olivine pyroxenite unit and are extensively metasomatically altered (Fig. 4E), having 20–22 wt% MgO, 3.0–3.3 wt% K_2O and 152–165 ppm Rb. The samples are classified as amphibolites based on the XRD-determined mineralogy presented in the following section (Table 1). No thin sections were made from these sections because of the general alteration.

The coarse-grained olivine pyroxenite unit below grades into a medium-grained pyroxenite above (Fig. 3). The pyroxenites are characterised by a lack of normative olivine, disseminated sulphides and a near-complete replacement of primary silicate minerals by green amphibole, chlorite and biotite. In sample *614*, some relict pyroxene outlines indicate a grain size between 0.8 and 2.3 mm (Fig. 4F). Upward, the pyroxenites grade into gabbro with interstitial plagioclase. The plagioclase is largely replaced by saussurite, and the primary ferromagnesian minerals are completely replaced by green amphibole (Fig. 4G). The gabbro is less altered at the top of drill core 03GD002, with a primary intergranular texture. In sample *603* (Fig. 3), saussuritised plagioclase (30–40 %) laths 1–2 mm long enclose secondary amphibole, chlorite and sagenitic biotite (Fig. 4H).

Between c. 16 and 25 m, the drilled section consists of a xenolithic block of metasedimentary rock (Fig. 3). The section is dominated by plagioclase and quartz (60–80 modal%) with a grain size of c. 100–400 μm, with bands of chlorite, biotite, muscovite and amphibole (Fig. 4I).

Above the metasedimentary rocks, the gabbro is hybrid and contains minor, partly consumed xenoliths (Fig. 4J). The hybrid gabbro sample *608* is intergranular with partly saussuritised plagioclase (30–40 %) laths between 200 and 800 μm long. The granules consist of secondary amphibole, chlorite and biotite. The included xenoliths have transitional contacts with the surrounding gabbro and contain c. 70 % fine-grained (c. 50–150 μm) granoblastic plagioclase and quartz, the remaining being amphibole and biotite.

Dykes are common in all the drill cores (Orvik et al., 2022). Samples *625* and *626* were collected from a c. 4 m-thick dolerite sheet with sharp contacts. The dolerites have an intergranular texture with partly saussuritised plagioclase (30–40 %) measuring from 200 to 500 μm in length. The granules consist of c. 10 % clinopyroxene, c. 3 % ilmenite, and the remaining being secondary amphibole and chlorite (Fig. 4K).

6. Results

6.1. XRD-results

Table 1 shows the major phases identified with XRD (>1 wt%). The complete phase list and diffractograms are presented in ES-3. The magmatic lithologies have suffered moderate to severe alteration with secondary minerals (∑amphibole ± muscovite ± chlorite ± talc ± serpentine) in the range 11–98 wt% (Table 1).

6.2. Geochronology

Fig. 5 presents the U–Pb zircon geochronological data in Tera-Wasserburg diagrams. In Fig. 5A-D, the 2σ data-point error ellipses are colour scaled by the estimated common lead concentration. Electronic supplement 4 gives the complete dataset with cathodoluminescence (CL) images of zircon crystals. All ages are quoted with 2σ uncertainties.

Sample *609* is a metamorphosed feldspathic sandstone that hosts the Gállojávri intrusion. The sample comprise 48 % plagioclase, 31 % quartz, 7 % muscovite, 5 % biotite and 3 % diopside (Table 1). The zircon grains from this sample are c. 50–180 μm, anhedral and sub-rounded to stubby with aspect ratios between 1:1 and 3:1. The zircons are generally dark in CL, although some grains have cores with faint to strong oscillatory zoning suggesting a magmatic origin (ES-4). Other grains have dark and homogenous cores with CL-bright rims; however, core-mantle relationships are not ubiquitous. Some of the larger stubby to slightly elongated zircon grains show no apparent discontinuity between core and rim. Fifteen of the 24 analyses are >90 % concordant and have $^{207}Pb/^{206}Pb$ ages between 3022 ± 34 and 2652 ± 36 Ma. The majority (50 %) of the $^{207}Pb/^{206}Pb$ ages in concordant zircons are between 2845 ± 34 and 2746 ± 34 Ma. The discordant zircon analyses lie close to a discordia with an imprecise lower intercept of 528 ± 120 Ma (N = 24 & MSWD = 17; Fig. 5A), interpreted to reflect Caledonian lead loss.

Sample *603* is a coarse-grained intergranular gabbro, where secondary minerals largely replace the primary ferromagnesian minerals (Fig. 4H, Table 1). The zircon grains from this sample are c. 70–440 μm and subhedral. They are commonly needle-shaped acicular with aspect ratios up to 5:1 (ES-4). The highly elongated grains are characteristic of rapid growth (Corfu et al., 2003). The zircon grains are dark in CL, some with faint oscillatory or lengthwise zoning along the c-axis. Many of the grains have homogenous or mottled CL textures. There is significant variation in the U-Pb isotopic composition of the 24 analyses, and only two zircons have estimated common lead concentrations <0.5 %. The highest common lead concentrations are in grains with mottled or dark CL textures. Common lead is positively correlated with $(La/Sm)_N$ (R ≈ 0.8), indicating metasomatic loss of Pb and gain in LREE. Calculating a discordia from 9 zircons with c. 1 % common lead or less gives upper and lower intercept ages of 2075 ± 16 and 368 ± 24 Ma (MSWD = 0.94), interpreted to reflect magmatic crystallisation and likely Caledonian Pb loss, respectively.

Sample *620* is an amphibolite where secondary minerals have entirely replaced the primary mineralogy (Table 1). The zircon grains from this sample are c. 80–240 μm, subhedral, stubby to prismatic with aspect ratios between 1:1 and 3:1. The zircons are dark in CL, some with faint oscillatory zoning (ES-4). Despite the general alteration of sample *620*, the zircon grains have lower estimated concentrations of common lead (<3.5 %) compared to sample *603*. Calculating a discordia based on

Table 1
Major phase XRD results (i.e. phase > 1 wt%) for samples analysed in this study. Lithological abbreviations: gabbro (GB), hybrid gabbro (HGB), metasediments (MS), ultramafic cumulate (UMC), amphibolite (AMP) and dolerite (DOL). Mineral abbreviations: quartz (Qz), plagioclase (Pl), olivine (Ol), diopside (Di), enstatite (En), biotite (bt), hornblende (Hb), kalifeldspar (Ksp), muscovite (Ms), chlorite (Chl), serpentine (Srp), magnetite (Mgt) and tremolite (Tr).

Sample	Depth (m)	Rock	Qz	Pl	Ol	Di	En	Bt	Hb	Ksp	Ms	Chl	Tlc	Srp	Mgt	Tr	Tot
603	7.6	GB	6	19		2		4	62	2		4					99
608	16.1	HGB	24	32		2		5	26			9					99
609	23.6	MS	31	48		3		5			7	5					99
610	25.3	GB	3	13		28	12	1	35			4	2				98
614	29.5	UMC							96	2		3					100
617	50	UMC			8	46	35		7		2			1			100
618	64.3	UMC										13			4	83	99
620	72.6	AMP						20	68			7	4				99
621	73.1	AMP						19	69			7	3		3		100
622	76.5	UMC			6		5					9		4	4	73	100
625	97	DOL	2	25		24			37	2	4	4					99
626	97.4	DOL		25		25			38	4	2	5					99
628	109.5	UMC			15	26	39		2		7			10			100

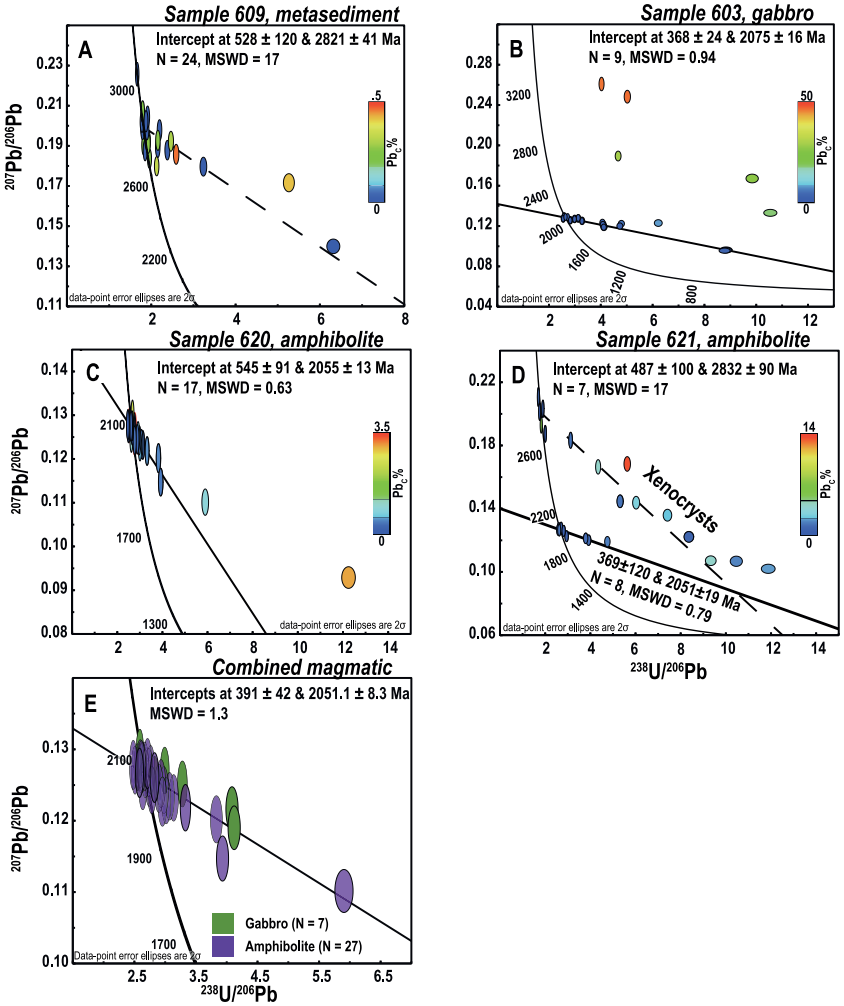

Fig. 5. U-Pb zircon geochronology. All the Tera-Wasserburg diagrams were created with Isoplot 4.15.11.10.15 using decay constants $\lambda_{238} = 1.55125 \times 10^{-10}$ and $\lambda_{235} = 9.8485 \times 10^{-10}$. (A) Metasediment wall-rock sample *609*. (B) Gabbro sample *603*. One outlier with 91 % common lead and a $^{207}Pb/^{206}Pb$ age of c. 5418 ± 30 Ma (i.e. *603–15*; ES-4) is omitted from the diagram. (C) Amphibolite sample *620*. (D) Amphibolite sample *621*. (E) shows a Tera-Wasserburg diagram with a discordia calculated by combining the magmatic zircon from the different samples.

24 analyses from 24 individual grains gives upper and lower intercept ages of 2041 ± 16 and 289 ± 33 Ma (MSWD = 2.8). The high MSWD indicates statistically significant deviation from linearity. Calculating a discordia based on 17 zircons with less than c. 1 % common lead gives upper and lower intercept ages of 2055 ± 13 and 545 ± 91 Ma (MSWD = 0.63; Fig. 5C), interpreted to reflect magmatic crystallisation and possibly Caledonian Pb loss, respectively.

Sample *621* is a amphibolite that resembles sample *620* chemically and mineralogically (Table 1). The primary mineralogy has been replaced entirely by secondary minerals. The zircon grains in this sample are c. 70–200 μm with aspect ratios between 1:1 and 3:1. The morphology of the zircon grains varies from anhedral to subhedral, subrounded or stubby to prismatic. The zircons are dark in CL, but some have brighter cores (ES-4). Some zircons are homogeneous and have faint oscillatory zoning from centre to rim, while others have rounded cores. Fig. 5D shows the 24 analyses from 23 zircon grains and shows that the sample contains two zircon populations. Regressing the individual populations of zircon with less than c. 1 % common lead gives one discordia with upper and lower intercept ages of 2832 ± 90 and 487 ± 100 Ma (MSWD = 17; N = 7) and another with upper and lower intercepts of 2051 ± 19 and 369 ± 120 Ma (MSWD = 0.79; N = 8). The lower intercepts are interpreted to reflect Caledonian Pb loss. The discordia with an upper intercept of 2832 ± 90 Ma is similar to the detrital zircon of sample *609*, indicating that these zircons are inherited. The high MSWD likely reflects the zircon grains' variable provenance (detrital). Only five xenocrystic zircons are > 90 % concordant with $^{207}Pb/^{206}Pb$ ages between 2912 ± 38 and 2720 ± 38 Ma. The discordia with an upper intercept age of 2051 ± 19 Ma is consistent with the

discordia ages of the magmatic zircons of sample *620* and *603* and likely reflect primary magmatic crystallisation.

The three U-Pb discordia ages from magmatic zircon range between 2051 ± 19 and 2055 ± 13 for the amphibolite samples and 2075 ± 16 Ma for the gabbro. The ages are statistically similar, and we cannot resolve a difference within a 2σ uncertainty. A combined regression of magmatic zircon analyses from all three samples with < 1 % common lead (N = 34) gives a well-defined discordia with upper and lower intercepts of 2051 ± 8 and 391 ± 42 Ma (MSWD = 1.3; Fig. 5E), taken here as the age of crystallisation of the Gállojávri intrusion.

6.3. Zircon Lu-Hf isotope data

Electronic supplement 5 presents the 55 in-situ Hf isotope analysis gathered from 54 zircon crystals selected from the four geochronology samples. Fourteen of the 55 analyses have propagated 2σ $^{176}Hf/^{177}Hf$ uncertainties above 5 ε-units and are therefore omitted from further reporting below. The initial epsilon Hf (εHf_t) is calculated relative to the upper intercept ages (c.f. Fig. 5). The εHf_t of xenocrystic and detrital zircon is calculated with the $^{207}Pb/^{206}Pb$ ages if < 10 % discordant; otherwise, initial values are relative to the upper intercept discordia age (2832 Ma) for xenocrystic zircon in sample *621*.

The nine zircon crystals analysed for Hf isotopes in the metasedimentary sample *609* show a range of εHf_t from −6.1 to 2.4, with a median value of 0.3 (Table 2). Except for the least radiogenic zircon, the values plot within the 3.0 and 3.5 Ga average crustal reference lines ($^{176}Lu/^{177}Lu = 0.015$) in the Hf isotope evolution plot (Fig. 6).

The ten xenocrystic zircons in sample *621* overlap with the detrital zircons of sample *609* in Fig. 6, with εHf_t from −3.6 to 4.6 and a median of 1.1 (Table 2). The four zircon grains from sample *621* interpreted to be magmatic have εHf_t from −14.4 to −10.0 and median of −10.6. These values overlap with sample *620*, which has εHf_t values from −11.5 to −8.2 and a median value of −10.2. As for sample *621*, it is noteworthy that these magmatic zircon grains indicate strong crustal involvement despite being collected from highly magnesian and LREE-depleted samples (see below).

The gabbroic sample *603* hosts the most radiogenic magmatic zircons identified in the Gállojávri intrusion (Table 2), although significant crustal involvement is still indicated by εHf_t from −7.5 to −1.4 with a median of −3.0 (Fig. 6). Two-stage depleted mantle model ages (T_{DM}) calculated relative to a depleted mantle model reservoir with present-day $^{176}Hf/^{177}Hf = 0.28325$ and $^{176}Lu/^{177}Hf = 0.0384$ and a crustal average $^{176}Lu/^{177}Hf = 0.015$ (Griffin et al., 2002; Griffin et al., 2000; Nowell et al., 1998) gives T_{DM} from c. 2.7 to 3.1 Ga, as opposed to zircons of the amphibolite samples giving model ages from c. 3.1 to 3.5 Ga.

6.4. Zircon trace element concentrations

Electronic supplement 6 presents the complete in-situ zircon trace element dataset. Although positively sloping, chondrite-normalised REE patterns characterise all samples, there is a relatively large variation between the samples and within a sample population. Therefore, we restrict further reporting on the trace element compositions to the 25 % and 75 % percentiles.

While overlapping in εHf_t and age in Fig. 6, the detrital- and xenocrystic zircon grains of samples *609* and *621* have distinctly different light- to middle-REE (L-/MREE) characteristics (Fig. 7A). Both zircon populations have positive Ce anomalies and similar $(La/Sm)_N$-ratios of 0.2–0.4 and 0.1–0.3 for *609* and *621*, respectively. However, the xenocrystic zircons of sample *621* have an order of magnitude higher LREE concentrations. The xenocrystic zircon is also distinguished by a positive Eu anomaly ranging from 1.2 to 7.4. A slightly negative Eu anomaly characterises the zircon of sample *609* (c. 0.6–1.1).

The magmatic zircons of samples *603*, *620* and *621* overlap in REE diagrams and are not easily distinguished (Fig. 7B). The magmatic zircons from sample *621* show the largest variation and are distinguished

Table 2
Summary of Lu-Hf isotope data.

Sample		Present-day $^{176}Hf/^{177}Hf$					εHf					T_{DM} (Ga)†				
	n	Min	1st quartile	Median	3rd quartile	Max	Min	1st quartile	Median	3rd quartile	Max	Min	1st quartile	Median	3rd quartile	Max
Metasediment																
609	9	0.28089	0.28096	0.28102	0.28105	0.28107	−6.1	−1.6	0.3	2.1	2.4	3.1	3.2	3.2	3.3	3.5
Gabbro																
603	10	0.28137	0.28146	0.28147	0.28149	0.28152	−7.5	−4.0	−3.0	−2.6	−1.4	2.7	2.8	2.8	2.9	3.1
Amphibolite																
620	8	0.28121	0.28121	0.28123	0.28126	0.28130	−11.5	−11.2	−10.2	−9.3	−8.2	3.1	3.2	3.3	3.3	3.3
621	4	0.28113	0.28116	0.28125	0.28126	0.28126	−14.4	−13.5	−10.6	−10.1	−10.0	3.2	3.2	3.3	3.4	3.5
Xenocryst																
621	10	0.28091	0.28100	0.28107	0.28113	0.28120	−3.6	−0.7	1.1	3.2	4.6	3.0	3.1	3.2	3.3	3.5

† Two-stage depleted-mantle model ages (T_{DM}) were calculated relative to a depleted mantle model reservoir with present-day $^{176}Hf/^{177}Hf = 0.28325$ and $^{176}Lu/^{177}Hf = 0.0384$, and the crustal average $^{176}Lu/^{177}Hf = 0.015$ for the Hf isotope evolution of crustal magma sources after separation from the depleted mantle.

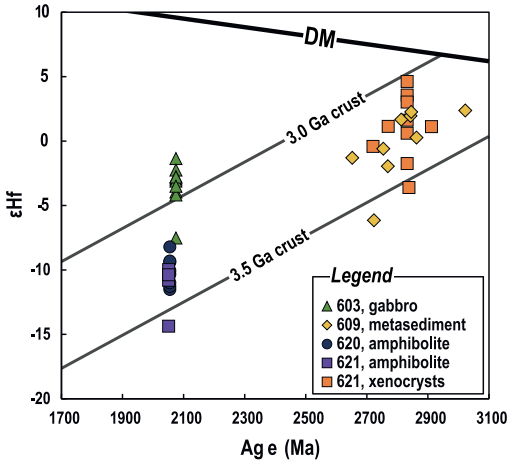

Fig. 6. Hf isotope evolution plot for the Gállojávri zircons. The isotope trajectories of the crust (formed at c. 2.9 and 3.5 Ga with $^{176}Lu/^{177}Lu = 0.015$) and depleted mantle (DM) are shown for reference.

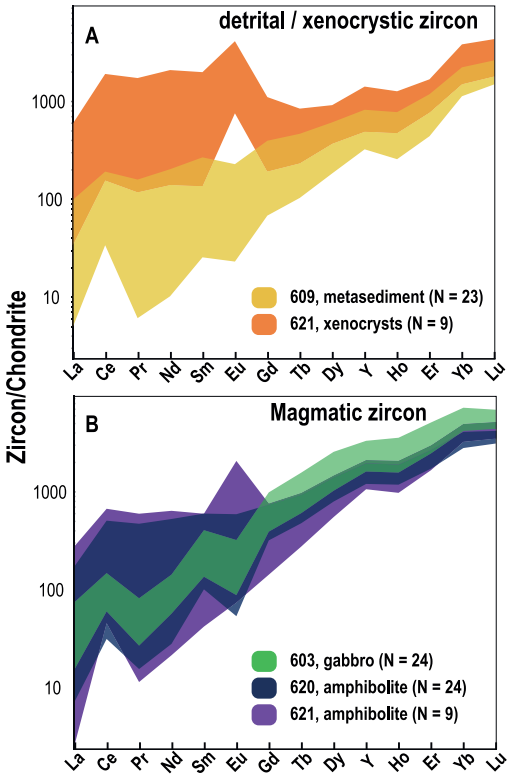

Fig. 7. Zircon trace element plots. (A) C1 chondrite normalised (Sun and McDonough, 1989) compositional fields (25 and 75% percentiles) for detrital and xenocrystic zircons. (B) C1 chondrite normalised fields for magmatic zircon.

by no to positive Eu anomalies (0.9–4.5); the other populations have negative Eu anomalies. The gabbroic zircons of sample *603* show the least variation with slightly higher heavy (H) REE concentrations.

6.5. Whole-rock Rb-Sr isotopes

The Rb-Sr isotope ratios are presented in Table 3 and Fig. 8. The initial Sr (Sr_i) compositions are calculated with a formation age of 2.05 Ga, except for the metasedimentary sample (*609*) calculated with the sample-specific zircon U-Pb age of 2.82 Ga (see Fig. 5A).

The hybrid gabbro (*608*) and metasedimentary rock (*609*) have the highest Sr_i compositions, with 0.70717 and 0.70709, respectively. There is considerable variation in Sr_i composition of the other magmatic rocks of the Gállojávri intrusion. The two gabbro samples range from 0.70002 (*610*) to 0.70477 (*603*). This range envelops the ultramafic cumulates with Sr_i from 0.70204 to 0.70413, excluding *618* that has Sr_i like the hybrid gabbro.

It is unlikely that sample *618* represents a closed system with respect to Sr as it is altered to a mineralogy dominated by tremolite and chlorite (Table 1). The two amphibolite samples (*620* and *621*) present clear evidence of Rb-Sr mobility with extremely high Rb concentrations (152, 165 ppm), present-day $^{87}Rb/^{86}Sr$ ranging from 27.1 to 28.2, and Sr_i initial ratios between 0.50410 and 0.57873; judging from mineralogy (Table 1), these values cannot represent primary magmatic ratios. The two dolerite samples also have unusually low Sr_i of 0.69192–0.69335, with mineral asseblages that indicates some alteration (Table 1). We note some uncertainty regarding the Sr_i of the dolerite dykes since we do not have a direct age. Regressing the magmatic whole-rock samples, excluding the hybrid gabbro, dolerite dykes and amphibolite sample *621* that contains abundant xenocrystic zircon, gives an errorchron age of 1691 ± 11 Ma (MSWD = 9) with a Sr_i of 0.7052 ± 0.0015 (Fig. 8). Despite the poor fit of the regression, the errorchron age might indicate when the Gállojávri Rb-Sr system was altered.

6.6. Whole-rock Sm-Nd isotopes

The whole-rock Sm-Nd isotope data are presented in Table 4 and Fig. 9, together with data compiled from the literature. As for Sr_i, all εNd_t values are calculated with a formation age of 2.05 Ga, except for the metasedimentary sample using the sample-specific zircon U-Pb age of 2.82 Ga. The compiled data presented in Fig. 9 have εNd_t calculated relative to the ages provided from the original references.

The magmatic whole-rock samples range about 19 ε-units, from −14.8 to 4.0 (Table 4). The ultramafic cumulates display the largest range from the most juvenile sample *622* ($\varepsilon Nd_t = 4.0$) to *617* with an εNd_t of −10.1. The εNd_t of sample *617* is less radiogenic than the extrapolated Nd isotope evolution trend of the metasedimentary sample (bold marked line in Fig. 9) and the exposed KGB Archaean basement, the Jergul Gneiss Complex (dark grey field; Fig. 9). The εNd_t of the two gabbro samples is consistent with the Sr isotopic data in that *610* is the most juvenile with an εNd_t of 2.5 and *603* being more evolved with an εNd_t of −1.4. The two dolerite samples have a narrow range close to that of sample *610*, with $\varepsilon Nd_t = 2.7–2.9$. The εNd_t of the hybrid gabbro (*608*) is −5.4, close to the Nd isotope evolution trend of the metasedimentary host rock (Fig. 9). There is an almost ten ε-unit difference between the two amphibolite samples, ranging from −14.8 to −5.0 for *620* and *621*, respectively. Sample *621* host a large amount of inherited zircon (see Fig. 5D) and plots close to the hybrid gabbro and the Nd evolution trend of the metasedimentary host rock (Fig. 9). Sample *620* has the most unradiogenic Nd composition of the dataset and plots well below the Nd isotope evolution trend of the local crystalline basement (Fig. 9).

6.7. Variation through the drill core

Fig. 10 shows the downhole variation in MgO wt.%, Nb/Th, εNd (2.05 Ga) and $^{87}Sr/^{86}Sr$ (2.05 Ga) in drill core 03GD002. Whole-rock

Table 3
Whole-rock Rb-Sr isotope data.

Sample no.	Rb (ppm)	Sr (ppm)	$^{87}Rb/^{86}Sr$	$^{87}Sr/^{86}Sr$	± 2σ	Age (Ma)	$^{87}Sr/^{86}Sr(t)$
Gabbro							
603	31.8	230	0.4005	0.716370	0.000008	2050	0.704768
610	26.8	109	0.7125	0.720658	0.000011	2050	0.700017
Hybrid gabbro							
608	49.5	289	0.4964	0.721547	0.000006	2050	0.707167
Dolerite							
625	46.1	174	0.7674	0.715577	0.000015	2050	0.693346
626	55	168.5	0.9458	0.719319	0.000014	2050	0.691921
Amphibolite							
620	165.5	18.8	27.1160	1.364232	0.000013	2050	0.578731
621	152.5	16.6	28.1838	1.320531	0.000016	2050	0.504099
Ultramafic cumulate							
614	2.6	13	0.5795	0.718823	0.000013	2050	0.702036
617	2.9	28.3	0.2967	0.710861	0.000009	2050	0.702267
618	1.7	19.7	0.2499	0.713758	0.000012	2050	0.706519
622	1	14.6	0.1983	0.709876	0.000013	2050	0.704132
628	3.2	22.2	0.4175	0.715386	0.000019	2050	0.703291
Metasediment							
609	63.4	298	0.6172	0.731825	0.000010	2821	0.707087

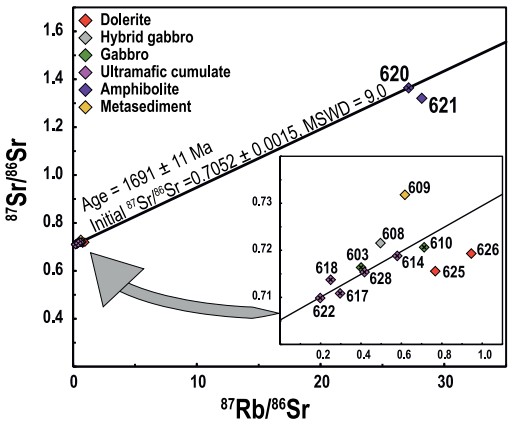

Fig. 8. Rb-Sr isochron diagram for whole-rock samples. For visibility, the lower-right isochron inset shows samples with $^{87}Rb/^{86}Sr < 1$. The errorchron (MSWD = 9.0) giving an age of 1691 ± 11 Ma and an initial $^{87}Sr/^{86}Sr$ of 0.7052 ± 0.0015 includes the eight samples marked with 'x'.

geochemistry for the samples in question is presented in ES-2, acquired from Orvik et al. (2022). From top to bottom in the drill core, the magmatic samples show increasing MgO (from 4 to 29 wt%) and uniformly low Nb/Th-ratios (c. 0.8–2.0). The low Nb/Th values are similar to the crustal average (~2.3; Weaver and Tarney, 1984) and may indicate significant contamination. The amphibolite and dolerite samples diverge from this generalisation (Fig. 10). The amphibolite samples (i.e. *620* and *621*) are texturally dissimilar from the surrounding ultramafic cumulate rocks but without distinct sharp boundaries. We note that the broken-up core makes definite contact relationships less clear (Fig. 4E). These samples have MgO in the range of 19–20 wt% and higher Nb/Th-values between 4.0 and 5.3. The dolerite samples are acquired from a fine-grained discontinuity (sheet) in the core and have MgO concentrations of c. 6 wt% with higher Nb/Th ratios in the range 5.5–6.0 (similar to primitive mantle Nb/Th ~ 8; Sun and McDonough, 1989).

The whole-rock isotopic data present a different and more complicated picture than the major- and trace elements (Fig. 10; c.f. Orvik et al., 2022). The large variation in Nd isotopic composition does not correlate with Nb/Th-ratios and shows erratic variation with depth. For example, the ultramafic cumulate samples have Nb/Th of 1.5 ± 0.3, suggesting uniform crustal contamination, but have εNd_t between −10.1 and +4 (Fig. 9). In the case of the dolerite samples, the positive εNd_t correlates with the highest Nb/Th ratios in the dataset. The amphibolite samples, however, also have high Nb/Th ratios but low to very low εNd_t values. In addition, the amphibolite samples and the most juvenile ultramafic cumulate sample (*622*) reveal highly localised variation in isotopic composition (Fig. 10). Fig. 4E shows the full range in Nd isotope composition within a core interval of c. 4 m.

7. Discussion

We interpret the upper intercept age of 2051 ± 8 Ma to correspond to crystallisation of the Gállojávri intrusion (Fig. 5E), similar to a geographically widespread c. 2.05 Ga group of (ultra)mafic intrusions and dykes in the Karelian province. In the Finnish CLGB, the c. 2.05 Ga group of layered intrusions locally cluster in the volcano-sedimentary Savukoski Group and consists of the 2063 ± 35 Ma Sakatti intrusion (re-Os isochron; Moilanen et al., 2021), the 2058 ± 4 Ma Kevitsa intrusion (U-Pb zircon; Mutanen and Huhma, 2001), the 2039 ± 14 Ma Moskuvaara intrusion (U-Pb zircon; Huhma et al., 2018), the 2035 ± 8 Ma Puijärvi gabbro and the 2025 ± 8 Ma Satovaara gabbro (average Pb-Pb; Huhma et al., 2018). If the Čorgaš formation-hosted Karenhaugen and Porsvann intrusions have similar ages to the Gállojávri intrusion, the c. 2.05 Ga (ultra)mafic intrusions likely extend throughout the KCLGB.

Considering Rb-Sr mobility, regional metamorphic history and the general alteration of the Gállojávri intrusion, the Rb-Sr isotope ratios are unlikely to represent primary magmatic ratios. The errorchron age of 1691 ± 11 Ma in Fig. 8 probably points to the timing of metamorphic overprinting and alteration and, although both age and significance remain speculative, we note that it broadly corresponds to hydrothermal activity, deformation and intrusion of pegmatite elsewhere in northern Fennoscandia (Bergh et al., 2015; Romer, 1996).

The two more immobile isotope systems (i.e., Lu-Hf and Sm-Nd) are more likely to represent primary magmatic ratios. The εHf_t magmatic zircon sample medians range from c. −11 to −3, with model ages between 2.8 and 3.3 Ga, implying a significant Archaean crustal contribution (Fig. 6). Crustal interaction is also evident from abundant xenocrystic zircon in sample *621* with Pb-Pb ages similar to the detrital zircon grains of sample *609*. Even larger variation is evident from the εNd_t data, ranging from depleted mantle values of c. 4 to strongly unradiogenic at c. −15. These findings align with the proposed multi-stage, polybaric petrogenetic model of the Gállojávri intrusion (Orvik et al., 2022). The large variation in εNd_t likely reflects the complexity of the evolution and the variable degree of interaction of the magmas with a continental crust of different ages and compositions. Furthermore, the

Table 4
Sm–Nd isotope data on whole rocks.

Sample no.	Sm (ppm)	Nd (ppm)	$^{147}Sm/^{144}Nd$	$^{143}Nd/^{144}Nd$	± 2σ	t (Ma)	εNd_t	T_{DM}(Ma)
Gabbro								
603	5.21	20.2	0.1559	0.512016	0.000005	2050	−1.4	2519
610	1.9	7.6	0.1511	0.512149	0.000007	2050	2.5	2068
Hybrid gabbro								
608	4.17	21.2	0.1189	0.511312	0.000004	2050	−5.4	2649
Dolerite								
625	3.06	11.2	0.1652	0.51235	0.000004	2050	2.7	2042
626	3.01	11.3	0.161	0.512305	0.000004	2050	2.9	2015
Amphibolite								
620	1.08	2.5	0.2612	0.512753	0.000007	2050	−14.8	
621	1.4	3.9	0.217	0.512658	0.000006	2050	−5	
Ultramafic cumulate								
614	0.98	3.3	0.1795	0.512346	0.000006	2050	−1.2	2740
617	0.86	2.4	0.2166	0.512394	0.000007	2050	−10.1	
618	0.91	2.6	0.2116	0.51251	0.000008	2050	−6.5	
622	0.54	2.1	0.1554	0.512284	0.000007	2050	4	1895
628	0.56	2.1	0.1612	0.51199	0.000007	2050	−3.3	2801
Metasediments								
609	4.61	29.8	0.0935	0.510908	0.000003	2821	3.8	2602

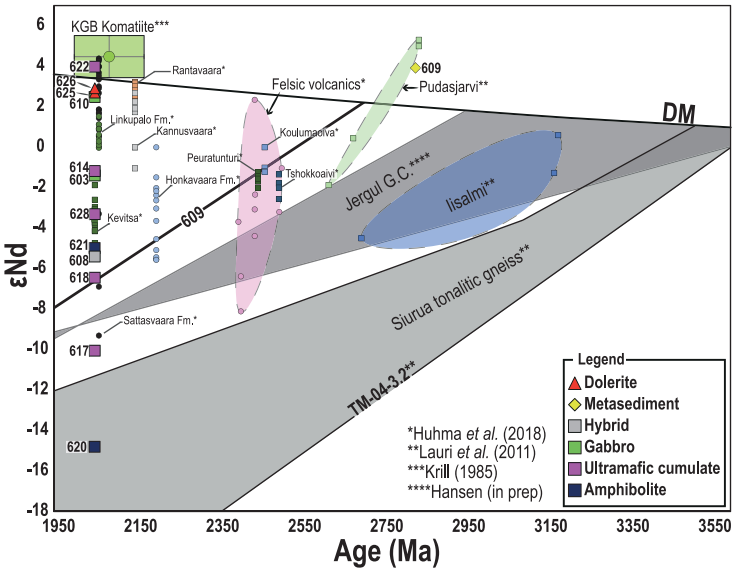

Fig. 9. Plot of εNd versus time for whole-rock samples of this study (identified in the legend) and compiled data from the Karelian province. Intrusions as squares, dykes as triangles and volcanic rocks as circles. The Palaeoproterozoic data from Linkupalo Fm., Kevitsa intrusion, Sattasvaara Fm., Rantavaara intrusion, Kannusvaara intrusion, Honkavaara Fm., felsic volcanic rocks (outlined), Peuratunturi intrusion, Koulumaoiva intrusion and the Tshokkoaivi intrusion were collected from the compilation of Huhma et al. (2018). Data for the Archaean Pudasjarvi (outlined) and Iisalmi (outlined) tonalite-trondhjemite-granodiorite-granite complexes and the Siurua tonalitic gneiss crustal evolution field are from Lauri et al. (2011). The shaded crustal evolution field of the Jergul Gneiss Complex (G.C.) is based on unpublished data (Hansen, in prep.). The Karasjok Greenstone Belt (KGB) komatiite average and 1σ error bars (green box) are based on data from Krill (1985). Depleted mantle (DM) evolution according to DePaolo (1981). (For interpretation of the references to colour in this figure legend, the reader is referred to the web version of this article.)

strongly unradiogenic Nd compositions documented for the ultramafic cumulate *617* ($\varepsilon Nd_t = -10.1$) and amphibolite *620* ($\varepsilon Nd_t = -14.8$) cannot be accounted for by interaction with local Archaean basement and indicate the presence of unidentified crustal components at depth (Fig. 9).

7.1. Testing the proposed petrogenetic model for the Gállojávri intrusion

The multistage (polybaric) recharge, assimilation and fractional crystallisation model of Orvik et al. (2022) used pillowed Karasjok-type komatiite (Barnes and Often, 1990) as the parental melt composition. In stage 1 of the model, the parental komatiite fractionated and interacted with crustal material at depth (700 MPa) represented by a weakly peraluminous normative granodiorite sample from the Jergul Gneiss Complex. The first simulation stage continued until the modelled melt had a composition similar to the chilled margin of the Gállojávri intrusion, represented by sample *610*. In stage 2 of the model, a melt with the composition of the chilled margin migrated to the middle crust (400 MPa), where it continued to fractionate and assimilate crustal material represented by the surrounding metasedimentary rocks. The stage 2 MCS simulation was constrained and tested by comparing the modelled solid and liquid phases with whole-rock and mineral chemistry. The modelling revealed that the system had to be open to recharge of melt to satisfactorily replicate the observed phase equilibria. Therefore, the second stage included the addition of juvenile komatiitic melt.

In the following, we implement the *MCS-PhaseEQ* models from Orvik et al. (2022) in *MCS-Traces* to test if the simulated variation in $^{87}Sr/^{86}Sr$ and $^{143}Nd/^{144}Nd$ is consistent with our reported ratios. We refer to the original paper for a detailed treatment of assumptions and choices of conditions and parameters. Table 5 gives the parental melt and wall rock composition used in the models. All isotopic ratios are back calculated to an age of 2.05 Ga.

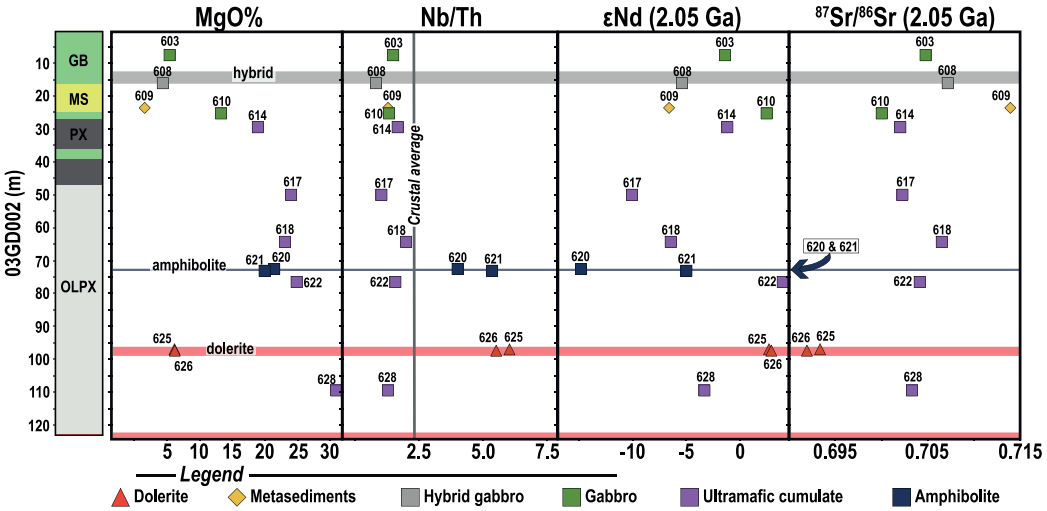

Fig. 10. Downhole variation in MgO wt.%, Nb/Th ratio, εNd (2.05 Ga) and $^{87}Sr/^{86}Sr$ (2.05 Ga) for drill core 03GD002. Crustal average Nb/Th from Weaver and Tarney (1984).

7.1.1. MCS-Traces parameters

Only sparse isotopic data exist for the KGB and the Archaean Jergul Gneiss Complex. Here, we use the average (N = 4) trace element composition and isotopic ratios of the 2085 ± 85 Ma (Sm-Nd error-chron) LREE depleted komatiite samples from Krill (1985) as the stage 1 parental melt and stage 2 recharge (Table 5). These samples are highly radiogenic with an εNd (2.05 Ga) of + 4.7, within error of expected depleted mantle values (Fig. 9; DePaolo, 1981). The initial wall rock parameters used for stages 1 and 2 of the isotope simulations are samples *041* and *103* (Table 5), collected from the Jergul Gneiss Complex (Hansen, in prep.) with crustal-like εNd (2.05 Ga) values of −8.7 and −8.6. The isotopic ratios of these samples were measured with the same methodology and instrumentation as in this study.

In the original *MCS-PhaseEQ* and trace element models, the stage 2 wall rock was assumed to be the metasedimentary host. Orvik et al. (2022) argued that the choice was somewhat arbitrary, as the Jergul Gneiss Complex samples and the metasedimentary host rocks are chemically similar. Indeed, the metasedimentary sample (*609*), a normative granodiorite, has an εNd (2.05 Ga) value of −6.6, making them hard to distinguish isotopically as well. Therefore, we use Jergul Gneiss Complex samples in both the lower- and middle crustal stages of the *MCS-Traces* simulation.

An irregularity in the original *MCS-PhaseEQ* model revealed by the isotopic data is that the assumed chilled margin (*610*) is too juvenile. The εNd (2.05 Ga) of + 2.5 is inconsistent with a melt that has experienced significant interaction with Archaean crustal material. Instead, in the stage 2 models, we use the modelled melt concentrations and isotopic ratios when the simulation has attained an MgO content of 12 wt%, like that of the previously assumed chilled margin.

The partition coefficients (K_{sm}) for both the resident magma body and wall-rock reservoirs are the same as in the original model. The values were collected from the EarthRef database (https://earthref.org/KDD/) and listed in the *MCS-Traces* output files provided in the supplementary material (Orvik et al., 2022, and references therein).

Table 5
Parental melt (PM), recharge (R) and wall rock (WR) compositions used in the models. Trace element concentrations in parts per million (ppm).

	Komatiite	041	103
	PM, R	WR	WR
Rb	0.1	114.5	62.4
Sr	55.9	134	248
Nd	2.9	31.3	12.9
Sm	1.1	5.8	3.29
$(^{87}Sr/^{86}Sr)_t$	0.702949	0.705622	0.714402
$(^{143}Nd/^{144}Nd)_t$	0.510225	0.509541	0.509545
εNd_t	4.7	−8.7	−8.6

Sources for the trace elements and isotope values are provided in the text. PM is the recharge magma composition in the stage 2 RAFC model. Initial isotope ratios calculated at 2.05 Ga.

7.1.2. MCS-Traces results

Fig. 11 shows the simulated variation in $^{143}Nd/^{144}Nd$ and $^{87}Sr/^{86}Sr$ compositions, together with most of the data from this study. The figure does not show the two amphibolite samples with $^{87}Sr/^{86}Sr$ (2.05 Ga) ratios between 0.50410 and 0.57873. The thick black lines in Fig. 11 reflect the two different wall-rock reservoirs. Electronic supplement 7 present the tabulated *MCS-Traces* output.

Most of the isotopic data match the simulated variation predicted by the *MCS-PhaseEQ* models (Fig. 11). Only a small amount of crustal contamination is needed to lower the $^{143}Nd/^{144}Nd$ composition initially, as the parental komatiite has a relatively low Nd concentration relative to the Jergul Gneiss Complex wall rocks and their partial melts. The rapidly decreasing $^{143}Nd/^{144}Nd$-ratio is especially apparent when the wall-rock reservoir has the composition of sample *041* with Nd = 31.3 ppm and $^{143}Nd/^{144}Nd$ (2.05 Ga) = 0.50954 (εNd_t = −8.7). In the model, the parental komatiitic melt, with a liquidus temperature of c. 1698 °C, intrudes the lower crust and after some heating of the wall rock, a 3 % addition of anatectic melt is needed to lower the $^{143}Nd/^{144}Nd$ from 0.51022 (εNd = +4.7) to 0.50994 (εNd = −0.8). When the parental melt has cooled to c. 1298 °C and has a composition consistent with the starting melt of the second-stage model, 15 % of anatectic crustal melt has been added, lowering the $^{143}Nd/^{144}Nd$-ratio of the melt in the resident magma chamber to 0.50967 (εNd = −6.1). The other assumed wall-rock reservoir, sample *103*, has a similar $^{143}Nd/^{144}Nd$-ratio, but because of the lower Nd concentration (12.9 ppm; Table 5), the simulation terminates with a $^{143}Nd/^{144}Nd$-ratio of 0.50980 (εNd = −3.7) after 15 % contamination (Fig. 11).

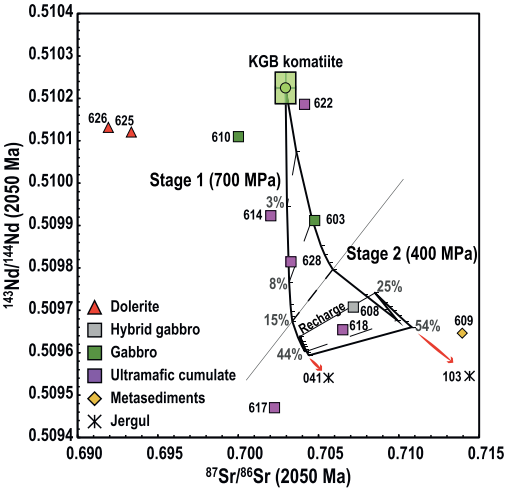

Fig. 11. Whole-rock Sr and Nd isotope ratio plot with the two-stage Magma Chamber Simulator models. The primary magma Sr and Nd isotope ratios for the stage 1 model are the averages of the LREE-depleted komatiite samples documented by Krill (1985).

In the second stage (400 MPa), the melt continues to fractionate and assimilate Jergul Gneiss Complex crustal material. When the melt in the resident magma chamber has cooled to c. 1026 °C, it has in total (stages 1 & 2) assimilated 44 % of anatectic melt and attained a slightly lower $^{143}Nd/^{144}Nd$ = 0.50960 (εNd = −7.5) when assimilating sample *041* (left; Fig. 11). At the same step in the model, using sample *103* to represent the wall-rock reservoir gives $^{143}Nd/^{144}Nd$ = 0.50968 (εNd = −6.0). The effects of contamination in the second stage are marginal compared to the first stage of the model. The hybrid resident melt has higher elemental concentrations and more similar isotopic ratios to the wall rock. Still, the variation predicted in the stage two simulations is consistent with our observations (Fig. 11).

In the original model by Orvik et al. (2022), a recharge of primitive komatiite is triggered at this step (at 1026 °C), adding a mass equivalent to 75 % of the starting resident melt mass. The relatively large mass only slightly increases the $^{143}Nd/^{144}Nd$ ratio of the melt in the resident chamber (Fig. 11). Although having a highly juvenile Nd isotope composition, the low Nd concentration of the recharge melt prevents it from significantly changing the resident melt composition.

The simulated compositional space follows similar trends but does not completely overlap with the available data. Inconsistencies include sample *610* with a Nd isotopic composition too juvenile to be consistent with a hybrid melt that has experienced significant crustal contamination. Sample *610* also plots off the trend of the other magmatic samples with a slightly lower $^{87}Sr/^{86}Sr$-ratio. It is also clear that our known wall-rock reservoirs cannot fully describe the observed variation. Both sample *617* and *620* are MgO-rich rocks with very low εNd values that require a more evolved crustal contaminant (Fig. 9).

8. Implications for crustal architecture, assembly of the Gállojávri intrusion, regional considerations and prospectivity

The Gállojávri intrusion exhibits a large variation in initial εNd, revealing the complexity of its composition, evolution and the variable degree of interaction of the parental magmas with crustal material. The isotopic variation is largely consistent with the previously suggested multistage and polybaric petrogenetic model of Orvik et al. (2022). Nevertheless, the lowest initial εNd values imply interaction with more evolved, unidentified continental crust in the KGB basement. This finding is not a complete surprise. In Finland, the Archaean basement of the western Karelian province contains compositionally diverse TTGGs formed between 3.5 and 2.8 Ga (Hölttä et al., 2012; Mutanen and Huhma, 2003). If the wall-rock reservoir had a composition similar to the c. 3.5 Ga Siurua tonalitic gneiss (Mutanen and Huhma, 2003), with an εNd (2.05 Ga) ~ −23 (Fig. 9; TM−04–3.2; Lauri et al., 2011), the first MCS model stage would result in a $^{143}Nd/^{144}Nd$ ratio of 0.50893 (εNd = −20.6; ES-8).

The simulated variation assumes complete mixing between the melt in the resident magma chamber and the added anatectic- and recharged melts. This assumption is unlikely to hold based on the downhole variation (Fig. 10) that shows large variations in isotopic signatures over very small distances (decimetres to a few metres). The heterogeneity implies incomplete mixing of isotopically distinct melts forming domains in the Gállojávri stratigraphy. A growing body of evidence suggests that several mid-to-upper crustal plutons are built by repeated injections into a crystal mush (Barboni et al., 2013; Bartley et al., 2008; Hepworth et al., 2020; Hepworth et al., 2017, 2018; Miller et al., 2011; Mungall et al., 2016; Nebel et al., 2020). For example, many of the major peridotite layers hosted in the Rum layered intrusion (NW Scotland) show lateral discontinuity, have upward-oriented apophyses and show cross-cutting relationships with the overlying troctolite, indicating that they formed via incremental sill emplacement (Hepworth et al., 2020; Hepworth et al., 2017, 2018). Geophysical imaging of active conduits has also revealed how the stacking of sills makes up part of smaller plumbing systems (Magee et al., 2018). For example, at various levels in the crust beneath the Afar depression (Ethiopia; Ebinger et al., 2008; Hammond, 2014), beneath the axis of the East Pacific Rise (Marjanović et al., 2014) and axial seamount in the northeastern Pacific Ocean (Carbotte et al., 2020). Also, high-precision U-Pb geochronology has led to the discovery of out-of-sequence layers in the Stillwater Complex (USA; Wall et al., 2018) and the Bushveld Complex (South Africa; Mungall et al., 2016). The zircon U-Pb geochronology recorded for the Gállojávri intrusion suggests an age difference between the younger isotopically evolved amphibolite samples and the older, more juvenile gabbro (Fig. 5). However, we are unable to resolve this with our current analytical precision.

In the case of the Gállojávri intrusion, the observed phase equilibria and the cumulate sequence can be satisfactorily replicated with thermodynamic modelling founded on classical ideas of magma chamber processes (Orvik et al., 2022). Therefore, we do not advocate a model where the random stacking of sills built the Gállojávri intrusion. However, this does not negate incomplete mixing with later magma injections, variable contamination by country rocks or local dissolution or melting of xenolithic blocks, which depends on rheological differences (e.g. Namur et al., 2015). If we exclude magma recharge, xenolith melting is the most efficient and quickest process leading to the hybridisation of a magmatic system (Robertson et al., 2015). It is also consistent with the presence of xenoliths in the hybrid zone (Fig. 4J) and the zircon xenocrysts distinguished in the U-Pb isotopic data (Fig. 5D). However, the lowest εNd values still require a crustal component different from what is documented in this study and suggest that some xenoliths derived from presently unexposed or unidentified crustal domains. The distance a xenolith can be transported would be contingent on the xenolith's lithology and the carrier magma's composition (McLeod and Sparks, 1998). If a xenolith is buoyant and takes a day to melt, the carrier magma could have flowed tens of kilometres (Barnes and Robertson, 2019).

Still, this does not explain the local juvenile isotope compositions observed in sample 622. Considering that most of the magmatic samples show signs of crustal interaction with an interquartile εNd range from −6.2 to −1.3, the local positive values suggest another mechanism leading to the juvenile domains. However, it is not uncommon for magmatic conduits to experience pulses of more primitive melt resulting in reverse compositional trends (Chistyakova and Latypov, 2012;

Latypov, 2015; Yudovskaya et al., 2015). This interpretation would be in-line with the MCS conduit model that requires recharge(s) of primitive, uncontaminated komatiite (Orvik et al., 2022).

We propose that the variability in the isotopic signature is the result of local dissolution or melting of xenoliths and incomplete mixing of late melt pulses injected into the hot and semi-consolidated Gállojávri chamber. We note that our interpretation is based on the variation observed in one drill core. To determine the spatial extent of the isotopically distinct domains would require a comprehensive drilling campaign and systematic sampling.

A possible KCLGB analogue is the contemporary Kevitsa Complex (c. 2.06 Ga; Mutanen and Huhma, 2001) that hosts an important Ni-Cu-PGE deposit. During the exploration and development of the Kevitsa mine (production began in 2012), the intrusion has benefited from multiple drilling campaigns (Santaguida et al., 2015). Luolavirta (2018), working with the extensive lithochemical database and drill cores, proposed a similar multistage and polybaric petrogenetic model. The intrusion represents a sub-volcanic conduit that, in the first stage, fed subaerial, contemporary picritic lavas (c. 2.06 Ga; Hanski et al., 2001). In the second stage, basaltic melt — fractionated in a staging magma chamber from the initial picrite, intruded through the same pre-established Kevitsa conduit (Luolavirta et al., 2018b, c). These stages resulted in a body of ultramafic cumulates that record a simple lithological stratigraphy with fairly constant $^{87}Sr/^{86}Sr$ compositions (Luolavirta, 2018; Luolavirta et al., 2018a; Luolavirta et al., 2018c) and average εNd (2.05 Ga) of -3.5 ± 0.5 (Huhma et al., 2018). The Ni-PGE ores hosted by the intrusion occur as irregular and discontinuous lens-like bodies (Yang et al., 2013). The ores are distinctly different to the surrounding cumulates, with complex internal architecture, cryptic variation and crustal isotopic signatures with high $^{87}Sr/^{86}Sr$ 0.709–0.711 (Luolavirta et al., 2018a) and low εNd −6.4 (Huhma et al., 2018). Luolavirta (2018) proposed a third stage of formation with repeated melt injections following a different route into the semi-consolidated Kevitsa magma chamber, which assimilated different and unidentified country-rock material and gave rise to the Ni-PGE ore (Luolavirta et al., 2018a; Luolavirta et al., 2018c).

The KCLGB contains numerous (ultra)mafic intrusive bodies and is considered highly prospective for Ni-Cu-(PGE) sulphides, with discoveries such as the Kevitsa and Sakatti deposits (Brownscombe et al., 2015). Orvik et al. (2022) noted that multiple injections of melt fractionated at various depths are probably widely applicable to the petrogenesis of Palaeoproterozoic Fennoscandian (ultra)mafic intrusions and a potentially effective mechanism for forming viable economic Ni-Cu-(PGE) deposits. In the Kevitsa intrusion, the high tenor Ni-PGE ores are interpreted to result from the assimilation of proto-ores (Mutanen, 1997; Yang et al., 2013), deposited with the ultramafic cumulates in the initial stages, by the repeated magma injections of the third stage (Luolavirta, 2018; Luolavirta et al., 2018a), similar to models proposed for ore mineralisations in Voisey's bay (Li and Naldrett, 1999), Noril'sk (Barnes and Lightfoot, 2005; Naldrett, 2004), Santa Rita (Barnes et al., 2011) and Kabanga (Maier and Barnes, 2010; Maier et al., 2010). The largest mafic layered intrusion on Earth, the Bushveld Complex in South Africa, contains significant quantities of Cr, Ni, V, Ti, Co and PGE. Despite the immense difference in size between the 2.3 km^2 Gállojávri intrusion and the ca. 60,000 km^2 Bushveld Complex, some tectonomagmatic aspects (plume related) and age (ca. 2050 Ma) appear to be similar (Cawthorn and Walraven, 1998; Scoates and Friedman, 2008). Several similarities also exist in terms of magmatic processes. In particular, the Bushveld Complex displays a range of isotopic compositions suggesting derivation from primitive mantle as well as enriched, subcontinental lithospheric sources, followed by variable interaction with lower cratonic crust and later by interaction with upper-crustal pelitic lithologies (e.g., Maier et al., 2000; Wilson et al., 2017). The existence of variably disaggregated xenolith of country rock also attest to interaction with the mafic magmas, with incomplete mixing and recharge of variably sourced and contaminated melts resulting in a lack of simple progressions in terms of magma evolution and stratigraphic control (Wilson et al., 2017). Studies of layered mafic intrusions invariably find evidence of extensive interaction with crustal rocks; however, although assimilation of S-rich rocks can be an important parameter for attaining sulphur saturation and, in turn, form a sulphide mineralization, the relationship between contamination and the formation of a deposit can be complex and in some cases dilute the metal tenors (Ihlenfeld and Keays, 2011).

This study and that of Orvik et al. (2022) have shown that the magmatic processes that operated in the Gállojávri intrusion are similar to those observed in similar, layered mafic intrusions of different age worldwide. In many cases, these intrusions carry significant occurrences of critical metals. Our work on the Gállojávri intrusion has provided new information about the magmatic evolution of the KGB and the composition of its Archaean substrate, and further work on the other ca. 2050 Ma mafic intrusions in the KGB, involving diamond drilling combined with petrographic, geochemical and isotopic studies, is likely to provide new information on the regional tectonomagmatic evolution and prospectivity of the region.

9. Conclusions

The data and modelling presented above lead to the following conclusions:

- Zircon U-Pb dating shows that the Gállojávri intrusion was emplaced at 2051 ± 8 Ma, suggesting it is part of a similarly aged group of (ultra)mafic intrusions in the KCLGB. Lower discordia intercept ages are consistent with Caledonian lead loss.
- The variation observed in the Sr–Nd–Hf isotopic data reveals the complexity of the magmatic evolution and aligns with the previously proposed multistage, polybaric petrogenetic model of the Gállojávri intrusion.
- The modelled isotopic variation is consistent with a previously proposed Karasjok-type komatiite parental magma; however, the strongly unradiogenic Nd compositions observed in ultramafic rocks suggest interaction with more evolved, unidentified crust in the KGB basement.
- Large variation in isotopic signatures over small distances suggests local dissolution or melting of xenoliths and incomplete mixing of isotopically distinct melts forming domains in the Gállojávri stratigraphy.

Funding

This research did not receive any specific grant from funding agencies in the public, commercial, or not-for-profit sectors. This study is part of Alf Andre Orvik's PhD Project on the Gállojávri intrusion in the Karasjok Greenstone Belt, funded by the Department of Geoscience and Petroleum, Faculty of Engineering, at the Norwegian University of Science and Technology and the Geological Survey of Norway. The Lu-Hf isotopic data were collected at the Norwegian Laboratory for Mineral and Materials Characterisation, MiMaC, for which the Research Council of Norway is acknowledged for support, project number 269842/F50.

CRediT authorship contribution statement

Alf Andre Orvik: Conceptualization, Investigation, Methodology, Data curation, Formal analysis, Writing – original draft. **Trond Slagstad:** Conceptualization, Investigation, Supervision, Data curation, Writing – review & editing. **Bjørn Eske Sørensen:** Data curation, Supervision, Writing – review & editing. **Ian Millar:** Investigation, Data curation, Writing – review & editing. **Harald Hansen:** Investigation, Resources, Writing – review & editing.

Declaration of Competing Interest

The authors declare that they have no known competing financial interests or personal relationships that could have appeared to influence the work reported in this paper.

Data availability statement

The data underlying this research are available in the article and in its online supplementary material.

Acknowledgements

We thank the reviewers and editor for constructive comments and suggestions that help clarify several aspects of the paper. We acknowledge the past drilling program by Tertiary Gold Ltd., which is a prerequisite for this study. We are grateful to Lars Petter Nilsson for sharing knowledge and providing insightful comments regarding the Gállojávri intrusion. We also want to acknowledge Doris Wagner and Nicola Atkinson at the British Geological Survey for their assistance with the Rb-Sr and Sm-Nd analysis.

Appendix A. Supplementary data

Supplementary data to this article can be found online at https://doi.org/10.1016/j.precamres.2022.106813.

References

Arndt, N.T., Jenner, G.A., 1986. Crustally contaminated komatiites and basalts from Kambalda, Western Australia. Chem. Geol. 56 (3-4), 229–255.
Barboni, M., Schoene, B., Ovtcharova, M., Bussy, F., Schaltegger, U., Gerdes, A., 2013. Timing of incremental pluton construction and magmatic activity in a back-arc setting revealed by ID-TIMS U/Pb and Hf isotopes on complex zircon grains. Chem. Geol. 342, 76–93.
Barnes, S.-J., Lightfoot, P.C., 2005. Formation of magmatic nickel-sulfide ore deposits and processses affecting their copper and platinum-group element contents. In: Hedenquist, J.W., Thompson, J.F.H., Goldfarb, R.J., Richards, J.P. (Eds.), One Hundredth Anniversary Volume. Society of Economic Geologists, Economic Geology, pp. 179–213. https://doi.org/10.5382/AV100.08.
Barnes, S.J., Cruden, A.R., Arndt, N., Saumur, B.M., 2016. The mineral system approach applied to magmatic Ni–Cu–PGE sulphide deposits. Ore Geol. Rev. 76, 296–316.
Barnes, S.-J., Often, M., 1990. Ti-Rich Komatiites from Northern Norway. Contrib. Miner. Petrol. 105 (1), 42–54.
Barnes, S.J., Osborne, G.A., Cook, D., Barnes, L., Maier, W.D., Godel, B., 2011. The Santa Rita Nickel Sulfide Deposit in the Fazenda Mirabela Intrusion, Bahia, Brazil: Geology, Sulfide Geochemistry, and Genesis. Econ. Geol. 106 (7), 1083–1110.
Barnes, S.J., Robertson, J.C., 2019. Time scales and length scales in magma flow pathways and the origin of magmatic Ni–Cu–PGE ore deposits. Geosci. Front. 10 (1), 77–87.
Bartley, J.M., Coleman, D.S., Glazner, A.F., 2008. Incremental pluton emplacement by magmatic crack-seal. Trans. Royal Soc. Edinburgh: Earth Sci. 97 (4), 383–396.
Bergh, S.G., Corfu, F., Priyatkina, N., Kullerud, K., Myhre, P.I., 2015. Multiple post-Svecofennian 1750–1560Ma pegmatite dykes in Archaean-Palaeoproterozoic rocks of the West Troms Basement Complex, North Norway: Geological significance and regional implications. Precambr. Res. 266, 425–439.
Bingen, B., Solli, A., Viola, G., Torgersen, E., Sandstad, J.S., Whitehouse, M.J., Røhr, T.S., Ganerød, M., Nasuti, A., 2015. Geochronology of the palaeoproterozoic kautokeino greenstone belt, finnmark, Norway: Tectonic implications in a Fennoscandia context. Norw. J. Geol. 95, 365–396.
Bohrson, W.A., Spera, F.J., Ghiorso, M.S., Brown, G.A., Creamer, J.B., Mayfield, A., 2014. Thermodynamic model for energy-constrained open-system evolution of crustal magma bodies undergoing simultaneous recharge, assimilation and crystallization: The magma chamber simulator. J. Petrol. 55, 1685–1717.
Bohrson, W.A., Spera, F.J., Heinonen, J.S., Brown, G.A., Scruggs, M.A., Adams, J.V., Takach, M.K., Zeff, G., Suikkanen, E., 2020. Diagnosing open-system magmatic processes using the Magma Chamber Simulator (MCS): part I—major elements and phase equilibria. Contrib. Miner. Petrol. 175, 1–29.
Braathen, A., Davidsen, B., 2000. Structure and stratigraphy of the Palaeoproterozoic Karasjok Greenstone Belt, north Norway - regional implications. Norw. J. Geol. 80 (1), 33–50.
Brownscombe, W., Ihlenfeld, C., Coppard, J., Hartshorne, C., Klatt, S., Siikaluoma, J.K., Herrington, R.J., 2015. The Sakatti Cu-Ni-PGE Sulfide Deposit in Northern Finland. In: Maier, W.D., Lahtinen, R., O'Brien, H. (Eds.), Mineral Deposits of Finland. Elsevier, pp. 211–252.
Carbotte, S.M., Arnulf, A., Spiegelman, M., Lee, M., Harding, A., Kent, G., Canales, J.P., Nedimović, M., 2020. Stacked sills forming a deep melt-mush feeder conduit beneath Axial Seamount. Geology 48, 693–697.
Cawthorn, R.G., Walraven, F., 1998. Emplacement and Crystallization Time for the Bushveld Complex. J. Petrol. 39 (9), 1669–1687.
Chistyakova, S., Latypov, R., 2012. Magma differentiation and crystallization in basaltic conduits by two competing petrogenetic processes. Lithos 148, 142–161.
Corfu, F., Hanchar, J.M., Hoskin, P.W., Kinny, P., 2003. Atlas of zircon textures. Rev. Mineral. Geochem. 53, 469–500.
DePaolo, D.J., 1981. Neodymium isotopes in the Colorado Front Range and crust–mantle evolution in the Proterozoic. Nature 291 (5812), 193–196.
Dickin, A.P., Durant, G.P., 2002. The Blackstones Bank igneous complex: geochemistry and crustal context of a submerged Tertiary igneous centre in the Scottish Hebrides. Geol. Mag. 139 (2), 199–207.
Ding, X., Ripley, E.M., Shirey, S.B., Li, C., 2012. Os, Nd, O and S isotope constraints on country rock contamination in the conduit-related Eagle Cu–Ni–(PGE) deposit, Midcontinent Rift System, Upper Michigan. Geochim. Cosmochim. Acta 89, 10–30.
Ebinger, C.J., Keir, D., Ayele, A., Calais, E., Wright, T.J., Belachew, M., Hammond, J.O.S., Campbell, E., Buck, W.R., 2008. Capturing magma intrusion and faulting processes during continental rupture: seismicity of the Dabbahu (Afar) rift. Geophys. J. Int. 174, 1138–1152.
Eilu, P., 2012. Mineral deposits and metallogeny of Fennoscandia. Geological Survey of Finland, Special Paper 53.
Fowler, S.J., Bohrson, W.A., Spera, F.J., 2004. Magmatic evolution of the Skye igneous centre, western Scotland: Modelling of assimilation, recharge and fractional crystallization. J. Petrol. 45, 2481–2505.
Ghiorso, M.S., Gualda, G.A.R., 2015. An H2O–CO2 mixed fluid saturation model compatible with rhyolite-MELTS. Contrib. Miner. Petrol. 169, 53.
Ghiorso, M.S., Hirschmann, M.M., Reiners, P.W., Kress, V.C., 2002. The pMELTS: A revision of MELTS for improved calculation of phase relations and major element partitioning related to partial melting of the mantle to 3 GPa. Geochem Geophy Geosy 3 (5), 1–35.
Ghiorso, M.S., Sack, R.O., 1995. Chemical mass transfer in magmatic processes IV. A revised and internally consistent thermodynamic model for the interpolation and extrapolation of liquid-solid equilibria in magmatic systems at elevated temperatures and pressures. Contrib. Miner. Petrol. 119 (2-3), 197–212.
Griffin, W.L., Pearson, N.J., Belousova, E., Jackson, S.E., van Achterbergh, E., O'Reilly, S. Y., Shee, S.R., 2000. The Hf isotope composition of cratonic mantle: LAM-MC-ICPMS analysis of zircon megacrysts in kimberlites. Geochim. Cosmochim. Acta 64 (1), 133–147.
Griffin, W.L., Wang, X., Jackson, S.E., Pearson, N.J., O'Reilly, S.Y., Xu, X., Zhou, X., 2002. Zircon chemistry and magma mixing, SE China: in-situ analysis of Hf isotopes, Tonglu and Pingtan igneous complexes. Lithos 61 (3-4), 237–269.
Gualda, G.A.R., Ghiorso, M.S., Lemons, R.V., Carley, T.L., 2012. Rhyolite-MELTS: a Modified Calibration of MELTS Optimized for Silica-rich, Fluid-bearing Magmatic Systems. J. Petrol. 53 (5), 875–890.
Hammond, J.O.S., 2014. Constraining melt geometries beneath the Afar Depression, Ethiopia from teleseismic receiver functions: The anisotropic H-k stacking technique. Geochem. Geophys. Geosyst. 15, 1316–1332.
Hansen, H., Slagstad, T., Bergh, S.G.. Geochemical volcanostratigrapy defines the tectonic evolution of the Karasjok Greenstone Belt, Finmark, The. https://doi.org/10.13140/RG.2.2.34380.16001.
Hanski, E., Huhma, H., 2005. Chapter 4 Central Lapland greenstone belt. In: Lehtinen, M., Nurmi, P.A., Rämö, O.T. (Eds.), Precambrian Geology of Finland Key to the Evolution of the Fennoscandian Shield. Elsevier, pp. 139–193. https://www.sciencedirect.com/science/article/abs/pii/S0166263505800052?via%3Dihub.
Hanski, E., Huhma, H., Rastas, P., Kamenetsky, V.S., 2001. The palaeoproterozoic komatiite-picrite association of Finnish lapland. J. Petrol. 42, 855–876.
Hanson, G.N., Langmuir, C.H., 1978. Modelling of major elements in mantle-melt systems using trace element approaches. Geochim. Cosmochim. Acta 42 (6), 725–741.
Hanson, G.N., 1989. An approach to trace element modeling using a simple igneous system as an example. In: Lipin, B.R., McKay, G.A. (Eds.), Geochemistry and Mineralogy of Rare Earth Elements. De Gruyter, p. 18. https://doi.org/10.1515/9781501509032-007.
Heinonen, J.S., Bohrson, W.A., Spera, F.J., Brown, G.A., Scruggs, M.A., Adams, J.V., 2020. Diagnosing open-system magmatic processes using the Magma Chamber Simulator (MCS): part II—trace elements and isotopes. Contrib. Miner. Petrol. 175, 1–21.
Heinonen, J.S., Luttinen, A.V., Spera, F.J., Bohrson, W.A., 2019. Deep open storage and shallow closed transport system for a continental flood basalt sequence revealed with Magma Chamber Simulator. Contributions to Mineralogy and Petrology 174, 87. https://doi.org/10.1007/s00410-019-1624-0.
Heinonen, J.S., Iles, K.A., Heinonen, A., Fred, R., Virtanen, V.J., Bohrson, W.A., Spera, F. J., 2021. From Binary Mixing to Magma Chamber Simulator: Geochemical Modeling of Assimilation in Magmatic Systems. In: Masotta, M., Beier, C., Mollo, S. (Eds.), Crustal Magmatic System Evolution, first ed. co-publication of the American Geophysical Union and John Wiley and Sons Inc, pp. 151–176.
Henriksen, H., 1986. Bedrock map Iddjajavri 2034 II M 1:50 000, preliminary edition. Geological Survey of Norway.
Hepworth, L.N., O'Driscoll, B., Gertisser, R., Daly, J.S., Emeleus, C.H., 2017. Incremental Construction of the Unit 10 Peridotite, Rum Eastern Layered Intrusion, NW Scotland. J. Petrol. 58, 137–166.
Hepworth, L.N., O'Driscoll, B., Gertisser, R., Daly, J.S., Emeleus, C.H., 2018. Linking In Situ Crystallization and Magma Replenishment via Sill Intrusion in the Rum Western Layered Intrusion, NW Scotland. J. Petrol. 59, 1605–1642.

Hepworth, L.N., Kaufmann, F.E.D., Hecht, L., Gertisser, R., O'Driscoll, B., 2020. Braided peridotite sills and metasomatism in the Rum Layered Suite, Scotland. Contributions Mineral. Petrol. 175, 17.

Huhma, H., Hanski, E., Kontinen, A., Vuollo, J., Mänttäri, I., Lahaye, Y., 2018. Sm–Nd and U-Pb isotope geochemistry of the Palaeoproterozoic mafic magmatism in eastern and northern Finland. Geological Survey of Finland. Bulletin 405, 150.

Ihlenfeld, C., Keays, R.R., 2011. Crustal contamination and PGE mineralization in the Platreef, Bushveld Complex, South Africa: evidence for multiple contamination events and transport of magmatic sulfides. Miner. Deposita 46, 813–832.

Hölttä, P., Heilimo, E., Huhma, H., Juopperi, H., Kontinen, A., Konnunaho, J., Sorjonen-Ward, P., 2012. Archaean complexes of the Karelia Province in Finland. *The Archaean of the Karelia Province in Finland.* Geological Survey of Finland, Espoo, Special Papers 54, 9–20.

Koistinen, T., Stephens, M., Bogatchev, V., Nordgulen, Ø., Wennerström, M., Korhonen, J., 2001. Geological map of the Fennoscandian Shield 1: 2 000 000. Espoo: Geological Survey of Finland, Trondheim: Geological Survey of Norway, Uppsala: Geological Survey of Sweden, Moscow: Ministry of Natural Resources of Russia. ISBN 951-690-812-8.

Krill, A.G., 1985. Rb-Sr, U-Pb and Sm-Nd isotopic dates from Precambrian rocks of Finnmark. Geological Survey of Norway Bulletin 403, 37–54.

Latypov, R., 2015. Basal Reversals in Mafic Sills and Layered Intrusions. In: Charlier, B., Namur, O., Latypov, R.M., Tegner, C. (Eds.), Layered Intrusions. Springer, Netherlands, pp. 259–293.

Lauri, L.S., Andersen, T., Hölttä, P., Huhma, H., Graham, S., 2011. Evolution of the Archaean Karelian Province in the Fennoscandian Shield in the light of U-Pb zircon ages and Sm-Nd and Lu-Hf isotope systematics. J. Geol. Soc. 168, 201–218.

Lesher, C.M., 2017. Roles of xenomelts, xenoliths, xenocrysts, xenovolatiles, residues, and skarns in the genesis, transport, and localization of magmatic Fe-Ni-Cu-PGE sulfides and chromite. Ore Geol. Rev. 90, 465–484.

Lesher, C.M., 2019. Up, down, or sideways: Emplacement of magmatic Fe–Ni–Cu–PGE sulfide melts in large igneous provinces. Can. J. Earth Sci. 56, 756–773.

Li, C., Naldrett, A.J., 1999. Geology and petrology of the Voisey's Bay intrusion: Reaction of olivine with sulfide and silicate liquids. Lithos 47, 1–31.

Luolavirta, K., 2018. Magmatic evolution of the Kevitsa igneous complex, northern Finland, and its relation to the associated Ni-Cu-(PGE) mineralization. University of Oulu, Res Terrae, p. 68.

Luolavirta, K., Hanski, E., Maier, W., Lahaye, Y., O'Brien, H., Santaguida, F., 2018a. In situ strontium and sulfur isotope investigation of the Ni-Cu-(PGE) sulfide ore-bearing Kevitsa intrusion, northern Finland. Miner. Deposita 53, 1019–1038.

Luolavirta, K., Hanski, E., Maier, W., Santaguida, F., 2018b. Characterization and origin of dunitic rocks in the NI-CU-(PGE) sulfide ore-bearing kevitsa intrusion, northern finland: Whole-rock and mineral chemical constraints. Bull. Geological Soci. Finland 90, 5–32.

Luolavirta, K., Hanski, E., Maier, W., Santaguida, F., 2018c. Whole-rock and mineral compositional constraints on the magmatic evolution of the Ni-Cu-(PGE) sulfide ore-bearing Kevitsa intrusion, northern Finland. Lithos 296–299, 37–53.

Magee, C., Stevenson, C.T.E., Ebmeier, S.K., Keir, D., Hammond, J.O.S., Gottsmann, J.H., Whaler, K.A., Schofield, N., Jackson, C.A.L., Petronis, M.S., O'Driscoll, B., Morgan, J., Cruden, A., Vollgger, S.A., Dering, G., Micklethwaite, S., Jackson, M.D., 2018. Magma Plumbing Systems: A Geophysical Perspective. J. Petrol. 59, 1217–1251.

Maier, W.D., Arndt, N.T., Curl, E.A., 2000. Progressive crustal contamination of the Bushveld Complex: evidence from Nd isotopic analyses of the cumulate rocks. Contrib. Miner. Petrol. 140, 316–327.

Maier, W.D., Barnes, S.-J., 2010. The Kabanga Ni sulfide deposits, Tanzania: II. Chalcophile and siderophile element geochemistry. Miner. Deposita 45, 443–460.

Maier, W.D., Barnes, S.J., Sarkar, A., Ripley, E., Li, C., Livesey, T., 2010. The Kabanga Ni sulfide deposit, Tanzania: I. Geology, petrography, silicate rock geochemistry, and sulfur and oxygen isotopes. Miner. Deposita 45, 419–441.

Marjanović, M., Carbotte, S.M., Carton, H., Nedimović, M.R., Mutter, J.C., Canales, J.P., 2014. A multi-sill magma plumbing system beneath the axis of the East Pacific Rise. Nat. Geosci. 7, 825–829.

McLeod, P., Sparks, R.S.J., 1998. The dynamics of xenolith assimilation. Contrib. Miner. Petrol. 132, 21–33.

Melezhik, V.A., Solli, A., Fallick, A.E., Davidsen, B., 2015. Chemostratigraphic constraints on the time of deposition of carbonate rocks in the Karasjok Greenstone Belt, northern Norway. Norw. J. Geol. 95, 299–314.

Miller, C.F., Furbish, D.J., Walker, B.A., Claiborne, L.L., Koteas, G.C., Bleick, H.A., Miller, J.S., 2011. Growth of plutons by incremental emplacement of sheets in crystal-rich host: Evidence from Miocene intrusions of the Colorado River region, Nevada, USA. Tectonophysics 500, 65–77.

Moilanen, M., Hanski, E., Yang, S.-H., 2021. Re-Os isotope geochemistry of the Palaeoproterozoic Sakatti Cu-Ni-PGE sulphide deposit in northern Finland. Ore Geol. Rev. 132, 104044.

Mungall, J.E., Kamo, S.L., McQuade, S., 2016. U-Pb geochronology documents out-of-sequence emplacement of ultramafic layers in the Bushveld Igneous Complex of South Africa. Nat. Commun. 7, 13385.

Mutanen, T., 1997. Geology and ore petrology of the Akanvaara and Koitelainen mafic layered intrusions and the Keivitsa-Satovaara layered complex, northern Finland. Geological Survey of Finland. Bulletin 395.

Mutanen, T., Huhma, H., 2001. U-Pb geochronology of the Koitelainen, Akanvaara and Keivitsa layered intrusions and related rocks. Geol. Surv. Finland Spec. Pap. 33, 229–246.

Mutanen, T., Huhma, H., 2003. The 3.5 Ga Siurua trondhjemite gneiss in the Archaean Pudasjarvi granulite belt, northern Finland. Bulletin-geological society of Finland 75, 51–68.

Naldrett, A.J., 2004. Magmatic Sulfide Deposits, 1 ed. Springer, Berlin, Heidelberg.

Namur, O., Abily, B., Boudreau, A.E., Blanchette, F., Bush, J.W.M., Ceuleneer, G., Charlier, B., Donaldson, C.H., Duchesne, J.-C., Higgins, M.D., Morata, D., Nielsen, T. F.D., O'Driscoll, B., Pang, K.N., Peacock, T., Spandler, C.J., Toramaru, A., Veksler, I. V., 2015. Igneous Layering in Basaltic Magma Chambers. In: Charlier, B., Namur, O., Latypov, R., Tegner, C. (Eds.), Layered Intrusions. Springer, Netherlands, pp. 75–152.

Nebel, O., Sossi, P.A., Ivanic, T.J., Benard, A., Gardiner, N.J., Langford, R.L., Arculus, R. J., 2020. Incremental Growth of Layered Mafic-Ultramafic Intrusions Through Melt Replenishment Into a Crystal Mush Zone Traced by Fe-Hf Isotope Systematics. Front. Earth Sci. 8, 1–10.

Nowell, G., Kempton, P., Noble, S., Fitton, J., Saunders, A., Mahoney, J., Taylor, R., 1998. High precision Hf isotope measurements of MORB and OIB by thermal ionisation mass spectrometry: insights into the depleted mantle. Chem. Geol. 149, 211–233.

Orvik, A.A., Slagstad, T., Hansen, H., Nilsson, L.P., Sørensen, B.E., 2022. The Palaeoproterozoic Gallujavri ultramafic intrusion, Karasjok Greenstone Belt; petrogenesis of a trans-crustal magma system. J. Petrol. 63, 28.

Peate, D.W., Barker, A.K., Riishuus, M.S., Andreasen, R., 2008. Temporal variations in crustal assimilation of magma suites in the East Greenland flood basalt province: Tracking the evolution of magmatic plumbing systems. Lithos 102, 179–197.

Puchtel, I.S., Mundl-Petermeier, A., Horan, M., Hanski, E.J., Blichert-Toft, J., Walker, R. J., 2020. Ultra-depleted 2.05 Ga komatiites of Finnish Lapland: Products of grainy late accretion or core-mantle interaction? Chem. Geol. 554, 119801.

Robertson, J., Ripley, E.M., Barnes, S.J., Li, C., 2015. Sulfur liberation from country rocks and incorporation in mafic magmas. Econ. Geol. 110, 1111–1123.

Romer, R.L., 1996. U-Pb systematics of stilbite-bearing low-temperature mineral assemblages from the Malmberget iron ore, northern Sweden. Geochim. Cosmochim. Acta 60, 1951–1961.

Santaguida, F., Luolavirta, K., Lappalainen, M., Ylinen, J., Voipio, T., Jones, S., 2015. The Kevitsa Ni-Cu-PGE Deposit in the Central Lapland Greenstone Belt in Finland. In: Maier, W.D., Lahtinen, R., O'Brien, H. (Eds.), Mineral Deposits of Finland, First ed. Elsevier, Amsterdam, Netherland, pp. 195–210.

Scoates, J.S., Friedman, R.M., 2008. Precise Age of the Platiniferous Merensky Reef, Bushveld Complex, South Africa, By The U-Pb Zircon Chemical Abrasion ID-TIMS Technique. Econ. Geol. 103, 465–471.

Skaar, J.A.A., 2014. 3D geophysical and geological modelling of the Karasjok Greenstone Belt. Norwegian University of Science and Technology, NTNU, Department of Geoscience and Petroleum, p. 158.

Stokmo, E.B., 2020. Superimposed macro- and mesoscale folds, and their relation to ductile shear zones in the Karasjok Greenstone Belt. UiT The Arctic University of Norway, UiT, Finnmark, Norway, Department Of Geosciences, p. 61.

Sun, S.S., McDonough, W.F., 1989. Chemical and isotopic systematics of oceanic basalts: implications for mantle composition and processes. Geological Society, London, Special Publications 42, 313–345.

Wall, C.J., Scoates, J.S., Weis, D., Friedman, R.M., Amini, M., Meurer, W.P., 2018. The Stillwater Complex: Integrating Zircon Geochronological and Geochemical Constraints on the Age, Emplacement History and Crystallization of a Large, Open-System Layered Intrusion. J. Petrol. 59, 153–190.

Weaver, B.L., Tarney, J., 1984. Empirical approach to estimating the composition of the continental crust. Nature 310, 575–577.

Wilson, A.H., Zeh, A., Gerdes, A., 2017. In Situ Sr isotopes in Plagioclase and Trace Element Systematics in the Lowest Part of the Eastern Bushveld Complex: Dynamic Processes in an Evolving Magma Chamber. J. Petrol. 58, 327–360.

Yang, S.-H., Maier, W.D., Hanski, E.J., Lappalainen, M., Santaguida, F., Määttä, S., 2013. Origin of ultra-nickeliferous olivine in the Kevitsa Ni–Cu–PGE-mineralized intrusion, northern Finland. Contrib. Miner. Petrol. 166, 81–95.

Yudovskaya, M.A., Naldrett, A.J., Woolfe, J.A.S., Costin, G., Kinnaird, J.A., 2015. Reverse Compositional Zoning in the Uitkomst Chromitites as an Indication of Crystallization in a Magmatic Conduit. J. Petrol. 56, 2373–2394.

Manuscript 3

The PGE sulphide mineralisation in the Gállojávri intrusion: implications for the formation of magmatic sulphide deposit in the Karasjok Greenstone Belt, Norway

Alf Andre Orvik[1], *, Eduardo Teixeira Mansur[2], Trond Slagstad[2], Bjørn Eske Sørensen[1], Kristian Drivenes[2], Lars Petter Nilsson[2]

[1]Department of Geoscience and Petroleum, Norwegian University of Science and Technology, 7491 Trondheim, Norway; [2]Geological Survey of Norway, 7491 Trondheim, Norway.

*Corresponding author. Department of Geoscience and Petroleum, Norwegian University of Science and Technology, 7491 Trondheim, Norway. Telephone: +47 93 444 158. E-mail: alf.a.orvik@ntnu.no

Keywords: Conduit-style sulphide mineralisation, Gállojávri intrusion, Karasjok and Central Lapland Greenstone Belt, LA-ICP-MS, S-isotopes

ISBN 978-82-326-6934-9 (printed ver.)
ISBN 978-82-326-6130-5 (electronic ver.)
ISSN 1503-8181 (printed ver.)
ISSN 2703-8084 (online ver.)

NTNU

Norwegian University of
Science and Technology